archive ouverte UNIGE
http://archive-ouverte.unige.ch

Thesis

Supersymmetric Beasts and Where to Find Them: from Novel Hadronic Reconstruction Methods to Search Results in Large Jet Multiplicity Final States at the ATLAS Experiment

VALENTE, Marco

Abstract

La supersymétrie (SUSY), une des extensions les plus attractives du Modèle Standard (MS), prédit l'existence d'un partenaire pour chaque particule du MS en introduisant une symétrie fermion-boson. Cette théorie offre une réponse à plusieurs des questions encore ouvertes de la physique, comme l'origine de la matière sombre, le problème de la hiérarchie de masse du boson de Higgs et l'unification des forces élémentaires à haute énergie. Les particules SUSY pourraient se manifester de plusieurs façons dans les collisions proton-proton (p-p) du Large Hadron Collider (LHC), ce qui permet la conception de plusieurs analyses de données visant à explorer leurs signatures caractéristiques. Ce travail se focalise sur l'analyse de données de la collaboration ATLAS qui explore les longues cascades de désintégration des particules SUSY. Celles-ci résultent en des états finaux avec zéro lepton, une large multiplicité de gerbes hadroniques (8-12 gerbes) et une Quantité de Mouvement Transverse Manquante (ETmiss) modérée. La stratégie de l'analyse ainsi que les résultats obtenus utilisant les [...]

Reference

VALENTE, Marco. *Supersymmetric Beasts and Where to Find Them: from Novel Hadronic Reconstruction Methods to Search Results in Large Jet Multiplicity Final States at the ATLAS Experiment*. Thèse de doctorat : Univ. Genève, 2020, no. Sc. 5446

DOI : 10.13097/archive-ouverte/unige:137281
URN : urn:nbn:ch:unige-1372814

Available at:
http://archive-ouverte.unige.ch/unige:137281

Disclaimer: layout of this document may differ from the published version.

UNIVERSITÉ DE GENÈVE

UNIVERSITÉ DE GENÈVE
Département de physique nucléaire
et corpusculaire (DPNC)

FACULTÉ DES SCIENCES
Professeure Anna Sfyrla

Supersymmetric Beasts and Where to Find Them: From Novel Hadronic Reconstruction Methods to Search Results in Large Jet Multiplicity Final States at the ATLAS Experiment

THÈSE

présentée à la Faculté des sciences de l'Université de Genève
pour obtenir le grade de Docteur ès sciences, mention physique

par

Marco Valente

de Chiasso (TI)

Thèse N° 5446

GENÈVE
Atelier d'impression ReproMail
2020

UNIVERSITÉ
DE GENÈVE

FACULTÉ DES SCIENCES

DOCTORAT ÈS SCIENCES, MENTION PHYSIQUE

Thèse de Monsieur Marco VALENTE

intitulée :

«Supersymmetric Beasts and Where to Find Them: From Novel Hadronic Reconstruction Methods to Search Results in Large Jet Multiplicity Final States at the ATLAS Experiment»

La Faculté des sciences, sur le préavis de Madame A. SFYRLA, professeure assistante et directrice de thèse (Département de physique nucléaire et corpusculaire), Monsieur T. GOLLING, professeur associé (Département de physique nucléaire et corpusculaire), Monsieur M. SWIATLOWSKI, docteur (Patricle Physics Department, TRIUMF Particle Accelerator Centre, Vancouver (CANADA)) et Monsieur M. WEBER, professeur (Laboratorium für Hochenergiephysik (LHEP), Universität Bern, Schweiz), autorise l'impression de la présente thèse, sans exprimer d'opinion sur les propositions qui y sont énoncées.

Genève, le 30 avril 2020

Thèse - 5446 -

Le Doyen

N.B. - La thèse doit porter la déclaration précédente et remplir les conditions énumérées dans les "Informations relatives aux thèses de doctorat à l'Université de Genève".

To my family,
because love is still today the strongest fundamental
force that humans have ever observed.

Alla mia famiglia,
perché l'amore é tutt'oggi la forza fondamentale
più forte che l'umanità abbia mai osservato.

RESUMÉ

La supersymétrie (SUSY), une des extensions les plus attractives du Modèle Standard (MS), prédit l'existence d'un partenaire pour chaque particule du MS en introduisant une symétrie fermion-boson. Cette théorie offre une réponse à plusieurs des questions encore ouvertes de la physique, comme l'origine de la matière sombre, le problème de la hiérarchie de masse du boson de Higgs et l'unification des forces élémentaires à haute énergie. Les particules SUSY pourraient se manifester de plusieurs façons dans les collisions proton-proton (p-p) du Large Hadron Collider (LHC), ce qui permet la conception de plusieurs analyses de données visant à explorer leurs signatures caractéristiques.

Ce travail se focalise sur l'analyse de données de la collaboration ATLAS qui explore les longues cascades de désintégration des particules SUSY. Celles-ci résultent en des états finaux avec zéro lepton, une large multiplicité de gerbes hadroniques (8-12 gerbes) et une Quantité de Mouvement Transverse Manquante (E_T^{miss}) modérée. La stratégie de l'analyse ainsi que les résultats obtenus utilisant les $139\,fb^{-1}$ de données du détecteur ATLAS à $\sqrt{s} = 13\,TeV$ pendant la durée complète du Run 2 du LHC sont présentés. Aucun excès par rapport à la prédiction du Modèle Standard n'a été trouvé, et plusieurs limites d'exclusions à 95% CL ont été placées sur différents modèles simplifiés de supersymétrie.

Cette analyse de données est la première analyse d'ATLAS à utiliser l'algorithme de reconstruction "Particle Flow" pour les gerbes hadroniques et E_T^{miss}, une technique qui combine l'information de plusieurs sous-détecteurs, ce qui permet d'améliorer la précision de reconstruction et donc la sensibilité à de la nouvelle physique. Ce travail décrit le développement de Particle Flow E_T^{miss}, une nouvelle technique de reconstruction pour cette quantité qui a été commissionnée pendant le Run 2 du LHC. Les améliorations fournies par cette quantité par rapport à la reconstruction actuelle, basée sur la seule information du calorimètre, sont démontrées. Ce travail présente également des nouvelles idées pour la suppression de la composante neutre des interactions p-p multiples du LHC (pileup). Ces études ont été réalisées dans le contexte de Particle Flow en utilisant des techniques d'analyse multivariée des données. À l'avenir, ces idées pourraient améliorer encore davantage la stabilité de l'algorithme Particle Flow d'ATLAS à ces effets.

En 2026, le LHC sera modernisé avec le High-Luminosity LHC (HL-LHC), qui sera capable de délivrer une luminosité cinq fois plus élevée comparée à la valeur de design du LHC. Ceci résultera en une augmentation du pileup et du taux des données, dépassant les fonctionnalités actuelles du détecteur ATLAS. Une révision du trigger et du système d'acquisition des données sera donc indispensable pour la réalisation du programme de physique du HL-LHC. De plus, un nouveau système de hardware tracking pour le trigger (HTT) sera inclus afin de réduire le taux de données et d'augmenter la sensibilité à la nouvelle physique. Ce travail présente aussi des études sur la suppression du pileup dans des sélections avec E_T^{miss} et avec plusieurs gerbes hadroniques (multi-jet), grâce aux traces fournies par le système

HTT. Ces études montrent une réduction significative du taux d'événements pour ces signatures, ce qui permet d'augmenter l'efficacité de détection de signaux physiques importants comme $ZH \to b\bar{b}\nu\bar{\nu}$ et $HH \to b\bar{b}b\bar{b}$.

ABSTRACT

Supersymmetry (SUSY) is one of the most appealing extensions of the Standard Model (SM), predicting the existence of a partner for each particle of the SM introducing a fermion-boson symmetry. This theory offers an answer to many of the current open questions of physics, such as the origin of Dark Matter, the Higgs boson mass hierarchy problem and the unification of elementary forces at high energy. SUSY particles could manifest themselves in different ways in the proton-proton (p-p) collisions of the Large Hadron Collider (LHC), allowing the design of dedicated searches that explore these characteristic signatures.

This work focuses on a search carried out by the ATLAS collaboration targeting SUSY particles that decay via long cascades, leading to final states with zero leptons, large jet multiplicities (8-12 jets) and moderate Missing Transverse Momentum (E_T^{miss}). The analysis strategy and results obtained using $139\,fb^{-1}$ of $\sqrt{s} = 13\,TeV$ data collected by the ATLAS experiment during the complete Run 2 of the LHC are presented. No significant excess above the SM prediction was found, and 95% CL exclusion limits were set on different simplified SUSY models.

This search is the first ATLAS analysis to use Particle Flow jet and E_T^{miss} reconstruction, a technique that combines information from different sub-detectors in order to improve the reconstruction precision and thus the sensitivity to new physics. This work describes the development of the ATLAS Particle Flow E_T^{miss}, a novel E_T^{miss} reconstruction technique commissioned during the second Run of the LHC. Improvements of this quantity with respect to standard calorimeter-based E_T^{miss} reconstruction techniques are shown. This work also presents novel ideas for the mitigation of the neutral component of the multiple p-p interactions of the LHC (pileup). These studies were made in the context of Particle Flow using multivariate analysis techniques. In future, these ideas might further improve the ATLAS Particle Flow stability to pileup.

In 2026, the LHC will be upgraded to the High-Luminosity LHC (HL-LHC), being able to deliver five times more luminosity than the original LHC design value. This will result in much higher pileup and data rates, exceeding the current design features of the ATLAS detector. The upgrade of the ATLAS Trigger and Data Acquisition system will be essential to realise the HL-LHC physics program. In this context, a novel Hardware Track Trigger (HTT) will be included for reducing the trigger rates and increase the sensitivity to new physics. This work presents a set of studies and techniques for the suppression of pileup using online HTT tracks in the context of multi-jet and E_T^{miss} triggers. These studies show significant reductions in the rates of these triggers, leading to better acceptance of important signals such as $ZH \to b\bar{b}\nu\bar{\nu}$ and $HH \to b\bar{b}b\bar{b}$.

ACKNOWLEDGMENTS

I would probably need an entire thesis to fully express my gratitude towards the many people that have contributed and sustained me during these four years as a Ph.D student. I will try to do this in a few pages here.

First of all, I want to deeply thank my mentors, Anna Sfyrla and Teng Jian Khoo, for the infinite support and advice they have provided me since the very first day of my doctoral degree. I will always remember the profound patience and enthusiasm that they used with me during these four years as a student, and I will never thank them enough for all the things that they transmitted to me, from a scientific and a personal point of view.

Secondly, I really wish to thank my colleagues, teammates and special friends of the University of Geneva (UNIGE), with whom I have shared amazing meetings, coffees, lunch breaks, beers, barbecues and ski adventures on the snow. You have always been available to support me during the difficult periods happening during every doctoral degree, and you have certainly made these moments much easier to live. Special thanks go to (without any particular order) Riccardo Poggi, Ece Akilli, Francesco Di Bello, Ettore Zaffaroni, Sofia Adorni Braccesi, Chris Delitzsch, Oliver Majersky, Anthony Lionti, Joaquin Hoya, Herjuno Nindhito, Noemi Calace, Julien Songeon, Yannick Demets, Rebecka Sax, Robert Amarinei, Francesco Lucarelli and all the other Ph.D. students of the Particle Physics department at UNIGE. Without you, these years would have never been so full of joy and I will always remember with deep affection all the moments we spent together in Geneva, at CERN and attending conferences around the world. Special thanks go also to all the ATLAS postdocs, in particular Steven Schramm, Moritz Kiehn, Olaf Nackenhorst, Andrea Coccaro, Johnny Raine, Stefan Gadatsch and Claire Antel, for having always been available to answer with infinite enthusiasm to all my questions about ATLAS, the (constantly non-working) cluster and Particle Physics. Thanks also to Sergio for letting me finish all his coffee stocks at CERN (I promise that I will pay you back one day).

CERN is an amazing place where people from all over the world join together to tackle unanswered questions of science. Inside this environment, I have had the unique chance to meet people from the entire world and to learn infinite things from them. I really want to thank all the members of the ATLAS Collaboration that contributed to my knowledge, especially the members of the ATLAS Jet/MET and SUSY groups. Among those, I really want to thank all the conveners, sub-conveners and students who contributed and supported my work with great passion and patience. In particular, I want to thank Zachary Marshall, Doug Schaefer, Emma Tolley, Claire Lee, Till Eifert, Federico Meloni, William Kalderon, Peter Loch, Marianna Testa, Francesca Ungaro, Maximilian Swiatlowski, David Miller and Christophe Clement. Special thanks to Christopher Young, for the extremely nice collaboration, for the amazing explanations about jet, MET and Particle Flow reconstruction and for assisting me when I had the crazy idea to supervise a CERN summer student. Thanks also to Melina Lüthi, for the amazing work we made together at CERN during summer

2018. Special thanks to Monica Dobre, for all the inspiring discussions, the personal support and the fantastic lessons about origami paper folding.

I also want to deeply thank my colleagues and friends of the Oxford SUSY multi-jet group, including William Fawcett, Jonathan Burr, Michael Nelson, Koichi Nagai, Alan Barr and Claire Gwenlan, from whom I have learned plenty of things during the last years and with whom I have had an immense pleasure and privilege to work with. Special thanks to Aaron O'Neill, for the fantastic efforts and for the awesome collaboration we had during my last year as a Ph.D. student in Geneva.

Last but not the least, I really also want to thank S.B. for taking care of me during the last months, for introducing me to cycling and for causing a slight delay to the submission of this thesis.

CONTENTS

1 INTRODUCTION

"Mary Lou: Are you a seeker? A seeker after truth?
a beat.
Newt: I'm more of a chaser, really."
– J.K. Rowling, *Fantastic Beasts and Where to Find Them*

What are we made of? How was the universe created and which features of nature allowed stars, planets and life to exist today? These are only some of the fundamental questions that have fascinated humans for centuries, and only partial answers to these have been found. Particle Physics provides a remarkable description of the atomic and subatomic world that, going back in time to the Big Bang, allows to explain many features of the current cosmological observations. However, not all features of our universe are currently understood and further investigations, based on the scientific method, have to be performed.

A long time has passed since ancient civilizations introduced for the first time the concept of symmetries inside art, music and mathematics. After many centuries, passing through the pioneering work of E. Noether and E. Wigner [1], physicists around the world started to understand that, similarly to how crystals are invariant under certain sets of rotation groups, symmetries can give rise to an extremely precise description of the atomic and subatomic world, also known as the *Standard Model of Particle Physics*. But, how is it possible that symmetries, a human concept expressed through mathematical laws, can describe the natural world in such a precise way? Does nature know what symmetry really is? The remarkable precision of the Standard Model suggests that this is the case, and that nature has induced in our mathematics the power to describe the natural world. However, it is not clear whether these symmetries can also describe nature at smaller and larger length scales with respect to what has been currently tested and, in this work, we will address this question.

One way to test the correctness of the Standard Model today is through dedicated physics experiments. Collider experiments are a particular category of such experiments, allowing to probe the existence of new phenomena at high energy. The Large Hadron Collider (LHC) is the largest and most energetic particle collider ever built for this scope. This machine collides protons at a center-of-mass energy of $13\,\mathrm{TeV}$ in the $27\,\mathrm{km}$ tunnel located one-hundred meters beneath the city of Geneva, in Switzerland. The ATLAS experiment is one of the apparatus recording the results of these proton-proton (p-p) collisions, chasing inconsistencies with the predictions provided by the mathematical framework of the Standard Model.

This thesis focuses on searches for new phenomena in events with high jet multiplicities produced during the Run 2 of the LHC between 2015 and 2018. Such phenomena may be interpreted within *Supersymmetry*, a popular theoretical model extending the Standard Model and aiming at solving many of its open questions such

as the origin of Dark Matter and the unification of elementary forces at high energies. This work illustrates also the recently developed ATLAS Particle Flow algorithm for jet and Missing Transverse Momentum (MET) reconstruction, a technique aiming at improving the sensitivity of these searches to new physics and the overall precision of the experiment.

This thesis is organized as follows. The first part of this work, including Chapter 2, 3, 4 and 5, is dedicated to the review of the Standard Model, Supersymmetry, the Large Hadron Collider and the ATLAS detector. After these reviews, a second part is dedicated to the performance of hadronic reconstruction in the ATLAS experiment. In particular, Chapter 6 reviews the Missing Transverse Momentum reconstruction and performance, Chapter 7 provides a description of Particle Flow jet and E_T^{miss} reconstruction commissioned during the Run 2 of the LHC. Chapter 8 provides a set of studies performed for further improvement of the current Particle Flow algorithm in the context of neutral pileup mitigation. In Chapter 9, an overview of track-based pileup mitigation techniques in multi-jet and MET triggers for High-Luminosity LHC is presented. The third part of this thesis is dedicated to description of the ATLAS search for new phenomena in events with large jet multiplicities, zero leptons and moderate E_T^{miss}. Chapter 10 provides a description of the different analysis versions performed during the second run of the LHC. Chapter 11 present the results obtained using the complete Run 2 dataset collected by the ATLAS experiment between 2015 and 2018.

PERSONAL CONTRIBUTIONS

The ATLAS collaboration is composed of more than 3000 scientists and students from all over the world working on the various operations of the experiment including the maintenance and construction of the detector, the collection and analysis of the data, the calibration of the detector, and many other tasks. The work presented in this thesis could not be performed by a single individual and it relies on the work of many people. The major contributions from the author of this thesis are listed below.

PART II — HADRONIC EVENT RECONSTRUCTION, PERFORMANCE AND PILEUP SUPPRESSION

The author was one of the major contributors to the commissioning of the ATLAS Particle Flow algorithm during the LHC Run 2. These contributions focused on the Missing Transverse Momentum (MET) reconstruction through the performance evaluation using early Run 2 data. This lead to the first publication documenting the ATLAS Particle Flow MET reconstruction in Run 2 [2].

The author has also significantly contributed to the offline MET reconstruction operations during the Run 2 of the LHC, studying the performance of this quantity during the 2015-2016 data taking periods and developing the framework necessary for the estimation of systematic uncertainties used by the ATLAS collaboration in Run 2. The uncertainties estimation was provided also for Particle Flow MET reconstruction.

The author is the principal designer and developer of the multivariate neutral pileup suppression techniques described in Chapter 8. Studies and plots have been made together with the CERN summer student (Melina Lüthi) and the master student (Julien Songeon) that the author supervised for the development of these techniques during 2018-2019.

The author has also made the studies, illustrated in Chapter 9, for the mitigation of pileup jets in multi-jet and MET triggers for the ATLAS trigger upgrade for High-Luminosity LHC. These studies document the features of the future ATLAS online tracking system, known as Hardware Track Trigger (HTT). This work is included in the Technical Design Report (TDR) of the upgraded ATLAS Phase-II Trigger and Data Acquisition system [3].

PART III — THE HUNT FOR NEW PHENOMENA IN SIGNATURES WITH LARGE JET MULTIPLICITIES

The author has been one of the main analyzers of the ATLAS zero-lepton search for new phenomena in events with large jet multiplicities and Missing Transverse Momentum using the complete Run 2 dataset. Contributions focused on the analysis of the collected dataset, definition of analysis objects, optimization of the analysis signal regions, estimation of Standard Model backgrounds and of experimental

systematic uncertainties. The author has also played the main role in the implementation of Particle Flow reconstruction in this analysis, leading to the first ATLAS search exploiting this novel reconstruction technique using the LHC Run 2 dataset [4]. Contributions were also made to the previous versions of this search with reduced Run 2 statistics [5, 6].

The author has also contributed to the derivation of the 95% CL exclusion limits for the ATLAS R-parity violating (RPV) reinterpretation in the context of the SUSY search mentioned above [7].

Part I

GENERAL OVERVIEW: FROM THEORY AND PHENOMENOLOGY TO EVENT RECONSTRUCTION AT THE ATLAS EXPERIMENT

2

THE STANDARD MODEL OF PARTICLE PHYSICS

"After all this time? 'Always' said Snape."
– J.K. Rowling, *Harry Potter and the Deathly Hallows*

Contents

The *Standard Model* is a theoretical model that aims at describing the properties and interactions of elementary particles composing the natural world at its most fundamental level. This model makes many predictions, some of which are tested experimentally at $O(10^{-12})$ precision [8]. We can certainly say then that, among other physical models describing the nature of the subatomic world, the Standard Model is the most descriptive and complete subatomic physical model ever created. However, it is far from being a complete model as several parameters take extremely precise values to fit certain observations[1] and it does not describe Nature in a complete way since gravity can not be accounted in its mathematical framework and it does not provide an explanation for the Dark Matter content of the universe.

The Standard Model is a Quantum Field Theory, a framework mixing *quantum mechanics* and *special relativity*, and describes elementary particles as quantizations of fields spread across the entire universe. Similarly to the classification developed by Mendeleev for the *Periodic Table of the Elements*, elementary particles can be classified through their interaction properties. In this context, as visually represented also in Figure 2.1, elementary particles can be divided in four main categories:

- The **gauge bosons**, represented by four different spin-1 particles mediating elementary forces such as the strong, electromagnetic and weak interactions. The Standard Model's gauge bosons include: the *gluon* mediating the strong force, the *photon* mediating the electromagnetic interaction and the *weak W, Z bosons* mediating the weak force.

[1] Also referred to as the *fine-tuning problems* of the Standard Model.

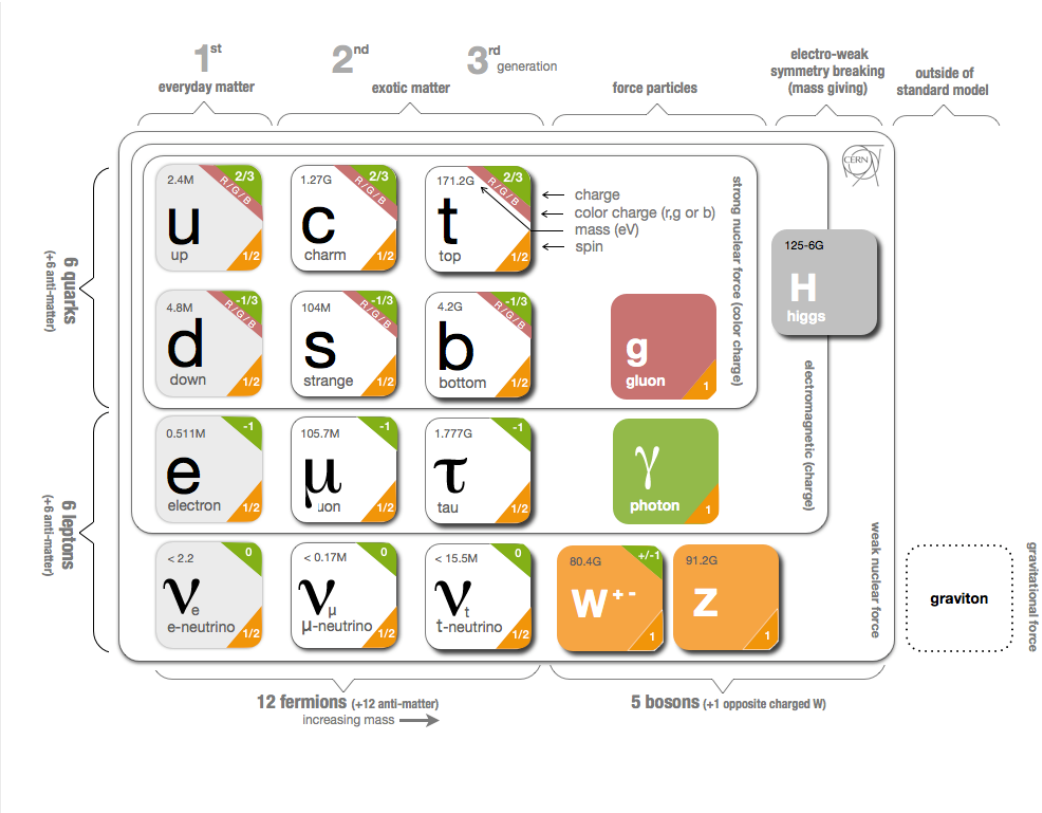

Figure 2.1 – Overview of the particles composing the Standard Model [9].

- The **quarks**, represented by six spin one-half fermions grouped in three families, being the only Standard Model fermions feeling the strong force. These particles also carry an electric and weak charge, making them interacting also through the electromagnetic and weak force. Among these particles we can find the quark *up* (u), *down* (d), *charm* (c), *strange* (s), *top* (t) and *bottom* (b).

- The **leptons** interact through the weak and electromagnetic force and are composed of electrons, muons and taus. Similarly to the quarks, leptons are also grouped in three families where each one of the previous particles is coupled to a neutrino. Neutrinos are a special type of lepton since they interact only weakly and do not carry any electric charge.

- The **Higgs boson** is the only scalar spin-zero particle of the Standard Model. Through the *spontaneous symmetry breaking* mechanism described in Section 2.3, it provides masses to the weak *W*, Z bosons and also to quarks and leptons. This boson differs from vector bosons as it couples only to particles carrying a mass, and not a charge as for the vector (spin-1) gauge bosons.

With the only exception of the top quark, quarks are only observed inside bound states known as *hadrons*. Many different types of hadrons have been observed in nature, for example *mesons* composed of two valence quarks and *baryons* composed of three valence quarks. However, hadrons also contain "sea quarks" represented by quark-antiquark pairs bound together to the valence quarks through the strong force

mediated by gluons. Typical examples of mesons are *pions* formed by combinations of up and down quarks whereas baryons are generally represented by protons and neutrons. Further states also exists, such as the recently discovered pentaquarks [10] having spin $3/2$ and $5/2$. Due to its large mass, the top quark decays very quickly ($\tau = \hbar/\Gamma \approx 5 \times 10^{-25}$ s where $\Gamma_t = 1.41$ GeV [11]) and it does not have the necessary time to create a bound state together with other quarks.

This chapter illustrates the Standard Model using the quantum field theory mathematical framework and it is largely based on the works of [12, 13, 14]. The Standard Model is described by a non-abelian Yang-Mills theory based on the invariance of the theory from the $SU(3)_C \otimes SU(2)_L \otimes U(1)_Y$ group. From Noether's theorem [1], it is well known that for each of these symmetry groups corresponds a conserved quantity, generally referred to as the *charges* of the symmetry group. For the $SU(3)_C$ group describing the strong interaction (also known as *Quantum Chromodynamics*) as illustrated in Section 2.1, three charges are present, and called *color charges* (or simply *colors*). The $SU(2)_L \times U(1)_Y$ group describes the electroweak interaction, resulting from the unification of the weak and electromagnetic forces. Two charges are associated to this symmetry group: the electric charge and the weak hypercharge described further in Section 2.2.

A short review of these theories and of gauge invariance is provided in the next sections but more details can be found in Appendix A.

2.1 QUANTUM CHROMODYNAMICS

Quantum chromodynamics (QCD) is the Yang-Mills theory associated to the symmetry group $SU(3)_C$ and it describes the strong interaction binding together the atomic nuclei. The number of degrees of freedom associated to this group is exactly 8 (further details can be found in Section A.2.2), corresponding to the 8 generators and gauge bosons fields $G^\mu_a(x)$ generally called *gluons*. In this notation, $a = 1, \dots, 8$. The *triplets* $q_f^T = (q_f^1, q_f^2, q_f^3)$, where q_f^i is the quark field with *flavour* $f = u, d, c, s, t, b$ and *color* $i = 1, 2, 3$, can be used in order to build the Lagrangian in the compact form

$$\mathcal{L} = -\frac{1}{4} G^a_{\mu\nu} G^{\mu\nu}_a + \sum_f \overline{q}_f i\gamma_\mu D^\mu q_f. \tag{2.1}$$

In this expression, the quark mass term has been explicitly ignored as it will be introduced by the Higgs mechanism in Section 2.3. The $SU(3)$ transformation U is described by

$$U = \exp\left\{ i g_S \frac{\lambda_a}{2} \theta^a \right\}, \tag{2.2}$$

where $\frac{\lambda_a}{2}$ are the *generators* of the fundamental representation of the $SU(3)$ group and θ^a are arbitrary parameters, acting on the quark and gluon fields as

$$\begin{aligned} q_f &\rightarrow (q_f)' = U q_f, \\ G^\mu_a(x) &\rightarrow (G^\mu_a(x))' = U G^\mu_a(x) U^\dagger + \frac{i}{g_S} (\partial^\mu U) U^\dagger. \end{aligned} \tag{2.3}$$

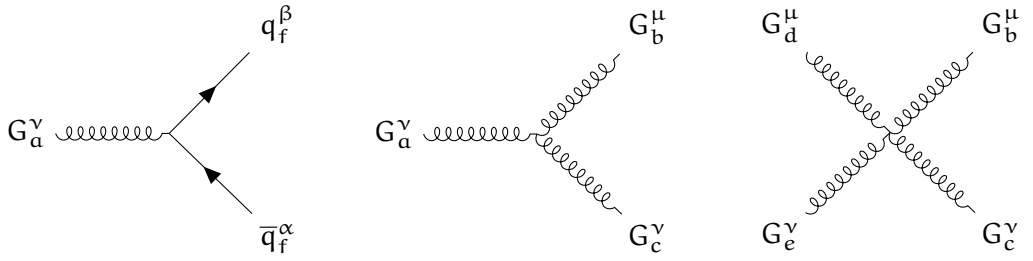

$\propto g_S \frac{\lambda^a_{\alpha\beta}}{2} \gamma_\mu$ $\propto g_S f^{abc}$ $\propto g_S^2 f^{abc} f^{ade}$

Figure 2.2 – QCD gauge interaction terms.

The *covariant derivative* D^μ, transforming as $(D^\mu)' = UD^\mu U^\dagger$, is defined as

$$D^\mu q_f = \left(\partial^\mu - i g_S \frac{\lambda^a}{2} G_a^\mu(x)\right) q_f, \tag{2.4}$$

where g_S is the *strong coupling constant* and λ^a are the *Gell-Mann matrices*:

$$\lambda^1 = \begin{pmatrix} 0 & 1 & 0 \\ 1 & 0 & 0 \\ 0 & 0 & 0 \end{pmatrix}, \quad \lambda^2 = \begin{pmatrix} 0 & -i & 0 \\ i & 0 & 0 \\ 0 & 0 & 0 \end{pmatrix}, \quad \lambda^3 = \begin{pmatrix} 1 & 0 & 0 \\ 0 & -1 & 0 \\ 0 & 0 & 0 \end{pmatrix},$$
$$\lambda^4 = \begin{pmatrix} 0 & 0 & 1 \\ 0 & 0 & 0 \\ 1 & 0 & 0 \end{pmatrix}, \quad \lambda^5 = \begin{pmatrix} 0 & 0 & -i \\ 0 & 0 & 0 \\ i & 0 & 0 \end{pmatrix}, \quad \lambda^6 = \begin{pmatrix} 0 & 0 & 0 \\ 0 & 0 & 1 \\ 0 & 1 & 0 \end{pmatrix},$$
$$\lambda^7 = \begin{pmatrix} 0 & 0 & 0 \\ 0 & 0 & -i \\ 0 & i & 0 \end{pmatrix}, \quad \lambda^8 = \frac{1}{\sqrt{3}} \begin{pmatrix} 1 & 0 & 0 \\ 0 & 1 & 0 \\ 0 & 0 & -2 \end{pmatrix}.$$

In the QCD Lagrangian provided in Equation (2.1), the gauge invariant kinetic tensors $G_a^{\mu\nu}$ are built from the gluon fields $G_\mu^a(x)$ of color a, and defined as

$$G_a^{\mu\nu} = \partial^\mu G_a^\nu - \partial^\nu G_a^\mu + g_S f^{abc} G_b^\mu G_c^\nu. \tag{2.5}$$

The QCD Lagrangian can be written in its extended form as

$$\begin{aligned} \mathcal{L} = & -\frac{1}{4} \left(\partial^\mu G_a^\nu - \partial^\nu G_a^\mu\right) \left(\partial_\mu G_\nu^a - \partial_\nu G_\mu^a\right) + \sum_f \overline{q}_f i \gamma_\mu \partial^\mu q_f \\ & - g_S f^{abc} \left(\partial_\mu G_{a\nu}\right) G_b^\mu G_c^\nu - \frac{g_S^2}{4} f^{abc} f^{ade} G_b^\mu G_c^\nu G_{d\mu} G_{e\nu} \\ & + g_S G_a^\mu \sum_f \overline{q}_f^\alpha \gamma_\mu \left(\frac{\lambda^a}{2}\right)_{\alpha\beta} q_f^\beta. \end{aligned} \tag{2.6}$$

In this expression, the first row represents the kinetic term of the gluon and quark fields. The second row represents the self-interacting terms of the gluon fields implied by the non-commutativity of the $SU(3)_C$ group and the presence of the additional terms proportional to the $SU(3)$ *structure constants* f^{abc} (see Appendix A for more details). The last row represents the gluon-quarks interaction introduced by

the gauge terms of the covariant derivative provided in Equation (2.4). Figure 2.2 shows the Feynman diagrams associated to these gauge interaction terms.

From these interaction terms it is possible to note that the strong interaction does not allow quark mixing as gluon-quark-quark interactions for different quark flavors are forbidden. This feature has deep phenomenological implications considering that only the weak interaction allows the mixing of quark families. However, a quark can change its color charge from emission or absorption of one of the eight gluons.

2.2 ELECTROWEAK UNIFICATION

The Electroweak (EW) interaction of the Standard Model is described by the symmetry group $SU(2)_L \otimes U(1)_Y$. Here, the index L denotes the act of the $SU(2)$ group on the left-handed components of the lepton and quark fields while Y denotes the *weak hyper-charge* acting on both left- and right-handed components of these fields.

Since $SU(2)_L$ acts only on the left-handed components of lepton and quark fields, it is convenient to write the left-handed components of these fields as *doublets*

$$l_L^f = \begin{pmatrix} \nu_{eL} \\ e_L \end{pmatrix}, \begin{pmatrix} \nu_{\mu L} \\ \mu_L \end{pmatrix}, \begin{pmatrix} \nu_{\tau L} \\ \tau_L \end{pmatrix}, \tag{2.7}$$

$$q_L^f = \begin{pmatrix} u_L \\ d'_L \end{pmatrix}, \begin{pmatrix} c_L \\ s'_L \end{pmatrix}, \begin{pmatrix} t_L \\ b'_L \end{pmatrix}, \tag{2.8}$$

where the fundamental representation of the $SU(2)_L$ group can act. The local transformations associated to these groups can be written as

$$U_{SU(2)_L} = \exp\left\{ig\frac{\sigma_i}{2}\alpha^i(x)\right\}, \tag{2.9}$$

$$U_{U(1)_Y} = \exp\left\{ig'\frac{Y}{2}\beta(x)\right\}, \tag{2.10}$$

where $\alpha_i(x)$ and $\beta(x)$ are general parameters of the transformation, g and g' are the *coupling constants* associated to the $SU(2)_L$ and $U(1)_Y$ gauge groups and σ_i are *Pauli matrices* generating the $SU(2)_L$ group transformations

$$\sigma_1 = \begin{pmatrix} 0 & 1 \\ 1 & 0 \end{pmatrix}, \quad \sigma_2 = \begin{pmatrix} 0 & -i \\ i & 0 \end{pmatrix}, \quad \sigma_3 = \begin{pmatrix} 1 & 0 \\ 0 & -1 \end{pmatrix}. \tag{2.11}$$

These transformations act on the left-handed lepton doublets and right-handed singlets as

$$\begin{aligned} l_L^f &\to \left(l_L^f\right)' = U_{U(1)_Y} U_{SU(2)_L}\, l_L^f, \\ e_R^f &\to \left(e_R^f\right)' = U_{U(1)_Y}\, e_R^f, \\ \nu_R^f &\to \left(\nu_R^f\right)' = U_{U(1)_Y}\, \nu_R^f. \end{aligned} \tag{2.12}$$

The same transformations are valid for q_L^f, u_R^f and d_R^f. Similarly to the QCD case described in Section 2.1, the EW Lagrangian invariant under $SU(2)_L \otimes U(1)_Y$ can be written as

$$\begin{aligned}\mathcal{L} = &-\frac{1}{4}B_{\mu\nu}B^{\mu\nu} - \frac{1}{4}W^i_{\mu\nu}W_i^{\mu\nu} \\ &+ \sum_f \bar{l}_L^f i\gamma_\mu D^\mu l_L^f + \bar{\nu}_R^f i\gamma_\mu D^\mu \nu_R^f + \bar{e}_R^f i\gamma_\mu D^\mu e_R^f \\ &+ \sum_f \bar{q}_L^f i\gamma_\mu D^\mu q_L^f + \bar{u}_R^f i\gamma_\mu D^\mu u_R^f + \bar{d}_R^f i\gamma_\mu D^\mu d_R^f,\end{aligned} \tag{2.13}$$

where $B^{\mu\nu}$ and $W_i^{\mu\nu}$ are the kinetic gauge tensor associated to the $U(1)_Y$ and $SU(2)_L$ groups described by

$$\begin{aligned}W_i^{\mu\nu} &= \partial_\mu W_\nu^i - \partial_\nu W_\mu^i + g f^{abc} W_\mu^i W_\nu^i, \\ B^{\mu\nu} &= \partial_\mu B_\nu - \partial_\nu B_\mu.\end{aligned} \tag{2.14}$$

We remark that the gauge invariance of the W_i^μ, B_μ fields implies once again the absence of any mass term associated to these gauge fields. The generation of this mass term represents the central motivation for the Higgs mechanism described later in Section 2.3.

The covariant derivatives applied in Equation (2.13) are defined according to the acting of the $SU(2)_L$ and $U(1)_Y$ groups on the left-handed and right-handed Dirac spinors

$$\begin{aligned}D^\mu l_L^f &= \left(\partial^\mu - ig\frac{\sigma_i}{2}W_i^\mu - ig'\frac{Y}{2}B^\mu\right) l_L^f, \\ D^\mu e_R^f &= \left(\partial^\mu - ig'\frac{Y}{2}B^\mu\right) e_R^f, \\ D^\mu \nu_R^f &= \left(\partial^\mu - ig'\frac{Y}{2}B^\mu\right) \nu_R^f.\end{aligned} \tag{2.15}$$

The same relations are valid for spinor quantities associated to quarks: q_L^f, u_R^f and d_R^f. The transformations of the lepton, quark and gauge fields are identical to the ones introduced for QCD in Equation (2.3).

Despite the fact that 4 gauge fields have been introduced for the description of the electroweak interactions (three associated to $W_i^\mu(x)$ and one associated to $B^\mu(x)$), these do not correspond yet to the *photon* and weak gauge bosons $W^\pm, Z$ introduced at the beginning of this chapter. In the next sections we will quickly discuss the derivation of such gauge boson fields by splitting the interaction terms of the EW Lagrangian into charged and neutral interactions.

2.2.1 *Charged interactions*

Electroweak charged interactions consist of the interaction terms of the EW Lagrangian provided in Equation (2.13) corresponding to a lepton-neutrino or up-type-down-type quark transition. These interactions are described by the off-diagonal terms of the $SU(2)_L$ generators (*i.e.* the Pauli matrices) and, as seen in Equation

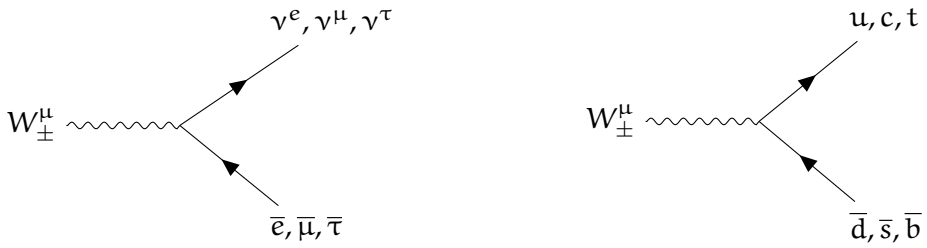

$$\propto \frac{g}{2\sqrt{2}}\,\gamma_\mu(1-\gamma_5) \qquad \propto \frac{g}{2\sqrt{2}}\,\gamma_\mu(1-\gamma_5)V_{ud}$$

Figure 2.3 – Electroweak charged interaction terms. V_{ud} corresponds to the CKM matrix term related to the up-quark and down-type quarks $u = u, c, t$ and $d = d, s, b$.

(2.11), the only terms bringing to off-diagonal terms are σ_1 and σ_2. Therefore, the charged interaction terms of the EW Lagrangian are

$$\begin{aligned}\mathcal{L}^C_{int} = &\frac{g}{2}\sum_f \bar{l}^f_L \gamma_\mu \left(\sigma_1 W^\mu_1 + \sigma_2 W^\mu_2\right) l^f_L \\ &+ \frac{g}{2}\sum_f \bar{q}^f_L \gamma_\mu \left(\sigma_1 W^\mu_1 + \sigma_2 W^\mu_2\right) q^f_L.\end{aligned} \tag{2.16}$$

In order to observe the gauge fields associated to the $W^\pm$ bosons, it is necessary to rewrite these terms as function of the complete diagonal basis given by

$$\sigma^+ = \frac{1}{2}\left(\sigma_1 + i\sigma_2\right) = \begin{pmatrix} 0 & 1 \\ 0 & 0 \end{pmatrix} \tag{2.17}$$

$$\sigma^- = \frac{1}{2}\left(\sigma_1 - i\sigma_2\right) = \begin{pmatrix} 0 & 0 \\ 1 & 0 \end{pmatrix} \tag{2.18}$$

such that, by defining the new gauge fields $W^\mu_+(x)$ and $W^\mu_-(x)$ as

$$W^\mu_\pm(x) = \frac{1}{\sqrt{2}}\left(W^\mu_1(x) \mp i W^\mu_2(x)\right), \tag{2.19}$$

it is easy to show that the interaction term of Equation (2.16) becomes, in the compact form

$$\begin{aligned}\mathcal{L}^C_{int} = &-\frac{g}{2\sqrt{2}}\left(\bar{\nu}^e, \bar{\nu}^\mu, \bar{\nu}^\tau\right)\gamma_\mu(1-\gamma_5)W^\mu_+ \begin{pmatrix} e \\ \mu \\ \tau \end{pmatrix} \\ &-\frac{g}{2\sqrt{2}}\left(\bar{u}, \bar{c}, \bar{t}\right)\gamma_\mu(1-\gamma_5)W^\mu_+ V_{CKM} \begin{pmatrix} d \\ s \\ b \end{pmatrix} + \text{h.c.}\end{aligned} \tag{2.20}$$

Here, V_{CKM} is the *Cabibbo-Kobayashi-Maskawa (CMK) unitary matrix* [11] providing the quark mixing through

$$\begin{pmatrix} d' \\ s' \\ b' \end{pmatrix} = V_{CKM} \begin{pmatrix} d \\ s \\ b \end{pmatrix} = \begin{pmatrix} V_{ud} & V_{us} & V_{ub} \\ V_{cd} & V_{cs} & V_{cb} \\ V_{td} & V_{ts} & V_{tb} \end{pmatrix} \begin{pmatrix} d \\ s \\ b \end{pmatrix}. \tag{2.21}$$

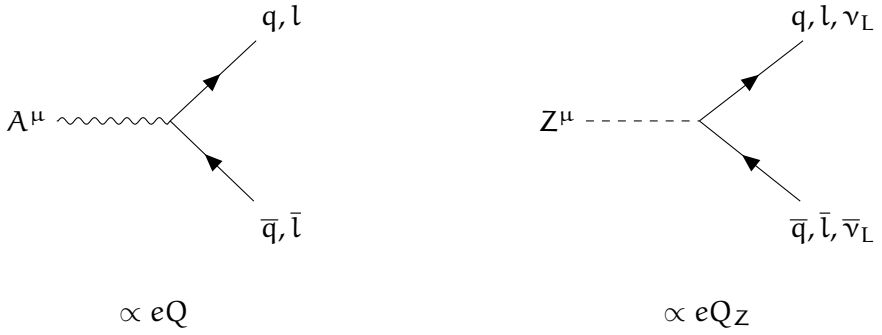

Figure 2.4 – Electroweak neutral interaction terms.

Figure 2.3 shows the Feynman diagrams associated to these charged interactions through the $W^\pm$ bosons. The precision on the single terms of V_{CKM} ranges from $O(10^{-2})$ to $O(10^{-4})$ [11], and the unitarity of the matrix is tested at high precision today. Further investigations on the violation of this unitarity due to the presence of new physics are currently performed at different experimental facilities, such as LHCb (LHC, CERN) and Belle II (SuperKEKB, Japan).

2.2.2 *Neutral interactions*

Neutral EW interactions correspond to the diagonal interaction terms of the EW Lagrangian provided in Equation (2.13). These interactions are described by the diagonal terms of the $SU(2)_L$ generators (*i.e.* Pauli matrices) as well as the interaction terms of the right-handed spinors. Looking at Equation (2.11), the only diagonal terms are those invoking the right-handed spinor plus the ones proportional to σ_3. Therefore, the neutral interaction terms of the EW Lagrangian are

$$\begin{aligned}\mathcal{L}^N_{int} = &\frac{g}{2}\sum_f W^\mu_3 \left(\overline{\nu}^f_L \gamma_\mu \nu^f_L - \overline{e}^f_L \gamma_\mu e^f_L\right) \\ &+ \frac{g'}{2}\sum_f Y\, B^\mu \left(\overline{\nu}^f_L \gamma_\mu \nu^f_L + \overline{e}^f_L \gamma_\mu e^f_L + \overline{\nu}^f_R \gamma_\mu \nu^f_R + \overline{e}^f_R \gamma_\mu e^f_R\right),\end{aligned} \tag{2.22}$$

or, in the compact form

$$\mathcal{L}_n = \sum_f \sum_{i=q,l} \overline{\Psi}^f_i \, \gamma_\mu \left(g T_3 W^\mu_3 + g' \frac{Y}{2} B^\mu\right) \Psi^f_i. \tag{2.23}$$

Here, Ψ is a column vector formed with all left-handed and right-handed fields of the theory (*i.e.* quarks and leptons) and T_3 is a new tensor defined with the following values

$$\begin{gathered}T_3(\nu^f_L) = T_3(u^f_L) = +\frac{1}{2}, \qquad T_3(e^f_L) = T_3(d^f_L) = -\frac{1}{2}, \\ T_3(\nu^f_R) = T_3(e^f_R) = T_3(u^f_R) = T_3(d^f_R) = 0.\end{gathered} \tag{2.24}$$

A valid description of the Weak and Electromagnetic interactions can be derived once the fields B^μ, W^μ_3 are rotated by an angle θ_W

$$\begin{pmatrix} B^\mu \\ W^\mu_3 \end{pmatrix} = \begin{pmatrix} \cos\theta_W & -\sin\theta_W \\ \sin\theta_W & \cos\theta_W \end{pmatrix} \begin{pmatrix} A^\mu \\ Z^\mu \end{pmatrix}. \tag{2.25}$$

Fermion	Electric charge Q	T_3	Y	Weak charge Q_Z $(\cdot \cos\theta_W \sin\theta_W)$
ν_L^f	0	$+\frac{1}{2}$	-1	$\frac{1}{2}$
e_L^f	-1	$-\frac{1}{2}$	-1	$-\frac{1}{2}+\sin^2\theta_W$
ν_R^f	0	0	0	0
e_R^f	-1	0	-2	$\sin^2\theta_W$
u_L^f	$+\frac{2}{3}$	$+\frac{1}{2}$	$+\frac{1}{3}$	$\frac{1}{2}-\frac{2}{3}\sin^2\theta_W$
d_L^f	$-\frac{1}{3}$	$-\frac{1}{2}$	$+\frac{1}{3}$	$-\frac{1}{2}+\frac{1}{3}\sin^2\theta_W$
u_R^f	$+\frac{2}{3}$	0	$+\frac{4}{3}$	$-\frac{2}{3}\sin^2\theta_W$
d_R^f	$-\frac{1}{3}$	0	$-\frac{2}{3}$	$\frac{1}{3}\sin^2\theta_W$

Table 2.1 – Electroweak charges for leptons and quarks.

θ_W is commonly known as the *Weinberg angle* or the *weak mixing angle*. By substituting inside Equation (2.23) we obtain a new compact Lagrangian under the form

$$\begin{aligned}\mathcal{L}_{\text{int}}^{N} = &\sum_f \sum_{i=q,l} \overline{\Psi}_i^f \gamma_\mu \left(g \sin\theta_W T_3 + g' \frac{Y}{2} \cos\theta_W \right) \Psi_i^f A^\mu + \\ &+ \sum_f \sum_{i=q,l} \overline{\Psi}_i^f \gamma_\mu \left(g \cos\theta_W T_3 - g' \frac{Y}{2} \sin\theta_W \right) \Psi_i^f Z^\mu,\end{aligned} \tag{2.26}$$

where the term proportional to A^μ has to match the EM interaction term given by [13]

$$\mathcal{L}_{\text{int}}^{EM} = e\left(\overline{e}_L \gamma^\mu e_L + \overline{e}_R \gamma^\mu e_R\right) A^\mu = e\overline{\Psi}\gamma^\mu Q \Psi A^\mu. \tag{2.27}$$

In this formula, Q corresponds to the electromagnetic charge obtained in the theory of Quantum Electrodynamics (QED). Therefore, it is simple to show that these terms are matched if

$$g' \cos\theta_W = g \sin\theta_W = e, \tag{2.28}$$

and if the hyper-charge Y, the electric charge Q and the tensor T_3 satisfies

$$\boxed{Q = T_3 + \frac{Y}{2}.} \tag{2.29}$$

Using these relations, it is possible to further simplify the neutral interaction Lagrangian provided inside Equation (2.26) and write it as

$$\mathcal{L}_{\text{int}}^{N} = \sum_f \sum_{i=q,l} e\overline{\Psi}_i^f \gamma^\mu Q \Psi_i^f A^\mu + e\overline{\Psi}_i^f \gamma^\mu Q_Z \Psi_i^f Z^\mu, \tag{2.30}$$

where

$$Q_Z = \frac{1}{\sin\theta_W \cos\theta_W}\left(T_3 - Q\sin^2\theta_W\right) \tag{2.31}$$

is the *weak charge*. Therefore, from the rotation of this neutral interaction Lagrangian by an angle θ_W two interaction terms, corresponding to the photon and Z-boson interactions, have been obtained.

Table 2.1 report a summary of the values of Y, Q, Q_Z and T_3 for each lepton and quark. From this table, it is possible to see that $Q(\nu_{eR}) = Q_Z(\nu_{eR}) = 0$,

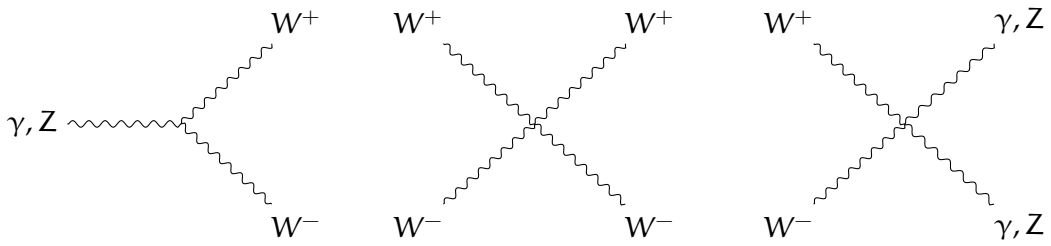

Figure 2.5 – Electroweak self-interaction terms.

implying that **right-handed neutrinos are completely decoupled from the Weak and Electromagnetic interactions** and so they are completely non-interacting (or *sterile*) particles. Due to this reason, only left-handed neutrinos interact weakly implying that the Z-boson can decay to left-handed neutrinos leading to important phenomenological consequences at particle colliders where Z-bosons are abundantly produced. This feature is represented also in Figure 2.4, where Feynman diagrams associated to EW neutral interaction terms are shown.

2.2.3 *Gauge bosons self-interactions*

It is possible to show that the kinetic terms of Equation (2.13) lead to the self-interacting terms of the W,Z and photon fields through

$$\begin{aligned}\mathcal{L}_{\text{kin}} = &-\frac{1}{4}F_{\mu\nu}F^{\mu\nu} - \frac{1}{4}Z_{\mu\nu}Z^{\mu\nu} - \frac{1}{4}W^{+}_{\mu\nu}W^{\mu\nu}_{-} \\ &+ ig\sin\theta_W\left(W^{+}_{\mu\nu}W^{\mu}_{-}A^{\nu} - W^{-}_{\mu\nu}W^{\mu}_{+}A^{\nu} + F_{\mu\nu}W^{\mu}_{+}W^{\nu}_{-}\right) \\ &+ ig\cos\theta_W\left(W^{+}_{\mu\nu}W^{\mu}_{-}Z^{\nu} - W^{-}_{\mu\nu}W^{\mu}_{+}Z^{\nu} + Z_{\mu\nu}W^{\mu}_{+}W^{\nu}_{-}\right) \\ &+ \frac{g^2}{2}\left(2g^{\mu\nu}g^{\rho\sigma} - g^{\mu\rho}g^{\nu\sigma} - g^{\mu\sigma}g^{\nu\rho}\right)\left[\frac{1}{2}W^{+}_{\mu}W^{+}_{\nu}W^{-}_{\rho}W^{-}_{\sigma}\right. \\ &\left. - W^{+}_{\mu}W^{-}_{\nu}\left(A_\rho A_\sigma\right)\sin^2\theta_W + Z_\rho Z_\sigma\cos^2\theta_W + 2A_\rho Z_\sigma\sin\theta_W\cos\theta_W\right]\end{aligned} \tag{2.32}$$

where the kinetic tensors are defined by

$$F^{\mu\nu} = \partial^{\mu}A^{\nu} - \partial^{\nu}A^{\nu}, \tag{2.33}$$

$$Z^{\mu\nu} = \partial^{\mu}Z^{\nu} - \partial^{\nu}Z^{\nu}, \tag{2.34}$$

$$W^{\mu\nu}_{\pm} = \partial^{\mu}W^{\nu}_{\pm} - \partial^{\nu}W^{\nu}_{\pm}. \tag{2.35}$$

Figure 2.5 shows the Feynman diagrams associated to these terms.

2.3 THE HIGGS MECHANISM

It was clear that the EW unification represented one of the greatest success of Yang-Mills theories and of the Standard Model. However, gauge invariance prevents mass terms for gauge vector bosons, implying that a piece of the puzzle is still missing for the correct description of the electroweak interaction considering the observation of two massive vector bosons associated to the W and Z bosons in 1983

by the UA1 Collaboration at the CERN Super Proton Synchrotron (SPS) [15, 16]. A very elegant solution to this problem was provided by R. Brout, F. Englert, P. Higgs, G. Guralnik, C. R. Hagen and T. Kibble in 1964 [17, 18, 19] following the work made in the context of broken symmetries for superconductivity theory with the introduction of a new complex scalar field commonly called the *Higgs field*. In 2012, after 48 years from its theorization, the massive scalar boson associated to this field known with the name of *Higgs boson* was successfully observed at CERN [20, 21] leading not only to a historical discovery, but also to an additional confirmation to the validity of the Standard Model. This section is dedicated to the description of such an important piece of the EW theory and of the Standard Model.

2.3.1 *Masses of vector bosons*

This section illustrates how the introduction of two massive complex scalar fields coupled inside an $SU(2)_L$ doublet can provide a mass to vector bosons through a process called *Spontaneous Symmetry Breaking* (SSB) or *Higgs-Kibble mechanism*. This doublet, invariant under $SU(2)_L$, can be written as

$$\Phi(x) = \begin{pmatrix} \phi_+(x) \\ \phi_0(x) \end{pmatrix}. \tag{2.36}$$

It is possile now to add to the EW Langrangian of Equation (2.13) the following potential using this new doublet

$$\mathcal{L}_H = (D^\mu \Phi)^\dagger D_\mu \Phi - V(\Phi) \tag{2.37}$$

where $V(\Phi)$ is the *Higgs potential* defined as

$$V(\Phi) = \mu^2 \Phi^\dagger \Phi + \lambda \left(\Phi^\dagger \Phi\right)^2. \tag{2.38}$$

Since $\Phi(x)$ is a $SU(2)_L$ doublet, the covariant derivative D^μ acting on this field is defined, similarly to left-handed leptons and quark components, as

$$D^\mu \Phi = \left(\partial^\mu - ig\frac{\sigma_i}{2} W_i^\mu - ig'\frac{Y}{2} B^\mu\right) \Phi. \tag{2.39}$$

Figure 2.6 shows a representation of this potential, for $\lambda > 0$ and different values of μ^2. In particular, it is possible to note how, in the case $\mu^2 < 0$, this potential has an infinite number of minima described by

$$|\Phi|^2 = \Phi^\dagger \Phi = \sqrt{-\frac{\mu^2}{2\lambda}}. \tag{2.40}$$

Additionally, it is possible to note how, by thinking of an observation point at $|\Phi|^2 = 0$, the potential is perfectly symmetric, while it is not when this observation point is moved to the local minima of the potential. This effect is crucial as it is the core idea behind the Higgs-Kibble mechanism. When the $\Phi(x)$ value is positioned at $|\Phi|^2 = 0$, everything is symmetric and gauge bosons do not carry any mass. When it moves to the minimum described by $|\Phi|^2 = \sqrt{-\frac{\mu^2}{2\lambda}}$, gauge symmetry is broken and all the

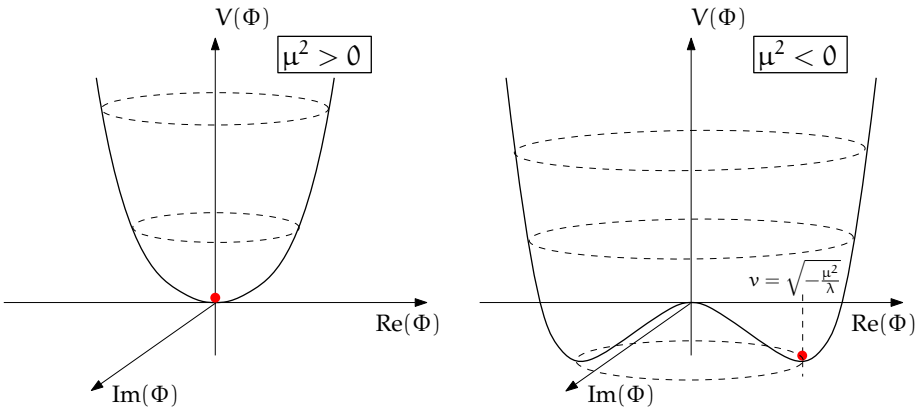

Figure 2.6 – Higgs potential representation.

Standard Model particles acquire a mass. In this scenario, we say that the symmetry is *spontaneously broken* by the new vacuum state $\langle 0|\,\phi_0(x)\,|0\rangle$.

In order to illustrate this effect, we decide to choose the minimum of this potential in

$$\langle 0|\,\phi_0(x)\,|0\rangle = \sqrt{-\frac{\mu^2}{2\lambda}}, \tag{2.41}$$

and to rotate the other components of Φ according to three new real scalar fields $\theta_i(x)$. The new parametrization for the field Φ becomes

$$\Phi(x) = \exp\left\{i\frac{\sigma_i}{2}\theta_i(x)\right\}\frac{1}{\sqrt{2}}\begin{pmatrix}0\\ H(x)+v\end{pmatrix}. \tag{2.42}$$

where $v = \sqrt{-\frac{\mu^2}{\lambda}}$ is the *vacuum expectation value* (or *VEV*). We will see that $\theta_i(x)$ corresponds to three *Goldstone bosons* that, being absorbed by the W, Z fields, provide them with masses. It will be shown that $H(x)$ is a new real scalar massive field corresponding to the *Higgs boson*.

By injecting now the new parametrization of the $\Phi(x)$ doublet around the v it is possible to see that the kinetic term of Equation (2.37) becomes

$$\begin{aligned}(D^\mu\Phi)^\dagger D_\mu\Phi = &+\frac{1}{2}\partial^\mu H\partial_\mu H\\ &+(v+H)^2\left(\frac{g^2}{4}\left(W_\mu^+\right)^\dagger W_+^\mu+\frac{g^2}{4}\left(W_\mu^-\right)^\dagger W_-^\mu+\frac{g^2}{8\cos^2\theta_W}Z_\mu Z^\mu\right).\end{aligned} \tag{2.43}$$

Here, the terms proportional to v^2 correspond to the mass terms of W_-^μ, W_+^μ and Z^μ, while the terms proportional to vH and to H^2 represent the interaction terms between the Higgs and the W, Z bosons. The photon field A^μ stays massless while the masses of the W and Z become [11]

$$M_W = \frac{vg}{2} = (80.379 \pm 0.012)\,\text{GeV}, \tag{2.44}$$

$$M_Z = \frac{vg}{2\cos\theta_W} = (91.1876 \pm 0.0021)\,\text{GeV}. \tag{2.45}$$

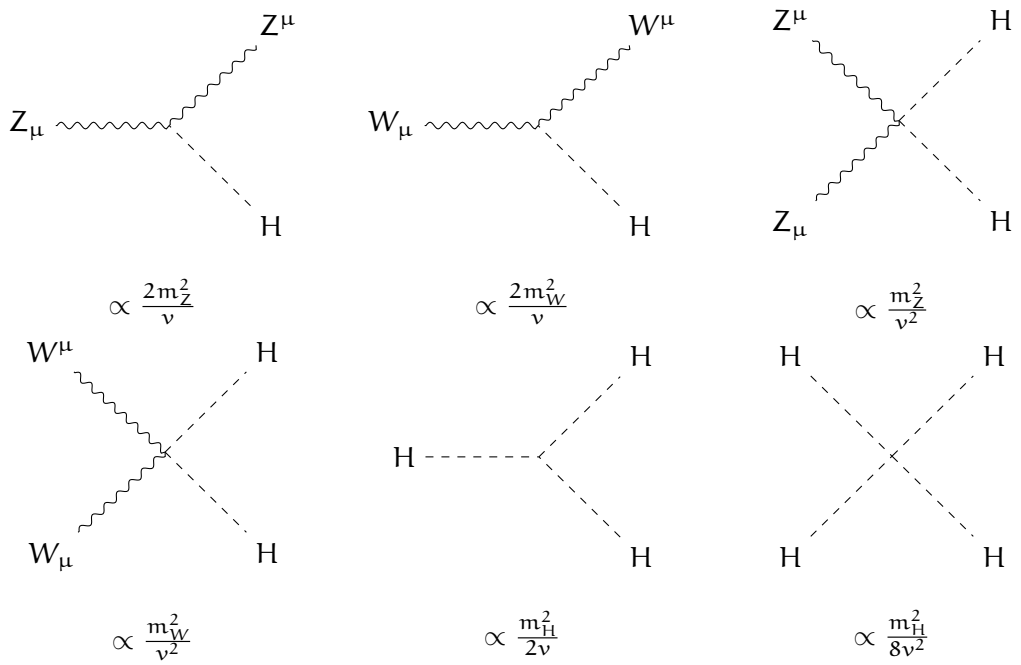

Figure 2.7 – Higgs interaction terms.

Due to this reason, photons do not interact directly with the Higgs, even though quark-mediated and W-mediated loop diagrams can lead to a Higgs-photon-photon process. The Higgs potential described inside Equation (2.38) becomes, in this new parametrization of $\Phi(x)$,

$$V(\Phi) = \frac{m_H^2}{2}H^2 + \frac{m_H^2}{2v}H^3 + \frac{m_H^2}{8v^2}H^4. \tag{2.46}$$

where the constant term has been ignored and where the term proportional to H^2 corresponds to the mass of the Higgs boson m_H defined as

$$m_H = \sqrt{-2\mu^2} = \sqrt{2\lambda}v. \tag{2.47}$$

The additional terms proportional to H^3 and H^4 are the self-interactions of the Higgs boson, created by the SSB mechanism.

All these relations between W, Z and Higgs boson are very consistent with the current observations provided by the LHC, illustrating the huge predictive power of the Standard Model [11].

2.3.2 *Masses of fermions*

It has been illustrated in the previous sections how the Higgs-Kibble mechanism can provide masses of W and Z bosons, resulting in the presence of Higgs-Z, Higgs-W and self-Higgs interactions. However, the fermion masses need an additional set of terms in the Standard Model Lagrangian in order to generate fermionic mass terms through spontaneous symmetry breaking. Fermion mass terms are forbidden

by the gauge invariance of the theory acting differently on left-handed and right-handed spinor components, making the Higgs-Kibble mechanism well suited for the generation of fermion masses.

The fermion masses can be provided by the *Yukawa interaction terms* of the Higgs [14]:

$$\mathcal{L}_Y = -\sum_f c_f^d \left(\overline{u}, \overline{d}\right)_L \Phi \, d_R - \sum_f c_f^u \left(\overline{u}, \overline{d}\right)_L \Phi^* \, u_R - \sum_f c_f^e \left(\overline{\nu}_e, \overline{e}\right)_L \Phi \, e_R + \text{h.c.} \tag{2.48}$$

After spontaneous symmetry breaking, it is possible to show that this Lagrangian becomes

$$\mathcal{L}_Y = -\frac{1}{\sqrt{2}} (v + H) \sum_f \left(c_f^d \overline{d}_f d_f + c_f^u \overline{u}_f u_f + c_f^e \overline{e}_f e_f\right). \tag{2.49}$$

The terms proportional to the VEV correspond to the mass terms of fermions, which can be written as

$$m_{d_f} = c_f^d \frac{v}{\sqrt{2}}, \quad m_{u_f} = c_f^u \frac{v}{\sqrt{2}}, \quad m_{e_f} = c_f^e \frac{v}{\sqrt{2}}. \tag{2.50}$$

The terms proportional to the Higgs field becomes Higgs-fermion-fermion interaction terms with coupling constant m_f/v. Therefore, the higher the mass of the fermion, the higher the coupling to the Higgs, as confirmed by the ATLAS and CMS experiments with the observation of the $t\bar{t}H$ and $H \to b\bar{b}$ processes [22, 23]. Figure 2.8 shows the Higgs cross-sections (normalized to Standard Model value) split by decay and production mode of the current observed Higgs modes. The compatibility of the measurements with the unity value illustrates the nice agreement of the formalism previously described with the experimental observations.

2.4 OPEN PROBLEMS AND QUESTIONS OF THE STANDARD MODEL

Figure 2.9 shows the fiducial cross sections measured by the ATLAS experiment for different Standard Model processes during Run 1 and 2. Despite the good agreement between the predictions and the observations, several questions are still open and can not be explained by the mathematical framework illustrated in the previous sections. In the following a summary of these questions is provided:

DARK MATTER

From astrophysical and cosmological results, we know that only 4% of our universe is composed of ordinary matter described by the Standard Model [12]. In fact, we know from cosmological and astronomical observations that the other 74% and 22% of the universe's energy is composed of the mysterious *dark energy* and *dark matter*. Additionally, we know that dark matter has to be more massive than other Standard Model particles (*e.g.* neutrinos) in order to be non-relativistic and form large galactic structures at the time of decoupling from the early universe plasma [12]. Considering that dark matter is also invisible in the current astronomical observations, a standard solution to this problem is the existence of a new unobserved particle - or a set of particles -

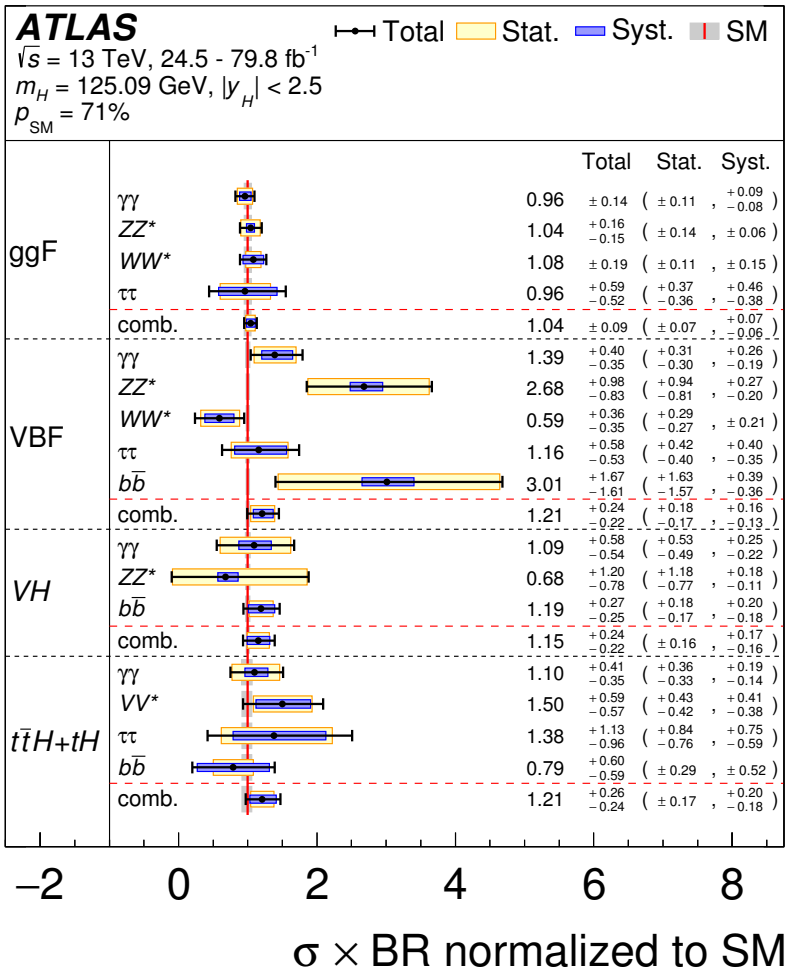

Figure 2.8 – Cross sections times branching fraction for ggF, VBF, VH and ttH+tH production in each relevant decay mode, normalized to their SM predictions [24].

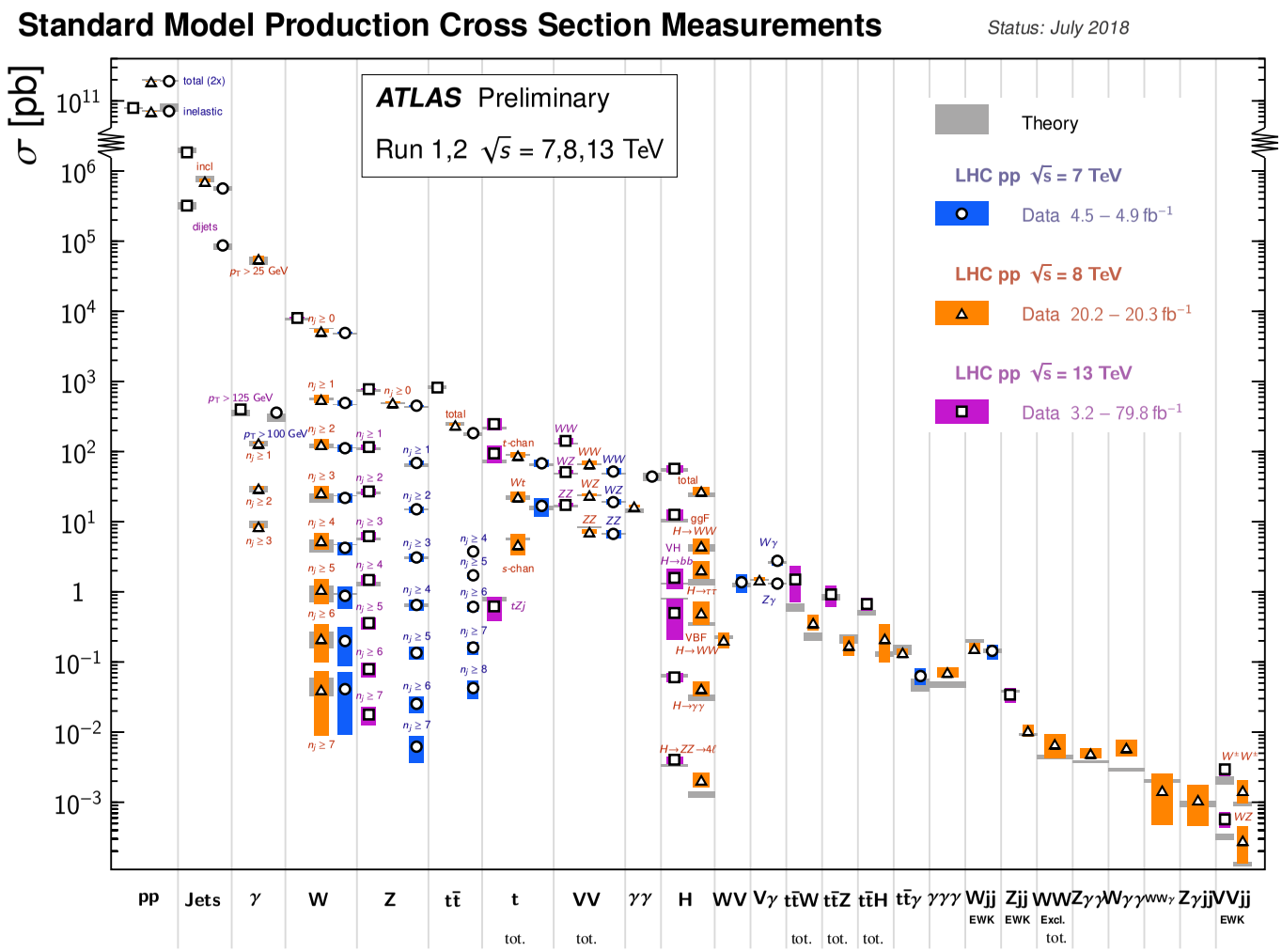

Figure 2.9 – Summary plot of the fiducial cross-sections measured by the ATLAS experiment for different processes [25].

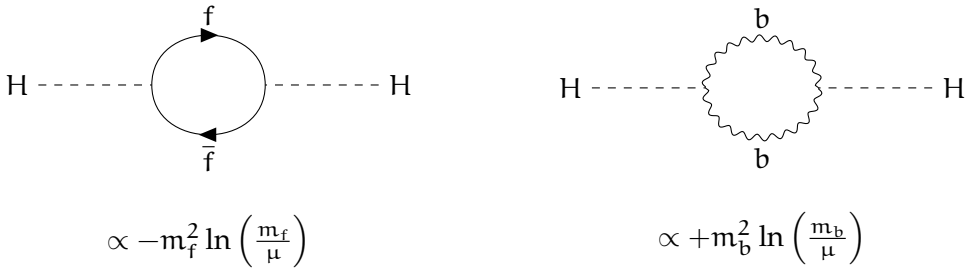

$$\propto -m_f^2 \ln\left(\frac{m_f}{\mu}\right) \qquad \propto +m_b^2 \ln\left(\frac{m_b}{\mu}\right)$$

Figure 2.10 – Higgs mass corrections from a fermions f and a boson b.

carrying a very high mass and interacting only through weak or gravitational interaction. This particle and the interactions related to its phenomenology is still unknown and it represents one of the biggest mysteries of our century.

HIERARCHY PROBLEM

As illustrated in the previous sections, the mass of the Higgs boson m_H is a free parameter of the Standard Model and it depends only on the Higgs potential and the VEV. However, the physical mass of the Higgs m_H is affected by the sum of the radiative loop corrections squared δm_H^2 as

$$m_H^2 = m_{H,0}^2 + \delta m_H^2, \tag{2.51}$$

where m_H^2 corresponds to the Higgs mass of Equation (2.47). Given that new physics is expected to be present between the electroweak and Planck scale due to the large number of unanswered question and the unification of gravity with the Standard Model, the δm_H^2 term makes the Higgs mass extremely sensitive to new physics, and with a value expected in the Planck energy scale ($m_P \approx 10^{18}\,GeV$). However, the Higgs mass has been measured to be $m_H \approx 125\,GeV$. This effect implies an exceptionally precise cancellation between $m_{H,0}$ and δm_H^2, also called *fine tuning* problem. It is known that fermions and bosons contribute with two opposite sign contributions to the Higgs mass (see Feynman diagrams of Figure 2.10)

$$\delta m_H^2 \propto -m_f^2 \ln\left(\frac{m_f}{\mu}\right), \tag{2.52}$$

$$\delta m_H^2 \propto +m_b^2 \ln\left(\frac{m_b}{\mu}\right), \tag{2.53}$$

where μ is a momentum scale. These two contributions might cancel when $m_f \approx m_b$, providing a possible solution to this problem assuming a boson-fermion symmetry (see *supersymmetry* description in Chapter 3).

UNIFICATION OF ELEMENTARY FORCES

Taking into account a theoretical simplicity argument, it is a desired feature the unification of the Standard Model $SU(3)_C \otimes SU(2)_L \otimes U(1)_Y$ into a single gauge group (*i.e.* a single force) at high energy. At 1-loop level, the Renormalization-Group (RG) equations of the Standard Model can be written as

$$\frac{d}{dt}\alpha_a^{-1}(t) = -\frac{b_a}{2\pi} \tag{2.54}$$

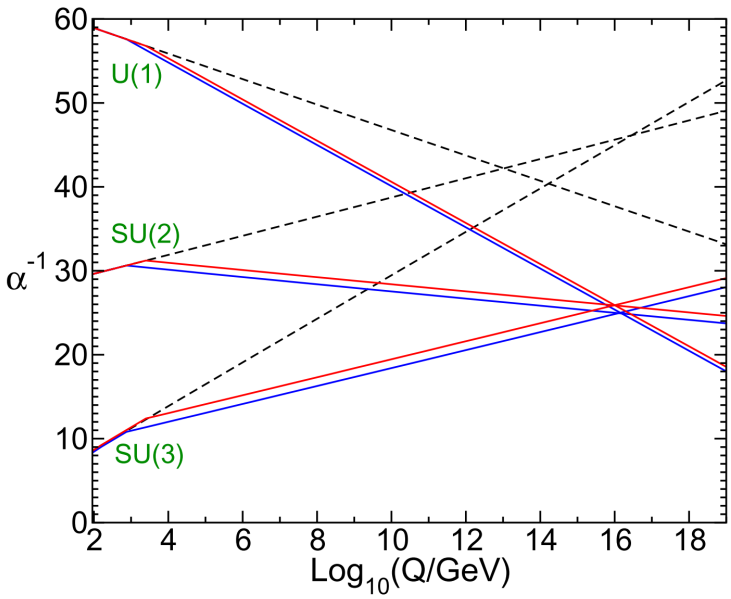

Figure 2.11 – Gauge couplings provided by the RG equations [26]. Dashed lines correspond to the Standard Model couplings, which do not merge into a single point. Solid lines corresponds to RG equations in the MSSM, which gets modified by the larger number of particles in this model. The blue and red lines corresponds to sparticle masses with a common threshold at 750 GeV and 2.5 TeV.

where Q is the RG energy scale, b_a are three constants depending on the number of particle in the theory and, for the Standard Model, these constants are $(b_1, b_2, b_3) = (41/10, -19/6, -7)$. The variable t is defined as $t = \ln(Q/Q_0)$ while α_a is defined as

$$\alpha_a = \frac{g_a^2}{4\pi}, \tag{2.55}$$

where g_1, g_2, g_3 are the Standard Model coupling constants.

Figure 2.11 shows the α_a parameters associated to these gauge couplings, and it is possible to note how these do not merge at high values of Q, creating a puzzle for the unification of forces at high energy. With supersymmetry, the $\{b_a\}$ factors are changed to $(33/5, 1, -3)$ above a certain mass threshold due to the larger number of particles in the theory, making the unification at high energy possible. This feature, together with the loop cancelations in the hierarchy mass problem previously illustrated, makes supersymmetry a good candidate for physics beyond the Standard Model at the TeV scale.

MATTER AND ANTI-MATTER ASYMMETRY

We know that the Standard Model does not allow any lepton or baryonic number violating decay. Considering that we are made of matter and not of anti-matter, and considering that before the Big Bang nothing was supposed to exist, there must be at high energy some fundamental interaction violating baryonic and leptonic number in order to explain the current universe observations. Additionally, CP-violation is also a fundamental ingredient to explain the matter-anti-matter asymmetry of the universe. Despite CP-violation is a well

known feature of weak interactions in the Standard Model, the intensity of this effect is not enough to explain the matter-dominated content of the universe, and new sources of CP-violation are expected to be present at higher energy scales.

ANOMALOUS MUON MAGNETIC MOMENT

It is well knows that particles carrying a spin $\mathbf{S}$, such as the muon, carry a magnetic moment $\mathbf{M}$ defined as

$$\mathbf{M} = g_\mu \frac{e}{2m} \mathbf{S}. \tag{2.56}$$

Here, m is the muon mass, e the fundamental charge and g_μ the muon *g-factor* taking the value of 2. This value is modified by radiative quantum corrections, making g_μ slightly larger than this value and measurable via the quantity $a_\mu = (g_\mu - 2)/2$. This quantity can be measured with extremely high precision by storing muons into storage rings using magnetic fields and then measuring the processing frequency of their spin. Recent measurements at Brookhaven National Laboratory (BNL) have reported [27]

$$\Delta a_\mu = a_\mu^{\text{obs}} - a_\mu^{\text{SM}} = (261 \pm 63 \text{ exp.} \pm 48 \text{ th.}) \cdot 10^{-11}, \tag{2.57}$$

corresponding to a 3.3σ deviation between the value experimentally measured and predicted by the Standard Model. If confirmed at 5σ in the next years, this measurement could be explained by the presence of new massive particles acting in the correction loops. Current experiments at Fermilab will soon increase the precision of this measurement, clearing the mystery behind this discrepancy of the Standard Model that stands for almost 20 years now.

2.5 CONCLUSION

This chapter introduced the Standard Model of strong and electroweak interactions, as well as the Higgs mechanism providing masses to vector boson and fermions. Additionally, some questions that this model fails to explain have also been illustrated. A popular extension of the Standard Model aiming at solving these questions is *supersymmetry*, a theory for which a description is provided in the next chapter.

3

SUPERSYMMETRY

"Ron: You're a little scary sometimes, you know that? Brilliant... but scary."
– J.K. Rowling, *Harry Potter and the Philosopher's Stone*

Contents

As described in the previous chapter, the Standard Model of high-energy physics provides a remarkably good description of the subatomic world. However, we have also seen how this theory fails to explain some important questions such as the origin the Dark Matter, the unification of elementary forces at high energy and the unification of gravity with the Standard Model. Additionally, considering the vast range between the electroweak and gravity (or Planck) energy scales[2], it is natural to expect new physics phenomena somewhere between these two energy scales.

Supersymmetry (or *SUSY*) is an extension of the Standard Model, aiming at solving several of these problems by introducing an additional symmetry between bosonic and fermionic particles. This is done by adding, for each Standard Model particle, a massive *supersymmetric partner* (or simply *super-partner*) differing by a half-integer spin from its Standard Model relative. Super-partners of fermions are generally spin-0 particles called *sfermions* – composed of *sleptons* and *squarks* – while super-partners of gauge bosons are spin-1/2 particles called *gauginos*. On the other hand, due to the impossibility to build a SUSY theory including a single Higgs doublet, two Higgs doublets are expected in the Standard Model (one coupling to up-quarks and the other to down-quarks) and four spin-1/2 super-partners of the Higgs boson are expected and referred to as *Higgsinos*.

This kind of theories started to become popular in the early 1970's with the works of Wess and Zumino [28], which are reviewed quickly in Appendix A.3. Additionally, the Coleman-Mandula theorem [29] largely restricts the possibilities of interacting

[2] We remind that the energy order of electroweak interactions is $O(100\,GeV)$, while Planck-scale gravity interactions are expected at $O(10^{18}\,GeV)$.

field theories extending the Standard Model, making supersymmetry one of the best candidates for physics beyond the Standard Model.

Similarly to *multiplets* (or *N-tuplets*) in Yang-Mills $SU(N)$ theories, SUSY single particle states are represented by *supermultiplets*. Each supermultiplet contains both fermion and boson states, which are the superpartner of each other. It can be shown that *Supercharges* Q are quantum operators transforming bosonic and fermionic states inside a supermultiplet [26]:

$$Q\,|\text{Boson}\rangle = |\text{Fermion}\rangle\,, \qquad Q\,|\text{Fermion}\rangle = |\text{Boson}\rangle\,. \tag{3.1}$$

Note that Q does not carry any spinor index here since a detailed description of these go beyond the scope of this work. In this simplified picture, the SUSY algebra is [26]

$$\{Q, Q\} = \{Q^\dagger, Q^\dagger\} = 0, \tag{3.2}$$

$$\{Q, Q^\dagger\} = P_\mu, \tag{3.3}$$

$$[Q, P_\mu] = [Q^\dagger, P_\mu] = 0. \tag{3.4}$$

These relations might seem meaningless, but they encode extremely important informations about the SUSY phenomenology. In particular, it is easy to show that Equation (3.4) imposes that the mass equality between fermionic and bosonic superpartners (*i.e.* $m_b = m_f$), since

$$\begin{aligned} m_b^2\,|\text{Boson}\rangle = P_\mu P^\mu\,|\text{Boson}\rangle &\overset{(3.1)}{=} P_\mu P^\mu Q\,|\text{Fermion}\rangle \overset{(3.4)}{=} Q P_\mu P^\mu\,|\text{Fermion}\rangle \\ &= Q m_f^2\,|\text{Fermion}\rangle = m_f^2\,|\text{Boson}\rangle\,. \end{aligned} \tag{3.5}$$

In this equation, we have considered $P_\mu P^\mu$ as the mass-squared quantum operator. However, this feature is unphysical since no bosonic partners having the same mass of electrons, muons, etc. has been observed so far. Therefore, considering that if supersymmetric partners exist their mass must be larger than the Standard Model relatives, this imposes that supersymmetry must be a broken symmetry. A possible way to solve this problem is that, similarly to how the W and Z boson acquire masses when gauge symmetry is spontaneously broken, superpartners obtain large masses through spontaneous symmetry breaking. This mechanism is also known as *spontaneous supersymmetry breaking*, and further discussion about it will be made in Section 3.1.4.

The next sections aim at reviewing the theory and phenomenology of the Minimal Supersymmetric Standard Model (MSSM) at the LHC. These are largely based on the works of [12, 30, 26].

3.1 THE MINIMAL SUPERSYMMETRIC STANDARD MODEL

The *Minimal Supersymmetric Standard Model* (MSSM) is a supersymmetric theory describing only the minimum number of new particle states and new interactions starting from the Standard Model components.

For the quark and lepton fields, superpartners are complex scalar fields (*i.e.* spin-0 particles) corresponding to the two spin states or the original particles. The

Names	Label	spin 0	spin 1/2	spin 1	$SU(3)_C \otimes SU(2)_L \otimes U(1)_Y$
Quarks, squarks	Q	$(\tilde{u}_L\ \tilde{d}_L)$	$(u_L\ d_L)$		$(3,2,\frac{1}{6})$
	$\overline{u}$	$\tilde{u}_R^*$	$u_R^\dagger$		$(3,1,-\frac{2}{3})$
	$\overline{d}$	$\tilde{d}_R^*$	$d_R^\dagger$		$(3,1,\frac{1}{3})$
Leptons, sleptons	L	$(\tilde{\nu}_L\ \tilde{e}_L)$	$(\nu_L\ e_L)$		$(1,2,-\frac{1}{2})$
	$\overline{e}$	$\tilde{e}_R^*$	$e_R^\dagger$		$(1,1,1)$
Higgs, higgsinos	H_u	$(H_u^+\ H_u^0)$	$(\tilde{H}_u^+\ \tilde{H}_u^0)$		$(1,2,+\frac{1}{2})$
	H_d	$(H_d^0\ H_d^-)$	$(\tilde{H}_d^0\ \tilde{H}_d^-)$		$(1,2,-\frac{1}{2})$
Gluon, gluino	$\widetilde{g}$		$\widetilde{g}$	g	$(8,1,0)$
W bosons, wino	$\widetilde{W}$		$\widetilde{W}^\pm, \widetilde{W}^0$	$W^\pm, W^0$	$(1,3,0)$
B boson, bino	$\widetilde{B}$		$\widetilde{B}$	B	$(1,1,0)$

Table 3.1 – Superfield content of the Minimal Supersymmetric Standard Model (MSSM).

supermultiplet associated to these fields is known as *chiral* (or *scalar*) *supermultiplet*, while the supermultiplet associated to gauge bosons is known as *vector* (or *gauge*) *supermultiplet*, and it is composed by the gauge boson and the spin-1/2 superpartners called *gauginos*. The last component of the MSSM are the spin-1/2 partners of the Higgs boson, also known as *higgsinos*. However, one chiral supermultiplet is not enough for the description of spontaneous symmetry breaking in SUSY due to the fact that one Higgs supermultiplet would lead to gauge anomalies that would be inconsistent as a quantum theory. However, two Higgs supermultiplets – one associated to up-type quarks and one to down-type quarks – would allow to solve this problem and to provide a good description of the Higgs mechanism in SUSY. Therefore, two scalar Higgs bosons are expected in the MSSM, meaning that the MSSM is a *Two-Higgs-Doublet model* (or 2HDM). Superpartners are generally labeled with the 'tilde' label, and the content of the MSSM is shown in Table 3.1.

3.1.1 *Superfields, superspace and SUSY invariant lagrangians*

We want to use now the supermultiplets in order to build a Lagrangian which is explicitly invariant under SUSY. This feature is provided by the *superfields formalism*.

In this formalism, the standard four-dimensional spacetime x^μ is extended with four anti-commuting coordinates, generally grouped into two spinors θ and $\theta^\dagger$ described by:

$$\theta = \begin{pmatrix} \theta^1 \\ \theta^2 \end{pmatrix} \quad \text{and} \quad \theta^\dagger = \begin{pmatrix} \theta^\dagger{}_1 \\ \theta^\dagger{}_{\dot{2}} \end{pmatrix}. \tag{3.6}$$

In this picture, the *action* S can be defined as

$$S = \int dx^\mu \int d^2\theta d^2\theta^\dagger \, \mathcal{L}\left(x^\mu, \theta, \theta^\dagger\right), \tag{3.7}$$

where $\mathcal{L}\left(x^\mu, \theta, \overline{\theta}\right)$ is the *superlagrangian* composed of the *superfields*

$$\Phi(x^\mu, \theta, \theta^\dagger). \tag{3.8}$$

The extension of the space-time x^μ with the four anti-commuting coordinates (also known as *Grassmann coordinates*) provided by θ and $\theta^\dagger$ is also known as the *superspace* of the theory. We remark that θ and $\theta^\dagger$ have no physical meaning, they are simply used to write supersymmetric invariant Lagrangians in a manifest way before being integrated out to form physical Lagrangians $\mathcal{L}(x^\mu)$.

In order to write down the most general SUSY invariant Lagrangian, we must define the superfields describing the chiral and gauge supermultiplets provided in Table 3.1. Is it possible to show [26], that the superfield describing the content of the most general chiral superfield composed of a scalar field $\phi(x)$ and a left-handed Weyl spinor $\psi(x)$ is provided by

$$\begin{aligned}\Phi(x, \theta, \theta^\dagger) =& \phi(x) + i\theta^\dagger \overline{\sigma}^\mu \theta \partial_\mu \phi(x) + \frac{1}{4}\theta\theta\theta^\dagger\theta^\dagger \partial_\mu \partial^\mu \phi(x) + \sqrt{2}\theta\psi(x) \\ &- \frac{i}{\sqrt{2}}\theta\theta\theta^\dagger \overline{\sigma}^\mu \partial_\mu \psi(x) + \theta\theta F(x),\end{aligned} \tag{3.9}$$

also known as *left-chiral superfield* due to the helicity of $\psi(x)$. Once this definition is included, it is possible to show that the superlagrangian defined by

$$\mathcal{L}\left(x, \theta, \theta^\dagger\right) = \Phi(x, \theta, \theta^\dagger)^* \Phi(x, \theta, \theta^\dagger), \tag{3.10}$$

provides, after integration on the superspace, a Lagrangian density corresponding to the kinetic terms of the Wess-Zumino model described in Appendix A.3

$$\begin{aligned}\mathcal{L}(x) &= \int d^2\theta d^2\theta^\dagger \left[\Phi(x, \theta, \theta^\dagger)^* \Phi(x, \theta, \theta^\dagger)\right] \\ &= -\partial^\mu \phi^*(x) \partial_\mu \phi(x) + i\psi^\dagger(x) \overline{\sigma}^\mu \partial_\mu \psi(x) + F^*(x) F(x)\end{aligned} \tag{3.11}$$

It is possible to show that any product of the left-handed chiral superfields provided in Equation (3.9) is also a left-handed chiral superfield. Additionally, since the dimension of $\phi(x)$ is 1 it is clear that also the dimension of the left-chiral superfield $\Phi(x)$ is 1. This defines the renormalizable *superpotential*

$$W(x, \theta, \theta^\dagger) = \frac{1}{2} M^{ij} \Phi_i \Phi_j + \frac{1}{6} y^{ijk} \Phi_i \Phi_j \Phi_k + \text{ h.c.} \tag{3.12}$$

where M^{ij} has dimension 1 (*i.e.* a mass dimension) and y^{ijk} has dimension zero and it corresponds, as we will see in the following sections, to the Yukawa couplings of

the Higgs superfields. It is possible to show that, after integration over the θ space we obtain the terms

$$\begin{aligned}\int d^2\theta\, W(x,\theta,\theta^\dagger) = &- M^*_{ik}M^{kj}\phi^{*i}\phi_j - \frac{1}{2}M^{ij}\psi_i\psi_j - \frac{1}{2}M^*_{ij}\psi^{\dagger i}\psi^{\dagger j} \\ &- \frac{1}{2}M^*_{in}y^{jkn}\phi^{*i}\phi_j\phi_k - \frac{1}{2}M^{in}y^*_{ikn}\phi_i\phi^{*j}\phi^{*k} - \frac{1}{2}y^{ijk}\phi_i\psi_j\psi_k \\ &- \frac{1}{2}y^*_{ijk}\phi^{*i}\psi^{\dagger j}\psi^{\dagger k} - \frac{1}{4}y^{ijn}y^*_{kln}\phi_i\phi_j\phi^{*k}\phi^{*l}\end{aligned} \tag{3.13}$$

which corresponds to the mass and interaction terms of the Wess-Zumino model. It is clear then why we call $W(x,\theta,\theta^\dagger)$ the superpotential: because it provides the interaction terms of the supersymmetric theory. The MSSM Lagrangian for a single chiral superfield is then

$$\mathcal{L}(x) = \int dx^\mu \int d^2\theta d^2\theta^\dagger \left[\Phi(x,\theta,\theta^\dagger)^*\Phi(x,\theta,\theta^\dagger)\right] + \int d^2\theta\, W(x,\theta,\theta^\dagger) \tag{3.14}$$

However, we can see that the gauge field interaction terms are missing in this Lagrangian. This is because the vector supermultipliets $V(x)$ have not been introduced this stage. It is possible to show that for each algebra generator T^a corresponding to the $SU(N)$ group the vector supermultiplet corresponding to the vector field $A^a_\mu(x)$, the spin-1/2 gaugino $\lambda^a(x)$ and the auxiliary field $D^a(x)$ is, in the Wess-Zumino gauge

$$V^a\left(x,\theta,\theta^\dagger\right) = \theta^\dagger\bar{\sigma}^\mu\theta A^a_\mu(x) + \theta^\dagger\theta^\dagger\theta\lambda^a(x) + \theta\theta\theta^\dagger\lambda^{\dagger a}(x) + \frac{1}{2}\theta\theta\theta^\dagger\theta^\dagger D^a(x). \tag{3.15}$$

It is possible to show that the supersymmetric invariant gauge interaction terms are provided by

$$\begin{aligned}\int d^2\theta d^2\theta^\dagger \left[\Phi^{*i}\left(e^{2igT^aV^a}\right)^j_i\Phi_j\right] = &-D_\mu\phi^{*i}D^\mu\phi_i + i\psi^{\dagger i}\bar{\sigma}^\mu D_\mu\psi_i \\ &- \sqrt{2}g\left(\phi^*T^a\psi\right)\lambda^a - \sqrt{2}g\lambda_{\dagger a}\left(\psi^\dagger T^a\phi\right) \\ &+ g\left(\phi^\dagger T^a\phi\right)D^a + F^{*i}F_i,\end{aligned} \tag{3.16}$$

where the D^μ, D_μ in the first rows corresponds to the covariant derivatives leading to the gauge interaction terms of the Standard Model and described in the previous sections. The second row of Equation (3.16) is extremely important as it expresses the gaugino-fermion-sfermion interaction terms. It is possible to note that gauge interaction terms are provided with the same coupling constants as the Standard Model, implying important production rates from gluons at the LHC as discussed later in this chapter.

From this section we can see that a good mnemonic rule for the SUSY interactions is to take the Standard Model interaction terms and simply exchange two fields with the superpartner fields.

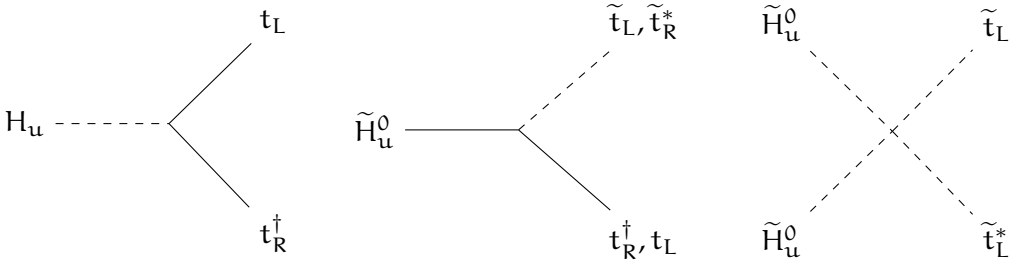

Figure 3.1 – Dominant MSSM superpotential interactions.

3.1.2 *MSSM superpotential*

It has been illustrated in the previous sections how to build a supersymmetric theory using superfields. It is now the moment to build the MSSM superpotential, providing the interaction terms of the Standard Model and of the superpartners. This superpotential can be written as

$$W_{MSSM} = \overline{u}\mathbf{y_u}QH_u - \overline{d}\mathbf{y_d}QH_d - \overline{e}\mathbf{y_e}LH_d + \mu H_u H_d, \tag{3.17}$$

where $H_u, H_d, Q, L, \overline{u}, \overline{d}, \overline{e}$ are the superfields listed in Table 3.1 and $\mathbf{y_u}, \mathbf{y_d}$ and $\mathbf{y_e}$ are the dimensionless Yukawa couplings determining, after spontaneous symmetry breaking of H_u and H_d, the masses and CKM mixing parameters associated to quarks and leptons. The interaction and mass terms provided by W_{MSSM} are provided by Equation (3.13). Figure 3.1 reports some of the interaction terms fundamental for phenomenology (see Section 3.2) where we have assumed only the presence of the top Yukawa coupling inside $\mathbf{y_u}$. It is possible to note that these diagrams, corresponding to the **Higgs-quark-quark and Higgsino-quark-squark share the same Yukawa coupling by construction**. This feature, valid also for the down-type quarks and leptons, has extremely important phenomenological effects and it illustrates a remarkable economy of supersymmetry: there are many interactions determined by one single coupling parameter. Moreover, due to the lower value of the electroweak Yukawa couplings with respect to strong interaction couplings, the production of SUSY particle at the LHC is dominated by the supersymmetric interactions of gauge-coupling strengths, as quickly explained in the previous section.

The two Higgs $SU(2)_L$ doublets will take two different vacuum expectation values (VEV) for their neutral components generating the masses of leptons, up-type and down-type quarks

$$\langle H_u^0 \rangle = v_u \quad \text{and} \quad \langle H_d^0 \rangle = v_d. \tag{3.18}$$

These two VEVs are related to the Standard Model one through the relation

$$v_u^2 + v_d^2 = v^2 = \frac{2m_Z^2}{g^2 + g'^2} \approx 174\,\text{GeV}^2, \tag{3.19}$$

where and angle β, not fixed by current and previous experiments, can be defined such as the two VEVs can be related through

$$v_u = v\sin\beta \quad \text{and} \quad v_d = v\cos\beta. \tag{3.20}$$

3.1.3 *R-parity*

Some supersymmetric Lagrangians are invariant under a global $U(1)_R$ symmetry commonly known as *R-symmetry*. This symmetry is imposed by the following transformations of the superspace coordinates

$$\theta \to e^{i\varphi}\theta, \qquad \theta^\dagger \to e^{-i\varphi}\theta^\dagger. \tag{3.21}$$

From these equations, a chiral superfield Φ will transform as

$$\Phi \to e^{ik\varphi}\Phi, \tag{3.22}$$

if

$$\phi \to e^{ik\varphi}\phi, \qquad \psi \to e^{-i(k-1)\varphi}\psi, \qquad F \to e^{-i(k-2)\varphi}F. \tag{3.23}$$

When $\varphi = \pi$, this $U(1)_R$ R-symmetry is known as *R-parity* (or *matter symmetry*). It is possible to see from Equation (3.23) that the R-parity between bosonic and fermionic states ϕ and ψ differ by a unity. From Equation (3.22) it is clear that the kinetic terms of the Wess-Zumino Lagrangian provided in Equation (3.11) are invariant under R-parity due to the multiplication of Φ by its complex conjugate. However, the renormalizable superpotential described in Equation (3.12) does not contain any term proportional to Φ^* meaning that it does not conserve R-parity in a trivial way. However, it is possible to show that all the terms of the MSSM superpotential defined in Equation (3.17) are invariant under R-parity thanks to the presence of Higgs-fermion-antifermion and Higgs-Higgs superfields interactions only, meaning that R-parity is conserved in the MSSM interactions [26]. This feature implies always the presence of two supersymmetric partners in Feynman vertices imposing that a SUSY partner can decay to a Standard Model particle plus a particle in the SUSY sector. One striking consequence of this feature is that, since there are no SUSY interactions in the MSSM implying a superpartner and two Standard Model particles, the *lightest supersymmetric particle* (LSP) could not decay to pure Standard Model states, meaning that it must be stable and have a long lifetime. As the LSP is stable and supposed of having been abundantly produced in the early phase of the universe after the Big Bang, these particles represent a perfect candidate to explain the Dark Matter content of our universe. Due to this reason, the SUSY models allowing to explain Dark Matter are generally those implying R-partity conservation, also known as *R-parity conserving* (or *RPC*) *SUSY scenarios*. Further discussion about possible terms allowing to violate R-parity are discussed later in Section 3.2.3.

R-parity can be also be associated to each MSSM particle through the equation

$$R = (-1)^{3(B-L)+2s}, \tag{3.24}$$

where B, L and s are the baryonic number, leptonic number and spin of the particle. From this expression it is possible to see that the parity between Standard Model particles and SUSY partners differ exactly by a unity.

3.1.4 *Soft supersymmetry breaking*

We have already illustrated how the algebra of supersymmetry charges imposes equal masses between Standard Model particles and respective superpartners (see

Equation (3.4)). However, SUSY particles have not yet been observed, meaning that these must exist at higher energy scales. The mechanism producing such mass difference has to be similar to the spontaneous symmetry breaking mechanism allowing to provide gauge bosons with masses in the Standard Model, and it is known in SUSY as *spontaneous supersymmetry breaking*.

In order to not break the loop corrections allowing SUSY to solve the hierarchy problem of the Higgs, this effect must be *soft*. Many different ways to break SUSY softly exists, and no physical observation indicates exactly how this is done [26]. However, it is possible to introduce in the MSSM Lagrangian some specific terms breaking SUSY and allowing to parametrize our ignorance. It is possible to show that the most general terms breaking supersymmetry in the MSSM, conserving R-parity and gauge invariance are:

$$\begin{aligned}\mathcal{L}^{\text{soft}}_{\text{MSSM}} = &-\frac{1}{2}\left(M_1\widetilde{B}\widetilde{B} + M_2\widetilde{W}\widetilde{W} + M_3\widetilde{g}\widetilde{g} + \text{ h.c.}\right)\\ &-\left(\widetilde{\bar{u}}\mathbf{a_u}\widetilde{Q}H_u - \widetilde{\bar{d}}\mathbf{a_d}\widetilde{Q}H_d - \widetilde{\bar{e}}\mathbf{a_e}\widetilde{L}H_d + \text{ h.c.}\right)\\ &-\widetilde{Q}^\dagger\mathbf{m_Q^2}\widetilde{Q} - \widetilde{L}^\dagger\mathbf{m_L^2}\widetilde{L} - \widetilde{\bar{u}}\mathbf{m_u^2}\widetilde{\bar{u}}^\dagger - \widetilde{\bar{d}}\mathbf{m_d^2}\widetilde{\bar{d}}^\dagger - \widetilde{\bar{e}}\mathbf{m_e^2}\widetilde{\bar{e}}^\dagger\\ &-m^2_{H_u}H^*_uH_u - m^2_{H_d}H^*_dH_d - (bH_uH_d + \text{ h.c.})\end{aligned} \tag{3.25}$$

In this equation, M_1, M_2 and M_3 correspond to the masses of the bino, wino and gluino while the other terms correspond to the masses of the other sfermions and symmetry-breaking contributions of the Higgs potential. It is possible to note that supersymmetry breaking, opposed to supersymmetry, introduces an extremely large number of parameters (roughly 100) in the MSSM.

3.1.5 *Charginos and neutralinos*

In the MSSM, due the effects of supersymmetry breaking and of the superpotential W_{MSSM}, the Higgsinos and and the electroweak gauginos mix with each other. In fact, in the basis formed by the neutral higgsinos (*i.e.* $\widetilde{H}^0_u$ and $\widetilde{H}^0_d$) and the neutral gauginos (*i.e.* $\widetilde{B}$ and $\widetilde{W}$) $\psi^0 = \left(\widetilde{B}, \widetilde{W}, \widetilde{H}^0_d, \widetilde{H}^0_u\right)$, the Lagrangian associated to the masses of these fields can be written as

$$\mathcal{L}_{\text{neutral mass}} = -\frac{1}{2}\left(\psi^0\right)^T\mathbf{M_N}\psi^0 + \text{ h.c.} \tag{3.26}$$

where

$$\mathbf{M_N} = \begin{pmatrix} M_1 & 0 & -g'\frac{v_d}{\sqrt{2}} & g'\frac{v_u}{\sqrt{2}} \\ 0 & M_2 & g\frac{v_d}{\sqrt{2}} & -g\frac{v_u}{\sqrt{2}} \\ -g'\frac{v_d}{\sqrt{2}} & g\frac{v_d}{\sqrt{2}} & 0 & -\mu \\ g'\frac{v_u}{\sqrt{2}} & -g\frac{v_u}{\sqrt{2}} & -\mu & 0 \end{pmatrix}. \tag{3.27}$$

In this expression, it is possible to see how the off-diagonal terms provides the mixing interactions allowing to form, after basis transformation, four diagonal mass eigenstates. These states corresponds to the *neutralinos*, noted $\widetilde{\chi}^0_1, \widetilde{\chi}^0_2, \widetilde{\chi}^0_3$ and $\widetilde{\chi}^0_4$ where the ordering is increasing in mass.

On the other hand, the charged higgsinos ($\widetilde{H}_u^+$ and $\widetilde{H}_d^-$) and winos ($\widetilde{W^+}$ and $\widetilde{W^-}$) will be subject to similar mixing effects through the matrix

$$\mathbf{M_C} = \begin{pmatrix} 0 & 0 & M_2 & g v_d \\ 0 & 0 & g v_u & \mu \\ M_2 & g v_u & 0 & 0 \\ g v_d & \mu & 0 & 0 \end{pmatrix} \tag{3.28}$$

expressed in the basis $\left(\widetilde{W^+}, \widetilde{H}_u^+, \widetilde{W^-}, \widetilde{H}_d^-\right)$. From diagonalization of this matrix, two mass eigenstates per electric charge ± 1 are formed and known as *charginos*. These states are noted $\widetilde{\chi}_1^\pm$ and $\widetilde{\chi}_2^\pm$.

When R-parity is conserved, the lightest neutralino generally provides the Dark Matter candidate, allowing to solve the Dark Matter issue of cosmology and of the Standard Model. Therefore, the phenomenology related to neutralinos and charginos is extremely important for SUSY searches and it will be discussed further in Section 3.2.

3.2 SUSY PHENOMENOLOGY AT THE LHC

Due to the large number of parameters and particles composing the SUSY particle spectrum, phenomenology of the hidden SUSY sector is very rich and largely dependent on the solutions provided to the open questions of physics discussed in the previous section. However, under some assumptions - in particular that the hierarchy mass problem is solved by SUSY - it is possible to provide a pretty clear set of signatures for SUSY at the LHC. The goal of this section is to illustrate such signatures, starting from typical productions of SUSY particles at the LHC and also the decay of the superpartners leading to new physics signatures at the LHC.

3.2.1 *SUSY production at the LHC*

If SUSY solves the hierarchy problem discussed in the previous section, the LHC has very strong chances to provide evidence for the existence of supersymmetric particles. SUSY production modes are fundamental for the identification of the best signatures for the observation of superpartners at the LHC. Differently from quark-antiquark colliders such as the Tevatron at Fermilab, the LHC can be seen as a gluon-gluon and a gluon-quark collider due to the large amount of gluons inside the proton Probability Density Functions (PDFs) [26]. Under the Higgs hierarchy mass problem constraint, gluinos, stops and sbottoms are the sparticles having the lower masses in the SUSY mass spectrum and are then expected to be observed first in the p-p collisions of the LHC.

It has been illustrated in the previous section that the Standard Model and SUSY sector shares the same gauge and Yukawa couplings. Therefore, it is expected that, if stops, gluinos and sbottom have masses in the TeV range these should be

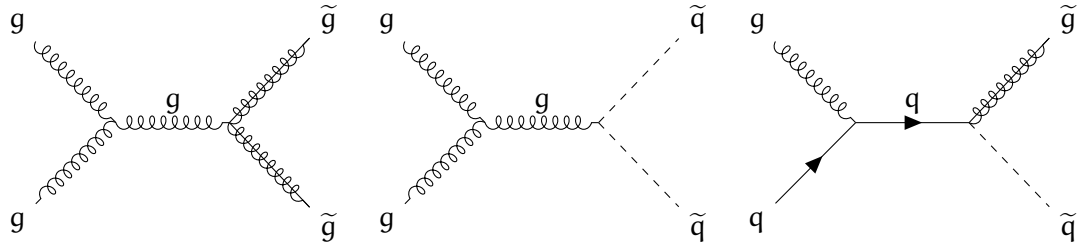

Figure 3.2 – Dominant SUSY diagrams for squark and gluino production.

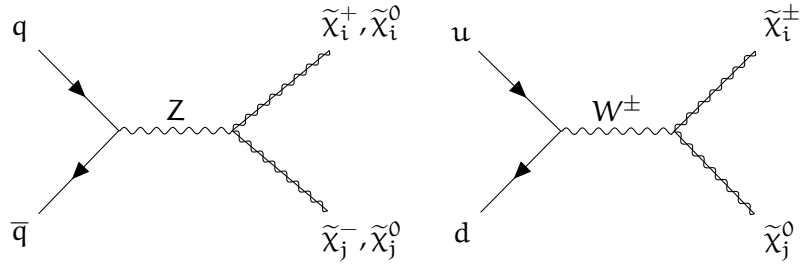

Figure 3.3 – Dominant SUSY diagrams for production of electroweakinos.

mostly produced by strong interactions. Under these assumptions, the processes contributing the most to the creation of these particles are

$$gg \to \tilde{g}\tilde{g}, \tag{3.29}$$
$$gg \to \tilde{q}_i \tilde{q}_j^*, \tag{3.30}$$
$$gq \to \tilde{g}\tilde{q}_i. \tag{3.31}$$

Feynman diagrams of these processes are reported in Figure 3.2. The squark-mediated diagrams also contribute to the production of such particles, but we usually assume at the LHC that all squarks and sleptons – with the exception of the stop – have very high masses and so these diagrams contribute much less to the production cross-section. Due to this reason, the $\tilde{g} - \tilde{q}$ production of Equation (3.31) is also considered to be largely suppressed in general searches for SUSY at the LHC. Therefore, we can note how, under the assumption that SUSY solves the hierarchy problem of the Standard Model, the primary source of SUSY particles at the LHC is provided by pairs of gluinos and squarks (in particular pairs of stops). This is well illustrated by Figure 3.4 where the production cross sections for strong (*i.e.* gluinos and stops) and electroweak sparticles (*i.e.* charginos and neutralinos) are compared.

When SUSY provides a Dark Matter candidate via the neutralino (*i.e.* the LSP), at least one or more neutralinos and charginos must have masses lower than the gluino and stop masses, meaning that these particles could also be directly produced at the LHC. However, since these particles are composed of the mass eigenstates of higgsinos and electroweak gauginos, the production of such particles happen

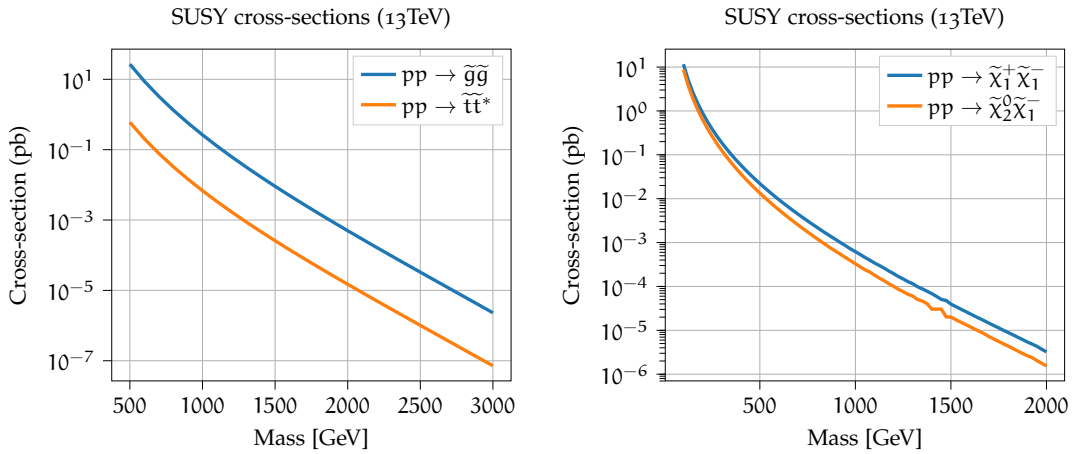

(a) Strong coloured SUSY cross-sections.

(b) Electroweak SUSY cross-sections.

Figure 3.4 – SUSY cross-sections for colored and electroweak superpartners. Here, the full degeneracy of the gluino and squark masses has been considered [31, 32].

only via electroweak and Yukawa interaction terms, meaning that the creation of charginos and neutralinos is provided by

$$q\overline{q} \to \widetilde{\chi}_i^+\widetilde{\chi}_j^-,\ \widetilde{\chi}_i^0\widetilde{\chi}_j^0, \tag{3.32}$$

$$u\overline{d} \to \widetilde{\chi}_i^+\widetilde{\chi}_j^0, \tag{3.33}$$

$$\overline{u}d \to \widetilde{\chi}_i^-\widetilde{\chi}_j^0. \tag{3.34}$$

It is possible to note that similarly to the gluino and stop production, charginos and neutralinos are also produced in pairs at the LHC. This feature is a direct consequence of R-parity conservation, illustrated in the previous sections. Feynman diagrams of these processes are provided in Figure 3.3. These processes are extremely suppressed also due to the lower amount of anti-quarks available inside protons compared to gluons. This makes the direct production of such particles more challenging but potentially the only way to observe SUSY at the LHC in case the gluino and stop have masses higher than $2-3$ TeV.

3.2.2 *Decays of SUSY particles*

Now that it has been illustrated how gluinos, stops and charginos can be produced in the p-p collisions of the LHC, it is the moment to explain how these particles can decay and manifest themselves inside the ATLAS detector. In the assumption that R-parity is conserved, all the SUSY particles are expected to decay to the LSP represented by the neutralino $\widetilde{\chi}_1^0$, which is stable and weakly interacting.

The decay of the gluino can only proceed via a virtual or on-shell squark through the the two-body decay $\widetilde{g} \to q\widetilde{q}$, as shown in Figure 3.5g. Depending on the mass of the squarks, we can then distinguish two decay cases:

- When light squarks are present (*e.g.* the stop $\widetilde{t}$ and the sbottom $\widetilde{b}$), the dominant two-body decays for the gluino is $\widetilde{g} \to q\widetilde{q}$.

- When squarks are all heavier than the gluino, the gluino will decay only through off-shell squarks inside the $\widetilde{g} \to qq\widetilde{\chi}_i^0$ and $\widetilde{g} \to qq'\widetilde{\chi}_i^{\pm}$ decays. Feynman diagrams of these processes are provided in Figure 3.5h and 3.5i.

About the squarks decays, if $\widetilde{q} \to q\widetilde{g}$ is not kinematically forbidden, then this decay mode will dominate the squark decay due to the QCD strength of this channel. On the other hand, when gluinos are more massive than squarks, these tend to decay via charginos $\widetilde{\chi}_i^{\pm}$ and neutralinos $\widetilde{\chi}_j^0$, as shown in Figure 3.5a, 3.5b and 3.5c. The resulting charginos and neutralinos are generally wino- or bino-like, considering that the Higgs Yukawa couplings are extremely low for most of the fermions and that electroweak coupling dominates. When squarks are stops or sbottoms, the Yukawa couplings become more important and the production of higgsino-like neutralinos and charginos become more feasible.

Once the heavy charginos and neutralinos are produced from the gluino and squark decays, they decay to the LSP $\widetilde{\chi}_1^0$ through emission of a electroweak or Higgs boson when sneutrinos and sleptons masses are large. Feynman diagrams of such processes are illustrated in Figure 3.5d, 3.5e and 3.5f.

Therefore, it is clear now that, assuming high masses of most sfermions, the signature for gluinos and squarks particles at the LHC is represented by chained decays of sparticles leading to n quarks (generally reconstructed as jets as illustrated later in Chapter 5), m leptons and Missing Transverse Momentum E_T^{miss}, where n and m are integers ranging from zero to $O(10)$ values depending on the length of the decay chain.

3.2.3 *R-parity violation*

In supersymmetry theories, the most generic superpotential implying violation of R-parity (RPV) is [26]

$$\mathcal{W}_{RPV} = \frac{\lambda_{ijk}}{2} L_i L_j \overline{e}_k + \lambda'_{ijk} L_i Q_j \overline{d}_k + \frac{\lambda''_{ijk}}{2} \overline{u}_i \overline{d}_j \overline{d}_k, \tag{3.35}$$

where i, j and k are quark and lepton generation indices. L_i and Q_i represents the $SU(2)_L$ lepton and quark superfields and H_u the Higgs superfield associated to up-type quarks. The $\overline{e}_i$, $\overline{d}_i$ and $\overline{u}_i$ are the lepton, down-type quark and up-type quark superfields respectively. The terms proportional to λ and λ' are the dimensionless RPV-couplings allowing for lepton-number violation while λ'' allows for baryon-number violation. The λ_{ijk},λ'_{ijk} and λ''_{ijk} terms are completely antisymmetric[3] meaning that diagonal tensor components (*i.e.* $i = j = k$) are zero by contruction. These terms are not considered in the MSSM superpotential, mainly because of the constrain imposed by proton decay[4] and the fact that, when R-parity is violated, the LSP is allowed to decay to two light Standard Model particles being unstable and not a suitable candidate to explain Dark Matter. However, constraints from proton decay are less strict when heavy quark flavours are considered in λ'' terms and also when squarks and sleptons are very massive due to the mediation of a virtual squark

[3] A tensor λ_{ijk} is completely antisymmetric if: $\lambda_{ijk} = -\lambda_{kij} = -\lambda_{jki}$

[4] Proton decay would require violation of both leptonic and baryonic number by at least a unity.

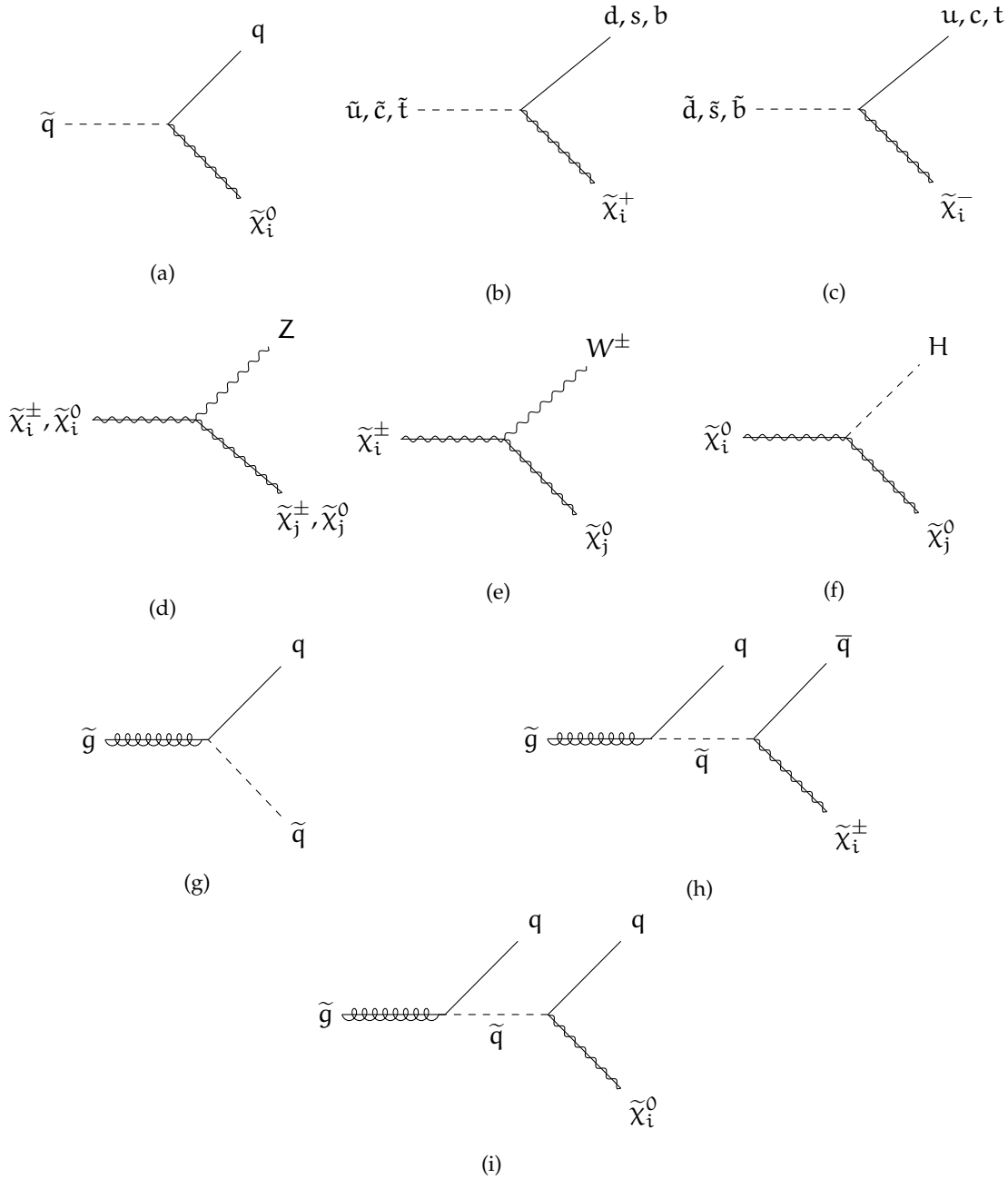

Figure 3.5 – Feynman diagrams for the decays of gluinos, squarks, charginos and neutralinos.

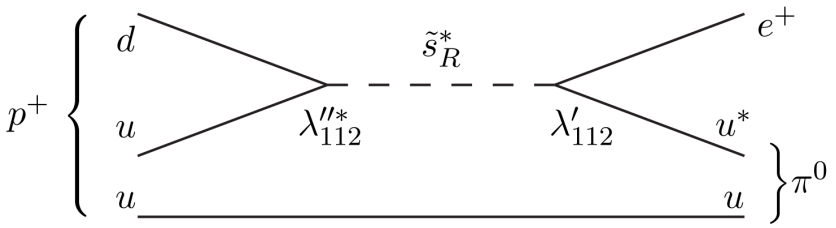

Figure 3.6 – Proton decay $p \to e^+\pi^0$ through λ', λ'' R-parity couplings [26].

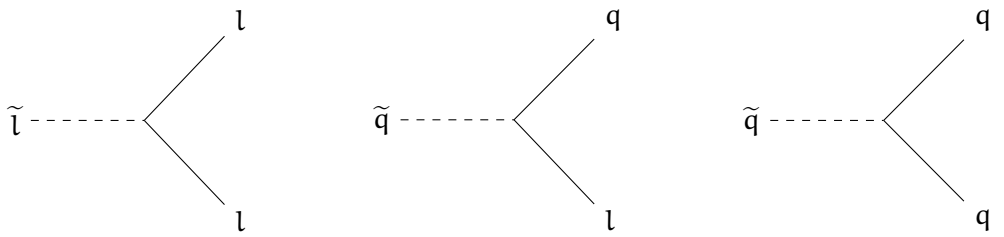

(a) $\propto \lambda$ (b) $\propto \lambda'$ (c) $\propto \lambda''$

Figure 3.7 – Feynman diagrams R-parity violating decays of SUSY particles associated to λ, λ' and λ''.

through a $p \to e^+\pi^0$ decay (see Figure 3.6). For example, in proton tree-level decay, at least one between λ'_{ijk} or λ''_{11k} for $i = 1, 2; j = 1, 2; k = 2, 3$ must be in the order of about 10^{-26} for squark masses of 300 GeV [33].

Figure 3.7 shows the feynman diagrams associated the slepton and squark decays implied by these new λ, λ' and λ'' couplings, which are not present in the Standard Model similarly to the gauge and Yukawa couplings. The presence of such terms in the MSSM Lagrangian has as primary effect the instability of the LSP, resulting in final states with lower E_T^{miss} and possibly larger numbers of leptons and jets when the λ couplings are large enough to guarantee a prompt decay of the SUSY LSP. On the other hand, when λ couplings are not too large, the LSP can be provided with a sufficiently long lifetime and leave a displaced signature at hadron colliders. These kind of models are ofter less constrained by current SUSY searches, and further discussion will be provided later in Chapter 11.

3.3 CONCLUSION

This chapter has introduced one of the most widely studied supersymmetric extensions of the Standard Model also known as Minimal Supersymmetric Standard Model (MSSM). Now that the phenomenology for the observation of such new physics processes has been established, it is the moment to illustrate how to observe such processes. In order to achieve this goal, physicists have built among the years amazing machines, able to collide particles at high energies and reveal hidden effects of nature. The Large Hadron Collider (LHC) is the collider that has been employed for this work, with the final state detection provided by the ATLAS experiment. These extraordinary machines are both illustrated in the next chapter.

4

THE ATLAS DETECTOR AT THE LARGE HADRON COLLIDER

"Ginny: The thing about growing up with Fred and George is that you sort of start thinking anything's possible if you've got enough nerve."
– J.K. Rowling, *Harry Potter and the Half-Blood Prince*

Contents

4.1 THE LARGE HADRON COLLIDER

The Large Hadron Collider (LHC) is a two-ring-superconducting-hadron collider located in the 27 km underground tunnel constructed between 1984 and 1989 for the Large Electron Positron collider (LEP) [34], at the Franco-Swiss border near Geneva (Switzerland). The accelerator has been designed to provide proton beams up to a design energy of 7 TeV. In 2011-2012, it operated at a center-of-mass energy of 8 TeV during the Run 1 of the LHC, and at 13 TeV between 2015-2018 during the LHC Run 2. Between each LHC Run, a 2-3 years long upgrade phase is performed, where the LHC is entirely non-operational and the detectors and accelerating devices can be repaired and upgraded. These upgrade periods are commonly known as Long Shutdowns (or simply LS) and, until now, two Long Shutdowns have taken place: the LS1 (2012-2015) and the LS2 started in 2018 and expected to end in 2021 with the start of the LHC Run 3.

The LHC tunnel is located at a depth of approximately 100 meters and the LHC represents the final step of a multi-stage accelerator system as shown in Figure 4.1. The proton beams are accelerated in opposite directions inside the LHC tunnel and then brought to collision at four specific interaction points where experiments are located. These experiments are:

- ATLAS and CMS, representing the two largest multi-purpose experiments located at the opposite sides of the LHC (Figure 4.1). These experiments are meant to probe new physics by exploiting as much as possible the large energy and luminosity of the LHC.

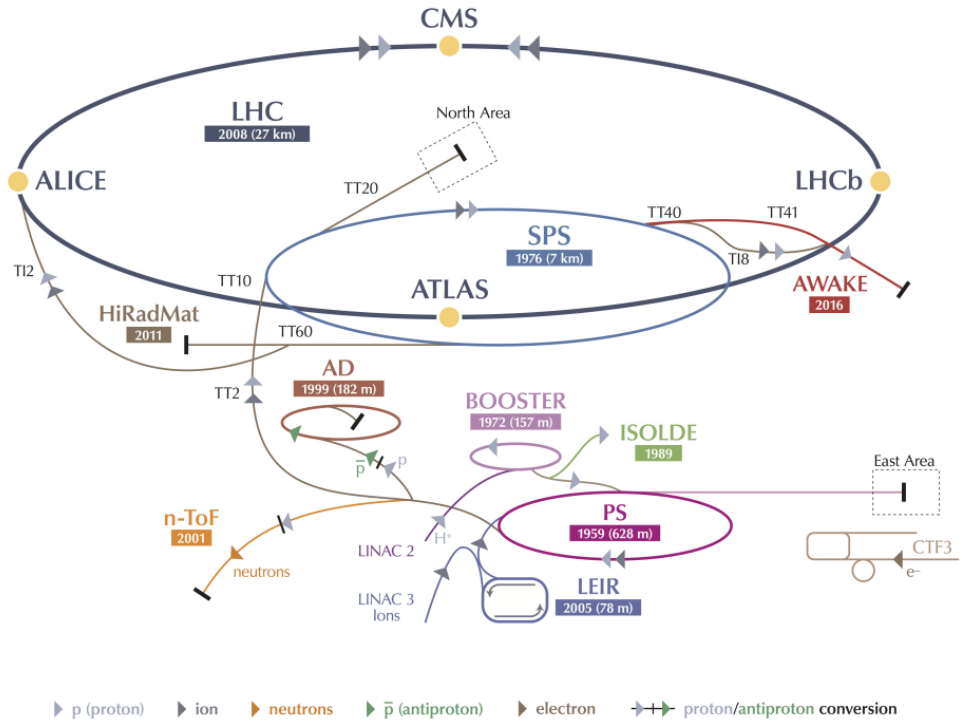

Figure 4.1 – CERN Accelerator's complex and LHC accelerator stages [35].

- LHCb, a single arm forward spectrometer aiming at measuring with large precision the CP violation occurring in the quark sector and rare decays of bottom and charm hadrons.
- ALICE, an experiment dedicated to study the properties of quark-gluon plasma created in heavy ions collisions.

Every circular particle accelerator needs two essential ingredients: the *Radio-Frequency (RF) cavities* providing the longitudinal acceleration necessary to increase the beam energy and the bending *Magnets* ensuring the transverse acceleration necessary to keep the particles in a circular trajectory. At the LHC, 1232 *dipole* superconducting magnets are used to maintain the protons in orbit at the design energy level of 7 TeV [36]. These magnets use Nb-Ti superconducting coils cooled down to a temperature of 1.9 K by superfluid helium and they provide a magnetic field of 8.33 T. Each dipole is 15 m long. A section view of the LHC dipoles is shown in Figure 4.2a. In order to guarantee p-p interactions, *quadrupole* magnets are designed to focalize the beams of the accelerator.

At the LHC, the usage of RF cavities imposes that protons must be accelerated using bunches instead of a continuous beam. For a collider, the *instantaneous luminosity* $\mathcal{L}$ can be defined as

$$\mathcal{L} = f\frac{N_b n_1 n_2}{A}, \tag{4.1}$$

where n_1, n_2 represent the number of protons in the colliding bunches, N_b the number of bunches in the accelerator, f the revolution frequency of one bunch and

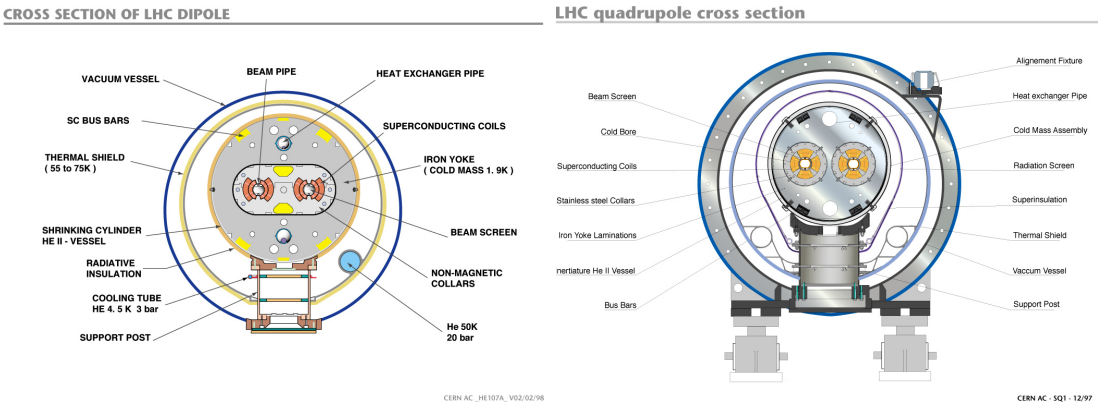

(a) Section view of the LHC dipole magnets [37].

(b) Section view of the LHC quadrupole magnets [38].

Figure 4.2 – Section view of LHC magnets.

A the total overlapping area of the colliding bunches. The *integrated luminosity* L^{int} directly quantifies the size of a dataset with respect to a certain process. This quantity is simply defined as

$$L^{int} = \int \mathcal{L} \, dt. \tag{4.2}$$

From this expression, it is easy to show that the total number of events N associated to a certain quantum process produced with a *cross-section* σ can be expressed as

$$N = L^{int} \cdot \sigma. \tag{4.3}$$

Equation (4.3) shows that, the larger the accelerator luminosity, the larger the number of signal events produced by a particle accelerator. Therefore, having the largest possible luminosity represents a key factor for a particle accelerator, and this can be achieved in different ways. By looking at Equation (4.1) it is possible to see that the luminosity can be increased by:

1. Increasing the bunch revolution frequency f and the number of colliding bunches N_b.
2. Increasing the number of protons in each bunch n_1, n_2.
3. Reducing the total bunch overlap area A by squeezing the proton beams in the transverse plane.

The first option is difficult to achieve considering that protons already travel very close to the speed of light at the LHC. However, the last two options represent key aspects for the performance of the LHC and of the High-Luminosity LHC, an upgrade of the accelerator expected to start in 2026 (see Chapter 9 for further details).

Since a larger number of bunches can provide a larger luminosity of the LHC, different bunch schemes have been adopted at the LHC during its operational period. In 2016, a vacuum leak present in the Super Proton Synchrotron (SPS) high energy beam dump limited the intensity that could be accelerated in the SPS [39] resulting in only 2220 bunches that could be stored in the LHC, corresponding to the filling

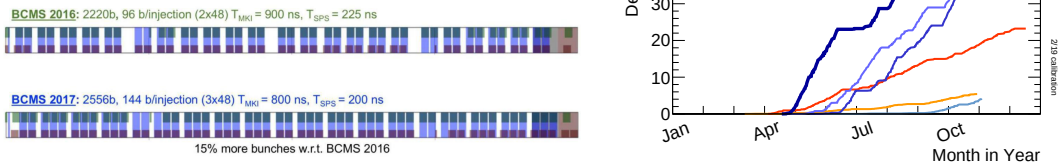

(a) Filling scheme used for physics production at the end of 2016 (top) and 2017 [39].

(b) LHC integrated luminosity L^{int} for different years [42].

Figure 4.3 – Bunch filling schemes and integrated luminosity for different data-taking periods for the LHC Run 2.

scheme illustrated in the top part of Figure 4.3a. In 2017, vacuum issues were fixed, which allowed the LHC to increase its brightness with respect to 2016. Due to some other issues caused by air trapped into the beam screen at 20 K, the filling scheme was changed to the so called 8b4e beam type consisting of 8 filled followed by 4 empty bunches [40]. This led to stable operations of the LHC with 2556 bunches providing larger luminosity with respect to 2016 operations as illustrated in Figure 4.3b. In 2018, the 2544 bunch filling scheme with 25 ns spacing was established again for stable collisions [41].

4.1.1 *Pileup at the LHC*

We have seen in Section 4.1 the importance of having a high luminosity for a particle accelerator. However, despite the gains in terms of production of new physics, a very high luminosity can result in a negative impact on the performance of the detectors, mainly due to difficulty to disentangle the interesting interactions from the rest of the particle interactions. We generally refer to this effect as the *pile-up* contamination of the event. We distinguish two types of pile-up effects:

- The *in-time* pile-up denoting the contamination of signal events due to multiple interactions happening simultaneously in the detector. This effect can be generally mitigated using the tracker of the detector through track and vertex reconstruction (further details are provided in Section 5.1).
- The *out-of-time* pile-up denoting the contamination of the detector from previous and subsequent collisions in the accelerator. This effect is generally caused by the calorimeter cells (see Section 4.2.3) being partially excited from a previous collision or by a subsequent collision contaminating the calorimeter during the readout of the detector.

Several variables are used for the quantification of pileup at the LHC. One of the most common ones is the *mean number of interactions per crossing* $\langle\mu\rangle$, calculated as the mean of the Poisson distribution of the number of interactions per crossing in each

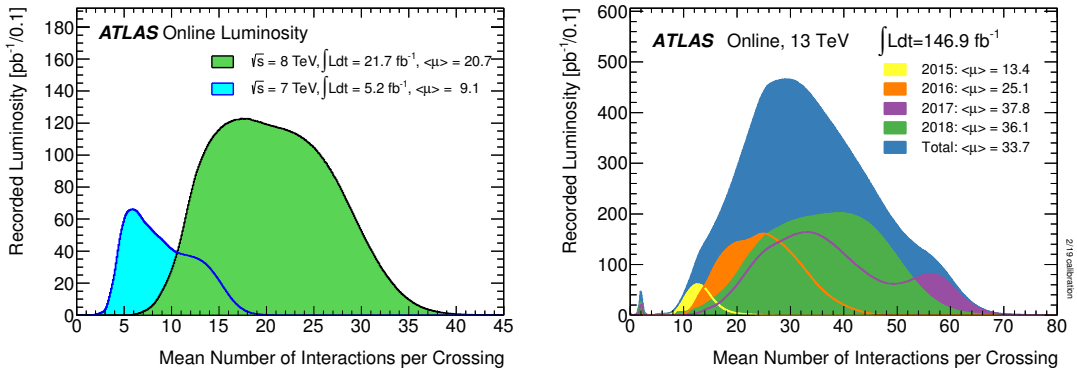

Figure 4.4 – Average number of interactions per bunch crossing $\langle\mu\rangle$ recorded in stable beam collisions of the LHC Run 1 [43] and Run 2 [42].

bunch μ. This quantity is computed from the instantaneous per bunch luminosity L_{bunch} as

$$\mu = \frac{L_{bunch}\sigma_{inel}}{f} \tag{4.4}$$

where σ_{inel} is the total inelastic cross-section corresponding to 80 mb for 13 TeV p-p collisions, and f is the LHC revolution frequency. Figure 4.4 shows the distributions associated to such variable in Run 1 and Run 2. From this figure it is possible to note how $\langle\mu\rangle$ increased through time due to the better knowledge of the LHC acquired year after year and the better operations resulting from this knowledge. Another useful variable is the number of primary vertices N_{PV}, computed after vertex reconstruction described in Section 5.1.

4.2 THE ATLAS EXPERIMENT

ATLAS [44] (**A** **T**oroidal **L**HC **A**pparatu**S**) is a multi-purpose detector aiming at probing new physics signals exploiting the high energy p-p collisions of the Large Hadron Collider. The detector has a cylindrical shape measuring 45 m in length and 25 m in height, and weights approximately 7000 tons. The LHC beams are injected through the end-caps and brought to collision in the middle of the cylinder. As shown in Figure 4.5, the detector has a layered structure composed of different sub-detectors arranged in a concentric way. Starting from the center of the detector, the sub-detectors comprise:

1. An *Inner Detector* measuring the tracks associated to charged particles produced by the p-p collisions.
2. The *Solenoid magnets* providing the magnetic field necessary to bend charged particles inside the Inner Detector.
3. Two *Calorimeters* measuring the energy of charged and neutral interacting particles.
4. The *Toroidal magnets* providing the magnetic field necessary to bend charged muons passing through the calorimeter system.

5. The *Muon spectrometer*, composed of different *muon chambers*, providing the measurement of the muon leptons possibly created in the center of the detector.

After a quick review of the ATLAS coordinate system, these sub-detectors will be described in the next sections of this chapter.

4.2.1 *Detector coordinate system*

In order to quantify directions and positions inside the detector, a suitable coordinate system has to be defined. At first, a cartesian xyz coordinate system can be considered where the nominal interaction point represents the origin of this coordinate system. The z-axis is chosen to be the beam axis while the xy-plane is transverse to the beam[5]. The positive x-axis is defined as pointing towards the centre of the LHC ring and the positive y-axis is defined as pointing in the upwards direction [44]. The *azimuthal angle* ϕ is measured as usual around the z-axis in the xy-plane while the *polar angle* θ is defined with respect to the beam axis.

Since the momentum of partons along the beam axis is unknown, it is useful to define boost-invariant transverse quantities, such as energy and momentum, through projection on the xy-plane:

$$p_T = \sqrt{p_x^2 + p_y^2} = |\mathbf{p}| \sin\theta, \quad E_T = E \sin\theta. \tag{4.5}$$

Another important quantity used to describe massive objects at hadron colliders is the *rapidity* y, defined as

$$y = \frac{1}{2} \ln\left(\frac{E + p_z}{E - p_z}\right). \tag{4.6}$$

It is possible to show that the difference in rapidity Δy between a pair of particles is invariant under a Lorentz boost along the beam axis, a feature which makes this quantity extremely useful at hadron colliders. When the particle mass is negligible with respect to its momentum, it is possible to approximate the rapidity y with the *pseudo-rapidity* η defined as

$$\eta = -\ln\left(\tan\left(\frac{\theta}{2}\right)\right). \tag{4.7}$$

This quantity is broadly employed in high energy physics experiments due to its simple estimation from θ and to the generally negligible masses of final state particles at high energy.

In the $\eta - \phi$ plane, the distance ΔR between two objects with coordinates (ϕ_i, η_i) and (ϕ_j, η_j) is defined as

$$\Delta R_{ij} = \sqrt{(\Delta\eta_{ij})^2 + (\Delta\phi_{ij})^2} = \sqrt{(\eta_i - \eta_j)^2 + (\phi_i - \phi_j)^2}. \tag{4.8}$$

The complete detector is split into Barrel Region (BR) sections and End-Cap (EC) Regions sections: in the former the detector layers are positioned on cylinders around the beam axis, in the latter these are positioned in wheels perpendicular to the beam pipe.

[5] The xy-plane is generally called the *transverse plane* of the collision.

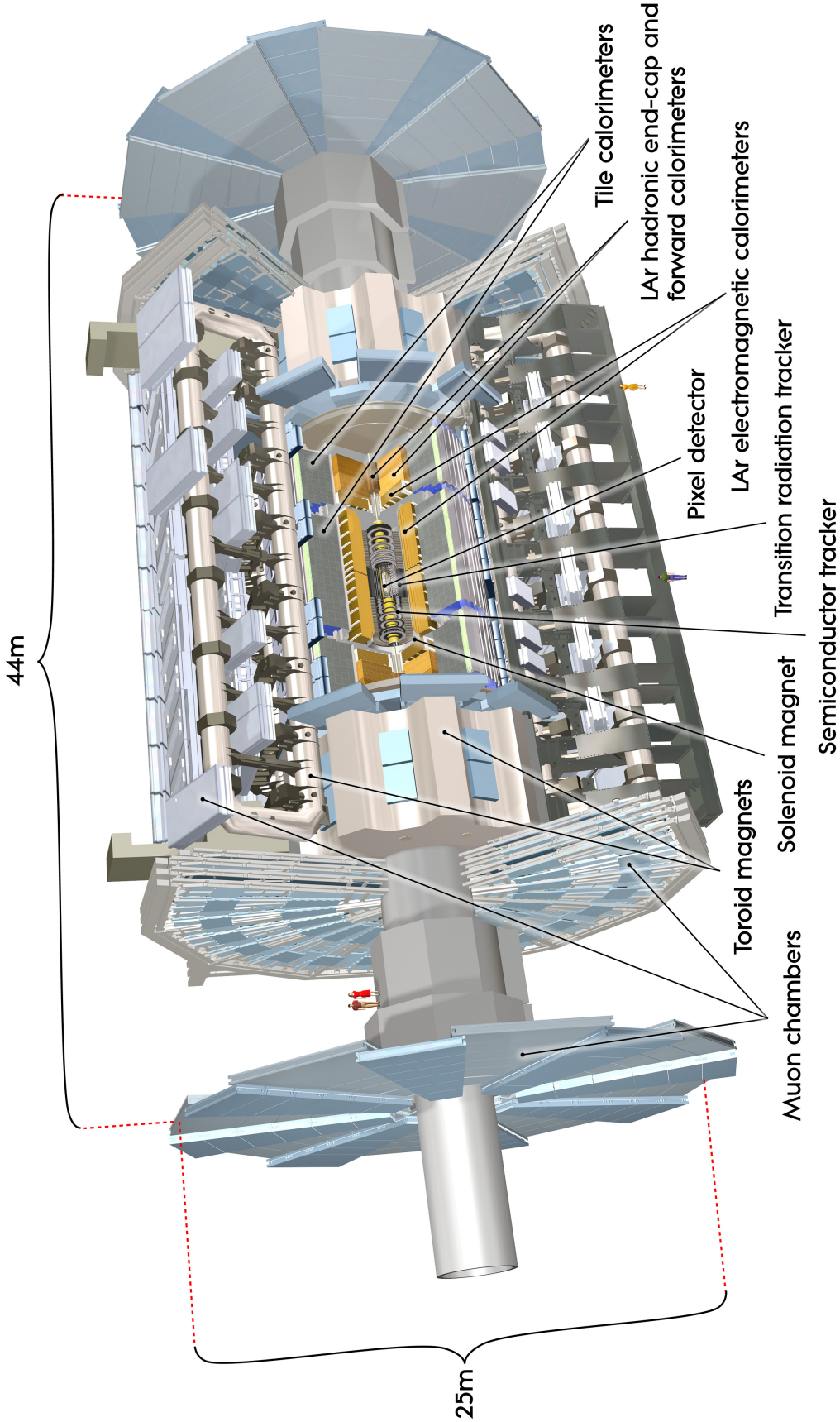

Figure 4.5 – Section view of the ATLAS experiment [44].

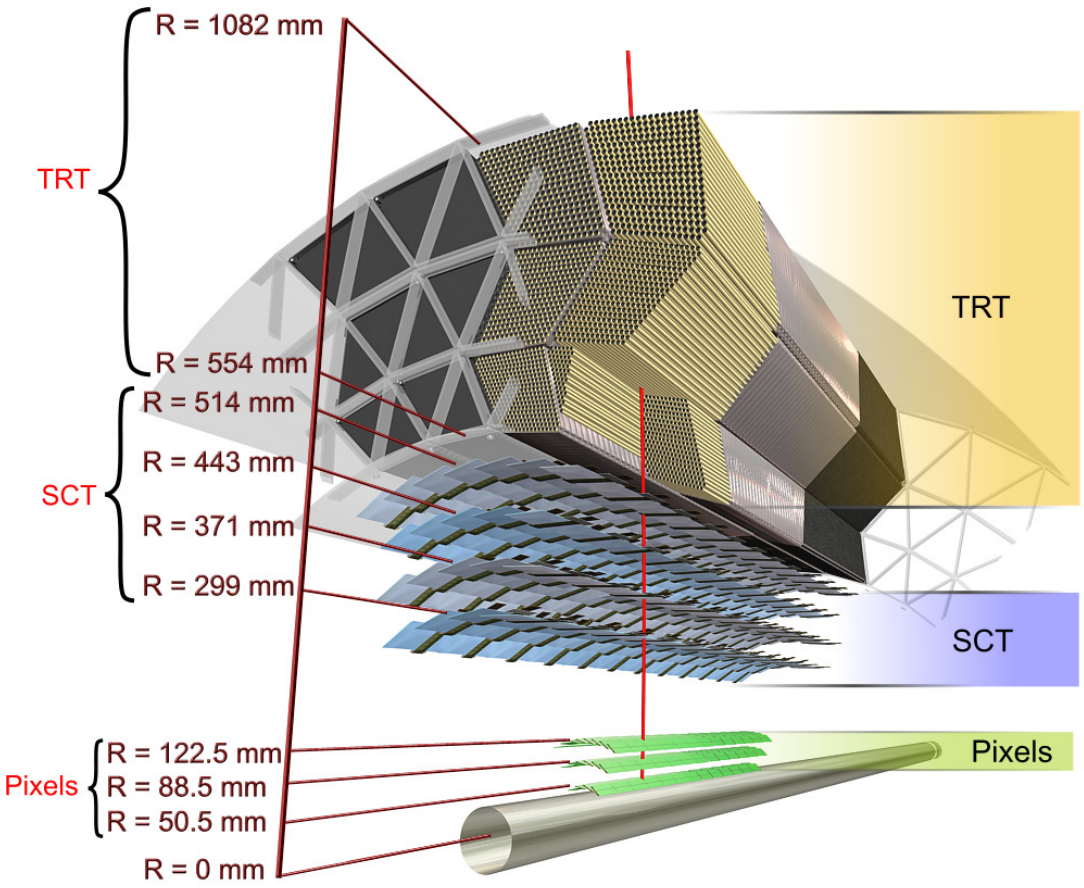

Figure 4.6 – Transverse section of the ATLAS Inner detector with structural elements [45].

4.2.2 *The Inner Detector*

The ATLAS *Inner Detector* (ID) is the innermost part of the ATLAS experiment and it is designed to perform robust track measurement of charged particles with excellent momentum resolution and both primary and secondary vertex identification [44]. This detector is expected to measure charged particle tracks within its $|\eta| < 2.5$ pseudorapidity range and track p_T down to 100 MeV. The ID is contained in a cylindrical envelope of length 7.024 m and of radius 1.15 m immersed in a solenoidal magnetic field of 2 T.

The ID is composed of three independent and complementary sub-detectors (see Figure 4.6):

- At inner radii, the silicon pixel layers provide highly precise bi-dimensional track hit measurement through planar pixel technologies.
- At approximately 30 cm from the beam axis, the *Semiconductor Tracker (SCT)* also provides bi-dimensional track hit measurements using different layers of silicon strip technologies in stereo arrangement.
- Finally, the outermost part of the ATLAS tracking system is composed of the *Transition Radiation Tracker (TRT)*, measuring track hits using straw tubes

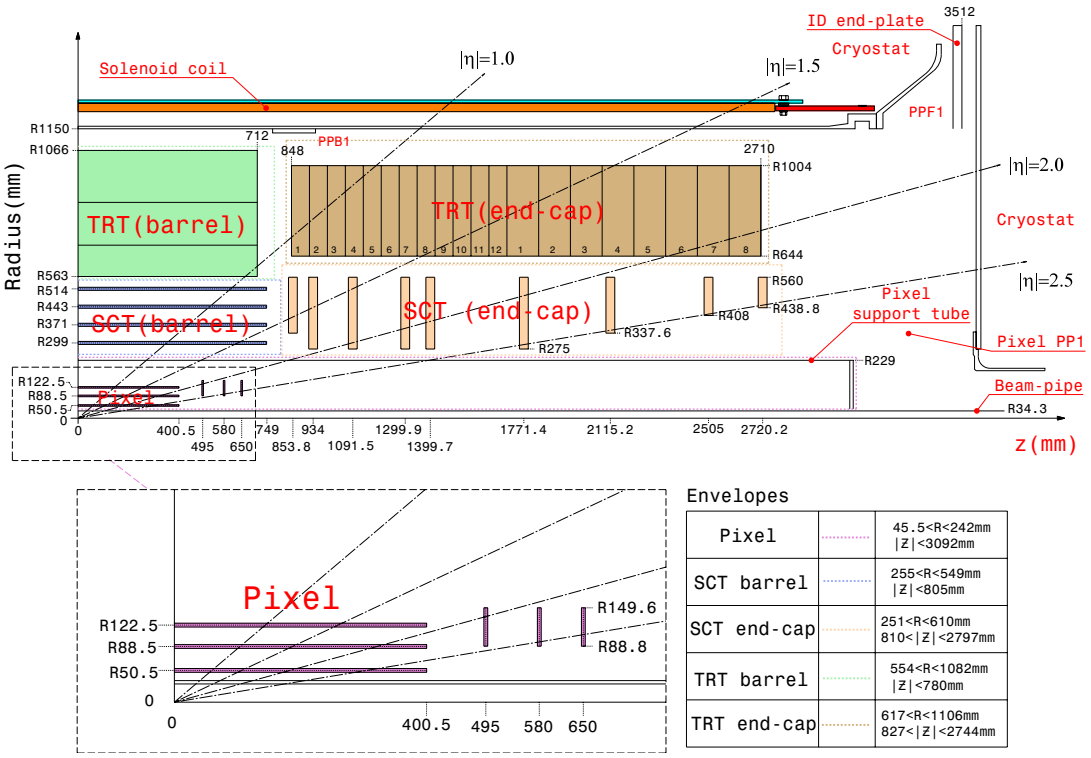

Figure 4.7 – Plan view of quarter section of the ATLAS Inner detector with η projections of different structural elements [45].

filled with transition radiation material. With an average of 36 hits per track, it provides continuous tracking and improves momentum resolution for the pseudorapidity range $|\eta| < 2.0$ and also electron identification complementary to the calorimeter.

4.2.2.1 *The Pixel detector*

The pixel detector is the innermost part of the ATLAS tracker and it plays a fundamental role for precise track and vertex measurements. These features make the pixel detector the most important detector for flavour tagging and pileup rejection. The working principle of silicon detectors is based on a silicon p-n junction operating in reverse bias voltage. A schematic of a planar pixel detector is shown in Figure 4.8, where a charged particle creates the electron-hole pairs by exciting electrons from the valence band to the conduction band in silicon creating an electric current passing through the electric circuit.

The ATLAS pixel detector is composed of 1744 pixel modules arranged in three barrel layers and two end-caps with three disks each as shown in Figure 4.7. 16 front-end electronic chips, each with 2880 electronics channels, are directly mounted on the detector providing sensor signals to the trigger and data acquisition system (see Section 4.2.5). The nominal pixel size is $50 \times 400\ \mu m^2$ (about 90% of the pixels) and is dictated by the readout pitch of the front-end electronics [44]. The remaining pixels size is $50 \times 600\ \mu m^2$ in the regions close to the front-end chips on the modules.

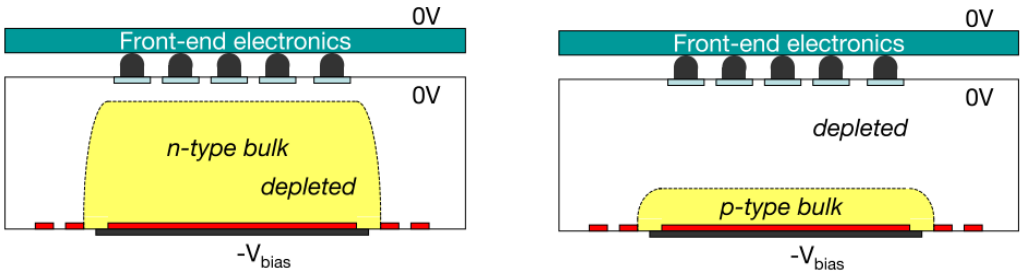

(a) Non-irradiated pixel detector

(b) Irradiated pixel detector

Figure 4.8 – Irradiated and non-irradiated ATLAS silicon pixel detectors [46]. After irradiation, the slightly doped n-type bulk becomes p-type but still keeping the functionalities of the pixels.

Being the closest detector to the interaction point, the damage caused to the silicon crystals by p-p radiations has very important consequences on the operations and design of this sensor. In particular, the required operating voltage is determined by the effective doping concentration of silicon which can be largely modified by irradiation through time. The n-type bulk material used for the design of the ATLAS pixel layers effectively becomes p-type after a fluency $F_{neq} \approx 2 \times 10^{13}\,cm^{-2}$ [44] (see Figure 4.8). In order to contain these effects, two operation requirements have been imposed:

1. The detector needs to be operated at a temperature range between $-5\,°C$ and $-10\,°C$ in order to reduce radiation damage effects.

2. The applied bias voltage needs to be increased from $150\,V$ to $600\,V$ over 10 years of operations in order to keep the charge collection efficient depending on sensor position, integrated luminosity, etc.

The sensors are $250\,\mu m$ thick and produced using oxygenated n-type wafers with readout pixels on the n^+-implanted side of the detector. This particular doping configuration was used mainly because of the good charge collection after type inversion of the n-type wafers (see Figure 4.8). On the other hand, the oxygen treatment has been proved to provide increased radiation tolerance to charged hadrons.

During the Long Shutdown 1, an additional pixel layer has been added inside the LHC beam pipe in order to increase the flavour tagging performance. Due to this reason, this detector is called the *Insertable B-Layer* (IBL) and, differently from other pixel layers, it is based on two different silicon sensor technologies: planar n^+-on-n pixels and 3D pixels with passing through columns. IBL consists of 14 carbon fibre staves each $2\,cm$ wide and $64\,cm$ long, and tilted by $14°$ in ϕ surrounding the beam-pipe at a mean radius of $33\,mm$ and covering a pseudo-rapidity up to $|\eta| < 3.0$ [47]. The planar pixel modules cover the central part of the stave while the 3D modules are positioned in the forward regions of both ends of the stave. This detector has been built around the new beryllium beam pipe and then inserted inside the Pixel detector in the core of the ATLAS detector.

4.2.2.2 *The Semiconductor Tracker (SCT)*

The SCT consists of 4088 modules, assembled in four cylindrical layers in the barrel region and two end-caps each containing nine disk layers [44].

Differently from the pixel layers, the SCT is based on silicon mono-dimensional strips and it represents the middle part of the ATLAS tracking system (see Figure 4.6). The larger detection surface ($63\,m^2$) and lower track hit precision required at this distance from the interaction point, made classical p-in-n strip technologies well suited for this detector. This technology has been also preferred due to its reliability, simple readout and low construction cost. Since silicon strips provide only mono-dimensional track hit measurement, each module is composed of a double layer of strips tilted by a stereo angle of $40\,mrad$[6].

The 15919 strip sensors composing the SCT system have a thickness of $285\,\mu m$ and a strip pitch of $80\,\mu m$. The sensors operates at $150\,V$ bias voltage, but operating voltages between 250 and $350\,V$ are required for good charge collection efficiency after ten years of operation.

4.2.2.3 *The Transition Radiation Tracker (TRT)*

The TRT is the outermost part of the ATLAS Inner Detector. This detector is based on drift tubes technologies of $4\,mm$ diameter filled with a gas mixture of 70% Xe, 27% CO_2 and 3% O_2 [48]. In the centre of each drift tube there is a gold-plated tungsten wire of $31\,\mu m$ diameter kept at the ground potential while the tube walls are kept at $-1.5\,kV$. When a charged particle passes through the gas, it creates electrons, which are then captured by the wire creating an avalanche effect which makes each tube acting as a proportional counter. Stacking multiple tubes together make tracking possible. Additionally, the spaces between the straws are filled with *transition radiation materials* which produce an X-ray radiation dependent on the type of the incident relativistic particle. These X-rays can be collected and used to identify electrons already in the tracking system providing a complementary electron identification to the calorimeter system in the $|\eta| < 2.0$ pseudorapidity range.

The TRT is composed of a barrel and two end-caps covering respectively the pseudorapidity range $|\eta| < 1.0$ and $1.0 < |\eta| < 2.0$ (see Figure 4.7). The barrel region contains 52544 straw tubes of $1.5\,m$ length located in a parallel direction to the beam axis and covering the radius range from $0.5\,m$ to $1.1\,m$. Each end-cap contains 122880 $0.4\,m$ long straw tubes disposed perpendicularly to the beam axis and covering the geometrical range $0.8\,m < |z| < 2.7\,m$. The transition radiation materials are made of polymer fibre in the barrel and foils in the end-cap.

4.2.3 *Calorimeters*

Immediately after the Inner Detector and the solenoid providing the magnetic field necessary to bend charged particles inside the tracker, a set of calorimeters measure the particle energies by completely absorbing them into their volumes. In contrast to the Inner Detector, this detector can detect both charged and neutral

[6] The small stereo angle is necessary to avoid a massive fake hit measurement.

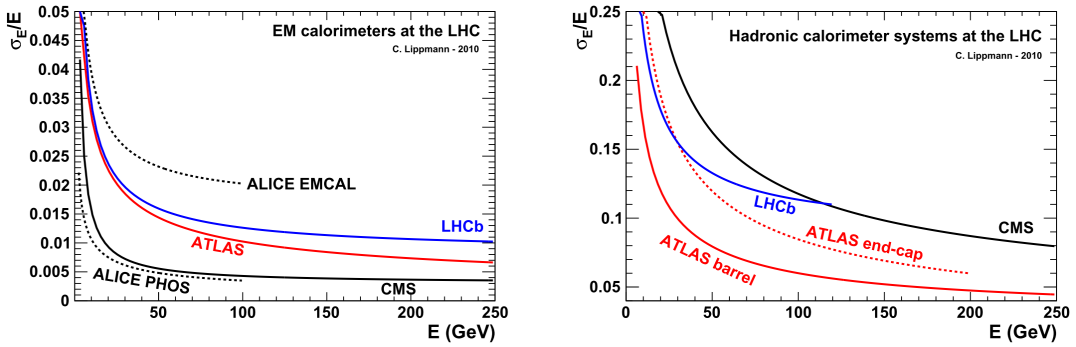

Figure 4.9 – Calorimeter resolutions of ATLAS and different LHC experiments [49]. We can see the excellent performance achieved by the ATLAS hadronic and electromagnetic calorimeter.

particles, with the exception of less interacting particles such as neutrinos and muons which can pass through the calorimeters undetected.

In general, particle physics calorimeters can be divided in two categories: *sampling* calorimeters and *homogeneous* calorimeters. These two types of calorimeters differ in the technologies used for the measurement of the incident particles. In the case of the sampling calorimeters, different layers of a heavy absorber[7] are alternated with different layers of an active material. The function of the absorber is to degrade progressively the energy of the incident particle by producing a sequential set of secondary particles also known as *particle showers*, whereas the active material is necessary for the generation of the electric signal used for the measurement of the particle energy. An homogeneous calorimeter is composed of a single active material providing both absorption and measurement functionalities. Due to the different natures of hadronic and electromagnetic showers, these calorimeters are generally *non-compensating*, meaning that the calorimeter signal formation is proportional to the energy of incoming electromagnetic particles (*i.e.* electrons, positrons and photons) but not for hadrons. This effect is generally compensated after collection of data by applying a calibration, as discussed later in Chapter 5.

The ATLAS calorimeter consists of two different sampling calorimeters with full ϕ symmetry and coverage around the beam axis [44] covering up to $|\eta| < 5.0$. This detector is composed of:

- An *electromagnetic calorimeter* based on liquid Argon (LAr), providing the measurement of light electroweak particles such as electrons, positrons and photons.

- A *hadronic calorimeter* based on steel/scintillator tiles in the barrel and copper/liquid-argon in the end-caps, allowing to measure the energies of the the hadronic particles such as pions, protons, neutrons, mesons, etc.

[7] In general, calorimeter absorbers are made of heavy materials such as lead or steal.

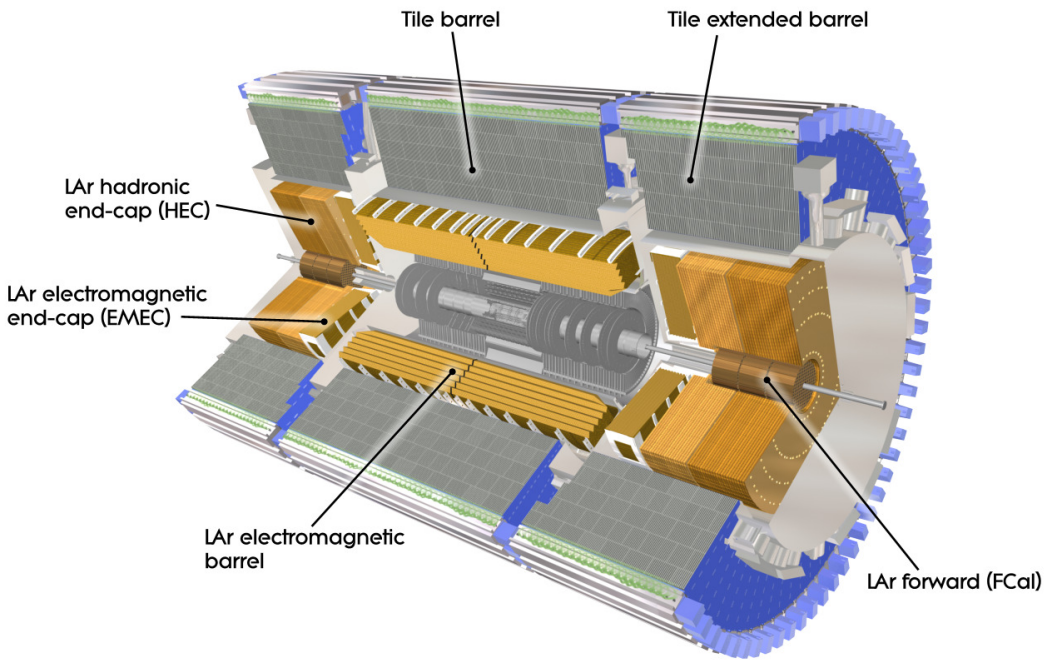

Figure 4.10 – Section view of the ATLAS calorimeters and schematic of sampling calorimeter technologies [45].

The calorimeter resolution represents one of the main figures of merit for describing and comparing the performance of calorimeters. This quantity is parametrized as:

$$\frac{\sigma(E)}{E} = \frac{S}{\sqrt{E}} \oplus \frac{N}{E} \oplus C, \tag{4.9}$$

where S, N and C are the so-called *stochastic*, *noise* and *constant terms* and $\oplus$ is a quadratic sum. The stochastic term accounts for energy fluctuations due to randomness of the number of particles in the shower evolution. The noise term N is independent of the deposited energy and it describes the effect of pile-up noise and noise from readout electronics. Lastly, the constant term accounts for systematic effects due to mis-calibration of the detector as well as detector inactive material. It is easy to understand that at very low energies the noise term is the dominant term of the calorimeter resolution, while at high energies is the constant term that limits the performance. For the ATLAS detector, the electromagnetic (hadronic) calorimeter has been designed to achieve an energy resolution with $S = 10\%(50\%)$, $N = 0.1\%(1\%)$ and $C = 0.7\%(3\%)$ [50, 51]. Figure 4.9 illustrates the resolution curves of the ATLAS calorimeters and compare them also with other LHC experiments.

4.2.3.1 *The Electromagnetic Calorimeter*

The ATLAS electromagnetic (EM) calorimeter is a liquid-argon (LAr) sampling calorimeter kept at the boiling temperature of Argon (88 K) by three cryostats surrounding the detector.

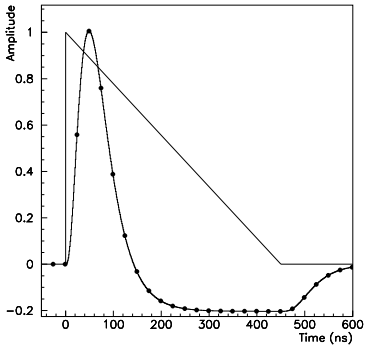

(a) LAr signal amplitudes vs time.

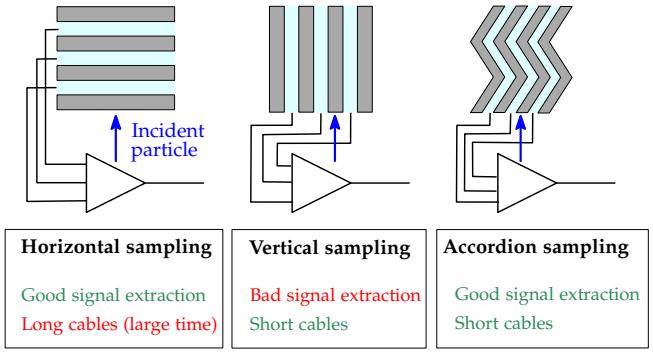

(b) Various LAr sampling options and advantages

Figure 4.11 – Amplitude versus time for triangular current pulse of the LAr calorimeter and for 50 ns integrated signal [44]. The solid points also illustrate the 25 ns sampling points.

Advantages	Drawbacks
Detector uniformity.	Sampling calorimeter (worse stochastic term resolution).
Response linearity (no signal amplification needed due to high density).	Cryogenics (difficult operations and more dead material).
Radiation hardness.	Slow charge collection (450 ns).
High ionisation yield and granularity.	
Stability with time.	

Table 4.1 – List of general advantages and drawbacks using a liquid-argon calorimeter.

Table 4.1 illustrates the main advantages and drawbacks of using a liquid-argon calorimeter. A particularly important drawback is represented by the slow collection of the charges produced in the liquid-argon (450 ns) at a nominal operational voltage of 2 kV for the calorimeter. This time is much larger than the 25 ns bunch crossing time gap of the LHC and this could create enormous issues with the extraction of physics signals from the EM calorimeter. This problem is solved integrating the signal current over a specific time t_p, which is fixed at 50 ns for the LAr calorimeter. This creates an ideal pulse shape for the electric signal as shown in Figure 4.11a, with the drawback of reducing the signal-to-noise fraction. Given these timing issues, also the length of the readout cables represent a potential problem that could delay the calorimeter readout by 10-20 ns. Sampling the LAr calorimeter with a vertical geometry instead of a horizontal one could reduce dramatically the time delay due to long cables (see Figure 4.11b). However, this option would result in poor interaction with the active material for particle aligned with the absorber layers. This is why an *accordion* geometry has been designed and employed for the entire LAr calorimeter, by stacking layers of lead absorber filled with liquid-argon.

This calorimeter aims at measuring the energies of particles stopped through electromagnetic showers[8] and it is composed of two sub-detectors: the *EM barrel* (EMB) LAr calorimeter covering the $|\eta| < 1.475$ region and the *EM EndCap* (EMEC) LAr calorimeter covering the $1.4 < |\eta| < 3.2$ region (see Figure 4.10). A *presampler* positioned inside the barrel cryostat consists of a separate thin liquid-argon layer (11 mm in depth), which provides shower sampling in front of the active electro-

[8] These showers are the result of sequential *Bremsstrahlung* and *Pair creation* processes from electrons, positrons and photons.

magnetic calorimeter [44]. The EMB is made of two half-barrels covering the region with $z > 0$ ($0 < \eta < 1.475$) and $z < 0$ ($-1.475 < \eta < 0$) respectively. The total barrel measures 6.4 m in length with an inner and outer diameter measuring respectively 2.8 m and 4 m. A half-barrel is made of 1024 accordion-shaped absorbers (see Figure 4.12a for an illustration), interleaved with readout electrodes. The electrodes are positioned in the middle of the gap by honeycomb spacers. The size of the drift gap on each side of the electrode is 2.1 mm, which corresponds to a total drift time of about 450 ns for an operating voltage of 2 kV. The total thickness of a module ranges from 22 X_0 to 33 X_0 [9] depending of the η positioning of the incoming particle. The depth segmentation is done using 3 layers:

- The strip cells representing the first layer of the calorimeter with an (η, ϕ) segmentation of 0.0031×0.098. The extremely fine granularity of this calorimeter allows optimal identification between π^0 and γ.
- The middle cells segmented with 0.025×0.025 in (η, ϕ) and representing the second layer of the calorimeter.
- The back cells having a 0.05×0.025 segmentation providing the last layer of the EMB calorimeter.

The EMEC calorimeters consist of two wheels, one on each side of the electromagnetic barrel. Each wheel is 63 cm thick and weighs 27 tonnes. Each end-cap contains 768 absorbers interleaved with readout electrodes in the outer wheel and 256 absorbers in the inner wheel. As for the barrel electromagnetic calorimeter, the precision region in the end-cap electromagnetic calorimeters is divided in depth into three longitudinal layers in order to ensure optimal particle identification.

4.2.3.2 *The hadronic calorimeter*

The hadronic calorimeter represents the outermost part of the ATLAS calorimeter system and it is designed to measure hadronic particles such as charged pions, protons, neutrons, etc. This calorimeter of ATLAS is composed of different modules made of different technologies: the *Tile* calorimeter, the liquid-argon *hadronic end-cap calorimeter* (HEC) and the liquid-argon forward calorimeter (FCal).

The Tile Calorimeter, represents the core of the ATLAS hadronic calorimeter system and it is composed of two sub-detectors: the *HAD Tile barrel* covering the $|\eta| < 1.0$ range and the *HAD Tile Extended barrel* covering the $0.8 < |\eta| < 1.7$ range (see Figure 4.10). Both these calorimeters are composed of alternated tiles of crystal scintillators and steel absorber oriented in a radial direction with respect to the beam line (see Figure 4.12b). This geometry allows to combine a homogeneous signal extraction with a low construction cost. The scintillators produce scintillation light from the deexcitation of electrons from an excited electric state and this light is collected by wavelength-shifting fibers and finally measured by photomultipliers positioned at the top of each module. Similarly to the EM calorimeter, front-end electronics also provide analogue sums of subsets of the channels, forming trigger towers, for the L1 trigger. The Tile barrel measures 5.8 m in length, whereas the two

[9] X_0 denotes here the *radiation length*.

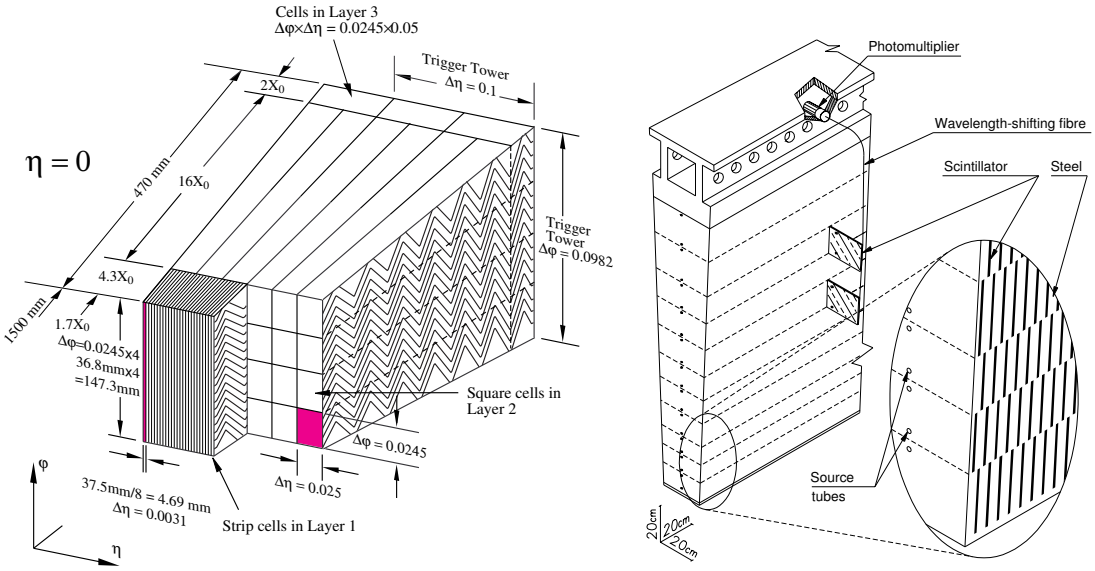

(a) LAr calorimeter barrel module

(b) Tile calorimeter module

Figure 4.12 – Sketches of barrel electromagnetic LAr and hadronic Tile calorimeters [44].

extended barrels 2.8 m each. Both systems have an inner radius of 2.28 m and an outer radius of 4.25 m.

Similarly to the LAr electromagnetic End-Cap calorimeter, the Hadronic End-Cap Calorimeter (HEC) uses liquid-argon technologies to measure the energy of hadronic particles in the $1.5 < |\eta| < 3.2$ range. However, the HEC uses copper instead of lead as absorber grouped inside different wheels with inner radius ranging from 372 mm to 475 mm. The modules of the front wheels are made of 24 copper plates, each 25 mm thick, plus a 12.5 mm thick front plate. In the rear wheels, the sampling fraction is coarser with modules made of 16 copper plates, each 50 mm thick, plus a 25 mm thick front plate. Three electrodes divide the 8.5 mm gaps into four separate LAr drift zones of 1.8 mm width each.

4.2.3.3 *The forward calorimeters*

The forward calorimeters (FCal) are also based on LAr technologies and they are located in the same cryostats as the end-cap calorimeters. These detectors are designed to provide coverage over the very forward region of the ATLAS detector ($3.1 < |\eta| < 4.9$) and they are located at approximately 4.7 m from the interaction point. Being extremely close to the LHC beamline, these modules are exposed to high particle fluxes implying the design of thiner liquid argon gaps in order to avoid ion build-up problems and to provide at the same time the highest possible density. These smaller gaps also lead to a faster signal with roughly the same instantaneous current but smaller integrated current.

Each FCal is split into three 45 cm deep modules: one electromagnetic module (FCal1) and two hadronic modules (FCal2 and FCal3). Figure 4.13 illustrates the amount of material associated to these modules and also to the other calorimeters. The FCal1 absorber is composed of lead while the two hadronic modules are provided

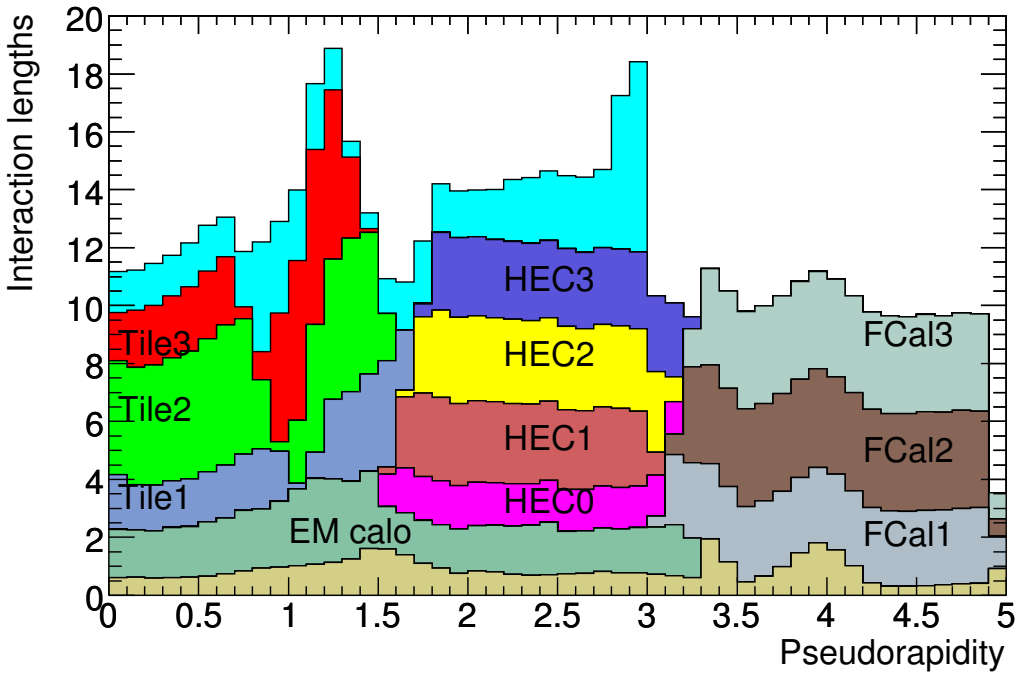

Figure 4.13 – Cumulative amount of material, in units of interaction length, as a function of $|\eta|$, in front of the electromagnetic calorimeters, in the electromagnetic calorimeters themselves, in each hadronic layer, and the total amount at the end of the active calorimetry [44]. Also shown for completeness is the total amount of material in front of the first active layer of the muon spectrometer (up to $|\eta| < 3.0$).

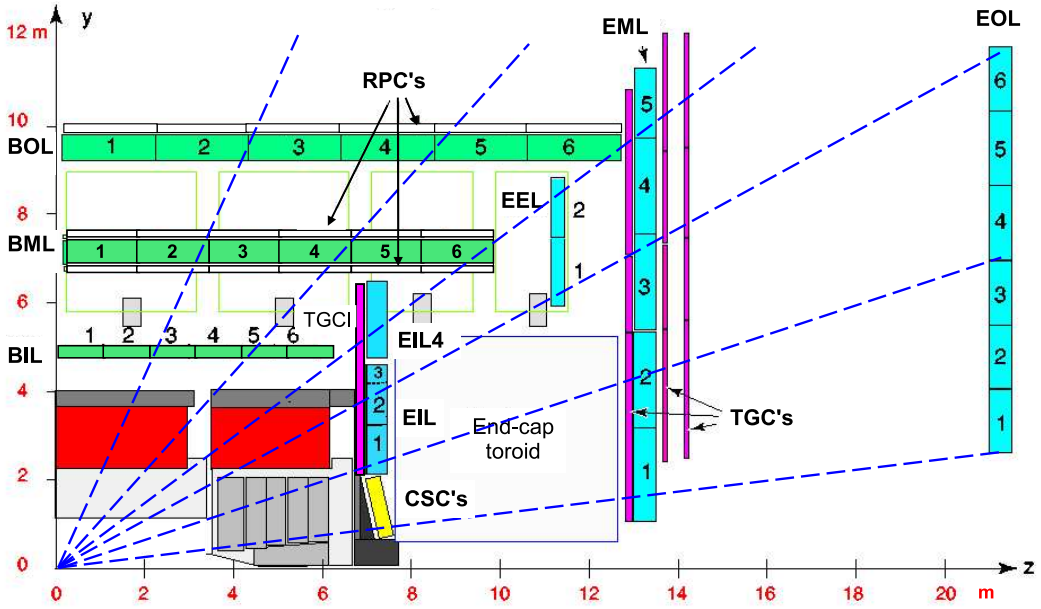

Figure 4.14 – Transverse view of the muon spectrometer in the plane containing the beam axis [44].

with tungsten plates. signals are read out from the side of FCal1 nearer to the interaction point and from the sides of FCal2 and FCal3 farther from the interaction point. This arrangement keeps the cables and connectors away from the region of maximum radiation damage. The three modules have a LAr gap of 0.269, 0.376 and 0.508 mm respectively.

4.2.4 *Muon Spectrometer*

When traversing the calorimeters, muons loe only a small fraction of energy and their precise detection needs a dedicated muon spectrometer (MS) in the outermost part of the ATLAS detector. This detector is based on the bending of muon tracks in the toroidal magnetic fields, and it can measure muons up to a pseudorapidity range $|\eta| < 2.7$ with a goal momentum resolution of 10% for 1 TeV muons.

In the barrel region ($|\eta| < 2.0$), the MS is composed of precision-tracking chambers located between and on the eight coils forming the superconducting barrel toroid magnet. The ϕ symmetry of the detector is also reflected in the symmetry of this subsystem, consisting in eight identical octants. In the transverse plane, barrel chambers are arranged in three concentric cylindrical shells, located around the beam axis at radii of approximately 5 m, 7.5 m and 10 m as shown in Figure 4.14. The precision momentum measurement is performed by the *Monitored Drift Tube chambers* (MDTs), combining high measurement accuracy and simplicity of construction. These chambers are composed of eight layers of drift tubes, operated at an absolute pressure of 3 bar, achieving an average resolution of 80 µm per tube, or about 35 µm per chamber [44].

In the forward region ($2 < |\eta| < 2.7$), the end-caps of the muon detector are composed of four layers of *Cathode Strip Chambers* (CSCs), assembled in large wheels and located at distances of 7.4 m, 10.8 m, 14 m, and 21.5 m from the interaction point and perpendicularly to the z-axis (see Figure 4.14). CSC's are multiwire proportional chambers with cathode planes segmented into strips in orthogonal directions. The resolution of a chamber is 40 µm in the bending plane and about 5 mm in the transverse plane [44].

While MDTs and CSCs can provide good muon reconstruction when combined with the inner detector measurement, these detectors can not supply muons with sufficient rapidity for the L1 trigger. This is why an additional muon system was designed in order to trigger on muons up to $|\eta| < 2.4$. This system is composed of *Resistive Plate Chambers* (RPC) in the barrel region up to $|\eta| < 1.05$, and *Thin Gap Chambers* (TGC) in the end-cap region ($1.05 < |\eta| < 2.4$). RPCs units are composed of two parallel resistive bakelite plates filled with a gas mixture, whereas TGCs are based on a similar concept to multi-wire proportional chambers. The combination of these two subsystems allow to deliver muon track information within a few tens of nanoseconds after the passage of the particle.

4.2.5 *The Trigger and Data Acquisition system*

The *Trigger and Data Acquisition system (TDAQ)* is an essential component of collider physics experiments as it is responsible for deciding whether an event will be kept for the offline physics analysis or not. It would be physically impossible to record all the collision events from the LHC due to the recording bandwidth and to the huge offline computing resources that would be needed to analyze such a large amount of data. However, characteristics of interesting events are mostly known and so the TDAQ system could already separate the interesting events from the less interesting ones.

During Run 2, the ATLAS TDAQ system was essentially composed of (see Figure 4.15 for a visual representation):

- A hardware-based **Level-1 trigger (L1)** responsible for taking the raw data from the various sub-detectors and making a first selection based on simplified object reconstruction. This system is composed of three subsystems: L1Calo, L1Muon and L1Topo.
- A software-based **High Level Trigger (HLT)** making an additional selection of the events accepted at Level-1 stage with the full detector readout available at L1 trigger rate.

Once the HLT accepts an event, after storage to disks, the events are sent to the *Tier-0* computer farm at CERN for preliminary analysis for calibration and trigger performance checks.

4.2.5.1 *The level-1 (L1) Trigger*

The *Level-1 (L1) Trigger* system represents the first stage of the ATLAS online selection process and it is designed to reach selection decisions within a latency

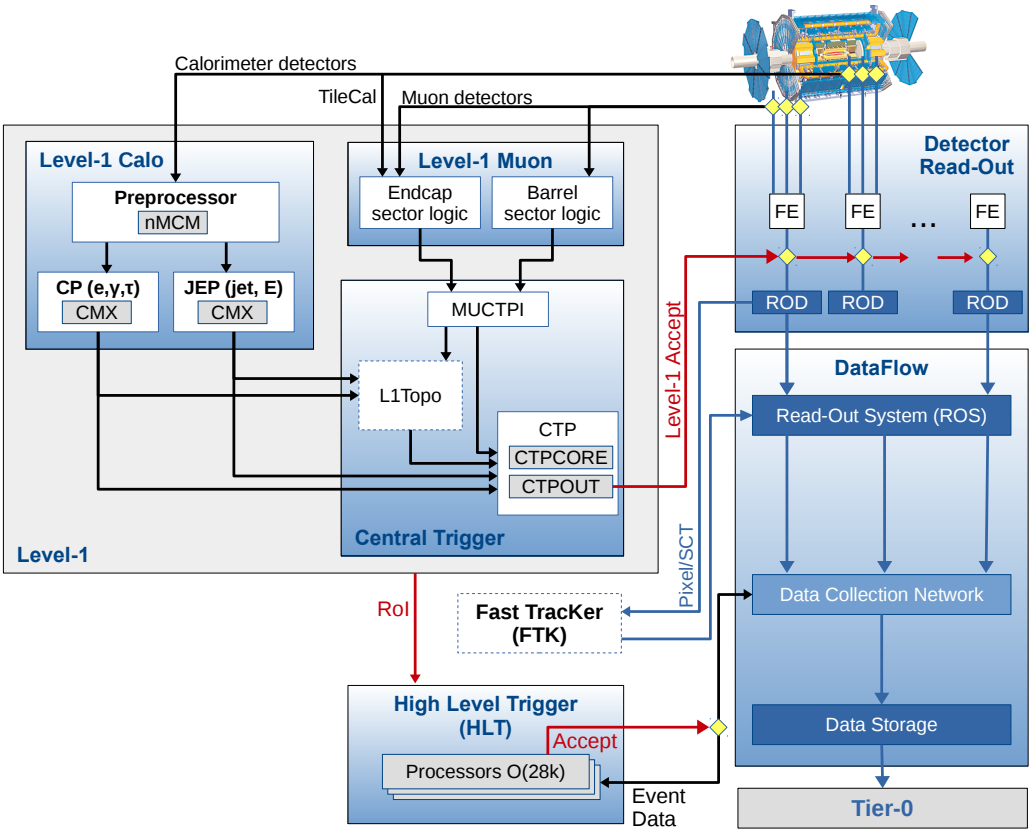

Figure 4.15 – ATLAS TDAQ system in Run 2. The Fast TracKer (FTK) was in commissioning stage during Run 2 [52].

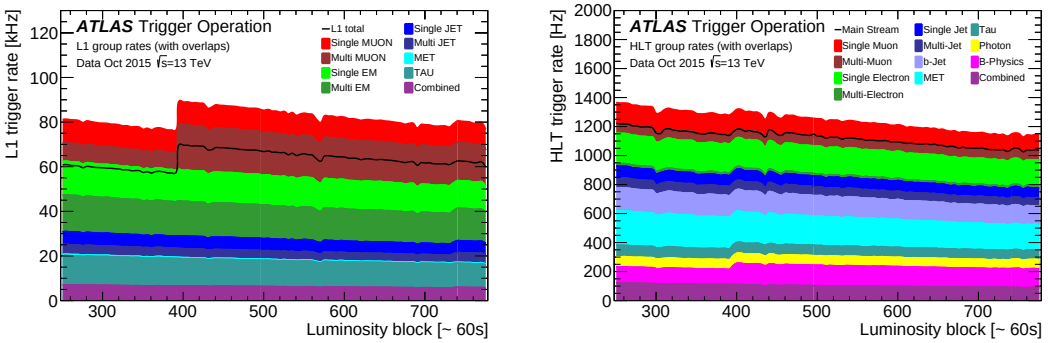

(a) L1 (b) HLT

Figure 4.16 – L1 and HLT trigger rates during an LHC fill in October 2015 with a peak luminosity of $4.5 \times 10^{33}\,\mathrm{cm}^{-2}\mathrm{s}^{-1}$ divided by trigger signature [52].

of less than 2.5 µs [53]. The L1 Trigger is implemented on custom-built electronics, and is designed to reduce the 40 MHz LHC input rate to the 100 kHz to be passed to the next selection stage represented by the HLT. This trigger is composed of two subsystems operating independently with Calorimeter and Muon information (*L1Calo* and *L1Muon*). Another subsystem known as *L1Topo* applies more complex topological cuts on jets, electrons, taus and muons after L1Calo and the resulting object are finally processed by a Central Trigger Processor (CTP) as illustrated in Figure 4.15. The final output of this trigger system is a single-bit *L1-accept* signal providing the relevant physics detectors the acceptance signal for the front-end electronics readout to be passed to the HLT. Figure 4.16a shows the L1 trigger rates split by physics signature.

The L1Calo trigger is dedicated to the analysis of analogue signals coming the ATLAS calorimeters (see Section 4.2.3 for more details). However, due to limited bandwidth capabilities, L1Calo can not read the calorimeter with its full granularity but instead it receives as input the sum of analogue signals formed by 0.1×0.1 (barrel) up to 0.4×0.4 (end-cap) $\eta \times \phi$ regions also known as *calorimeter trigger towers*. In total, 7168 trigger towers are formed [53] separately for electromagnetic and hadronic layers of the ATLAS calorimeters. From central towers ($|\eta| < 3.2$), jets, electrons/photons and hadronic taus are formed using a sliding window algorithm searching for local energy maxima against thresholds defined in the trigger menu. Trigger towers in the forward calorimeter (FCAL) are used for forward jet triggers as well as 'global' trigger items such as Missing Transverse Momentum (MET) triggers. Around these objects, *Regions of Interests* (RoIs) are formed in order to allow further processing at the HLT.

The L1Muon trigger searches for coincident muon hits using the Resistive-Plate and Thin-Gap chambers (RPCs and TGCs), being designed for fast muon reconstruction. For muon objects, RoIs are also created for further processing at the HLT.

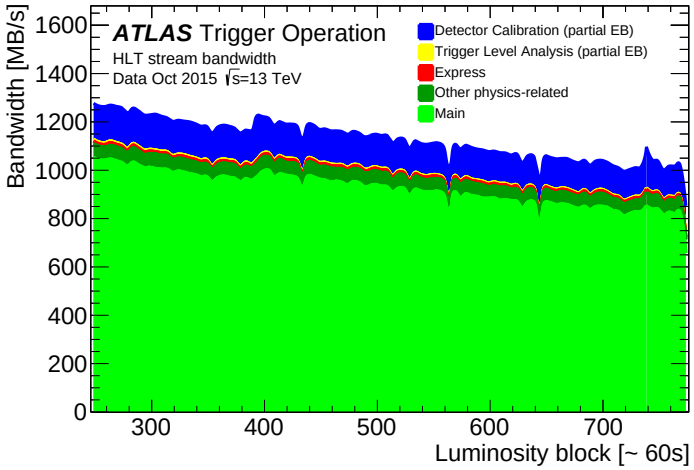

Figure 4.17 – Output bandwidth during an LHC fill in October 2015 with a peak luminosity of $4.5 \times 10^{33}\,\mathrm{cm}^{-2}\mathrm{s}^{-1}$ [52].

4.2.5.2 *The High Level Trigger*

The *High Level Trigger* (HLT) is the last step of the ATLAS trigger system and it takes the 100 kHz L1 input rate and reduces it down to 1 kHz by applying a more sophisticated object and event reconstruction. The HLT is composed of a CPU farm of 28000 CPU cores where software algorithms are run. The processing of the data starts once the events are accepted by the L1 trigger, through the event buffering provided by the Read-Out System (ROS). The event reconstruction exploits offline-like reconstruction algorithms, full detector granularity and partial track reconstruction based on the RoIs provided by the L1 trigger.

The events accepted by the HLT are separated in different *streams*, characterizing their function (debug, physics, etc.) and transferred to local storage in order to be processed by the Tier-0 facility. The *Main Physics stream* is the main stream for physics analyses and it selects different categories identified by their physics signatures relevant for physics analysis (b-jets, muons, electrons, taus, etc.). Figure 4.16b shows the HLT trigger rates split by physics signatures in early Run 2 data taking conditions. A small fraction of the Main stream events (roughly $10 - 20$ Hz) are also written to an *Express* stream that is promptly reconstructed offline in order to provide calibration and data quality information. The reconstruction of the Main physics stream generally happens up to 36 hours after the end of the stable beams status. Events that can not be processed by the HLT or for which there was a data flow processing issue are stored to the *debug* stream for further diagnosis of potential issues. Figure 4.17 shows the output bandwidth for the different HLT streams in early Run 2.

4.3 CONCLUSION

This chapter illustrated how the ATLAS detector extract signals from particles produced in the p-p collisions of the Large Hadron Collider and interacting with

the different sub-detectors. After that data are selected by the Trigger and Data Acquisition system, the process of offline reconstruction begins, providing physics objects needed for the physics analyses carried out by the ATLAS collaboration. This process is reviewed in the next chapter.

5 ATLAS OBJECT RECONSTRUCTION

" Vernon: What were you doing under our window, boy?
Harry: Listening to the news.
Vernon: Listening to the news! Again?
Harry: Well, it changes every day, you see."
– J.K. Rowling, *Harry Potter and the Order of the Phoenix*

Contents

The previous chapters have introduced the incompleteness of the Standard Model and how the ATLAS detector can detect particles resulting from the p-p collisions of the LHC. However, four-vectors suitable for the interpretation of physics collisions are needed instead of raw detector signals in order to verify the existence of new phenomena at high energy. These four-vercors are generally known as the *physics objects* of the collision as they represent the quarks, leptons and gauge bosons resulting from the p-p collisions of the LHC. This chapter illustrates how these objects were reconstructed by the ATLAS experiment during the Run 2 of the LHC.

5.1 TRACK AND VERTEX RECONSTRUCTION

Before constructing the interaction vertices which ideally represent single p-p interactions, *tracking* needs to be performed. This step is fundamental for precise measurement of charged particle momentum and for the suppression of the mis-reconstruction effects due to pileup interactions. Tracks are described through a

reference point – generally the *beamspot* position [10] – and five track parameters $(d_0, z_0, \phi, \theta, q/p)$. These parameters correspond to:

- The polar and azimutal angles θ and ϕ.
- The *transverse impact parameter* d_0, defined as the closest point in the transverse plane to the reference position.
- The *longitudinal impact parameter* z_0, defined as the closest point in the longitudinal plane to the reference position.
- The ratio q/p of the reconstructed track charge q and momentum p.

Figures of merit for good track reconstruction are represented by low resolution on these parameters, high reconstruction efficiency (*i.e.* the fraction of tracks that are generated by a true particle) and low fake reconstruction rate.

In ATLAS, tracking is performed from pure Inner Detector information and using an *inside-out* track finding strategy at first, where tracks are formed starting from the innermost pixel layer, followed by an *outside-in* tracking approach [54], where the track formation built starting from the TRT. The procedure of the inside-out approach is as follow:

TRACK SEEDING provides the necessary input objects for track finding in three-dimensional space. *Track seeds* are created as sets of three space points in the pixel, strip or in a combination of both silicon detectors (see Figure 5.1a for a schematic). Once these seeds are found, a rough estimation of the seed parameters - such as p_T, d_0 and ϕ - is performed and a preselection based on these track parameters is applied.

TRACK FINDING is done by combining track seeds together using a window search performed with a combinatorial Kalman filter [54].

AMBIGUITY SOLVING allows to select the best tracks based on a score assigned using the track parameter. Track candidates can also be merged within this stage in order to favor complete over incomplete track segments or purely random hit combinations [55].

EXTENSION TO THE TRT is performed in order to check whether the silicon track candidates left a useful set of hits also in the TRT. The quality of the resulting extension is evaluated based on the track fit and a track score calculated using tools similar to those used in the ambiguity solving. Any track which is successfully extended from the silicon detectors into the TRT is said to have a TRT extension [54].

Once the inside-out tracking is performed, the outside-in approach takes place in order to enhance the efficiency to TRT initiated tracks. In this second tracking iteration, standalone TRT track segments are considered in regions seeded by the electromagnetic calorimeter. The resulting TRT segments can then be extended back into the silicon detectors by using the leftover silicon hits from the inside-out

[10] The beamspot position is generally the average position of the p-p interactions in the Inner Detector.

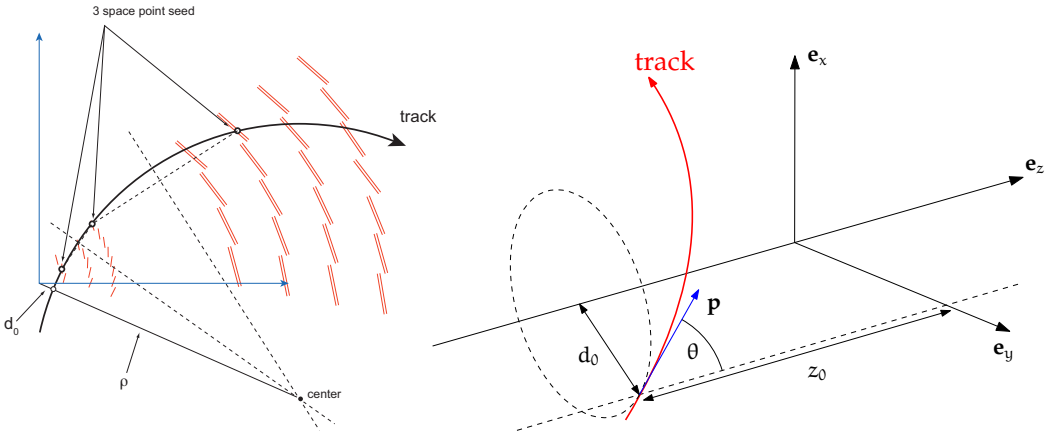

(a) Track seeding schematic [55]

(b) Tracks parameters schematic

Figure 5.1 – Schematics of tracking inside-out approach.

approach. TRT segments without any silicon hit are also kept and used for tasks as photon conversion reconstruction [54].

Once tracks are created, *primary vertices* (PV) are reconstructed in order to identify the *hard-scatter* (HS) interaction, *i.e.* the interaction having the largest collision energy. Primary vertex finding is divided in two steps: vertex finding and vertex fitting [56]. This procedure allows to identify possible primary vertex candidates and it can be summarized as follows:

- Selection of tracks passing specific quality criteria [57].
- Creation of a vertex seed by looking for the global maximum in the z-distributions of track coordinates.
- Association of tracks to this seed vertex and determination of the best vertex position through an iterative approach.
- Once the iterative approach stops, the full procedure is repeated on the tracks incompatible with the previously reconstructed primary vertex.

The procedure stops when the full set of tracks is used and vertices having at least two associated tracks are considered as primary vertices. The number of primary vertices N_{PV} in the event corresponds to the total number of primary vertices resulting from this procedure. Finally, a list of three-dimensional vertices positions and covariance matrices are provided as a result of the vertex finding algorithm.

The hard-scatter interaction, corresponding to the vertex where interesting physics is more likely to have been produced, is identified as the primary vertex carrying the largest amount of squared transverse track momenta defined, for each primary vertex PV_i, as

$$\sum_{\text{track} \in PV_i} p_T^2. \tag{5.1}$$

Once the hard-scatter vertex has been identified, all the other vertices are considered as *pile-up* vertices.

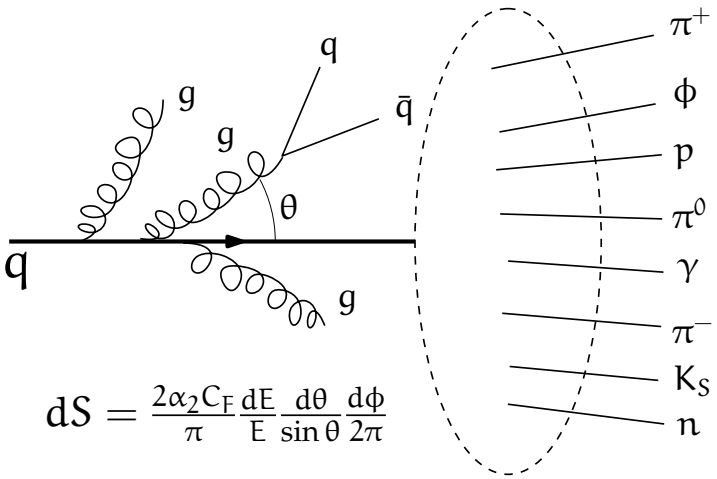

Figure 5.2 – Schematic of a jet creation from soft QCD radiation.

5.2 JET RECONSTRUCTION

Jets represent a key observable for the searches for new physics carried out by the ATLAS experiment. These objects are sprays of well collimated particles resulting from the radiative showering of strongly interactive particles (*i.e.* quarks and gluons) being produced at high energy regimes. The probability of a quark to emit a gluon can be written as

$$dS = \frac{2\alpha_2 C_F}{\pi} \frac{dE}{E} \frac{d\theta}{\sin\theta} \frac{d\phi}{2\pi}. \tag{5.2}$$

Here, C_F is the QCD color factor corresponding to the value of $4/3 \approx 1.33$. From this expression, it is possible to note that it diverges in two cases:

- For $E \to 0$. We generally refer to this feature as the **infrared (or soft) divergence** of the gluon emission.
- For $\theta \to 0$ and $\theta \to \pi$. We generally refer to this feature as the **collinear divergence** of the gluon emission.

These two divergences implies that an initial high energy quark radiates with an *infinite* probability soft gluons along the same axis of the initial quark. This process happens iteratively for each radiated gluon until the energy of the initial partons is reduced to a hadronisation energy scale. This process is called the *showering of the initial parton* and the result is a large set of well-collimated hadronic particles also known as *jets*. Figure 5.2 provides a schematic illustrating this process. The same reasoning is valid for an initial gluon parton with the only difference that the C_F factor must be replaced by another constant, namely $C_A = 3$. From this value we remark that gluons have more tendency to radiate gluons rather than quarks, resulting in a larger number of final particles in gluon-initiated jets rather than quark-initiated jets. This effect generally implies a larger number of particles composing gluon-initiated jets, representing a key observable for the tagging of quark- and gluon-initiated jets.

5.2.1 *Jet constituents and calorimeter topoclusters*

Now that the jet composition and its origin has been described, it is possible to describe how these objects are reconstructed inside a particle detector such as ATLAS. From the previous discussion, it is natural to split jet building in two steps:

1. Building constituents resulting from the showering of the initial parton. This can be done using several techniques such as topoclustering and calorimeter towers as we will explain below.

2. Use the constituents built from raw detector signals to form the groups of particles representing the physical jets. This step can be done using several iterative algorithms, which will be described later in this chapter.

This procedure is currently used by the ATLAS jet reconstruction algorithm, even though different techniques have been historically employed for this task. In the context of constituent building, several approaches based on pure calorimeter measurements have been explored. In this context, the inclusion of additional detector information rather than calorimeter only information has been recently explored at ATLAS in the *Particle Flow algorithm* that combines tracker and calorimeter information as described in Chapter 7.

In what follows *topoclustering*, the standard ATLAS jet constituent reconstruction technique, is described. This procedure consists in the clustering of entire calorimeter cells into three-dimensional clusters using an algorithm based on the absolute value of the cell energy significance [58]

$$\epsilon^{EM}_{cell} = \frac{E^{EM}_{cell}}{\sigma^{EM}_{noise,cell}}. \tag{5.3}$$

The EM index indicates that E^{EM}_{cell} and σ^{EM}_{cell} are measured at the electromagnetic (EM) scale, where the energy of electrons and photons is reconstructed correctly but not the one of hadronic particles since no corrections for the non-compensating character of the ATLAS calorimeters have been taken into account [58]. In Run 2, ATLAS compensated this effect in jet calibrations as described in Section 5.2.3.

The topoclustering algorithm works as follows:

1. The clustering starts from a seed calorimeter cell with $|\epsilon^{EM}_{cell}| > S$. Here, S represents the primary seed threshold set to $S = 4$ in Run 2.

2. The cluster then grows around the seed cell adding neighboring cells satisfying $|\epsilon^{EM}_{cell}| > N$. The threshold N is known as the growth control threshold and it was set to $N = 2$ in Run 2.

3. Finally, cluster boundaries are created by adding cells satisfying $|\epsilon^{EM}_{cell}| > P$. In Run 2, the value of P was set to 0.

A schematic of this procedure is given in Figure 5.3. The three parameters (S, N, P) completely defines the topoclustering algorithms and, considering the $(4, 2, 0)$ values used in Run 2, this clustering procedure is commonly known as the *420 ATLAS*

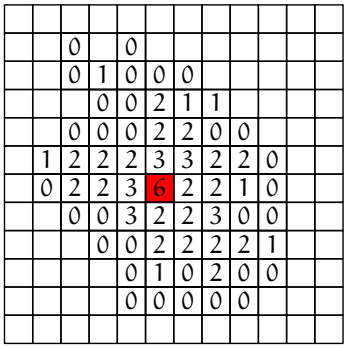

(a) Clustering of $|\epsilon^{EM}_{cell}| > 4$ cells.

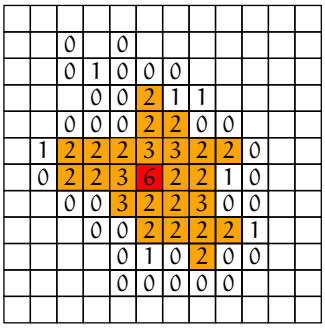

(b) Clustering of $|\epsilon^{EM}_{cell}| > 2$ cells.

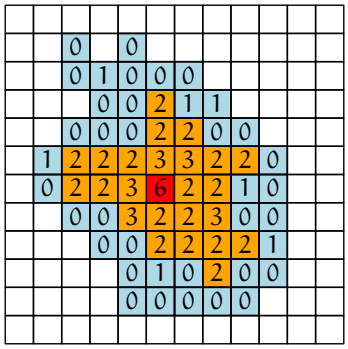

(c) Clustering of $|\epsilon^{EM}_{cell}| > 0$ cells.

Figure 5.3 – Topocluster formation schematic.

topoclustering algorithm. This algorithm represents the standard ATLAS jet constituent reconstruction technique.

While this procedure is very robust for identifying the energy deposits in the calorimeter, large topoclusters can easily originate from the merging of different particles decaying very close in the calorimeter. In order to avoid biases in jet-finding, to support good jet substructure analysis and E_T^{miss} reconstruction, topoclusters with two or more local maxima are split between each signal peaks in three dimensions passing through a procedure called *cluster splitting*. A local signal maximum is defined by $E^{EM}_{cell} > 500\,MeV$ and by the presence of at least four neighbor cells out of which none of the neighbor has larger signal. Moreover, the local maxima cells are restricted to the EM sampling layers `EMB2` , `EMB3` , `EME2` , `EME3` and `FCAL1` in order to exploit the high granularity of these calorimeter layers for better identification of separated clusters. The cluster splitting algorithm finds cells which are neighbors of two or more local signal maxima. Calorimeter cells can be shared once at most between two local clusters and the sharing of its signal is done for two clusters of energies E_1^{EM} and E_2^{EM} with the following set of weights:

$$w_{cell,1} = \frac{E_1^{EM}}{E_1^{EM} + rE_2^{EM}}, \tag{5.4}$$

$$w_{cell,2} = 1 - w_{cell,1}, \tag{5.5}$$

$$r = \exp(d_1 - d_2). \tag{5.6}$$

Here, d_1 and d_2 represent the position of the center of gravity of the two clusters. After splitting, the two subclusters are considered as two topoclusters exactly like the others and as input for jet reconstruction.

Once the topoclusters are formed, *cluster kinematic quantities* are defined starting from the associated cluster cells. For this purpose, it is useful to define the total energy of the topocluster as

$$E^{EM}_{clus} = \sum_{i=1}^{N_{cell}} w_{cell,i} E^{EM}_{cell,i}. \tag{5.7}$$

The kinematic quantity x associated to a topocluster can be defined as the energy-average across each topocluster cell

$$x_{clus} = \frac{\sum_{i=1}^{N_{cell}} w_{cell,i} \cdot |E^{EM}_{cell,i}| \cdot x_{cell,i}}{\sum_{i=1}^{N_{cell}} w_{cell,i} \cdot |E^{EM}_{cell,i}|}. \tag{5.8}$$

We generally refer to these quantities as the *topocluster moments*. Here, the absolute value of the energy has been used to avoid distortions due to negative signals.

From this definition, it is possible to define cluster directions as

$$\eta_{clus} = \frac{\sum_{i=1}^{N_{cell}} w_{cell,i} \cdot |E^{EM}_{cell,i}| \cdot \eta_{cell,i}}{\sum_{i=1}^{N_{cell}} w_{cell,i} \cdot |E^{EM}_{cell,i}|}, \tag{5.9}$$

$$\phi_{clus} = \frac{\sum_{i=1}^{N_{cell}} w_{cell,i} \cdot |E^{EM}_{cell,i}| \cdot \phi_{cell,i}}{\sum_{i=1}^{N_{cell}} w_{cell,i} \cdot |E^{EM}_{cell,i}|}. \tag{5.10}$$

Other important cluster moments are provided in Table 5.1.

5.2.2 *Jet building: the anti-kt algorithm*

Jet building uses topoclusters as inputs to reconstruct jets. Historically, several jet building algorithms have been employed at hadron colliders. A very important feature of jet finding algorithms is represented by *infrared* and *collinear* (IRC) safety, defined as the ability of a jet finding algorithm to create a final set of jets which can not be modified by an arbitrary collinear or soft gluon emission. In general, two different sets of jet algorithms are considered:

- *cone algorithms*: jets are defined using a top-down approach where jets are represented with stable cones found using a certain set of initial seeds. Most of these algorithms are affected by IRC unsafety issues.
- *sequential algorithms*: jets are defined with a bottom-up approach, starting to cluster particles which are the closest according to different distance measures [60]. These algorithms are widely used at the LHC due to their IRC safety.

In this section we describe the *anti-*k_t *algorithm* [61], one of the most common jet-finding algorithms employed at the LHC. This algorithm is a sequential recombination algorithm allowing to create regular jet cones using a distance measure, which can be generally written as

$$d_{ij} = \min\left(p^{2p}_{T,i}, p^{2p}_{T,j}\right) \frac{\Delta R^2_{ij}}{R^2}, \qquad d_{iB} = p^{2p}_{T,i}, \tag{5.11}$$

Name	Description	Definition
Timing	Derived from the peak amplitude of the time-sampled analogue signal from the calorimeter shaping amplifiers.	$t = \frac{\sum_{\left(i \mid \epsilon^{EM}_{cell,i} > 2\right)} \left(w_{cell,i} \cdot E^{EM}_{cell,i}\right)^2 \cdot t_{cell,i}}{\sum_{\left(i \mid \epsilon^{EM}_{cell,i} > 2\right)} \left(w_{cell,i} \cdot E^{EM}_{cell,i}\right)^2}$
Isolation	Quantity included between 0 and 1 measuring the activity in the calorimeter cells surrounding the topocluster. If $f_{iso} = 1$ the topocluster is completely isolated, if $f_{iso} = 0$ the topocluster is completely surrounded by other topoclusters.	$f_{iso} = \frac{\sum_{s \in \left(\text{sampling with } E^{EM,tot}_s > 0\right)} E^{EM,tot}_s \frac{N^{noclus}_{cell,s}}{N^{neighbor}_{cell,s}}}{\sum_{s \in \left(\text{sampling with } E^{EM}_s > 0\right)} E^{EM,tot}_s}$
Average LAr quality	The average LAr calorimeter quality is measured by comparing the signal pulse shape with a reference shape in each cell, and then applying the cell average described in Equation (5.8).	$\langle Q_{LAr} \rangle = \frac{\sum_{i=1}^{N_{cell}} w_{cell,i} \cdot \lvert E^{EM}_{cell,i} \rvert \cdot Q^{LAr}_{cell,i}}{\sum_{i=1}^{N_{cell}} w_{cell,i} \cdot \lvert E^{EM}_{cell,i} \rvert}$
Average Tile quality	The average Tile calorimeter quality is measured by comparing the signal pulse shape with a reference shape in each cell, and then applying the cell average described in Equation (5.8).	$\langle Q_{Tile} \rangle = \frac{\sum_{i=1}^{N_{cell}} w_{cell,i} \cdot \lvert E^{EM}_{cell,i} \rvert \cdot Q^{Tile}_{cell,i}}{\sum_{i=1}^{N_{cell}} w_{cell,i} \cdot \lvert E^{EM}_{cell,i} \rvert}$
Fraction of bad LAr quality cells	Fraction of cells in a topocluster having a bad LAr quality (*i.e.* $Q_{LAr} > 4000$) [59].	$f_{BadLArQ} = \frac{N_{cells}(Q_{LAr} > 4000)}{N^{tot}_{cells}}$

Table 5.1 – Other useful topocluster moments [58].

where d_{ij} represents the distance between particle i and j and d_{iB} the distance between particle i and the beam. The parameter R is generally called the *jet radius* and it represents the only free parameter of the algorithm configurable by the user. ΔR_{ij} represents the $\eta - \phi$ distance defined in Equation (4.8). The parameter p is an integer defining different types of algorithms of the sequential-recombination family: $p = 1$ defines the k_t *algorithm* [62], $p = 0$ represents the *Cambridge/Aachen* (C/A) algorithm and $p = -1$ defines the *anti*-k_t *algorithm* [61].

The sequential procedure to find jets with these algorithms consists of the following steps:

1. Compute the distance between each particle i and j d_{ij} and between each particle i and the beam d_{iB} as described in Equation (5.11) and store them into a database.

2. Find the smallest d_{ij} and the smallest d_{iB} in the previous database and:

   - If $d_{ij} < d_{iB}$, recombine the two particles into single one noted as ij, remove particle i and j from the database and add particle ij to this list.
   - If $d_{iB} < d_{ij}$, call the particle i a jet and remove it from the list of particles.

3. Repeat the above procedure until there are no particles left in the database.

Considering the anti-k_t algorithm ($p = -1$), it is easy to understand quantitatively how this clustering procedure works. When particle i and j are very close and very high in p_T, d_{ij} will be extremely small causing the certain merging of these particles at first. Once these energetic particles are clustered together, the minimum term in Equation (5.11) will add the nearby soft particles to the energetic ones due to the ΔR term in d_{ij}. This procedure will allow to build IRC-safe cone-like jets as shown in Figure 5.4.

ATLAS can reconstruct jets using several techniques, but topocluster-based anti-k_t jets are certainly the most historically used jet collections today. This list of jets is built by running the anti-k_t algorithm on the calorimeter topocluster defined earlier in Section 5.2.1. In general, ATLAS uses two kind of jets:

- the *small-R jets* where anti-k_t is run using $R = 0.4$ for the jet radius parameter. These jets generally reconstructs quark/gluon initiated jets and are employed by most of the ATLAS analyses.

- the *large-R jets* where anti-k_t is run using $R = 1.0$ for the jet radius parameter. These jets are particularly useful to reconstruct boosted particles decaying to quarks (*e.g.* top,W,Z, etc.) and their identification can be performed by looking at the internal structure of the jets. The domain studying the internal structure of these objects is known as *jet substructure*.

5.2.3 *Jet calibrations*

It has been previously mentioned in Section 5.2.1 that the energy measurement provided by the calorimeters is at the right scale for electromagnetic particles (electrons, positrons and photons) while it is underestimated for hadronic particles due

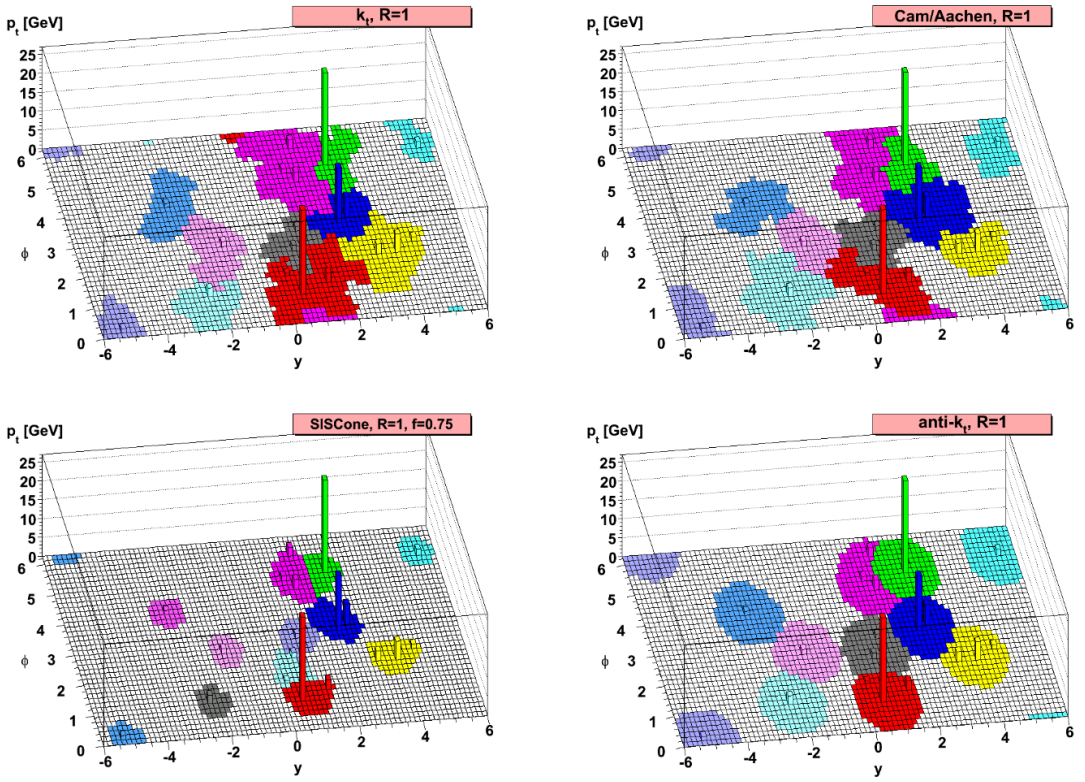

Figure 5.4 – Comparison of different jet algorithm with anti-k_t [61].

to their interaction processes creating undetectable energy in the calorimeters. Other effects, such as pileup and energy leaks, can also cause energy loss in the final jet measurement which has to be accounted for correct reconstruction. In what follows, the calibration procedure which adjusts the energy, momentum and direction of the reconstructed jets in order to match the truth jets is described.

The different stages of the ATLAS jet calibration for small-R jets are shown on Figure 5.5. After jet finding, during the 2015-2016 period the first calibration step consisted in the recalculation of the four-momentum of the jets in order to point to the hard-scatter primary vertex rather than the center of the detector. This step was known as the *Origin correction* of the jet and it allowed to improve the η resolution of these objects. This quantity represents the distance between the pseudorapidity of the reconstructed jet and the truth jet. With this correction, the η resolution improved from roughly 0.06 to 0.045 at a jet p_T of 20 GeV and from 0.03 to below 0.006 above 200 GeV [63]. Since 2017, the four-momenta of topoclusters was corrected in order to point to the hard-scatter primary vertex and the jet calibration procedure was simplified by discarding the Origin correction.

The next calibration step consists in the removal of the in-time and out-of-time pileup effects (see Section 4.1.1 for more details) using two consecutive correction techniques:

1. The ρ-*area subtraction* where an average pileup contribution is subtracted using the area A of the jet and the median p_T density ρ of jets in the $\eta - \phi$ plane. The value of ρ is adjusted on a per-event basis.

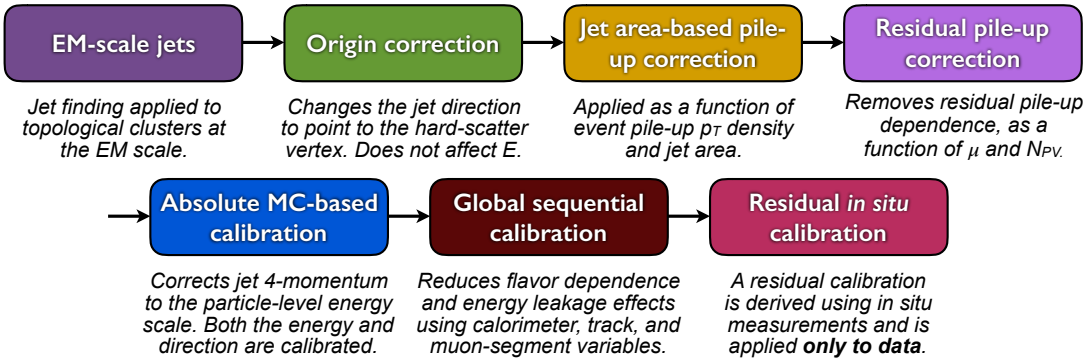

Figure 5.5 – ATLAS calibration stages for EM-scale small-R jets [63]

2. The *residual correction* where an additional subtraction is parametrized using the number of interaction per bunch crossing μ and the number of primary vertices N_{PV}. This correction aims at removing residual dependencies from pileup after the ρ subtraction.

The total area correction can be parametrized as

$$p_T^{corr} = p_T^{reco} \underbrace{-\rho \cdot A}_{\rho\text{-area subtraction}} \overbrace{-\alpha \cdot (N_{PV} - 1) - \beta \cdot \mu}^{\text{residual correction}}, \tag{5.12}$$

where p_T^{reco} refers to the EM-scale p_T of the reconstructed jet, A is the *area* of the jet and α, β the different parameters of the residual correction parametrized separately in bins of p_T^{truth} and $|\eta|$ (see Figure 5.6a).

Once the jet area subtraction is performed, we need to compensate the energy loss due to the hadronic showers. This step is generally called the *Jet Energy Scale* (JES) correction and it relies on the measurement of the *jet energy response* defined as

$$R = \frac{E_{jet}^{reco}}{E_{jet}^{truth}}. \tag{5.13}$$

In this formula, reconstructed jets are matched to truth jets – *i.e.* jets reconstructed by running anti-k_t of the truth simulated hard-scatter particles – within $\Delta R = 0.3$. The response R is then binned in E_{jet}^{truth} and η_{jet}^{reco}. The resulting R distributions are then fitted using a gaussian distribution and the average values $\langle R \rangle$ are used to invert the jet energy through a procedure called *numerical inversion*

$$E_{jet}^{calibrated} = E_{jet}^{reco} \cdot \langle R \rangle^{-1}. \tag{5.14}$$

Figure 5.6 shows the distribution of $\langle R \rangle$ as a function of η_{jet}^{reco}. Gaps and transitions between calorimeter sub-detectors result in a lower energy response due to the undetected particles.

After the previous jet calibrations, residual dependencies of the JES on longitudinal and transverse features are observed as well as effects due to the jet particle composition and the internal jet energy distribution. In order to correct such effects, a sequence of different sub-calibrations accounting for different physical effects also

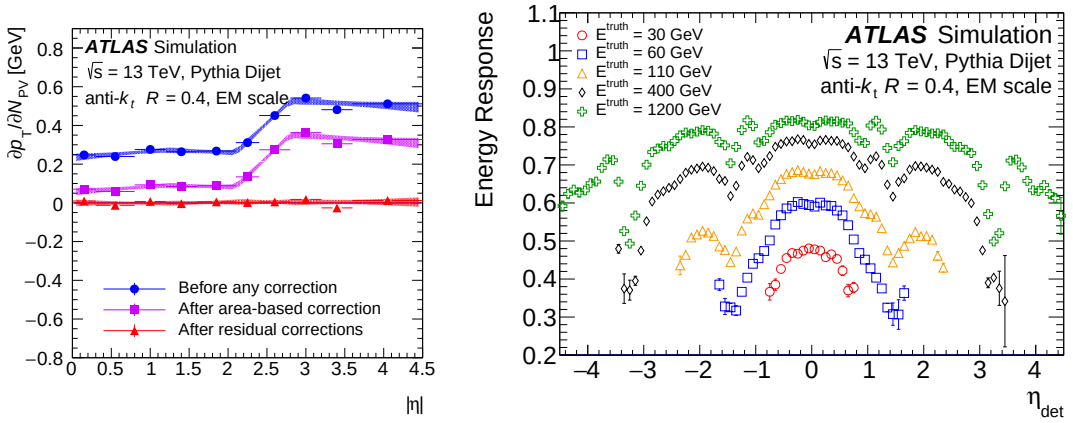

(a) Residual calibration effects vs $|\eta|$

(b) Jet energy response

Figure 5.6 – Effects of residual calibration and jet energy response [63].

known as *Global Sequential (GSC) Calibration* is applied. Five observables have been identified for correcting such effects:

1. The fraction of energy in the first layer of the of the hadronic Tile calorimeter f_{Tileo}.
2. The fraction of energy in the third layer of the LAr calorimeter f_{LAr_3}.
3. The number of tracks with $p_T > 1\,\text{GeV}$ ghost-associated with the jet n_{trk}. In this association technique, tracks are treated as infinitesimally soft and, after setting their p_T to 1 eV, these are added to the list of inputs for jet finding algorithm. After jet-finding is finished, tracks entering in the jet are considered as ghost-associated with this jet.
4. The average p_T-weighted distance in the $\eta - \phi$ plane between the jet axis and all tracks of $p_T > 1\,\text{GeV}$ ghost-associated with the jet $\mathcal{W}_{\text{trk}}$.
5. The number of muon track segments ghost-associated with the jet n_{segments}.

The n_{segments} correction is particularly useful to account for energy leaks in the calorimeter due to extremely energetic jets for which the calorimeter is not able to collect the full shower. These kind of jets are called *punch-through jets* and this specific correction is also known as the *punch-through* correction.

The p_T response of each variable is shown on Figure 5.7. After the full GSC calibration is applied, the response dependency is reduced to less than 2% for each variable.

The last step of the calibration chain consists in the reduction of the disagreement of the jet response between data and MC simulations. Such differences arise from the imperfect simulation of detector material, pileup and particle showering. In order to achieve this goal, a measurement of the jet response in data has to be performed. However, differently from MC simulation, data events do not have accessible the generator information necessary for the estimation of the truth energy in Equation (5.13). This is why well-identified and calibrated physics objects (photons, Z boson,

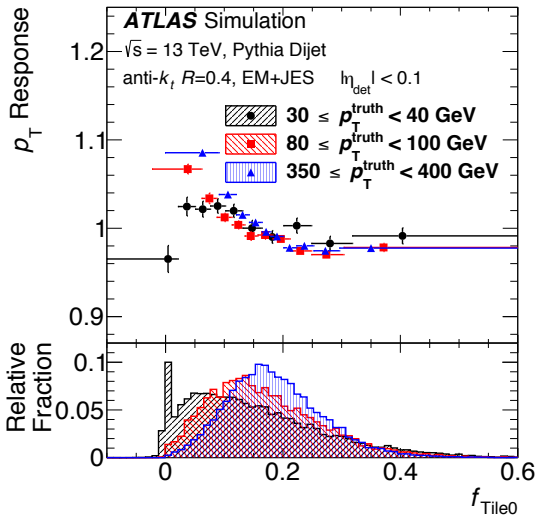

(a) f_{Tile0} response

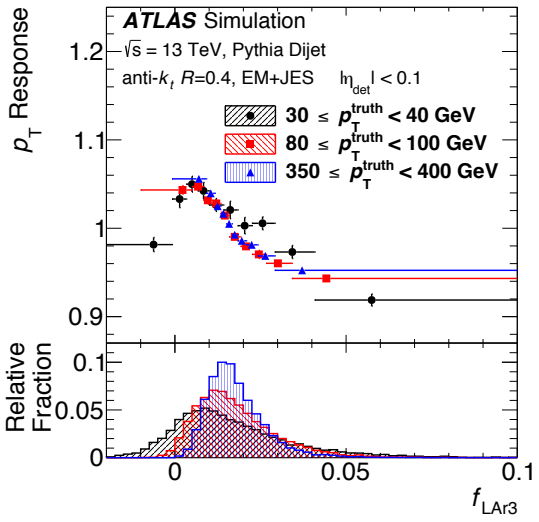

(b) f_{LAr3} response

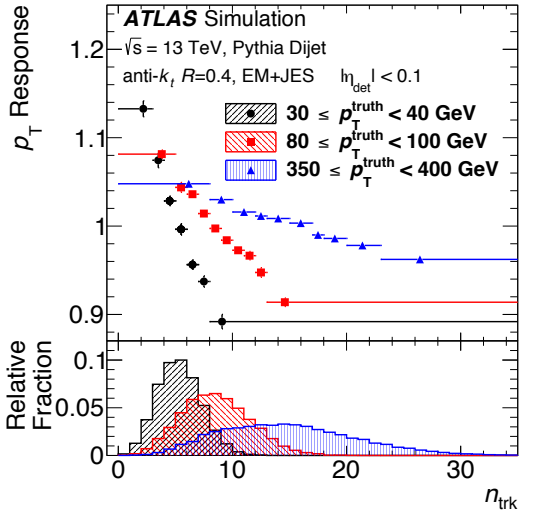

(c) n_{trk} response

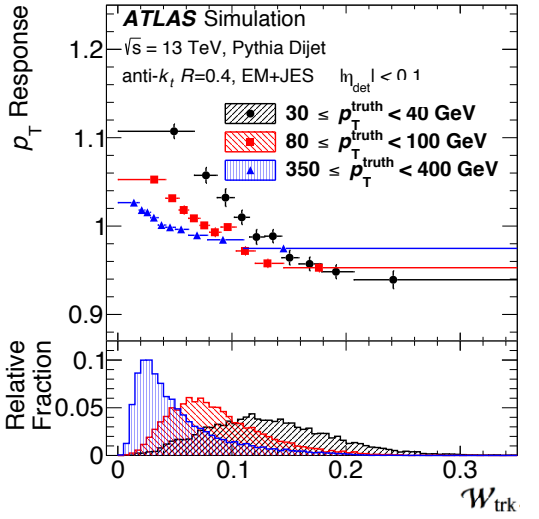

(d) $\mathcal{W}_{trk}$ response

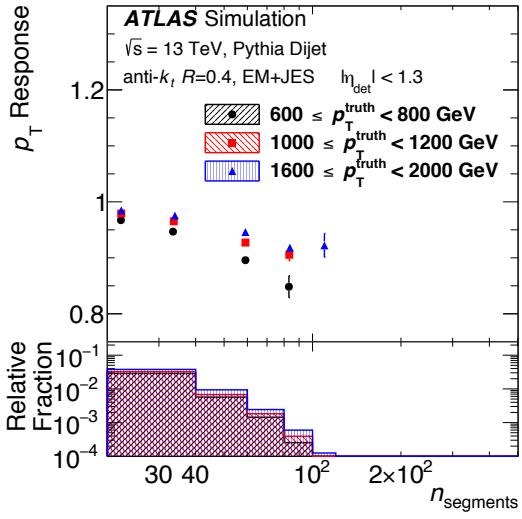

(e) $n_{segments}$ response

Figure 5.7 – Different responses for GSC calibration variables [63].

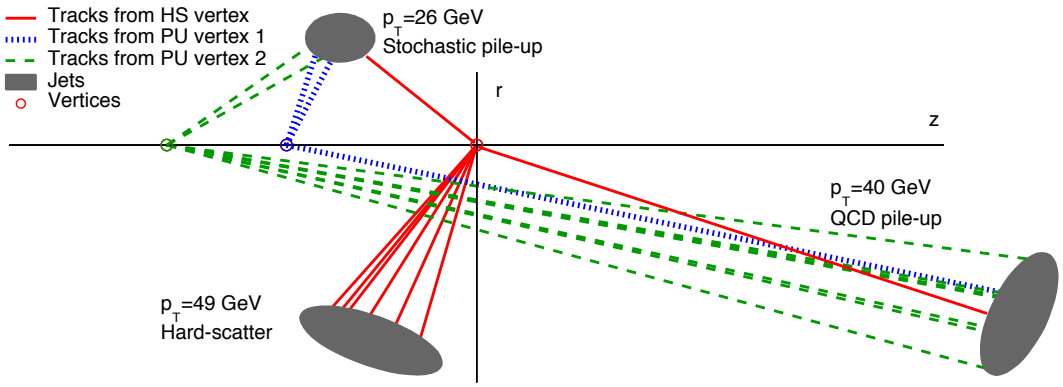

Figure 5.8 – Different pileup jet types inside the ATLAS detector [64].

multijets) recoiling against a jet can be used for the estimation of the correct jet energy through the following quantities:

$$R_{\text{in-situ}} = \frac{p_T^{\text{jet,reco}}}{p_T^{\text{ref,reco}}}. \tag{5.15}$$

Here, $p_T^{\text{ref,reco}}$ is the transverse momentum of the reference object while $p_T^{\text{jet,reco}}$ the transverse momentum of the recoil jet. This calibration procedure is also known as the *in-situ calibration* and it is performed by applying numerical inversion through the quantity

$$c = \frac{R_{\text{in-situ}}^{\text{data}}}{R_{\text{in-situ}}^{\text{MC}}}. \tag{5.16}$$

Different in-situ calibrations are applied in sequence in order to correct the discrepancies in different p_T ranges. At first, the Z/γ + jets correction is performed using well calibrated photons and Z bosons, the latter decaying to electron and muon pairs, to measure the p_T response of the recoiling jet up to a p_T of 950 GeV. After this correction, the multijets balance (MJB) is performed for the high-p_T jet range $300 < p_T < 2000$ GeV using events with multiple well calibrated recoil low-p_T jets.

5.2.4 *Pileup jet identification*

The high number of simultaneous collisions of the LHC allows to probe new physics with very low production cross-section. However, multiple p-p collisions can significantly contaminate the physics objects produced by the hard-scatter interaction. In the context of jets, pileup could only modify the readout of interesting objects, but also cause additional fake jets to be reconstructed generally called *pileup jets*. In order to keep sensitivity to new physics, these jets need to be suppressed.

Pileup jets can be split in two categories:

- *Stochastic pileup jets* representing pileup jets created from random fluctuations of particles in specific regions of the ATLAS calorimeters.

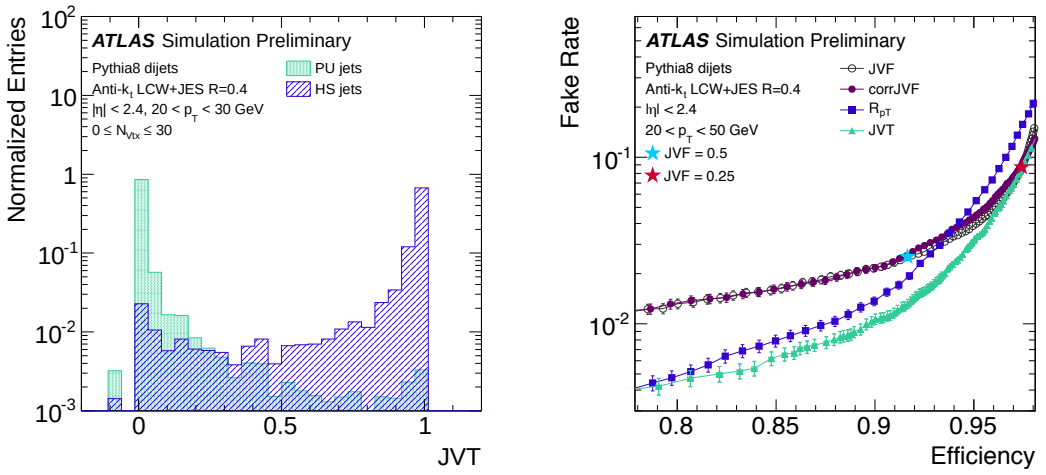

(a) (b)

Figure 5.9 – (a) JVT distribution for hard-scatter and pileup initiated jets. (b) Fake rate from pileup jets versus hard-scatter efficiency curves for different pileup jet classification observables [65].

- *QCD pileup jets* where jets are created from hard pileup interactions creating real jets having back-to-back topologies.

Figure 5.8 illustrates these two jet categories and their creation from pileup interactions.

Tracking provides the necessary information for the suppression of these pileup jets, and their identification is performed after jet building. The pileup jet classification is performed in ATLAS using a discriminant called *Jet Vertex Tagger* (JVT). This quantity is constructed from a two-dimensional likelihood based on a k-nearest neighbor (kNN) algorithm of two variables [65]:

$$R_{p_T} = \frac{\sum_k p_T^k(PV_{HS})}{p_T^{jet}}, \tag{5.17}$$

$$\text{corrJVF} = \frac{\sum_k p_T^{trk_k}(PV_{HS})}{\sum_l p_T^{trk_l}(PV_{HS}) + \frac{\sum_{n\geqslant 1}\sum_k p_T^{trk_k}(PV_n)}{k\cdot n_{PU}^{trk}}}. \tag{5.18}$$

In these expressions, $\sum_k p_T^k(PV_{HS})$ is the scalar p_T sum of the tracks associated to the jet and originating from the hard-scatter vertex. The term $\sum_{n\geqslant 1}\sum_k p_T^{trk_k}(PV_n)$ represents the scalar p_T sum of the rest of the jet tracks associated to the pileup vertices PV_n and n_{PU}^{trk} the total number of pileup tracks in the event. k is a constant value taking the value $k = 0.01$. The distribution of JVT for hard-scatter and pileup initiated jets, as well as the hard-scatter jet efficiency versus fake rate is provided in Figure 5.9.

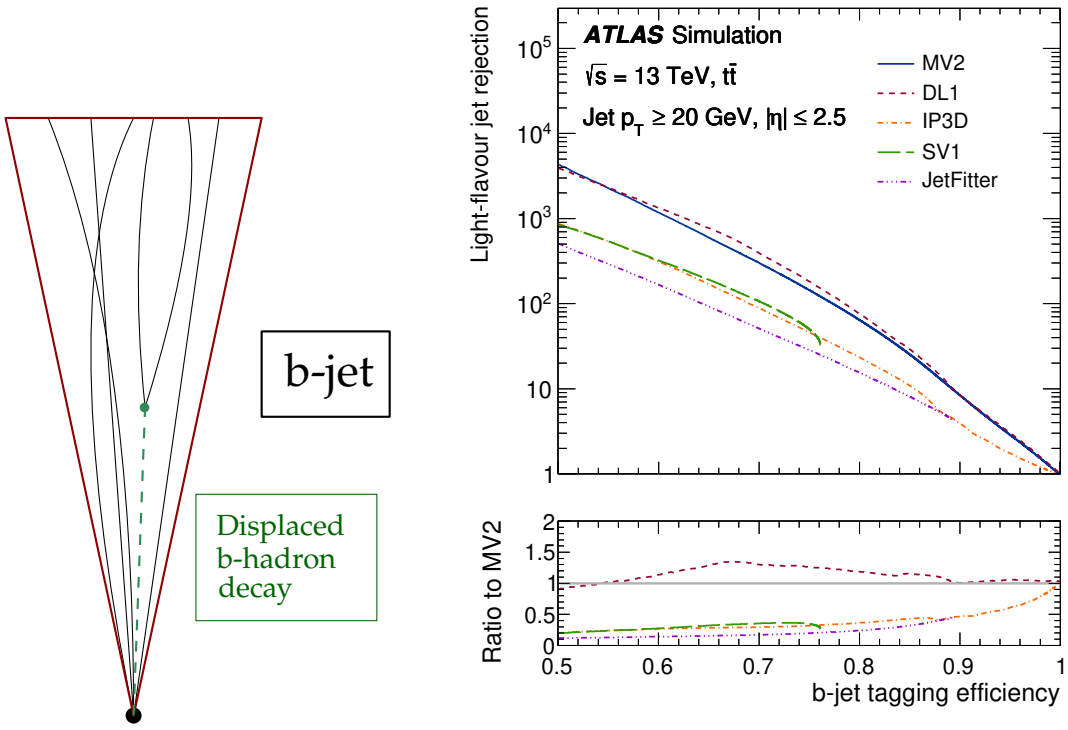

(a) (b)

Figure 5.10 – (a) Schematic of b-jet having a displaced b-hadron decay and (b) b-tagging efficiency ϵ_b versus light-flavour jet rejection $1/\epsilon_l$ for different b-tagging algorithms [66].

5.3 FLAVOUR TAGGING

The identification of jets being initiated by bottom quarks represents a major task for the physics analyses performed by the ATLAS experiment, such as top, Higgs and SUSY physics analyses. In this context, particles composing bottom-initiated jets (or *b-jets*) are characterized by the presence of a long-lived b-hadron, having a lifetime of the order of $\tau = 1.5\,\mathrm{ps}$ and an average decay length in the order of of $\langle c\tau \rangle \approx 0.45\,\mathrm{mm}$. These displaced decays inside the jet volume are generally exploited for the identification of bottom-quark-initiated jets.

The ATLAS experiment uses different algorithms for the identification of b-jets, also known as *b-tagging* algorithm, all exploiting the informations related to the b-hadron decay as well as the properties of the b-quark fragmentation [66]. The developed strategy consists of two stages:

- Firstly, two low-level algorithms exploit the individual properties of charged-particle tracks and of the displaced vertex in order to identify b-hadron decays inside jets. In the first case, the IDP2 and IDP3 algorithms [66] exploits the large impact parameters of tracks originating from b-hadron decays. In the second case, displaced vertices are formed starting from the tracks reconstructed in the ID.

- In the second stage, the outputs of the two low-level algorithms are combined into a single output using multivariate techniques in order to increase the performance of the b-jet identification. The default algorithm of ATLAS is the MV2 algorithm [66] combining different input variables using a Boosted Decision Tree (BDT). In order to optimize the b-tagging efficiency in a full jet p_T spectrum, the training is performed using a mixed sample of $t\bar{t}$ and $Z' \to b\bar{b}$ events.

The performance of these algorithms is generally studies by looking at the *b-jet efficiency* defined as the probability of identifying a real b-jet as a b-jet ϵ_b and at the probability of mistakenly tagging a light quark jet as a b-jet ϵ_l. The quantity $1/\epsilon_l$ is generally referred to as the *light-flavour jet rejection*. A better performance of a b-tagging algorithm is characterized by a higher light-flavour jet rejection at a fixed b-tagging efficiency. Several curves associated to different b-tagging algorithm are shown on Figure 5.10b, showing the strong performance of the MV2 algorithm.

5.4 ELECTRON AND PHOTON RECONSTRUCTION

Electrons and photons are generally reconstructed starting from similar energy deposits in the EM calorimeter due to the similar showers they produce in this subsystem. In the case of electrons, one or more tracks in the Inner Detector allows to identify an electron/positron candidate from an EM shower, while photons are characterized from energy deposits inside the EM calorimeter only. However, these characteristics can be further complicated by the emission of bremsstrahlung photons from electron/positron particles or conversion of photons into an electron-positron pair in the Inner Detector due to the large probability of a electron-positron pair emission at high energy. Since 2017, in replacement to the sliding-window algorithm employed for the reconstruction of fixed-size clusters of calorimeter cells [67], the ATLAS electron/photon reconstruction has been improved with a dynamic, variable-size, cluster type called *supercluster* [68]. Superclusters are particularly useful to recover the energy from bremsstrahlung photons or from electrons emitted by photon conversions.

The procedure to form superclusters can be summarized as follow:

- In the first stage, all the 420 topoclusters employed also for jet reconstruction are tested to be seeds for superclustering. An electron supercluster seed is required to have a minimum E_T of 1 GeV with a matched track containing at least four hits in the silicon tracking detectors. For photon supercluster seeds, topoclusters are required to have a minimum E_T of 1.5 GeV, without any requirement on tracks.

- The second stage is composed of the supercluster satellites identification, based on a $\Delta\eta \times \Delta\phi$ window centered on the seed barycenter. For both electrons and photons, a topocluster is considered a satellite if it falls within a $\Delta\eta \times \Delta\phi = 0.075 \times 0.125$ range as these generally represents secondary showers generated by the original electron or photon. For electrons only, a broader window range of $\Delta\eta \times \Delta\phi = 0.125 \times 0.300$ around the seed barycenter is also applied.

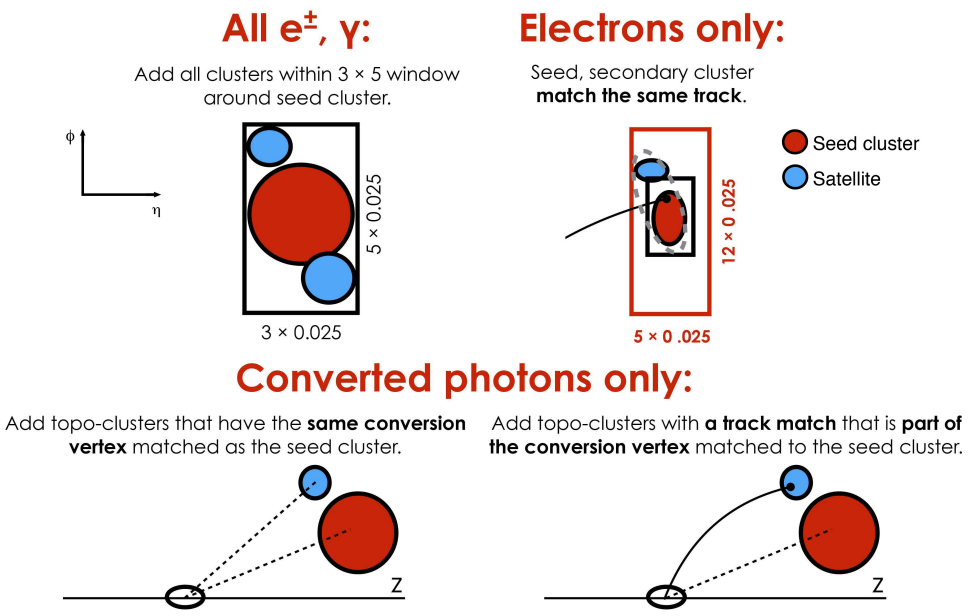

Figure 5.11 – Schematic of the superclustering formation for electrons and photons [68]. Seed clusters are shown in red while satellite clusters in blue.

For photon conversion with a conversion vertex identified by silicon tracks, an identified electron satellite is added to the supercluster if it matches the conversion vertex.

- Superclusters are formed by all seed clusters with their associated satellites. The last step consists in the creation of the supercluster starting from the EM calorimeter cells composing the seed and satellite topocluster.

Figure 5.11 shows the different possible superclusters formed by seed and satellite topoclusters.

5.4.1 *Electron and photon calibration*

After supercluster creation, the electron and photon candidates are calibrated. The calibration procedure is composed of different steps:

1. A correction to the truth electron/photon calorimeter energy is applied using a multivariate algorithm trained on MC simulation. This regression is based on the shower properties in the EM calorimeter.
2. Residual corrections for the non-uniformities in the calorimeter response and non-nominal high-voltage settings for some parts of the calorimeter.
3. Adjustment for the data-to-simulation agreement using a set of high-purity $Z \to e^+e^-$ data events. Corrections are applied to simulated events in order to better match the data.

The invariant mass of di-electron pairs in $Z \to e^+e^-$ events is illustrated in Figure 5.12a for both data and MC simulation, showing good agreement after calibration.

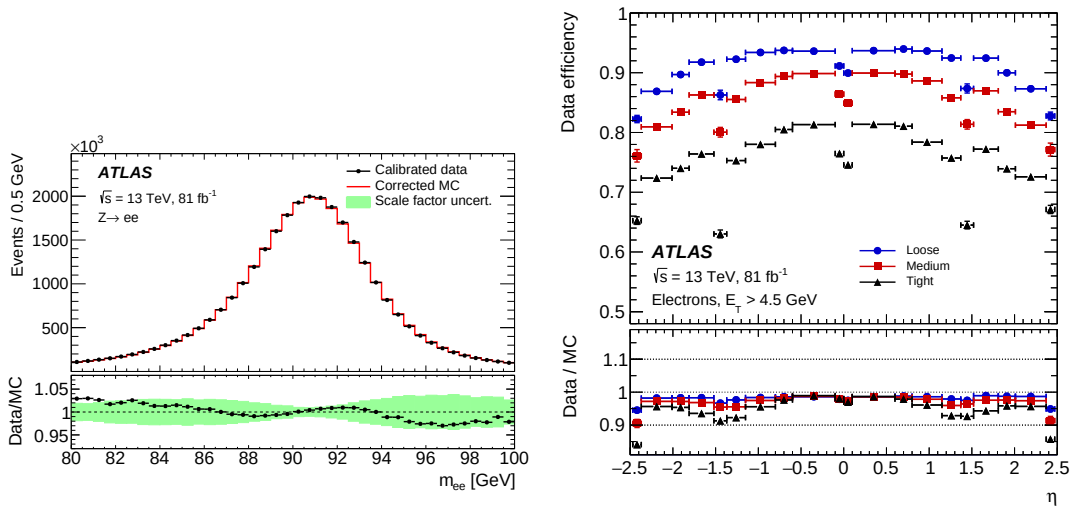

(a) (b)

Figure 5.12 – (a) Invariant mass distribution of two electrons passing a $Z \to e^+e^-$ selection and (b) efficiency of different electron identification working points as a function of η [68].

5.4.2 *Electron identification*

In order to improve the quality of electrons and photons, different identification and quality requirements have been defined.

For electrons, their identification relies on a likelihood discriminant constructed from quantities based on the Inner Detector track and the longitudinal/lateral development of the shower in the EM calorimeter [68]. The likelihood discriminant pdfs are fixed for signal and background (*i.e.* true and fake electrons) using a sample of simulated dijet, $Z \to e^+e^-$ and $W \to e\nu$ events and binned in η and E_T. From these likelihoods, three working points called *Loose*, *Medium* and *Tight* are defined starting from three likelihood discriminant thresholds based on the average electron efficiencies of 98%, 90% and 80%. Further requirements on the track quality and p_T are applied for the Medium and Tight working point. Figure 5.12b shows the efficiency of such working points on Run 2 data as a function of the pseudorapidity η.

For details about photon identification the reader can refer to [68].

5.5 MUON RECONSTRUCTION

Muon reconstruction provides muon objects for ATLAS analyses and, in a first step, is performed separately using track hits in the Inner Detector (ID) and in the Muon Spectrometer (MS). After reconstruction in each subsystem, the track segments are further combined in order to provide precise muon measurements for physics analyses. The reconstruction in the Inner Detector happens exactly as for all the other tracks (see Section 5.1 for further details). In the MS, muon reconstruction starts with a search for track patterns inside each muon chamber in oder to form segments. In the CSC, segments are built using a separated combinatorial search in

the $\eta - \phi$ plane of the detectors [69]. Muon track candidates are then built by fitting together track segments found in each layer. The combination starts from segments in the middle layers of the detector for then adding the segments in the outer and inner layers. At least two matching segments are required to form a muon track candidate, with the exception of the barrel-endcap transition region where only one single high-quality segment can be used to build a track. A χ^2 fit is then performed using the hits provided by each track candidate and a track is accepted only if the χ^2 fit satisfies certain selection criteria.

Once MS muon tracks are formed, combination with the ID track is performed. Four muon types can then be defined [69]:

- *Combined (CB) muons*: provided by a global fit taking all the hits associated to tracks in the ID and MS. During the global fit, MS hits might be added or removed in order to improve the track fit quality.

- *Segment-tagged (ST) muons*: corresponding to tracks in the ID that, after extrapolation to the MS, match at least one local track segment in the MDT or CSC chambers. These are particularly useful for low p_T muons where only one segment is found in the MS or regions with reduced MS acceptance.

- *Calorimeter-tagged (CT) muons*: where a muon is identified from an ID track with a matched calorimeter energy deposit compatible with a minimum-ionizing particle. These muons are useful to recover muon acceptance in regions of the detector where the MS is only partially instrumented due to cabling and services for the ID and the calorimeters.

- *Extrapolated (ME) muons*: corresponding to a MS track with a loose requirement on the compatibility with an origin on the p-p interaction point. These muons are mainly intended to extend the muon reconstruction acceptance to the region not covered by the ID ($2.5 < |\eta| < 2.7$).

5.5.1 *Muon calibration*

After reconstruction, different corrections are applied to muon candidates in order to achieve a per mille and percent precision on the muon momentum scale and resolution respectively. In this context, correction factors are derived by looking at $Z \to \mu^+\mu^-$ and $J/\Psi \to \mu^+\mu^-$ processes in data and MC simulated events. The correction factors to be applied to MC simulation are defined in $\eta - \phi$ detector regions [69]. These corrections are derived using only CB muons and they are based on the transverse momentum measured in the ID and MS separately. Different effects are corrected which are not account in simulation, such as inhomogeneities of the magnetic fields and the dimensions of the detector perpendicular to the magnetic field. The effects of the calibration can be seen in Figure 5.13a, where the data and corrected/ uncorrected simulation are shown. The simulated Z mass peak is narrower and slightly shifted before calibration, showing the beneficial effects on the calibration procedure.

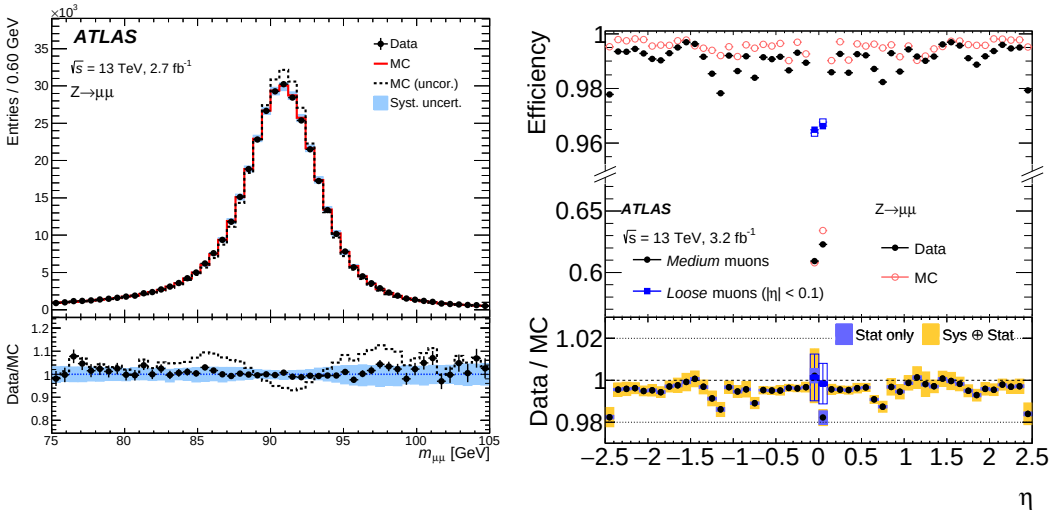

(a) Muon calibration effects

(b) Muon efficiency versus η

Figure 5.13 – Muon calibration effects (a) and reconstruction efficiency (b) for $Z \to \mu^+\mu^-$ events [69]. It is possible to note the beneficial effects of the muon momentum calibration allowing to better match the data at the Z mass peak in the corrected simulation.

5.5.2 *Muon identification*

After reconstruction, muon identification is performed by applying different quality requirements to disentangle signal muons from background induced from the decay of hadronic particles such as pions and kaons. All the different muon classifications in ATLAS are based on different quantities, characterizing the quality of the track in the ID and in the MS. Among these quantities we can find the ID track q/p *significance*[11], the absolute value of the difference between the p_T measured in the ID and in the MS divided by the p_T of the combined track notes as ρ' and the normalized χ^2 of the combined track fit [69]. For muon identification, four working points are defined [69]:

- The *Medium* working point, representing the ATLAS default working point, allowing to minimize the uncertainties related to muon reconstruction and calibration. In this selection, only CB and ME muon tracks are considered. The ME muons are supposed to extend the acceptance outside the ID geometrical coverage. An upper cut un the q/p significance is also applied in order to suppress contamination from hadrons misidentified as muons.

- The *Loose* working point, designed to maximize the muon reconstruction efficiency while providing acceptable-quality muon tracks. All muon types are used and all Medium quality muons are also classified as Loose muons. In this selection, CT and ST muons are also used and restricted to the region $|\eta| < 0.1$.

- The *Tight* working point, designed to maximize the muon purity at the cost of loosing in efficiency. Starting from Medium quality muons, Tight muons are

[11] This is defined as the absolute value of q/p divided by the sum in quadrature of all the uncertainties related to this quantity in the ID and MS.

required to be provided only by CB tracks and to pass different quality requirements on the fit χ^2, q/p significance and ρ' in order to remove pathological tracks.

- The *High*-p_T working point, specially designed to improve the momentum resolution for muon tracks above 100 GeV.

The resulting efficiency of Medium and Loose muons in a $Z \to \mu^+\mu^-$ event selection is provided in Figure 5.13b

5.6 MISSING TRANSVERSE MOMENTUM

The Missing Transverse Momentum (E_T^{miss}) is a key quantity for ATLAS as it allows to measure the amount of transverse momentum carried out by invisible particles produced in p-p collisions and escaping the detection. The measurement of this quantity relies on the perfect conservation of transverse momentum as:

$$\sum_{\substack{i\in \\ \{\text{Particles}\}}} \mathbf{p_T}^i = \sum_{\substack{i\in \\ \left\{\begin{smallmatrix}\text{Visible}\\ \text{Particles}\end{smallmatrix}\right\}}} \mathbf{p_T}^i + \sum_{\substack{j\in \\ \left\{\begin{smallmatrix}\text{Invisible}\\ \text{Particles}\end{smallmatrix}\right\}}} \mathbf{p_T}^j = 0. \tag{5.19}$$

In fact, defining $\mathbf{E_T}^{miss}$ as the total transverse momentum carried out by invisible particles it is possible to show using Equation (5.19) that

$$\mathbf{E_T}^{miss} = \sum_{\substack{i\in \\ \left\{\begin{smallmatrix}\text{Invisible}\\ \text{Particles}\end{smallmatrix}\right\}}} \mathbf{p_T}^i = -\sum_{\substack{i\in \\ \left\{\begin{smallmatrix}\text{Visible}\\ \text{Particles}\end{smallmatrix}\right\}}} \mathbf{p_T}^i. \tag{5.20}$$

Therefore, the magnitude E_T^{miss} of this vector can be used to "observe" invisible particles produced in p-p collisions, by looking at all the visible particles in the event. A complete review of the reconstruction and performance of this quantity in Run 2 is provided in Chapter 6.

5.7 CONCLUSION

This chapter illustrated how ATLAS performs the reconstruction of physics objects and how these can be calibrated and identified. The E_T^{miss} reconstruction is essential for supersymmetry searches and, due to its centrality in this work, further details about the reconstruction performance of this quantity in Run 2 are provided in the next chapter, composing the second part of this work.

Additionally, this chapter has shown how the calorimeter-only information is used to build jets in ATLAS and how tracking information is exploited only after jet building for the jet measurement corrections and suppression of pileup effects. A possible way to enhance even further the reconstruction of such quantities is to include the tracking information before the jet building stage and to enhance the resolution of low p_T constituents using the better resolution of the Inner Detector at low momenta. This is the core idea the Particle Flow algorithm, described also in the next part of this work (Chapter 7).

Part II

HADRONIC EVENT RECONSTRUCTION, PERFORMANCE AND PILEUP SUPPRESSION

6

PERFORMANCE OF MISSING TRANSVERSE MOMENTUM

"Hagrid: Yer a wizard Harry!"

– J.K. Rowling, *Harry Potter and the Sorcerer's Stone*

Contents

It has been quickly illustrated in Section 5.6 that the Missing Transverse Momentum represents the total transverse momentum carried out by invisible particles produced in the p-p collisions of the LHC. The choice of the transverse momentum is not accidental and it is due to the lower uncertainty on the particle momenta in the transverse plane. The longitudinal component of the momentum is largely affected by the loss of particles in the beam pipe and to the unknown momentum of partons along the beam axis due to the compositeness of the proton.

At the LHC, the presence of hadronic jets generally dominates the resolution of E_T^{miss}. Due to this reason, E_T^{miss} is considered as an *hadronic-based quantity* and it is also extremely sensitive to the pileup conditions of the collider. In this chapter, further details about the ATLAS E_T^{miss} reconstruction and performance in Run 2 is provided.

6.1 E_T^{miss} RECONSTRUCTION

It has been shown in Equation (5.20) that the Missing Transverse Momentum can be computed from the negative vector sum of the p_T of all the visible particles resulting from p-p collisions. Considering all the possible objects reconstructed by ATLAS, it is possible to define

$$\begin{aligned} \mathbf{E_T}^{miss} &= \mathbf{E_T}^{miss,hard} + \mathbf{E_T}^{miss,soft} = -\left(\mathbf{p_T}^{hard} + \mathbf{p_T}^{hard}\right) \\ &= \underbrace{\mathbf{E_T}^{miss,\mu} + \mathbf{E_T}^{miss,e} + \mathbf{E_T}^{miss,\gamma} + \mathbf{E_T}^{miss,\tau} + \mathbf{E_T}^{miss,j}}_{\text{hard term}} + \underbrace{\mathbf{E_T}^{miss,soft}}_{\text{soft term}} \end{aligned} \tag{6.1}$$

where μ, e, γ, τ, j correspond to muons, electrons, photons, taus and jets while $\mathbf{E_T}^{miss,soft}$ denotes the *soft term* of the event. This term represents the negative

p_T sum of all the particles which can not be well identified and calibrated in the detector and associated to the hard-scatter primary vertex. On the other hand, the total missing transverse momentum associated to the well identified and calibrated ATLAS objects (also know as the *hard objects*, including μ, e, γ, τ, j) is noted $\mathbf{E_T}^{\text{miss,hard}}$ and it is generally referred to as the *hard-term* of the E_T^{miss}. A detailed description about the reconstruction, calibration and quality selection of these objects have been provided in Chapter 5.

The $\mathbf{E_T}^{\text{miss}}$ vector can be described using its x and y components in the transverse plane (see Section 4.2.1 for more details) and also using the magnitude E_T^{miss} and azimuthal angle ϕ^{miss} of the E_T^{miss} vector

$$\mathbf{E_T}^{\text{miss}} = \left(E_{T,x}^{\text{miss}}, E_{T,y}^{\text{miss}}\right), \tag{6.2}$$

$$E_T^{\text{miss}} = |\mathbf{E_T}^{\text{miss}}| = \sqrt{\left(E_{T,x}^{\text{miss}}\right)^2 + \left(E_{T,y}^{\text{miss}}\right)^2}, \tag{6.3}$$

$$\phi^{\text{miss}} = \arctan\left(E_{T,y}^{\text{miss}} / E_{T,x}^{\text{miss}}\right). \tag{6.4}$$

Additionally to these quantities, the *total transverse energy* $\sum \mathbf{E_T}$ of the collision is computed for each event starting from the scalar sum of the transverse momentum of the objects entering in the E_T^{miss} calculation:

$$\sum \mathbf{E_T} = p_T^{\mu} + p_T^{e} + p_T^{\gamma} + p_T^{\tau} + p_T^{j} + p_T^{\text{soft}} \tag{6.5}$$

This quantity is used to quantify the hardness of the hard-scatter event in the transverse plane.

Due to dependency of E_T^{miss} from the good functioning of the overall ATLAS detector and the accuracy with which all other particles can be reconstructed, the reconstruction of this quantity is very challenging and depends on data-taking conditions. In this context of pileup, several techniques have been studied for the mitigation of pileup contamination, in particular the usage of JVT for the suppression of central pileup jets as described in Section 5.2.4, the definition of different E_T^{miss} working points (further details in Section 6.3) and the development of a soft term stable to pileup. Further details about the latter are provided in the next section.

An additional E_T^{miss} reconstruction method is represented by the *track* E_T^{miss} where the soft term is treated in the same way as TST while the jet p_T is estimated using tracking information only. Since this quantity is purely track-based, it is referred to as p_T^{miss} instead of E_T^{miss} and it has different advantages and disadvantages, at it will be discussed later in Section 6.4.

6.1.1 *The E_T^{miss} soft term*

The soft term is a challenging but essential ingredient for the E_T^{miss} reconstruction. Historically, the estimation of this term has been based on two different ways techniques:

- The *Calorimeter-based Soft Term* (CST) where the soft component is estimated using all the calorimeter topoclusters not associated to any hard object.

Quantity	Requirement
p_T	$p_T > 0.5\,GeV$
η	$\lvert\eta\rvert < 2.5$
d_0 significance	$\frac{d_0}{\sigma(d_0)} < 2.0$
z_0	$\lvert z_0 \sin\theta\rvert < 3\,mm$

Table 6.1 – Track selection requirements for track-based soft term [2]. d_0 and z_0 denote the transverse and longitudinal track impact parameters with respect to the hard-scatter vertex position.

- The *Track-based Soft Term* (TST) where the soft term is estimated using the tracks not associated to any hard object and associated to the hard-scatter primary vertex.

In the case of TST, the soft term is less dependent to pileup effects even though the pseudorapidity range is reduced to the tracker acceptance ($|\eta| < 2.5$) and the neutral particle component is not accounted. On the other hand, CST allows to exploit a larger η coverage ($|\eta| < 5.0$) and also to include the neutral particle information. Due to the large dependency of CST on pileup and the exceptional luminosity of the LHC during Run 2, the TST has shown better reconstruction resolution and robustness, making this term the default soft term reconstruction at ATLAS during Run 2. However, the extension of the pseudorapidity acceptance and the inclusion of the hard-scatter neutral information are two features that would make the TST estimation more precise, leading to better E_T^{miss} reconstruction performance.

For topocluster-based jets, the track-based soft term is reconstructed using the requirements listed in Table 6.1. Among these requisites, the cuts on the d_0 and z_0 parameters allow to obtain an optimal association to the hard-scatter vertex and consequently a good mitigation of soft pileup tracks. Additionally, by not including the neutral contributions, the track-based reconstruction entirely removes the out-of-time pileup contributions affecting CST. All the tracks associated to the hard-objects previously defined are discarded from the soft term calculation. In particular, the following classes of tracks are excluded from the soft term calculation [2]:

- Tracks with $\Delta\eta < 0.2$ and $\Delta\phi < 0.05$ with respect to electron and photon candidates.
- Tracks within a $\Delta R = 0.2$ cone around hadronically decaying τ-leptons.
- ID tracks associated with an identified muon.
- Tracks matched to jets using the ghost-association technique described in Section 5.2.3.
- Isolated tracks with $p_T > 120\,GeV$ (or $p_T > 200\,GeV$ for $|\eta| < 1.5$) having estimated relative resolution on their p_T larger than 40% or having no associated calorimeter energy deposit with p_T larger than 65% of the track p_T. This cut removes mis-measured tracks produced from association of random hits in the Inner Detector.

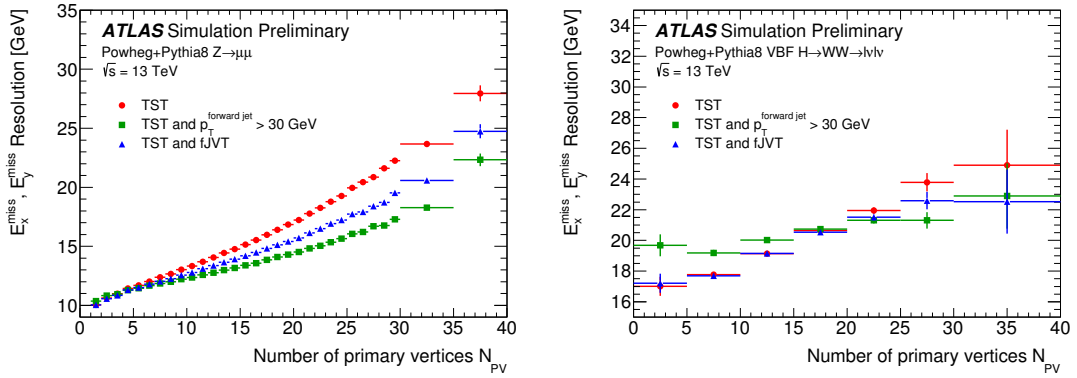

(a) E_T^{miss} resolution in $Z \to \mu^+\mu^-$ events (b) E_T^{miss} resolution in VBF Higgs events

Figure 6.1 – E_T^{miss} resolution for $Z \to \mu^+\mu^-$ and VBF Higgs production as a function of the number of primary vertices N_{PV} [2]. The red and green lines denote the Loose and Tight E_T^{miss} working points while the blue one shows the effects of the forward Jet Vertex Tagger (see Section 5.2.4 for more details).

6.2 OVERLAP REMOVAL TREATMENT

ATLAS carries out an independent reconstruction of different physics object (electrons, muons, jets, etc.) before combining these into the E_T^{miss} reconstruction. This means that the same calorimeter and tracker signals can result in different objects causing a double-counting in the E_T^{miss} calculation leading to a wrong estimation of this quantity. Therefore, the treatment of ambiguities between close-by physics objects represents a key aspect of E_T^{miss} reconstruction and is generally referred to as *overlap removal*.

Mutually exclusive detector signals are guaranteed using an object filling sequence starting to reconstruct the E_T^{miss} from muons (μ), electrons (e) followed by photons (γ), then hadronically decaying taus (τ_{had}) and finally jets (j).

6.3 E_T^{MISS} WORKING POINTS

The resolution of E_T^{miss} is largely affected by the pileup jets entering in the hard term reconstruction, specially in the forward region ($|\eta| > 2.4$) where the tracker information is missing. In order to mitigate these effects, different E_T^{miss} working points (WPs) have been defined, allowing physics analysis to choose their preferred jet selection. This feature is important since physics analyses might have different requirements on jet selection due to their targeted signal events. In Run 2, the set of ATLAS E_T^{miss} working points included:

- The *Loose* working point, including central jets ($|\eta| < 2.4$) with $p_T > 20\,GeV$ passing JVT requirement (see Section 5.2.4) and forward jets ($|\eta| > 2.4$) with $p_T > 20\,GeV$.

- The *Tight* working point, including central jets ($|\eta| < 2.4$) with $p_T > 20\,GeV$ passing JVT requirement and forward jets ($|\eta| > 2.4$) with $p_T > 30\,GeV$.

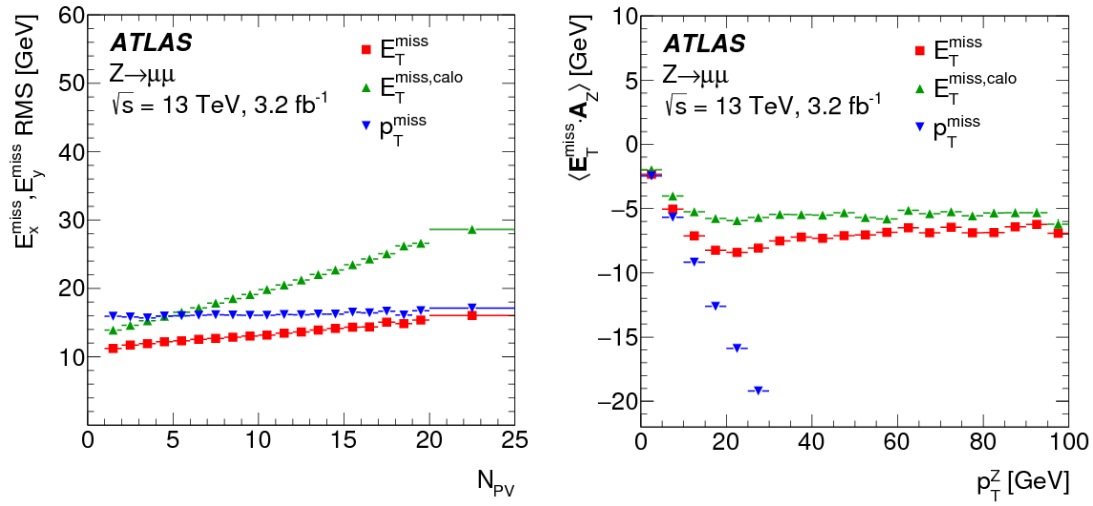

(a) $E_{T,x}^{miss}$,$E_{T,y}^{miss}$ resolution vs. N_{PV}

(b) E_T^{miss} scale vs p_T^Z

Figure 6.2 – E_T^{miss} resolution and scale for different E_T^{miss} reconstruction techniques [70]. The red and green curves reports respectively the TST and CST reconstruction, while the track E_T^{miss} is reported in blue.

Figure 6.1 reports the resolutions of these WPs as a function of the number of primary vertices N_{PV}. Here, we can see how the E_T^{miss} resolution in low jet signatures (*e.g.* $Z \to \mu^+\mu^-$ events) improves when we reject more pileup jets in the forward region. Furthermore, the *forward Jet Vertex Tagger* [64] allows to remove pileup jets in the forward region ($|\eta| > 2.5$), improving the E_T^{miss} resolution while keeping the resolution of VBF Higgs signatures[12] high.

6.4 E_T^{miss} PERFORMANCE

The performance of E_T^{miss} can be studied using different quantities and event topologies. Due to their abundance, extensive knowledge and selection purity, $Z \to \mu^+\mu^-$ and $Z \to e^+e^-$ final states are widely employed for the study of fake E_T^{miss} effects.

The first quantity generally used to describe the performance of missing transverse momentum is the x, y E_T^{miss} *resolution*, defined as the Root Mean Square (RMS) value of the residuals $\Delta E_T^{miss,x,y}$ where

$$\Delta E_T^{miss,x,y} = E_T^{miss,x,y} - E_T^{miss,x,y,truth}. \tag{6.6}$$

An example of E_T^{miss} resolution plot as a function of the number of primary vertices N_{PV} is shown in Figure 6.2a for different E_T^{miss} reconstruction techniques. The red and green curves report respectively the TST and CST reconstruction, while the track E_T^{miss} is reported in blue. It is possible to note the importance of the soft term for keeping the E_T^{miss} resolution low. In particular, we can note the large pileup dependency of the CST reconstruction compared to the TST and p_T^{miss} ones. However,

[12] These signatures generally have a lot of forward jets due to their kinematics.

even if p_T^{miss} has almost no pileup dependency across N_{PV}, the lack of neutral information in the track jets made the TST E_T^{miss} reconstruction the most performant and used E_T^{miss} quantity in ATLAS analyses during the second run of the LHC.

For $Z \to l^+l^-$ signatures, the E_T^{miss} *scale* can be defined as the average value of the projection of $\mathbf{E_T}^{miss}$ along the Z-boson-axis $\mathbf{A_Z}$ defined as

$$\mathbf{A_Z} = \frac{\mathbf{p_T^Z}}{p_T^Z}, \tag{6.7}$$

where $\mathbf{p_T^Z}$ is the transverse momentum of the Z boson. This quantity $\langle \mathbf{E_T}^{miss} \cdot \mathbf{A_Z} \rangle$ allows to characterize the E_T^{miss} direction and its dependence on different E_T^{miss} objects well. Ideally, this quantity should be zero for a perfect E_T^{miss} reconstruction. Figure 6.2b reports an example of the scale plot for different E_T^{miss} reconstruction techniques as a function of the Z-boson transverse momentum p_T^Z. From this plot, we can note how the E_T^{miss} scale is always negative with respect to the Z boson direction, indicating that the quantity recoiling against the Z boson is generally underestimated. However, different regimes can be identified for different ranges of p_T^Z in the plot. For $p_T^Z < 20\,GeV$ the quantity recoiling against $\mathbf{A_Z}$ is represented by the soft term considering that the jet p_T threshold is generally fixed at $20\,GeV$. Looking at the various curves, we see that all of them generally have an underestimated soft term, even though the inclusion of neutral particles make the CST reconstruction slightly better than p_T^{miss} and TST. However, for $p_T^Z > 20\,GeV$ where the jet component starts to dominate the E_T^{miss} reconstruction, showing very different behaviors between each E_T^{miss} reconstruction technique. In particular, we can note how p_T^{miss} is biased along the Z-boson direction due to the total lack of neutral particles in track jets reconstruction. For TST and CST reconstruction we can see that at very high values of p_T^Z the two scale plots are merging due to the dominant jet term.

Another useful quantity for studying the E_T^{miss} performance is represented by the E_T^{miss} *linearity* defined as

$$\Delta_T^{lin} = \left\langle \frac{E_T^{miss} - E_T^{miss,true}}{E_T^{miss,true}} \right\rangle \tag{6.8}$$

This value describes a good E_T^{miss} performance when its value is null. An example of this plot as a function of the true E_T^{miss} is shown in Figure 6.3. For $W^\pm \to e^\pm\nu$ and $W^\pm \to \mu^\pm\nu$ signatures, when $E_T^{miss,true}$ is larger than $70\,GeV$, the reconstructed E_T^{miss} estimation is 2% close to the truth one due to the reconstruction of the hadronic recoil. On the other hand, for $E_T^{miss,true}$ lower than $40\,GeV$, the E_T^{miss} is consistently overestimated with respect to $E_T^{miss,true}$ (*i.e.* $\Delta_T^{lin} > 0$). This feature is mainly due to the track-based soft term not accounting for the soft neutral component and the contamination of pileup jets. The independence of such observations from the lepton flavour is confirmed by the similarity of the $W^\pm \to e^\pm\nu$ and $W^\pm \to \mu^\pm\nu$ curves. For $t\bar{t}$ simulated events, the resolution effects tend to dominate for $E_T^{miss,true} < 120\,GeV$. These effects are larger than $W^\pm \to l^\pm\nu$ due to the presence of at least four jets with low p_T and the high sensitivity to pileup-induced fluctuations in $t\bar{t}$ signatures.

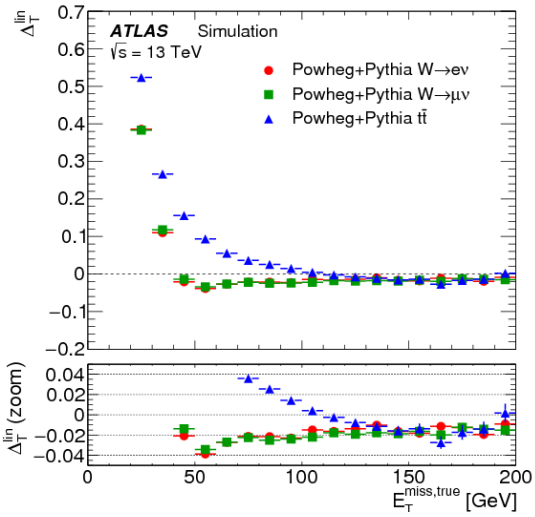

Figure 6.3 – E_T^{miss} linearity as a function of truth E_T^{miss} for different simulations ($W^{\pm} \to e^{\pm}\nu$, $W^{\pm} \to \mu^{\pm}\nu$ and $t\bar{t}$) [70].

6.5 THE TRACK-BASED SOFT TERM SYSTEMATICS

Due to its compositeness with respect to other ATLAS objects, the E_T^{miss} does not have a dedicated uncertainty and various object uncertainties are generally propagated during the E_T^{miss} calculation. However, the soft term represents a component uniquely estimated for the E_T^{miss} calculation and it needs a dedicated uncertainty. In this section, we want to provide a description of the parametrization and estimation of the Track-based Soft Term systematics.

The uncertainty on the soft term is characterized by how well this term is modeled in MC simulation. In an event topology with zero true E_T^{miss}, the soft term momentum $\mathbf{p_T}^{soft}$ is expected to be perfectly balanced against $\mathbf{p_T}^{hard}$. Detector resolution effects spoil the equality between p_T^{hard} and p_T^{soft}. Different projections of p_T^{soft} along p_T^{hard} in data and MC can be used to study the modeling of the soft term. Three projected quantities illustrated in Figure 6.4 are studied:

- **The parallel scale (Δ_L)**, representing the mean value of the parallel projection of p_T^{soft} along p_T^{hard}. The component from the projection is labelled $p_T^{soft,\parallel}$.
- **The parallel resolution ($\sigma_{\parallel}$)**, defined as the root-mean-square (RMS) of $p_T^{soft,\parallel}$.
- **The transverse resolution ($\sigma_{\perp}$)**, defined as the root-mean-square (RMS) of the perpendicular component of p_T^{soft} with respect to p_T^{hard}. The component from the projection is labelled $p_T^{soft,\perp}$.

The transverse scale is not of physical interest as it is consistent with zero in data and simulation.

The systematic uncertainty is computed from the maximal disagreement between the data and different Monte Carlo generators plus parton shower models for a certain set of p_T^{hard} bins. To account for any differences between event topologies with large numbers of jets and those without any jets, the total systematic is additionally split

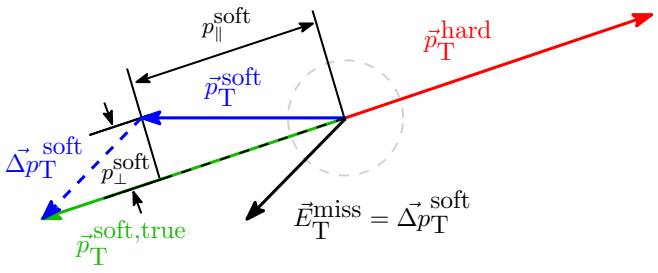

Figure 6.4 – Sketch of the track-based soft term projections with respect to $p_{\text{T}}^{\text{hard}}$ for the calculation of the TST systematic uncertainties.

$p_{\text{T}}^{\text{hard}}$ bin [GeV]	$\sigma_{\parallel}$[GeV]	$\sigma_{\perp}$[GeV]	Δ_{L}[GeV]
0-10	1.87	2.00	0.25
10-15	1.77	1.97	0.50
15-20	1.73	1.98	0.63
20-25	1.91	2.09	0.71
25-30	2.20	2.24	0.75
30-35	2.21	2.29	0.85
35-40	2.36	2.36	0.96
40-50	2.69	2.38	1.07
50-200	3.71	3.04	1.96

Table 6.2 – TST systematic envelope derived using the 2015-2016 ATLAS dataset, computed as the maximal differences between data and Monte Carlo samples for the parallel scale Δ_{L}, parallel and transverse resolutions $\sigma_{\parallel}, \sigma_{\perp}$.

into jet-inclusive and jet-veto selections and merged later as the maximal variation of these two cases. Figure 6.5 shows the three projected quantities for the jet-inclusive and jet-veto cases. The resulting systematic envelope (see Table 6.2) is shown centered on data, and by construction, all the considered simulated samples are covered by this systematic envelope. The resolutions in simulation are typically smaller than that observed in data as seen in Figure 6.5. The uncertainty increases with $p_{\text{T}}^{\text{hard}}$ due to the increasing amount of missing neutral information in the soft term estimation, and the final uncertainty values typically range from 2 GeV to 5 GeV.

To apply the systematic uncertainties from Table 6.2, the projection of the soft term is smeared by a Gaussian of the width corresponding to its $p_{\text{T}}^{\text{hard}}$ value for the resolution uncertainties. The scale variation adds the value corresponding to its $p_{\text{T}}^{\text{hard}}$ to the $p_{\text{T}}^{\text{soft},\parallel}$ and it is subtracted for the opposite variation.

6.6 OBJECT-BASED $E_{\text{T}}^{\text{MISS}}$ SIGNIFICANCE

The degree to which the reconstructed $E_{\text{T}}^{\text{miss}}$ is compatible with momentum resolution and particle identification efficiencies can be identified by evaluating the E_{T}^{miss} *significance* $\mathcal{S}(E_{\text{T}}^{\text{miss}})$.

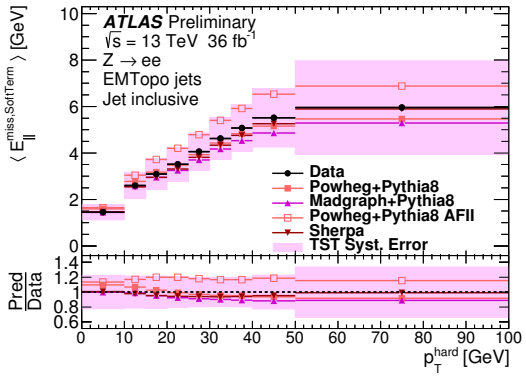

(a) Parallel scale, jet inclusive selection

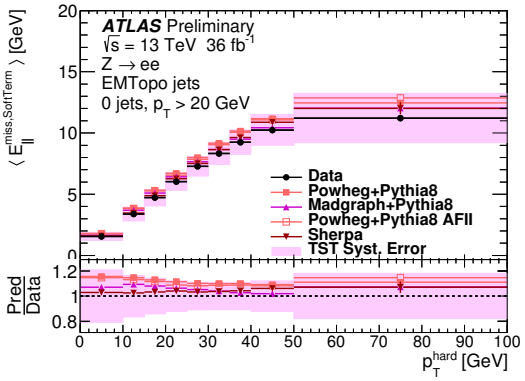

(b) Parallel scale, zero jet selection

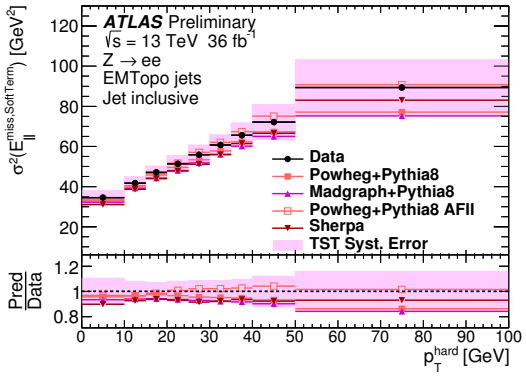

(c) Parallel resolution squared, jet inclusive selection

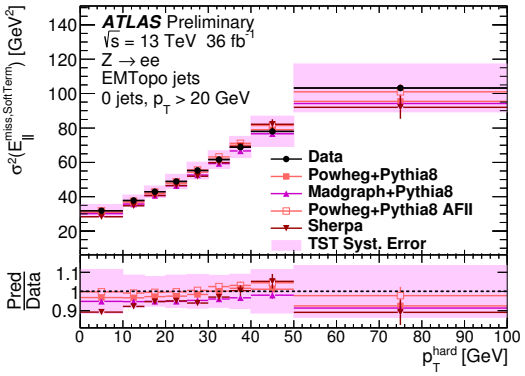

(d) Parallel resolution squared, zero jet selection

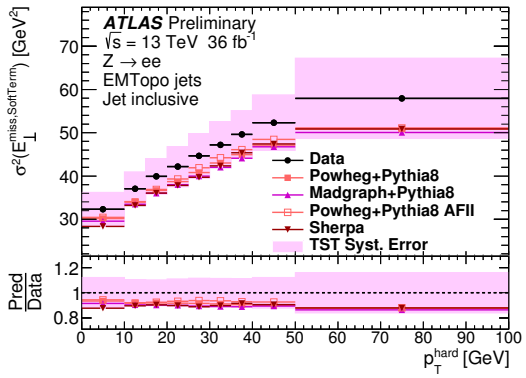

(e) Transverse resolution squared, jet inclusive selection

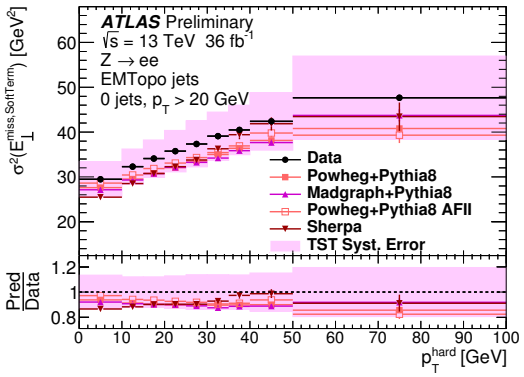

(f) Transverse resolution squared, zero jet selection

Figure 6.5 – Parallel scale, parallel and transverse resolution plots for the Track-based Soft Term (TST) in the 2015-2016 ATLAS dataset. The pink band represents the resulting TST systematic uncertainty applied to the $Z \to e^+e^-$ Monte Carlo simulation. This band is shown centered on data and it proves the coverage of the discrepancies with respect to simulations.

The E_T^{miss} significance is defined to test the hypothesis that the total transverse momentum carried by invisible particles (named $\mathbf{p_T}^{inv}$) is zero (null hypothesis) against the hypothesis that $\mathbf{p_T}^{inv}$ is different than zero (alternative hypothesis) [71]

$$\mathcal{S}(E_T^{miss})^2 = 2\ln\left(\frac{\max_{\mathbf{p_T}^{inv}\neq 0}\mathcal{L}\left(\mathbf{E_T}^{miss}|\mathbf{p_T}^{inv}\right)}{\max_{\mathbf{p_T}^{inv}=0}\mathcal{L}\left(\mathbf{E_T}^{miss}|\mathbf{p_T}^{inv}\right)}\right). \tag{6.9}$$

An event-by-event likelihood can be calculated assuming that

- The measurement of each particle i is independent of one another.
- For each object, the probability distribution of measuring $\mathbf{p_T}^{i}$ given true transverse momentum value $\mathbf{p_T}^{i,true}$ is represented by a Gaussian probability distribution with covariance matrix V_i.
- Due to the transverse momentum conservation: $-\mathbf{p_T}^{inv} = \sum_i \mathbf{p_T}^{i,true}$.

Under these assumptions, the likelihood function has the form of a two dimensional Gaussian:

$$\mathcal{L}\left(\mathbf{E_T}^{miss}|\mathbf{p_T}^{inv}\right) \propto \exp\left(-\frac{1}{2}\left(\mathbf{E_T}^{miss}-\mathbf{p_T}^{inv}\right)^T\left(\sum_i V_i\right)^{-1}\left(\mathbf{E_T}^{miss}-\mathbf{p_T}^{inv}\right)\right), \tag{6.10}$$

and the E_T^{miss} significance becomes a simple χ^2 distribution

$$\mathcal{S}(E_T^{miss})^2 = 2\ln\left(\frac{\mathcal{L}\left(\mathbf{E_T}^{miss}|\mathbf{E_T}^{miss}\right)}{\mathcal{L}\left(\mathbf{E_T}^{miss}|0\right)}\right) = \left(\mathbf{E_T}^{miss}\right)^T\left(\sum_i V_i\right)^{-1}\left(\mathbf{E_T}^{miss}\right). \tag{6.11}$$

It is possible to show [71] that, in the coordinate system composed of the parallel (*i.e.* longitudinal L) and perpendicular (*i.e.* transverse T) axes to the direction of $\mathbf{E_T}^{miss}$, the total $\mathcal{S}(E_T^{miss})$ can be written as

$$\mathcal{S}(E_T^{miss})^2 = \frac{|E_T^{miss}|^2}{\sigma_L^2\left(1-\rho_{LT}^2\right)}, \tag{6.12}$$

where σ_L is the total E_T^{miss} variance in the longitudinal directions to the $\mathbf{E_T}^{miss}$ respectively and ρ_{LT} is the correlation factor between these two directional measurements. This expression is not surprising considering as it corresponds to the definition of statistical significance, where the numerator corresponds to the observation and the denominator to the error on that observation. Assuming events where only jets are present and a dominance of the stochastic term of the jet resolution, σ_L can be estimated as

$$\sigma_L = \sqrt{\sum_{\text{jet } i}\sigma_i^2} \propto \sqrt{\sum_{\text{jet } i}\left(\sqrt{p_T^i}\right)^2} = \sqrt{\sum_{\text{jet } i} p_T^i} = \sqrt{H_T}, \tag{6.13}$$

leading to the standard event-based E_T^{miss} significance approximation

$$\mathcal{S}(E_T^{miss}) \approx \frac{E_T^{miss}}{\sqrt{H_T}}, \tag{6.14}$$

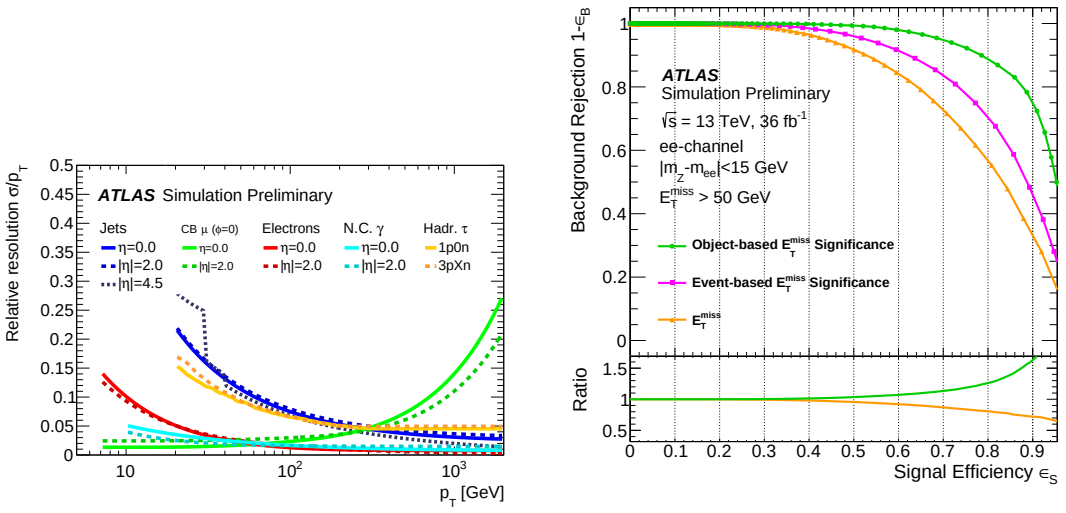

(a) (b)

Figure 6.6 – (a) Relative resolution of different ATLAS physics objects entering in the E_T^{miss} significance calculation. (b) ROC curve showing better acceptance of events carrying invisible particles at equal background rejection rates from the object-based E_T^{miss} significance with respect to different approaches [71].

used by different ATLAS analyses.

In the object-based E_T^{miss} significance approach, the longitudinal E_T^{miss} variance σ_L is determined from the resolutions of each physics object entering in the E_T^{miss} calculation. Figure 6.6a shows the magnitude of these object resolutions entering in the $\mathcal{S}(E_T^{miss})$ calculation. Additionally, due to their large contributions to the total E_T^{miss} resolution, this approach specially treats pileup jets that are not removed by the Jet Vertex Tagger requirement, by adding to the total $\mathcal{S}(E_T^{miss})$ denominator the p_T of these jets multiplied by the probability of the jet to have originated from pileup, which is estimated from MC simulations.

Figure 6.6b shows that this object-based definition allows to better separate events carrying real and fake E_T^{miss}, enhancing the sensitivity of physics analyses targeting invisible particles to new physics.

6.7 CONCLUSION

This chapter illustrated the reconstruction and performance of E_T^{miss}, as well as the systematic uncertainties associated to this quantity. This object represents a fundamental observable for the searches carried out by the ATLAS experiment (in particular supersymmetry), and its optimal performance in Run 2 has played an essential role in providing these analyses with excellent sensitivities to new physics in Run 2. However, further improvements can be achieved, specially considering that E_T^{miss} is very dependent by jets and pileup jet identification. In this context, improvements to jet reconstruction made significant enhancement to the performance of this quantity in Run 2. The next chapter is dedicated to the description of Particle Flow jet and E_T^{miss} reconstruction, where the improved low-p_T jet resolution and

better pileup jet identification led to significant improvements of this quantity and consequently of the ATLAS sensitivity to new physics.

7

PARTICLE FLOW RECONSTRUCTION

"I am a wizard, not a baboon brandishing a stick."
– J.K. Rowling, *Harry Potter and the Half-Blood Prince*

Contents

The best possible identification and reconstruction of final states particles represents an important pursuit of collider experiments. Composite objects (*e.g.* jets) relying on lower level particles can be intrinsically improved when better calibration and identification of lower level particles is provided, resulting in higher sensitivities of ATLAS analyses to new physics.

The goal of *Particle Flow* (or *PFlow*) algorithms is to identify the individual particles in the detector and combine the measurement of the different ATLAS sub-detectors in an optimal way. This can be achieved with a particle detector allowing to efficiently separate between charged and neutral particles, a feature provided by a large magnetic field and good calorimeter granularity. One typical Particle Flow approach is the combination of the tracker and calorimeter subsystems. When these sub-detectors are combined, the combination procedure relies on the fact that charged particles can be measured much better by the tracker when the particle p_T is low due to the large bending offered by the ID solenoid, while the calorimeter provides a better measurement at high p_T where the particle tracks are closer to straight lines. Additionally, this algorithm could provide identification of neutral particles nearby charged objects after association between charged tracks and calorimeter objects. These algorithms were first pioneered in the ALEPH experiment at LEP [72] and later by CMS [73] and were shown to improve the resolution of the reconstructed jets.

7.1 THE ATLAS PARTICLE FLOW ALGORITHM

In Run 1 the ATLAS detector used pure calorimeter-based jets for the reconstruction of p-p collisions. Once the jets were built, the tracker information was used for

the identification of pileup objects and for the calibration of the hard-scatter process. The *Particle Flow* algorithm introduces an alternative approach, where the tracker and calorimeter information are combined prior to jet and E_T^{miss} reconstruction. The final objects provided by this algorithm represents ideal particles in the detector, generally known as *Particle Flow objects* (or *PFOs*). The energy deposited by the track of charged particles is "removed" from the calorimeter in order to better identify neutral signals. Jet reconstruction is then performed on the "particle flow objects" coming from the hard-scatter vertex, providing charged pileup subtraction prior to jet building. Such approach started to be studied and discussed within ATLAS during the first long shutdown of the LHC (2012-2015). Further work, bringing to the final commissioning of the algorithm, has been performed during the second Run of the LHC and this techniques is now ready to be employed for the LHC Run 3.

Additionally to the neutral particle identification, Particle Flow aims at improving the resolution of each particle combining in an optimal way the information from the sub-detectors. As discussed in Section 4.2.3, the resolution of the ATLAS calorimeter can be quantified as

$$\frac{\sigma(E)}{E} = \frac{50\%}{\sqrt{E}} \oplus 3.4\% \oplus \frac{1\%}{E}. \tag{7.1}$$

Furthermore, the inverse transverse momentum resolution for the ATLAS tracker is [51]

$$\sigma\left(\frac{1}{p_T}\right) p_T = 0.036\% \cdot p_T \oplus 1.3\%. \tag{7.2}$$

In both formulas, energies and transverse momenta are measured in GeV. Therefore, for low momenta the tracker provides better resolution while the calorimeter makes better at high p_T. This feature can be understood with the following qualitative argument: at high p_T, particle tracks have a very small bending angle, making its momentum estimation difficult and the calorimeter energy measurement effectively better due to the low stochastic component resulting from the high number of particles in the calorimeter shower. However, at low p_T, the large stochastic uncertainty and large noise in the calorimeter makes the tracker transverse momentum estimation more suited for a precise p_T estimation. Therefore, it is natural to use the tracker information for low p_T tracks while the calorimeter in the high p_T regime. This is exactly what the Particle Flow algorithm exploits.

Another useful feature of the tracker-calorimeter association for jet building is represented by the difficulty to estimate correctly the azimuthal angle ϕ of charged low p_T particles due to the large bending power of the ATLAS 2 T solenoidal field[13]. In fact, these particles can sweep out of the jet cone before reaching the calorimeter, leading to an imperfect reconstruction of low p_T jets. By using the ϕ of the tracks at interaction point, these particles can be included in the jet clustering, leading to a better jet estimation of the jet ϕ direction.

The steps of the ATLAS Particle Flow algorithm are described on Figure 7.1.

[13] This feature is even more important for CMS, where the Inner Detector magnetic field reaches values of 4 T.

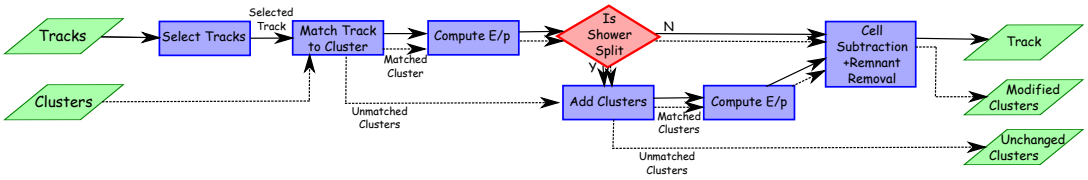

Figure 7.1 – Schematic of the ATLAS Particle Flow algorithm [51].

7.1.1 *Track selection*

The inputs of the Particle Flow algorithm are tracks and topoclusters reconstructed using pure tracker and calorimeter information. In order to perform the matching between tracks and topoclusters (see next section), a selection of good quality tracks is performed for the so called *tight tracks*. These tracks require at least nine hits in the silicon detectors, no missing hit in the Pixel detector and to pass $|\eta| < 2.5$ and $p_T > 500\,MeV$. At this stage, no selection on vertex association is made in order to subtract pileup clusters in the calorimeter in an optimal way later.

Considering that at very high p_T the momentum resolution of the tracks is lower than the calorimeter measurements, tracks having $p_T > 40\,GeV$ were excluded in the first version of the algorithm studied using Run 1 samples. This requirement evolved later in Run 2. Tracks matched to medium quality electrons and muons are excluded from the calorimeter subtraction as the algorithm is optimized for hadronic shower subtraction.

7.1.2 *Track-to-topocluster matching*

The first step of the tracker-calorimeter combination procedure consists of matching between tracks and topocluster in order to identify calorimeter energy deposits caused by charged particles and perform the energy subtraction. The matching is performed using the modified ΔR metric

$$\Delta R' = \sqrt{\left(\frac{\Delta\phi}{\sigma_\phi}\right)^2 + \left(\frac{\Delta\eta}{\sigma_\eta}\right)^2} \tag{7.3}$$

where σ_η, σ_ϕ correspond to the angular topocluster widths, computed as the standard deviation of the displacements of the topocluster's cells in η, ϕ with respect to its barycentre. This modified metric has been preferred as it allows to account the spatial extent of the topoclusters which may contain energy deposits from multiple particles.

A preliminary selection of topoclusters to be matched to tracks is performed in order to reduce the amount of wrongly matched topoclusters. This is done requiring $E^{clus}/p^{trk} > 0.1$, where E^{clus} is the energy of the topocluster and p^{trk} the momentum of the reconstructed track. This preselection allows to reject 10% of incorrect topoclusters for $1\,GeV < p_T < 2\,GeV$ and $30-40\%$ for $p_T > 5\,GeV$ while keeping the rejection of correct topoclusters below 1% [51].

After this preliminary selection of topoclusters, the $\Delta R'$ metric defined in Equation (7.3) is used to match tracks and topoclusters by associating the closest track and topocluster. If no preselected topocluster is found within $\Delta R' < 1.64$, it is assumed

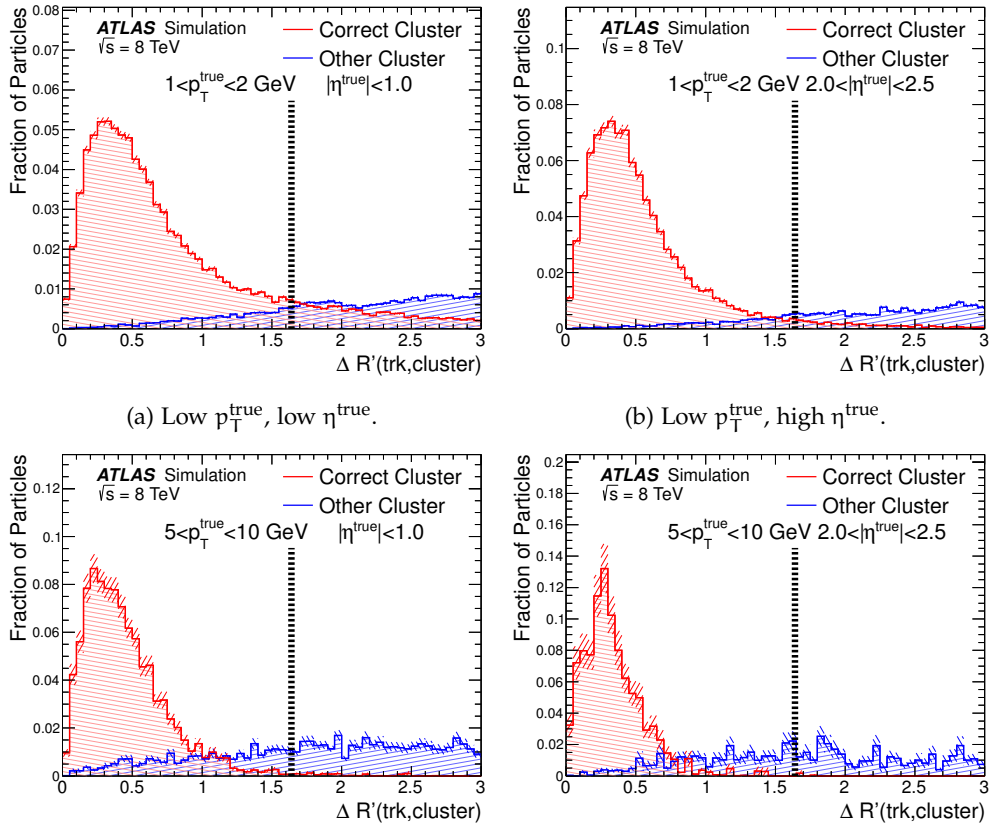

(a) Low p_T^{true}, low η^{true}.

(b) Low p_T^{true}, high η^{true}.

(c) High p_T^{true}, low η^{true}.

(d) High p_T^{true}, high η^{true}.

Figure 7.2 – $\Delta R'$ distribution of topoclusters correctly and incorrectly associated to a track [51].

that the particle has not formed a sufficiently high energy deposit and the track is retained without performing the subsequent energy subtraction. Figure 7.2 shows the $\Delta R'$ distributions of the correctly and incorrectly matched topoclusters to a track. On these figures, the dashed black line illustrates the $\Delta R' < 1.64$ cut used for the association of the tracks and topocluster objects.

7.1.3 *Energy subtraction*

The subtraction of the energy deposited by particle tracks in the calorimeter represents a key aspect for the identification of neutral particles being merged with a charged object. However, in order to subtract the right amount of charged particle energy, an estimation of the average energy deposited by each track in the calorimeter needs to be estimated. This step is performed by evaluating the average value of $E^{clus}_{ref}/p^{trk}_{ref}$ from a single pion reference sample simulated without pileup. A lookup table is then built for $\langle E^{clus}_{ref}/p^{trk}_{ref}\rangle$ as a function of p_T, η and the *layer of highest energy density* [14] (LHED). Only pions have been used since these compose most of the charged particles in a jet and this lookup table would provide the energy deposited in the calorimeter by these tracks. Once this lookup table is available, the energy deposited by a track having a momentum p^{trk} will be simply estimated as

$$E^{clus} = \langle E^{clus}_{ref}/p^{trk}_{ref}\rangle \cdot p^{trk}. \tag{7.4}$$

At this stage, we need to subtract the energy in our calorimeter in order to identify possible neutral objects merged with charged particles in our calorimeter. We distinguish now two cases:

1. The expected energy from the track E^{clus} is larger than the energy of the topocluster E. In this case, the entire topocluster is simply removed.
2. If $E^{clus} < E$ then the cell subtraction is performed. This is done starting with the extrapolation of the track position inside the LHED and forming equally-spaced rings in each calorimeter layer as a function of η and ϕ. These rings are wide enough to contain at least one cell inside the respective layer. Afterwards, the subtraction begins from the layer with the higher energy density (*i.e.* the LHED) according to a parametrization of the shower shape mapping the most likely energy density profile in each layer. The subtraction is performed from the innermost ring going outwards, ranking the rings according to their energy density extrapolated from the single pion MC samples.

A schematic of the energy subtraction in each layer is provided in Figure 7.3 showing the identification of the neutral object after the complete subtraction of the charged object energy.

[14] The layer of highest energy density (LHED) is the layer of the calorimeter having the largest increase in energy density as a function of the number of interaction lengths from the front face of the calorimeter for a given topocluster. The energy density of the j-th cell in the j-th layer is calculated as

$$\rho_{ij} = \frac{E_{ij}}{V_{ij}}, \quad \left[GeV/X_0^3\right]$$

where E_{ij} is the energy of the cell in GeV and V_{ij} the volume of the cell expressed in radiation lengths X_0.

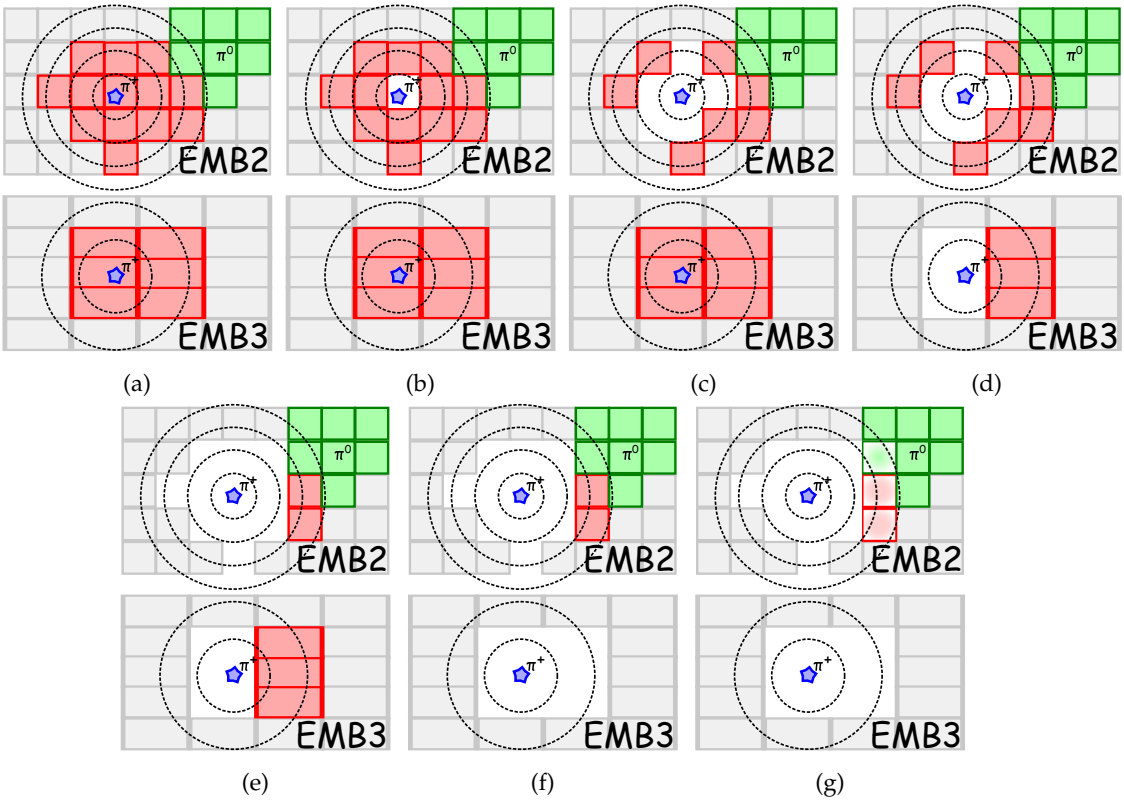

Figure 7.3 – Particle Flow step-by-step energy subtraction in two different EMB layers [51].

7.1.4 *Remnant removal*

Once the energy subtraction has been performed, we can use the spread of the estimated energy deposition $\sigma\left(E^{clus}\right)$ estimated from the standard deviation of $E^{clus}_{ref}/p^{trk}_{ref}$ in single pion samples in order to evaluate if the total track energy has been removed by the energy subtraction. In the ATLAS Particle Flow algorithm, we assume that if the energy left in the topocluster after energy subtraction is consistent with the width of the reference energy distribution (*i.e.* it is less than $1.5\sigma\left(E^{clus}\right)$) then it is assumed that the topocluster was completely originated from a single object and so the remaining energy is removed. This $1.5\sigma\left(E^{clus}\right)$ criterion was chosen as it optimally separated cases where the matched topocluster has true deposited energy only from a single particle and those where there are multiple contributing particles [51]. If this requirement is not satisfied, the remnant is retained considering that the cluster could have been originated by the overlapping of different particles.

7.2 PARTICLE FLOW JET AND E_T^{miss} PERFORMANCE

It has been described in the previous section how the Particle Flow algorithm is improving the jet reconstruction performance. In this section, the jet performance is shown. Additionally, the propagation of these effects to the E_T^{miss} reconstruction performance is presented.

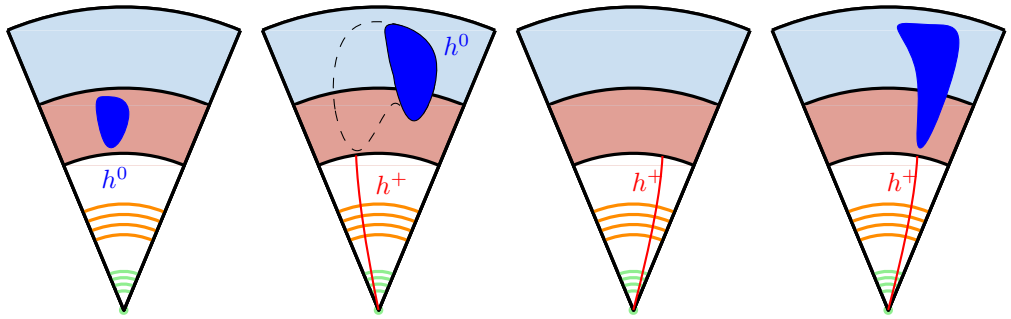

(a) Neutral PFO, isolated topocluster. (b) Neutral PFO, subtraction remnant. (c) Charged PFO, isolated track. (d) Charged PFO, track and topocluster.

Figure 7.4 – Charged and neutral Particle Flow objects (PFOs).

7.2.1 *Particle Flow jets*

Once topoclusters and tracks have been associated, their combined information is passed as input to a jet building algorithm. This is done by combining the tracks and topoclusters inputs into two sets of *Particle Flow objects* (PFOs):

- The *Neutral Particle Flow objects* composed of topoclusters not associated to any track or calorimeter signals surviving the subtraction procedure (see Figure 7.4a and 7.4b).
- The *Charged Particle Flow objects* composed of isolated tracks or tracks and topoclusters matched by the PFlow algorithm (see Figure 7.4c and 7.4d).

The inputs to the jet finding algorithm are then represented by:

- The full set of neutral PFOs, represented by topoclusters unmatched to any ID track and calorimeter energy deposits resulting from the charged energy subtraction procedure.
- The charged PFOs matched to hard-scatter vertex. This step is possible due to the available tracker information, allowing to discard calorimeter energy deposits associated to pileup interactions before building jets.

The Particle Flow jets are finally formed by running the anti-k_t algorithm on these input constituents.

The Particle Flow jets are improved in several ways with respect to topocluster jets. Considering that the algorithm uses the tracking information at low p_T, improvements are expected in terms of energy and angular resolution for low p_T jets. Additionally, since charged pileup constituents are already removed before building jets, we also expect pileup PFlow jets to be partially suppressed prior to jet creation. The effects of the better tracker resolution are illustrated in Figure 7.5, where the jet resolutions of the jet η, ϕ and p_T are shown as a function of p_T. In these figures we can note that the improvements in the jet p_T mostly appear for $p_T < 100\,GeV$ if compared to the locally-calibrated (LC) jets. The angular resolution of the jet is also improved in η, ϕ, and this happens because of three reasons:

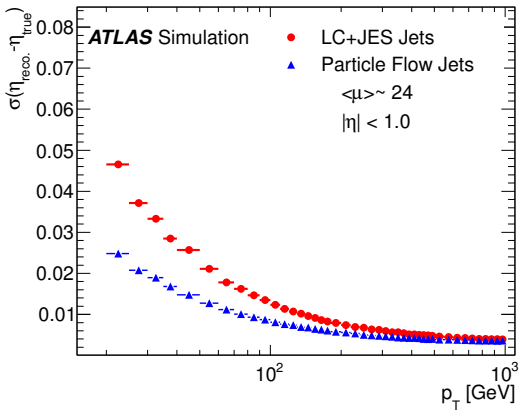

(a) η resolution vs p_T

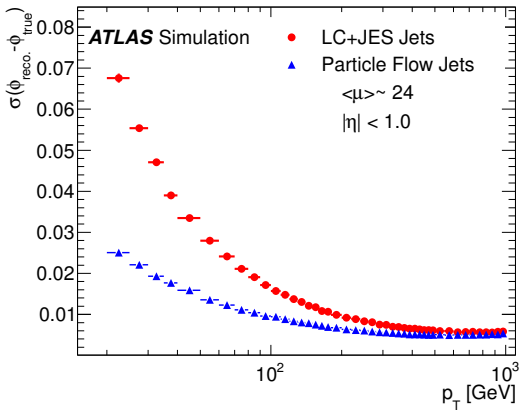

(b) φ resolution vs p_T

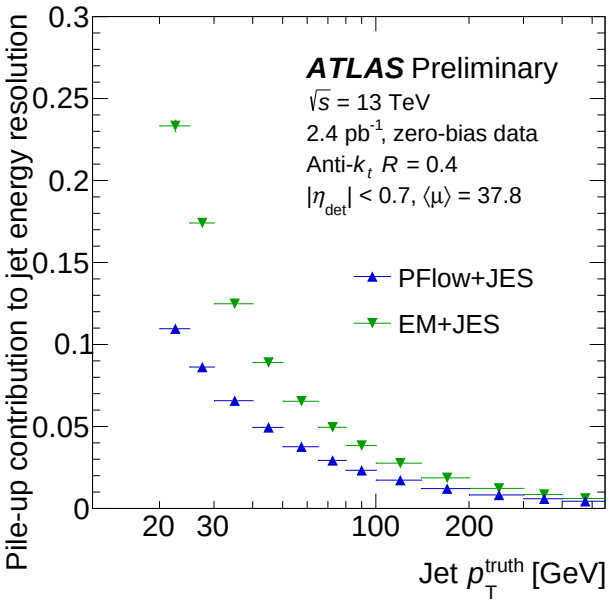

(c) Energy resolution vs p_T

Figure 7.5 – Resolutions of Particle Flow jets compared to topocluster-based jets [51, 74]. (a) and (b) report the η and φ resolutions extracted from a Run 1 simulated di-jet sample with $\langle\mu\rangle = 24$. (c) shows the energy resolution as a function of the simulated truth jet p_T using a fraction of the 2017 (Run 2) collected dataset with $\langle\mu\rangle = 37.8$.

1. The tracker angular resolution is far superior to the one estimated with the large shower objects in the calorimeter.

2. The track angular position can be measured at the perigee, allowing to reduce the spread due to the magnetic field surrounding the Inner Detector.

3. Charged pileup topoclusters are removed before jet building leading to a better estimation of the jet direction.

It is also possible to note how the ϕ resolution matches the η one for Particle Flow jets while this is not true for LC jets. This is due to the correction of the magnetic field effects in ϕ provided using the tracking information in the Particle Flow approach.

At high p_T, the transverse momentum resolution of Particle Flow jets gets slightly worse than the LC-calibrated jets. This happens because of two reasons:

- The dense core of high-energy jets comes with challenges for tracking algorithms, causing the tracking efficiency and accuracy to degrade at high p_T.

- The proximity of the different showers within the high-momentum jets increases the probability of mismatching between tracks and topoclusters, resulting in an incorrect energy subtraction leading to a wrong final jet energy estimation. This effect is also known as the *confusion* of the Particle Flow algorithm.

This affected the Particle Flow algorithm evaluated using Run 1 data, and it was partly removed by applying the energy subtraction from tracks satisfying $p_T < 40\,GeV$. In Run 2, a smooth disabling of the algorithm for individual tracks in dense environments better restores the performance of Particle Flow jets at high p_T. For all tracks up to 100 GeV of p_T, the energy subtraction is not performed if [76]

$$\frac{E^{clus} - \left\langle E_{exp}^{clus} \right\rangle}{\sigma\left(E_{exp}^{clus}\right)} > 33.2 \cdot \log_{10}\left(40\,GeV/p_T^{trk}\right), \tag{7.5}$$

where E^{clus} is the calorimeter energy in a cone $\Delta R < 0.15$ around the extrapolated track, $\left\langle E_{exp}^{clus} \right\rangle$ and $\sigma\left(E_{exp}^{clus}\right)$ are the average expected energy deposited by a pion and its variation. This cut practically truncates tracks above 40 GeV but it also excludes lower p_T tracks from the energy subtraction if these are found to be in very dense environments [76].

Figure 7.6 shows the amount of pileup and hard-scatter jets which are selected by the Particle Flow and topoclustering jet building approach. In particular, we can note in Figure 7.6b how better the Particle Flow pileup jet rejection is compared to the standard topocluster jets, specially after JVT requirement (refer to Section 5.2.4 for further details). The JVT still has an effect on Particle Flow jets as pileup jets can be created by the neutral pileup particles which can not be removed through the utilization of the tracker information. On the other hand, the efficiency of hard-scatter jets shown in Figure 7.6a shows that while Particle Flow provides a better pileup jet rejection it also provides a larger acceptance of the hard-scatter jets, proving that the pileup jet removal is effectively more efficient for Particle Flow jets across the tracker acceptance ($|\eta| < 2.4$). Moreover, we can note how the shape of the Particle

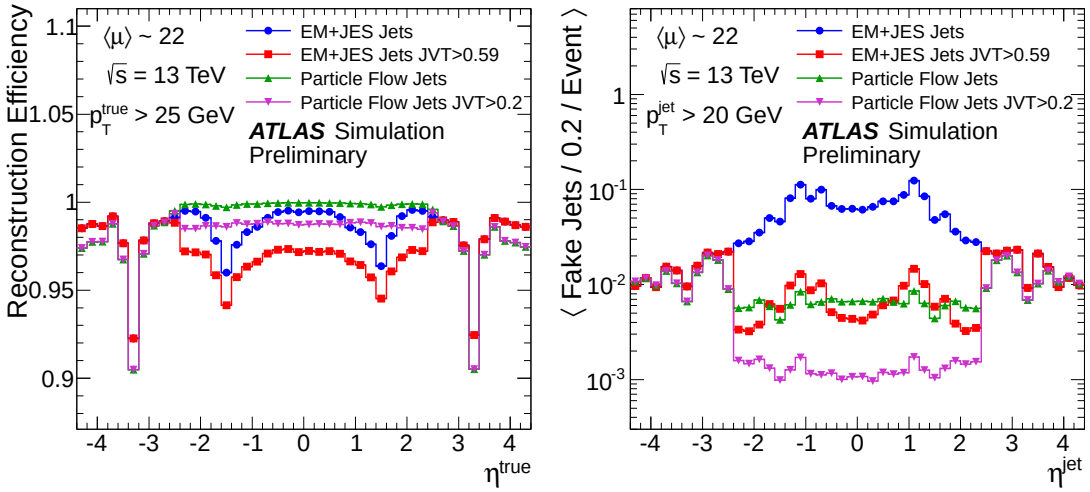

(a) Hard-Scatter jet efficiency, $p_T > 25$ GeV

(b) Average pileup jets, $p_T > 20$ GeV

(c) Hard-Scatter jet efficiency, $p_T > 40$ GeV

(d) Average pileup jets, $p_T > 40$ GeV

Figure 7.6 – Reconstruction efficiency of hard-scatter (HS) jets and average amount of pileup (fake) jets for Particle Flow and Topocluster-based jet collections [75]. The first row reports the result for jets having $p_T > 20$ GeV, 25 GeV while the second one $p_T > 40$ GeV.

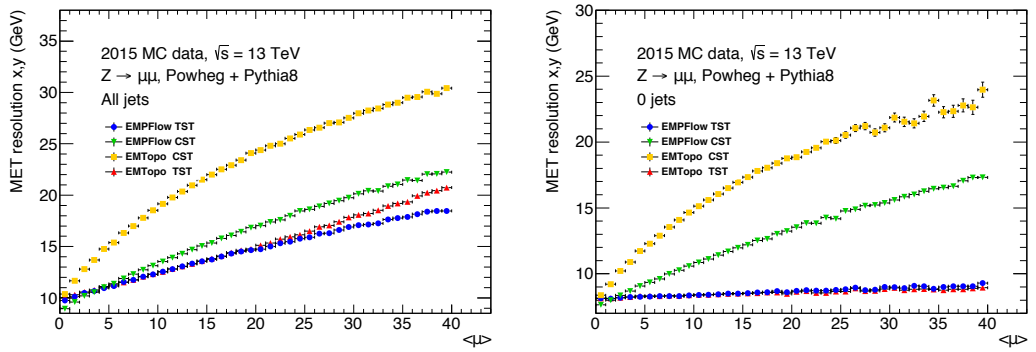

(a) E_T^{miss} x-y resolution vs $\langle\mu\rangle$, all jets selection (b) E_T^{miss} x-y resolution vs $\langle\mu\rangle$, no jets selection

Figure 7.7 – E_T^{miss} x-y resolution vs $\langle\mu\rangle$ in 2015 MC $Z \to \mu^+\mu^-$ simulated events. The different curves show the resolution of the TST and CST soft term reconstruction in the topocluster-based (EMTopo) and Particle Flow (EMPFlow) approaches.

Flow hard-scatter and pileup jets is more regular within $|\eta| < 2.4$ compared to the pure calorimeter-based jets. These feature is due to the removal of the pileup effects affecting the transition region between between the barrel and the extended barrel of the Tile calorimeter (see Section 4.2.3 for more details). Differences in the topocluster and Particle Flow jet reconstruction approach are much less evident for $p_T > 40\,GeV$ due to the lower presence of pileup jets at higher jet p_T as shown in Figure 7.6c and 7.6d.

7.2.2 *Particle Flow* E_T^{miss}

We have already illustrated in Chapter 6 how E_T^{miss} is reconstructed at the ATLAS experiment. In particular, we have highlighted the importance of the soft term for the reconstruction of this quantity and the advantages and disadvantages of the track-based and calorimeter-based soft terms (TST and CST), mainly related to the utilization of the pure charged and neutral particle information for the soft term estimation. With Particle Flow, we now have the possibility to exploit a set of separated charged and neutral objects and to improve the E_T^{miss} in two ways:

1. Through the better reconstruction of Particle Flow jets: p_T, η, ϕ resolution and pileup jet removal.

2. Through inclusion of the neutral information inside the TST estimation.

Similarly to the topocluster E_T^{miss}, for Particle Flow E_T^{miss} we distinguish a TST and a CST approach. In the Particle Flow TST, we essentially reconstruct the soft term from all the tracks of the hard-scatter charged Particle Flow objects, not associated to any hard object. The tracks are considered to come from the hard-scatter vertex if

$$|z_0 \sin\theta| < 2.0\,mm. \tag{7.6}$$

Since the tracks are reconstructed only within the tracker acceptance, this implies that the Particle Flow TST is essentially identical to the topocluster-based TST, and that the Particle Flow E_T^{miss} improvements are due to the improvements to the jet term

only. On the other hand, the Particle Flow CST represents the second reconstruction approach and it is composed of:

- All the soft charged Particle Flow objects associated to hard-scatter vertex through the requirement provided in Equation (7.6).
- All the neutral Particle Flow objects not associated to any hard object.

From this definition it clear then that the Particle Flow CST represents the ideal way to reconstruct the E_T^{miss} soft term in the ATLAS detector as it exploits maximally the tracker information for pilup mitigation and it also includes the soft neutral information within the full detector acceptance.

Figure 7.7 shows the resolution of the topocluster and Particle Flow-based TST and CST reconstruction as a function of $\langle\mu\rangle$. In these plots we can see how the E_T^{miss} resolution of Particle Flow is better than the topocluster TST approach (EMtopo TST). These improvements are mostly caused by the better estimation of the jet term, even though the JVT requirements were applied only on the topocluster jets as these were not investigated for Particle Flow jet only during the 2016 data taking. The resolution plot for $Z \to \mu^+\mu^-$ events with zero jets shows the effect of the Particle Flow soft term. In particular, it is possible to note that Particle Flow CST does not perform better than TST, as it could have been expected while Particle Flow TST performs similarly to the standard TST E_T^{miss}. Moreover, the zero jet plot shows a worsening on Particle Flow CST with $\langle\mu\rangle$ suggesting that the worse performance is caused by the presence of neutral pileup clusters which can not be removed by the Particle Flow algorithm.

The effects of JVT applied to Particle Flow E_T^{miss} are shown in Figure 7.9 using 2015 and 2016 simulated ATLAS $Z \to \mu^+\mu^-$ events for three different jet selections: inclusive jet selection, forward jet veto (*i.e.* no jets with $|\eta| > 2.4$) and jet veto (*i.e.* zero jets). In the resolution plots shown on Figure 7.9b, 7.9d and 7.9f it is possible to see that the JVT improves even further the resolution of Particle Flow TST E_T^{miss} compared to the standard topocluster approach and that these improvements are mostly due to the central reconstruction of the detector ($|\eta| < 2.4$). When the event selection requires to have zero jets in the $Z \to \mu^+\mu^-$ final state, the resolution of Particle Flow and topocluster-based E_T^{miss} become identical. The tails of the E_T^{miss} distribution are also nicely reduced as shown on Figure 7.9a, Figure 7.9c and Figure 7.9e.

7.3 CONCLUSION AND FUTURE PROSPECTS

This chapter has illustrated the improvements that the charged energy subtraction and pileup suppression of the ATLAS Particle Flow algorithm provided to the ATLAS jet and E_T^{miss} reconstruction during Run 2. However, even if Particle Flow reconstruction is now well established within the ATLAS experiment for Run 3, further improvements of the algorithms are possible for the next years. In particular, suppression of neutral pileup constituents could represent a very interesting domain for improving the Particle Flow jet performance even further. In this context, some possible techniques for neutral pileup mitigation in Particle Flow has been explored

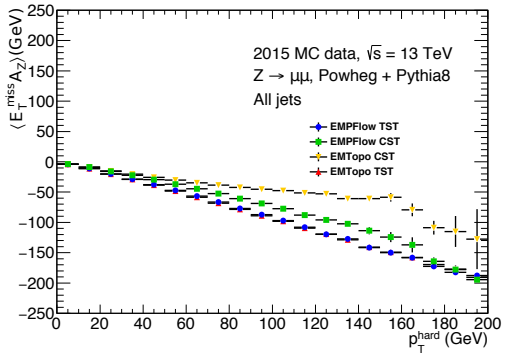

(a) E_T^{miss} scale vs p_T^{hard}, all jets selection

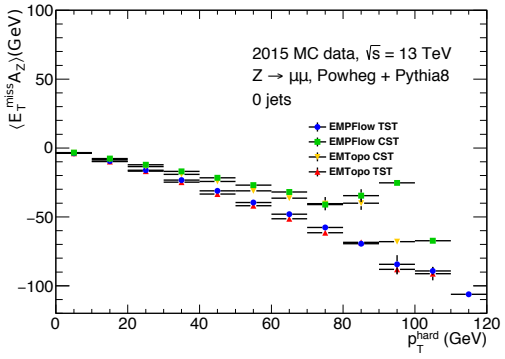

(b) E_T^{miss} scale vs p_T^{hard}, no jets selection

Figure 7.8 – E_T^{miss} scale vs p_T^{hard} in 2015 MC $Z \to \mu^+\mu^-$ simulated events. The different curves show the scale plot of the TST and CST soft term reconstruction in the topocluster-based (EMTopo) and Particle Flow (EMPFlow) approaches.

in ATLAS during Run 2. One specific approach [77], based on multivariate analysis techniques, is presented in the next chapter.

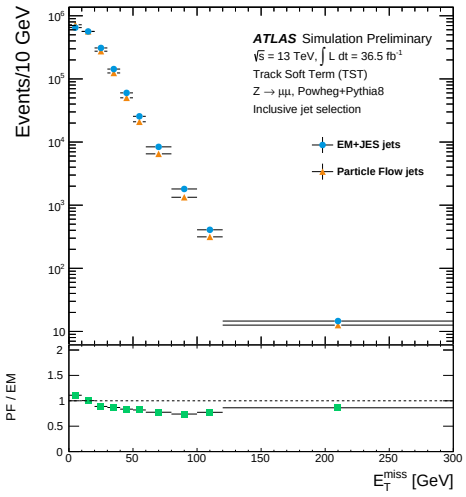

(a) E_T^{miss} distribution (inclusive jet selection)

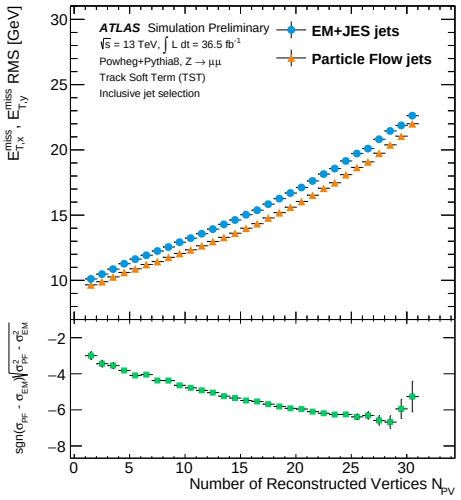

(b) E_T^{miss} x-y resolution (inclusive jet selection)

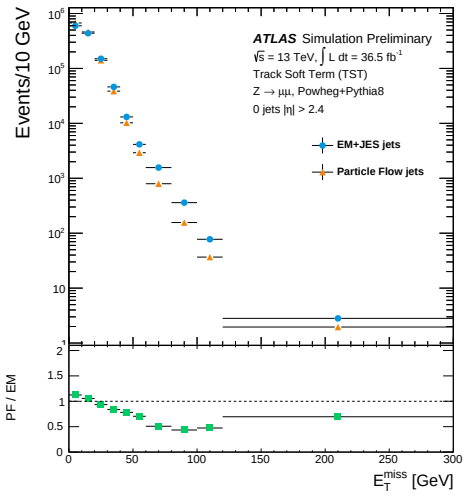

(c) E_T^{miss} distribution (no jets $|\eta| > 2.4$)

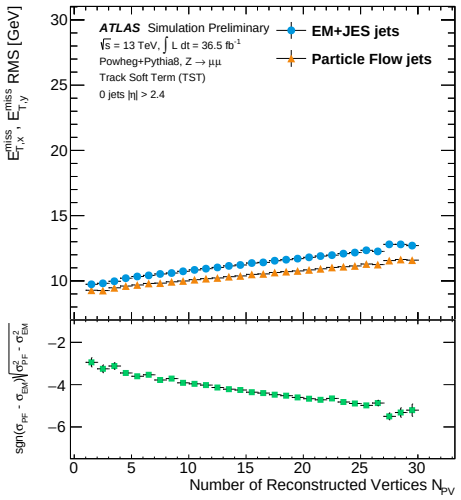

(d) E_T^{miss} x-y resolution (no jets $|\eta| > 2.4$)

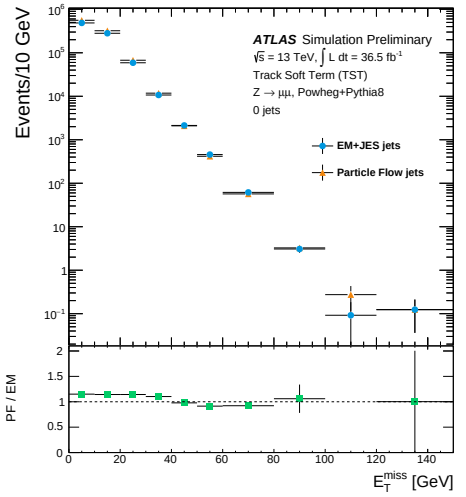

(e) E_T^{miss} distribution (no jets)

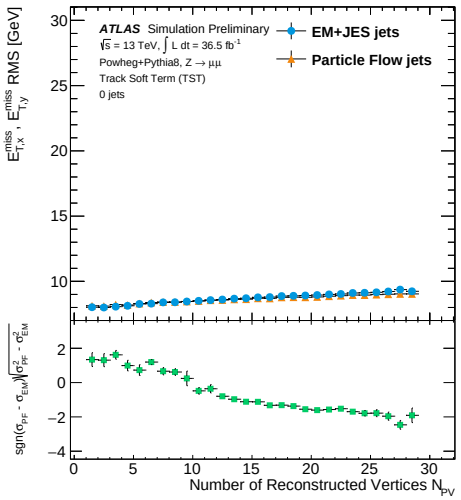

(f) E_T^{miss} x-y resolution (no jets)

Figure 7.9 – E_T^{miss} distributions and x-y E_T^{miss} resolutions for $Z \to \mu^+\mu^-$ simulated events for three different jet selections: inclusive jet selections, forward jet veto selection (no jets with $|\eta| > 2.4$) and no jets.

8

CONSTITUENT PILEUP SUPPRESSION TECHNIQUES

"The events of the world do not form an orderly queue, like the English. They crowd around chaotically, like Italians."

– C. Rovelli, *The Order of Time*

Contents

It has been shown in Chapter 7 how the tracking information, exploited before the jet-building stage, can improve the resolution of jets, E_T^{miss} and also enhance their stability to pileup. However, the current ATLAS Particle Flow algorithm does not apply any kind of pileup mitigation to neutral particles before building jets, a step which could increase even further the reconstruction performance of such quantities. Several techniques already exist for the mitigation of neutral pileup topoclusters and new approaches have been investigated using multivariate analysis techniques [77].

8.1 OVERVIEW OF CURRENT CONSTITUENT PILEUP MITIGATION TECHNIQUES

Constituent-level pileup mitigation techniques are designed to improve jet resolutions on an jet-by-jet basis by cutting on different observables related to jet constituents prior to jet building. Several techniques have been studied inside and outside of the ATLAS experiment [78, 79] and this section aims at reviewing some of these techniques studies before describing their application in the context of pileup mitigation for neutral Particle Flow constituents.

8.1.1 *Soft Killer*

Soft Killer [79] represents an event-by-event pileup mitigation technique based on the suppression of all the jet constituents not satisfying a certain p_T cut. This cut -

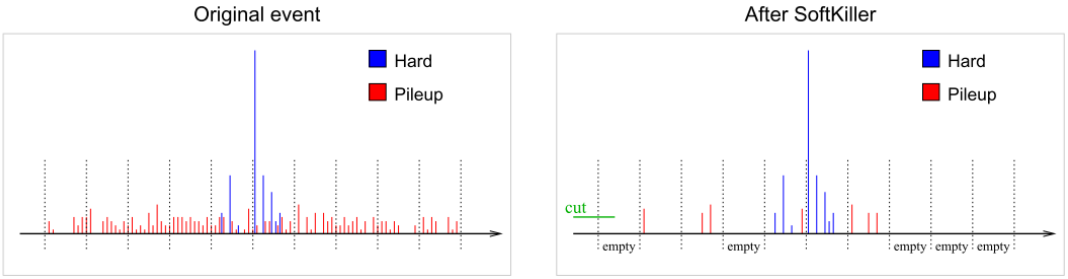

Figure 8.1 – Schematic of the Soft Killer p_T^{SK} definition [79]. The x-axis illustrates a generic η or ϕ axis divided into multiple patches and delimited by dotted lines.

noted as p_T^{SK} - is chosen for each event in order to set to a zero value the median of the energy density ρ used in the pileup-area subtraction defined in Section 5.2.3:

$$\rho = \underset{i \in \text{ patches}}{\text{median}} \left(\frac{p_{Ti}}{A_i} \right) \tag{8.1}$$

This is done by dividing the $\eta - \phi$ plane into a set of squared patches of size 0.6×0.6 and by choosing a value of p_T^{SK} such that half of the patches are filled with particle constituents. Such technique is schematically shown in Figure 8.1.

8.1.2 *Cluster timing cleaning*

In Run 2, it has been observed that the 25 ns spacing between LHC p-p bunches led to significant contamination of the calorimeter readout from out-of-time pileup contamination (see Section 4.1.1 for more details). In this context, Figure 8.2 shows the timing distribution of neutral Particle Flow objects associated to hard-scatter and pileup interactions. Indeed, we know that most of the out-of-time contamination is neutral since the timing window of silicon detectors is much shorter than the calorimeter one, meaning that no track is generally associated to out-of-time objects. In this picture, it is possible to note the two peaks at ± 25 ns corresponding to the contamination from the previous and next bunch crossing of the LHC, leading to contaminations in the calorimeter that can not be removed using tracking information.

In order to deal with this contamination, a specific set of rectangular cuts have been suggested and studied by the ATLAS collaboration in order to suppress such pileup contamination in an efficient way. A jet constituent is removed if the following requirements are passed:

1. It falls in the central region of the detector ($\eta < 2.5$). This feature is required to the bad timing resolution in the forward region of the detector.

2. The topocluster time t is greater than 5 ns if the average LAr quality Q_{LAr}[15] is larger than 0.02. This cut aims at suppressing constituents which are very consistent with an out-of-time readout shape and it is applied only using the LAr quality due to the larger impact of pileup to the LAr calorimeter.

[15] This quantity represents an integer number between 0 and 1 quantifying the consistency of the calorimeter readout with a pre-loaded reference. When Q_{LAr} is close to zero the readout shape is very consistent with the reference and very different when close to 1.

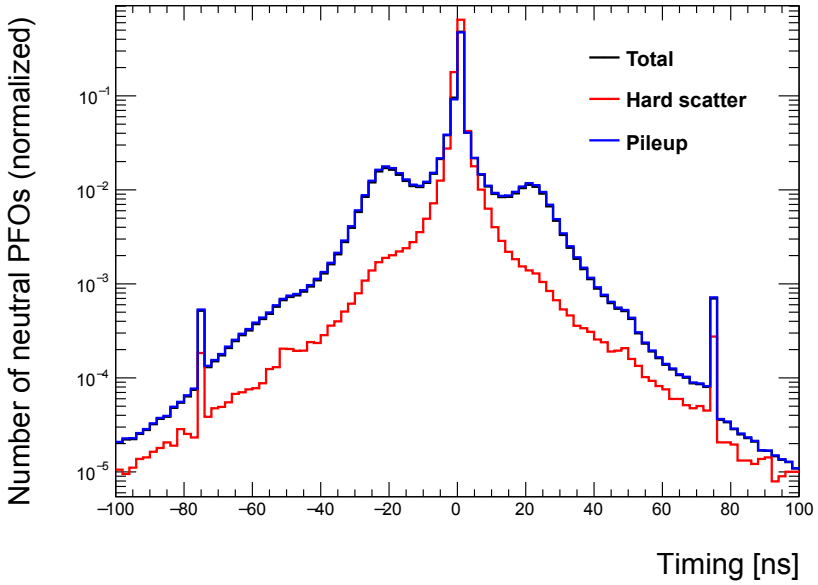

Figure 8.2 – Neutral PFOs timing for dijet MC sample [77]. The figure reports the total, hard-scatter and pileup contributions and the two peaks associated to $\pm 25\,ns$ shows the contamination from out-of-time pileup.

3. The topocluster time t is greater than $15\,ns$ if the average LAr quality Q_{LAr} is lower than 0.02. The requirement on the topocluster time is larger here due to the larger quality of the LAr readout shape, indicating a possibly good topocluster.

Looking at Figure 8.3 it is possible to note how important this selection is for the suppression of secondary peaks at $\pm 25\,ns$ when compared to standard constituent suppression techniques such as Soft Killer. This picture shows how the simple p_T selection applied with this technique is insufficient to kill the out-of-time pileup contamination showing the importance of this cluster cleaning in combination with such techniques.

8.2 MULTIVARIATE NEUTRAL PILEUP SUPPRESSION

We have illustrated in the previous sections the importance of combining different calorimeter-based information in order to reject the pileup contamination of neutral particles. Additionally, we have illustrated in Chapter 7 how the tracker information can be exploited prior to jet building in order to reject calorimeter pileup constituents. In this context, Particle Flow objects offer an ideal framework for rejecting such contamination due to the natural separation between neutral and charged particles.

Due to these reasons, in 2018 we started to investigate even further the calorimeter informations stored inside neutral Particle Flow objects and try to observe if the combination of several calorimeter quantities could have achieved a better pileup suppression compared to other constituent-based pileup mitigation techniques for neutral particles. For this task, a Boosted Decision Tree (BDT) has been explored [77].

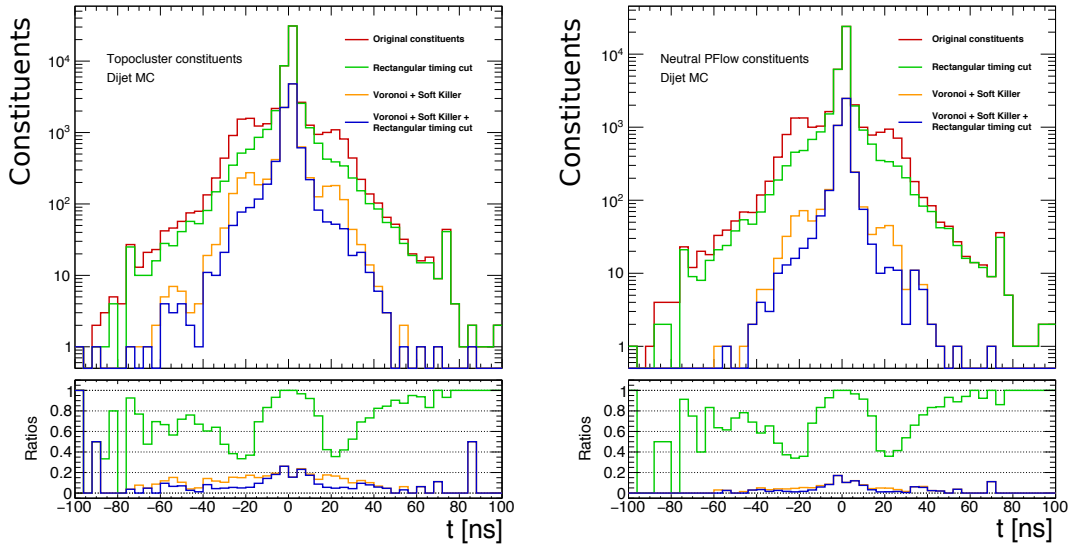

(a) Topoclusters

(b) Neutral Particle Flow objects

Figure 8.3 – Effects of rectangular timing cleaning on topoclusters and neutral Particle Flow objects, after application of Voronoi area subtraction [80] and Soft Killer [79].

8.2.1 *Boosted Decision Trees*

Boosted Decision Trees (BDTs) are common classification algorithms used in high energy physics. A binary classification algorithm consists of a function f that, given a certain set of inputs $\{x_i\}$, provides an output identifying a specific class type y, typically represented by a 0 or 1 integer:

$$y = f(\{x_i\}), \quad \text{where } y \in \{0, 1\}. \tag{8.2}$$

These algorithms are generally based on a set of *weights* $\{w_j\}$, fixed during an iterative process on a well known set input and output variables $(\{x_i\}, y)_l$. This stage is generally called the "training" of the classifier.

BDTs are a specific type of function f, based on *Decision Trees*. A Decision Tree is a sequence of binary splits applied to the input variables $\{x_i\}$ as represented in Figure 8.4. Despite their simplicity, Decision Trees are extremely affected to overfitting[16] and, in order to avoid this effect, a *boosting* procedure is generally applied to them. In this procedure, a large number N_{trees} of small Decision Trees is trained and, once the trees output $h_t(\{x_i\})$ is fixed, a combined output is provided through a specific set of weights $\{w_t\}$ through

$$h(\{x_i\}) = \sum_{t}^{N_{trees}} w_t h_t(\{x_i\}). \tag{8.3}$$

[16] An *overfitted model* consists in a mathematical model having more parameters than the ones justified by the data observations.

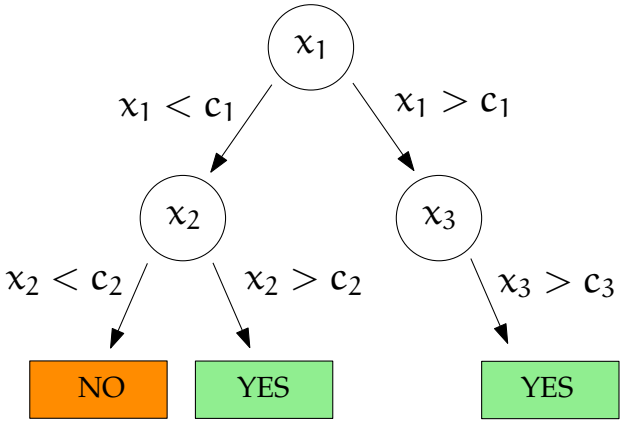

Figure 8.4 – Decision Tree schematic

The weights $\{w_t\}$ are fixed according to the single tree accuracies. The output of $h(\{x_i\})$ is generally a continuous number and binary classification can be applied through definition of a specific cut value C such that

$$y = h(\{x_i\}) > C. \tag{8.4}$$

8.2.2 *Input variables and hard-scatter cluster definition*

In order to understand which variables to combine inside the multivariate neutral pileup mitigation algorithm, several calorimeter-based variables associated to the neutral Particle Flow objects have been studied by comparing them between hard-scatter and pileup. For this study, for each neutral PFO, we have measured the energy of the reconstructed PFO E_{PFO} and the truth energy associated to the hard-scatter interaction E_{PFO}^{truth}. Therefore, we have defined a neutral PFO as a hard-scatter object if at least half of its energy, normalized to the truth hard-scatter energy, is coming from the hard-scatter interaction:

$$\text{isHS} = \left(\left| \frac{E_{PFO} - E_{PFO}^{truth}}{E_{PFO}^{truth}} \right| < 0.5 \right). \tag{8.5}$$

Figure 8.5 shows the distributions of different topocluster moments, also described in Section 5.2.1, considered as inputs for this multivariate analysis algorithm that were found to provide the largest separation between hard-scatter and pileup. Further details about these quantities can be found in Section 5.2.1.

The *separation* $\langle S^2 \rangle$ of a variable y used by the TMVA toolkit [81] provides a good quantity for describing the separation power of these variables. This quantity is defined as

$$\langle S^2 \rangle = \frac{1}{2} \int \frac{(f_S(y) - f_B(y))^2}{f_S(y) + f_B(y)} dy \ , \tag{8.6}$$

where $f_S(y)$ and $f_B(y)$ are the *Probability Density Functions (PDFs)* of the signal and background distributions associated to these variables. Looking at this formula, it is easy to see that when the distributions $f_S(y), f_B(y)$ are very close to each other, the quantity $\langle S^2 \rangle$ becomes close to zero while when this separation is large this

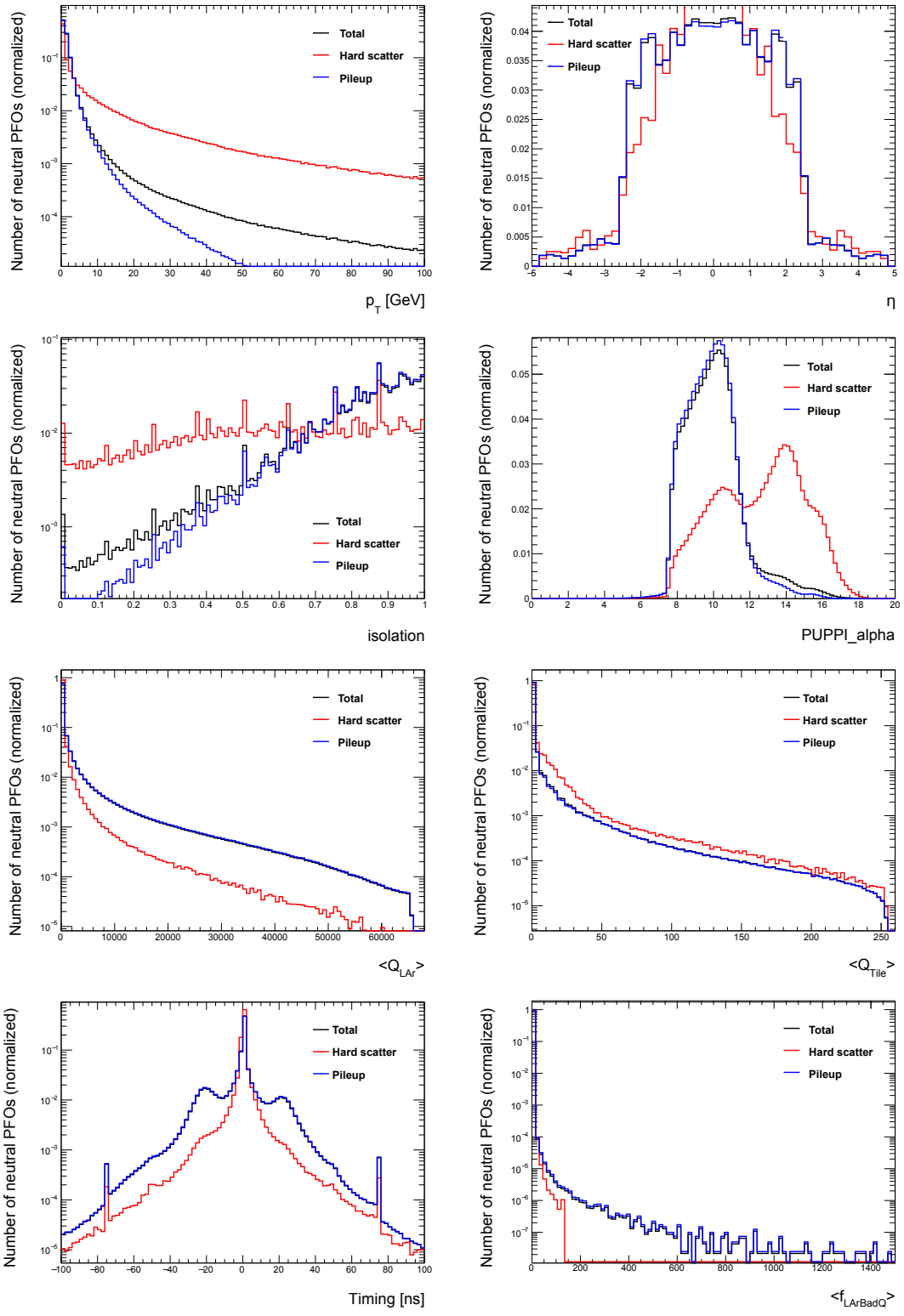

Figure 8.5 – Neutral PFO variables offering good separation between hard-scatter and pileup in dijet MC samples [77].

rank	variable	Separation $\langle S^2 \rangle$
1	p_T	9.781×10^{-2}
2	|timing|	6.026×10^{-2}
3	$\|\eta\|$	4.188×10^{-2}
4	$\langle Q_{LAr} \rangle$	2.572×10^{-2}
5	isolation	1.688×10^{-2}
6	PUPPI_alpha	1.169×10^{-2}
7	N_{PV}	4.629×10^{-3}
8	$\langle f_{LArBadQ} \rangle$	1.675×10^{-3}
9	$\langle \mu \rangle$	1.551×10^{-3}
10	$\langle Q_{Tile} \rangle$	1.184×10^{-3}

Table 8.1 – Variables separation provided and variable ranking by the TMVA toolkit [81]. The definition of the separation is given in Equation (8.6). The variable ranking is based on the separation between the variables.

quantity become large and positive, giving a good estimator of the separation power of these variables. Table 8.3 provides the separation and ranking of each variable in a kinematic slice of the dijet MC having the leading jet p_T included between the values 20 GeV and 60 GeV. From this table, it is possible to see that the variables providing the largest separation are:

- The transverse momentum p_T of the neutral PFO. This result is not surprising considering that particles with large transverse momentum are more likely to come from the hard-scatter interaction.

- The cluster timing t of the neutral PFO. This quantity is extremely useful for the identification of the neutral energy deposits coming from out-of-time pileup interaction (see Section 4.1.1 for more details).

- The neutral PFO pseudorapidity $|\eta|$.

- The average LAr quality $\langle Q_{LAr} \rangle$ previously defined in Section 8.1.2 and 5.2.1.

- The *alpha PUPPI* [78] defined as

$$\alpha^i_{PUPPI} = \log \left(\sum_j \frac{p_T^j}{\Delta R_{ij}} \theta \left(0.02 < \Delta R_{ij} < 0.3 \right) \right), \tag{8.7}$$

  where the sum j is performed over the charged particle flow object coming from the hard-scatter interaction in the central region ($|\eta| < 2.5$) and over all the charged and neutral objects in the forward region ($|\eta| > 2.5$) due to the restricted coverage of the ATLAS Inner Tracker. ΔR_{ij} represents the $\eta - \phi$ distance between two objects defined in Equation (4.8) while $\theta(x)$ represents the Heaviside step function.

Variable name	Settings
Boosting algorithm	AdaBoost
Number of trees N_{trees}	200
Maximum tree depth	4
Number of hard-scatter neutral PFOs	92 693
Number of pileup neutral PFOs	4 108 217

Table 8.2 – Specifics of the BDT training performed using dijet events with leading jet p_T included between 20 and 60 GeV [77].

rank	variable	importance
1	p_T	$2.039 \cdot 10^{-1}$
2	|timing|	$1.665 \cdot 10^{-1}$
3	$\|\eta\|$	$1.632 \cdot 10^{-1}$
4	$\langle Q_{LAr} \rangle$	$1.352 \cdot 10^{-1}$
5	PUPPI_alpha	$1.172 \cdot 10^{-1}$
6	isolation	$8.724 \cdot 10^{-2}$
7	N_{PV}	$7.240 \cdot 10^{-2}$
8	$\langle \mu \rangle$	$5.441 \cdot 10^{-2}$
9	$\langle Q_{Tile} \rangle$	$0.000 \cdot 10^{0}$
10	$\langle f_{LArBadQ} \rangle$	$0.000 \cdot 10^{0}$

Table 8.3 – Variables importance and ranking obtained by the TMVA toolkit [81] after training. The importance is defines as the total occurrence of a variable inside the trees of the BDT.

8.2.3 *Training and performance*

The training of several algorithms has been performed using the *Toolkit for Multivariate Data Analysis with ROOT* (TMVA) [81]. After evaluation of the performance of different algorithms, a Boosted Decision Tree (BDT) has been chosen for the classification of the neutral Particle Flow objects. Specifics about the trained BDT algorithm are reported in Table 8.2. Roughly 4 million neutral objects have been used for the training, all taken from a MC simulated dijet sample having leading jet p_T included between 20 and 60 GeV simulated using the 2017 LHC pileup profile shown in Figure 4.4. Table 8.3 shows the importance, calculated by the TMVA toolkit of the variables resulting from the BDT training and their ranking. Unsurprisingly, the transverse momentum represents the most important variable for the classification, while timing, quality and cluster isolation quantities also play significant roles for the classification of neutral particles.

The output of the trained BDT on a test sample, disentangled from the training dataset, is shown in Figure 8.6a for hard-scatter (HS) and pileup (PU) neutral PFOs. By probing different cuts on this output, a Receiver-Operating-Characteristic (ROC) curve has been derived (see Figure 8.6), showing on the y axis the fraction of rejected pileup objects and, on the x axis, the fraction of accepted hard-scatter objects. When comparing different classification algorithms, their performance can be compared by looking at these curves in order to understand which algorithm allows to accept

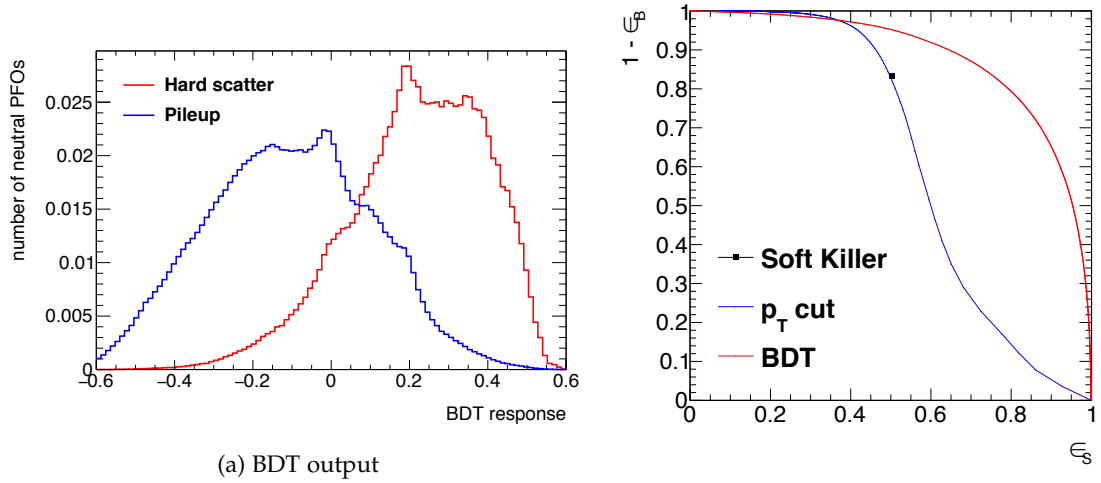

(a) BDT output

(b) ROC curve

Figure 8.6 – Output distribution and Receiver-Operating-Characteristic (ROC) curve curve of trained BDT for neutral pileup suppression with PFlow [77].

more signal and reject more background. On this figure, the ROC curve associated to a simple p_T cut is also reported, showing the better performance of the BDT approach including more information instead of p_T only. Additionally, the Soft Killer algorithm is also displayed, showing small deviations from the p_T only curve as expected.

8.2.4 *Impact on* E_T^{miss} *reconstruction*

The trained BDT has been used for the classification of neutral clusters in dijet and $Z \to \mu^+\mu^-$ samples. Negligible differences have been found in the classification variables and training due to the presence of leptons in the final state. For the classification, three different working points have been developed:

- A *tight* working point, corresponding to a cut of 0.077 on the BDT output and corresponding to a signal efficiency of 90%.
- A *medium* working point, corresponding to a cut of −0.023 on the BDT output and corresponding to a signal efficiency of 80%.
- A *loose* working point, corresponding to a cut of −0.108 on the BDT output and corresponding to a signal efficiency of 60%.

Figure 8.7 illustrates the impact of these three working point on key distributions for neutral pileup objects in dijet samples, having leading jet p_T between 20 GeV and 1300 GeV. This larger p_T range for the performance evaluation has been chosen with respect to the training samples in order to verify the survival of very high p_T neutral objects after multivariate classification. In these figures, it is possible to note how the BDT approach allows to remove higher p_T neutral pileup objects with respect to the simple Soft Killer approach, where the bulk of the removal is concentrated below 2 GeV. This feature is made possible by the combination of

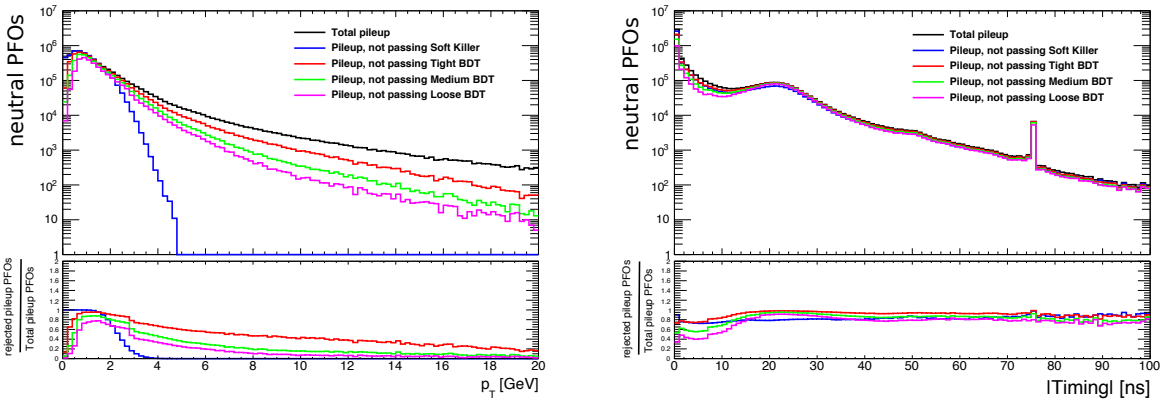

(a) (b)

Figure 8.7 – Distributions showing the impact of different BDT working points, corresponding to the Tight (0.077), Medium (−0.023) and Loose (−0.108) BDT selections [77]. The black curves show the distributions associated to the total neutral pileup objects. The blue curve corresponds to the neutral pileup objects removed by the Soft Killer (SK) procedure, while the red, green and purple curves show the neutral pileup objects removed by the three BDT working points.

different variables, allowing to exploit the different correlations between different quantities and resulting in a better performance than pileup mitigation techniques based simple assumptions on p_T and $\eta - \phi$ separation of neutral objects. The removal of higher p_T pileup clusters could represent an important improvement for the removal higher p_T pileup jets, leading to further improvements of the ATLAS Particle Flow algorithm. Additionally, it is possible to see how the BDT is able to remove also the peaks at ± 25 ns, corresponding to the out-of-time pileup contamination which is always measured due to the lack of tracking information. In order to verify the correct acceptance of signal particles, Figure 8.8 shows the same BDT evaluation but applied on hard-scatter neutral objects. In this figure it is possible to see how the BDT allows to accept high-momentum neutral objects coming from the hard-scatter interaction.

The impact on MET has been evaluated using $Z \to \mu^+\mu^-$ events with zero jets. The jet veto has been applied to standard Particle Flow jets since the Particle Flow jet collections modified by the BDT would need a dedicated calibration that has not been derived for this work. However, the track-based soft term does not include any neutral particle information and, after neutral pileup suppression, the Particle Flow calorimeter-based soft term could lead to improvements on this quantity. Therefore, the resolution and E_T^{miss} has been evaluated for Particle Flow TST, CST and the BDT classification on neutral CST constituents. Figure 8.9 shows the results, showing significant improvements of the BDT-based approach with respect to the CST distribution alone. However, the resolution of the BDT-based E_T^{miss} soft term is still worse than the TST-based approach, meaning that further work needs to be done in order to adopt this approach in ATLAS.

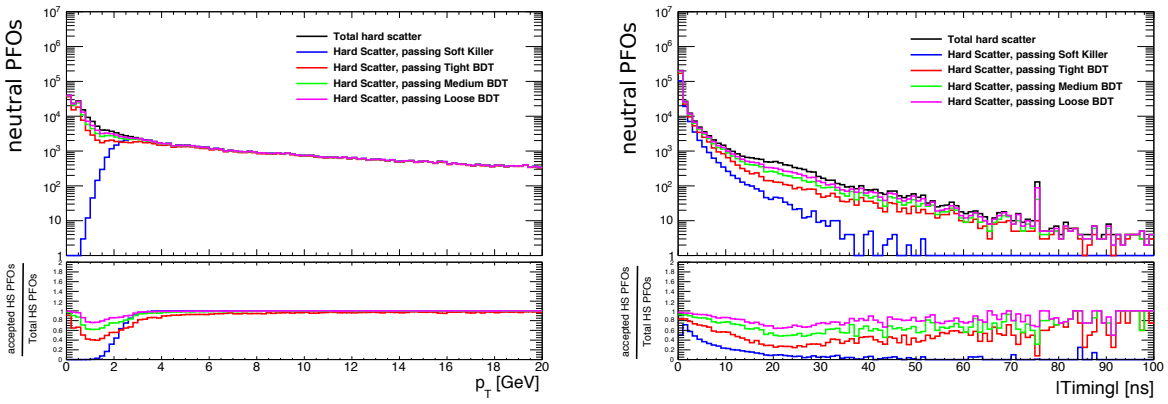

(a) (b)

Figure 8.8 – Distributions showing the impact of different BDT working points, corresponding to the Tight (0.077), Medium (−0.023) and Loose (−0.108) BDT selections [77]. The black curves show the distributions associated to the total neutral hard-scatter objects. The blue curve corresponds to the neutral hard-scatter objects accepted by the Soft Killer (SK) procedure, while the red, green and purple curves show the neutral hard-scatter objects accepted by the three BDT working points.

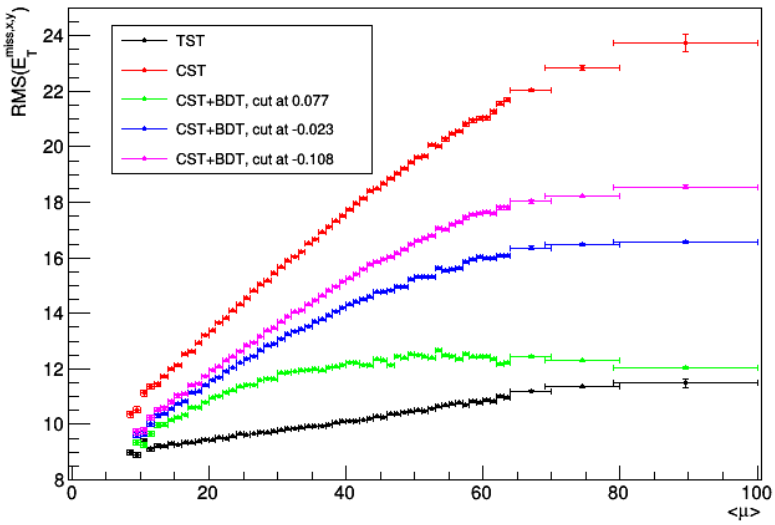

Figure 8.9 – E_T^{miss} resolution for $Z \to \mu^+\mu^-$ events with zero jets [77]. Reported are the standard Particle Flow track-based soft term (TST) and calorimeter-based soft term (CST) reconstructions, as well as the CST reconstructions having neutral pileup suppression applied.

8.3 CONCLUSION

It has been presented in this chapter a novel approach for combining calorimeter information for the suppression of neutral particles resulting from pileup interactions. Despite the simplicity of the method, this first study has shown potential for improving the Particle Flow algorithm even further. However, further ideas and possible selection improvements will be needed in future in order to evaluate the possible implementation within the ATLAS offline reconstruction software. These ideas might include the implementation of more sophisticated Machine Learning techniques, as well as the utilization of lower level calorimeter cell and tracker information.

9 HADRONIC TRIGGER RECONSTRUCTION FOR THE HL-LHC

"Fred: He can move faster than Severus Snape confronted with shampoo."
– J.K. Rowling, *Harry Potter and the Deathly Hallows*

Contents

The High-Luminosity LHC (HL-LHC), an upgrade of the LHC planned to be operative starting from 2026 (Run 4), will raise the instantaneous luminosity of the LHC up to $7.5 \times 10^{34}\,cm^{-2}s^{-1}$, resulting in a number of simultaneous p-p collisions $\langle\mu\rangle = 200$ [3]. The ATLAS detector is expected to collect an integrated luminosity of approximately $3000\,fb^{-1}$ after 10 years of operations, improving the sensitivity to rare new physics channels. Without rejecting the events faking interesting physics topologies, this would require significant increases of the trigger thresholds and subsequently to losses of new physics events. Jet and E_T^{miss} triggers largely rely on calorimeter information and, without the presence of online tracking, the trigger thresholds of these signatures will largely increase in Run 4. In view of these increases, the ATLAS trigger system will be subject to major upgrades for the HL-LHC. One of these upgrades include a completely revisited Trigger and Data Acquisition system that, through a new online tracking system, will provide fast track reconstruction for better physics object identification, calibration and pileup suppression.

After a brief introduction about the main ATLAS detector upgrades for HL-LHC, this chapter presents a set of studies illustrating how track-based pileup mitigation will improve E_T^{miss} and multi-jet triggers at the HL-LHC.

9.1 HL-LHC DETECTOR UPGRADES

Additionally to the upgrades provided to the ATLAS detector during LS2, two major upgrades are expected to happen between the third and fourth Run of the LHC: the replacement of the ATLAS Inner Detector - also known as *Inner Tracker*

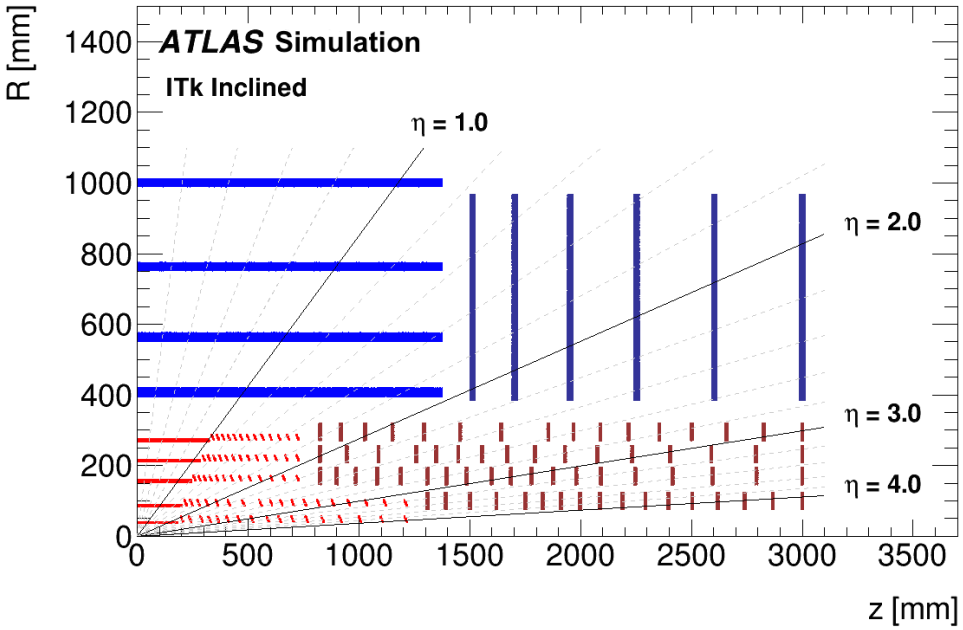

Figure 9.1 – Schematic view of the baseline ITk inclined layout [82]. In this schematic, the x-axis is parallel to the beamline while the y-axis represents the radius from the interaction point. The active elements of Strip and Pixel Detector are shown respectively in blue and red.

(ITk) - and the complete upgrade of the TDAQ system. In this section are illustrated the main features of these changes to the ATLAS detector expected for Run 4.

9.1.1 *The Inner Tracker*

The Inner Tracker (ITk) is an entirely revisited tracking detector for the ATLAS experiment, expected to be installed in the ATLAS cavern between 2024 and 2026. Differently from the current ATLAS Inner Detector based on silicon and drift gas chamber technologies, ITk will exploit pure silicon detectors for charged particle detection due to the difficulty to use gas-based technologies in such a high pileup regime. The new tracker is composed of five barrel pixel layers instrumented with new sensor and readout electronics technologies allowing to improve the tracking performance and cope with the high HL-LHC radiation. The baseline pixel technology is a *planar hybrid* technology, which uses a sensor and a readout chip bonded together at the pixel level. 3D sensor modules will be preferably used for the innermost layers, because of their advantages in power consumption and radiation tolerance [83]. In the barrel, an inclined layout of the outer pixel modules has been planned in order to allow to reduce the number of modules and the construction costs. The pixel detector will also include ring-shaped supports in the end-cap region, allowing to extend the pseudorapidity acceptance up to $|\eta| < 4.0$ [82]. The strip detectors are formed by 4 barrel and 6 endcap layers, each composed of a pair of tilted silicon strip modules allowing to perform a two-dimensional track-hit measurement. This system covers up to $|\eta| < 2.7$. Figure 9.1 shows a schematic view

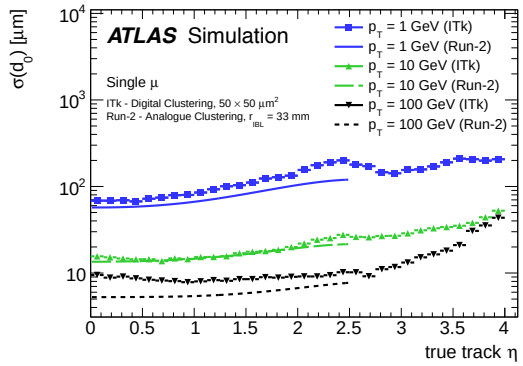

(a) d_0 resolution

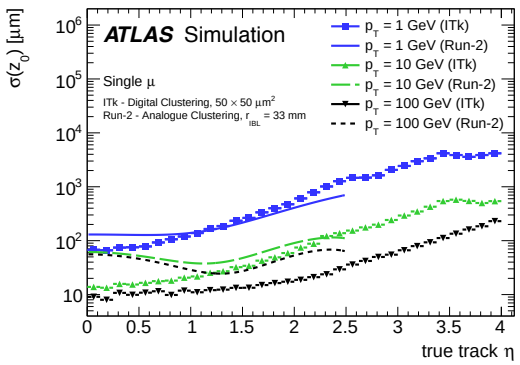

(b) z_0 resolution

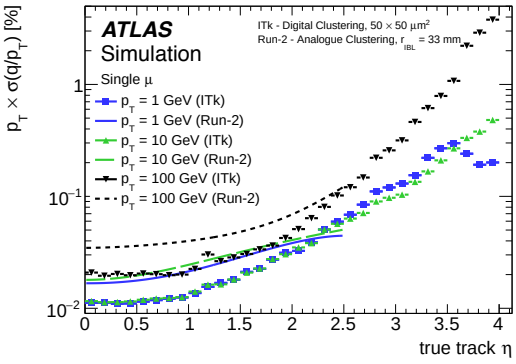

(c) z_0 resolution

Figure 9.2 – ITk d_0 and z_0 track parameter resolutions [82].

of the layout of the different pixel and strip modules composing the baseline ITk design.

The large number of average interactions per bunch crossing expected from the HL-LHC every 25 ns implies two primary features of the new tracking detector:

- Resistance to high radiation levels (up to 9.9 MGy).
- Optimal longitudinal track impact parameter z_0 resolution for pileup track identification.

Both these features have been demonstrated in feasibility and performance studies. The z_0 resolution is shown in Figure 9.2b. Performance studies also shown that the transverse impact parameter d_0 resolution has decreased for track $p_T > 100$ GeV (see Figure 9.2a) due to the larger radius of the innermost pixel layer [17] while the p_T resolution is improved up to a factor of 2 for $p_T > 100$ GeV due to the substitution of the TRT with strip detectors (see Figure 9.2c).

[17] The innermost pixel layer will be placed at 39 mm from the interaction point due to the larger irradiation from the HL-LHC. The current innermost pixel layer radius is 33.5 mm [82].

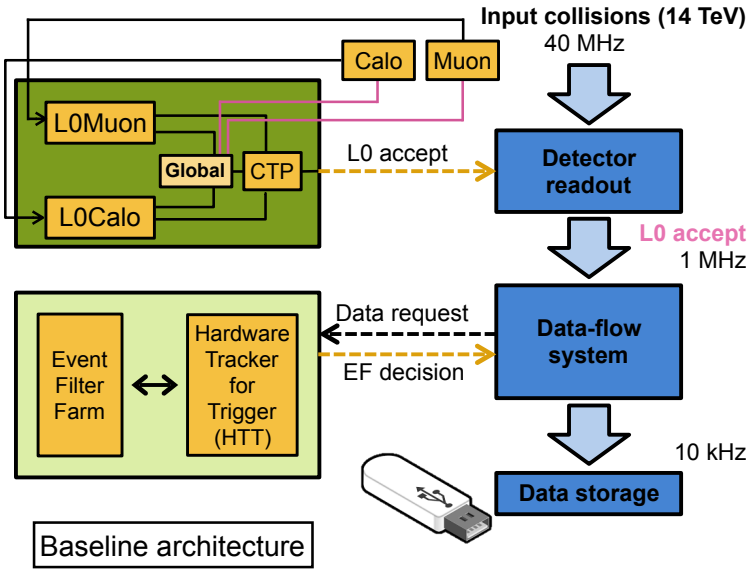

Figure 9.3 – Schematic of baseline design Phase-II ATLAS TDAQ architecture [85].

9.2 THE PHASE-II ATLAS TDAQ UPGRADE

The Phase-II upgrade of the ATLAS TDAQ system aims at improving the online event selection in order to deal with the large luminosities provided by the HL-LHC. This upgrade is complementary to the different upgrades of the ATLAS sub-detectors for Run 4, including:

- The new *Inner Tracker* (ITk) described in the previous section.
- The upgraded calorimeter readout electronics of both Liquid Argon (LAr) and Tile calorimeters providing the trigger with full-granularity information.
- The upgrade of the Muon Trigger Chambers and readout electronics meeting the Level-0 trigger requirements and extending the acceptance of muons in the trigger.

In addition to these features, the ATLAS HL-LHC TDAQ upgrade will also rely on the TDAQ upgrades made during LS2 such as the upgraded calorimeter trigger processors and *Feature Extractors* (FEX) [84].

Two possible architectures have been defined for the Phase-II upgrade of the ATLAS TDAQ system [3]:

- A *baseline architecture* composed of a hardware-based Level-0 (L0) trigger running at 40 MHz input rate and a CPU farm-based Event Filter (EF) assisted by hardware-based track reconstruction and running at 1 MHz input rate.
- An *evolved version* of the baseline architecture where an intermediate Level-1 (L1) trigger with 2-4 MHz input rate provides an additional filtering step between the Level-0 and Event Filter. In this scenario, the EF input rate is reduced to 800-600 kHz compared to the baseline scenario.

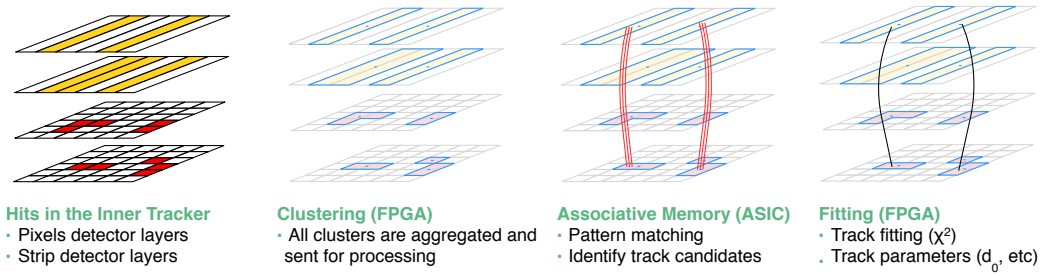

Figure 9.4 – Schematic of associative-memory-based tracking sequence performed by the Hardware Track Trigger (HTT) [86].

Both architectures are designed to provide a 10 kHz output rate. A simplified schematic of the baseline architecture design is reported in Figure 9.3.

9.2.1 *Level-o trigger*

The Level-o trigger is the first step of the new ATLAS trigger system and it will reduce the 40 MHz HL-LHC rate to the 1 MHz output in the baseline trigger design. This trigger is based on a hardware system composed of the *Level-o Calorimeter Trigger* (LoCalo), the *Level-o Muon Trigger* (LoMuon), the *Global Trigger* and the *Central Trigger* (CTP) sub-systems [3].

LoCalo provides reconstruction of calorimeter objects using different FPGA-based FEXs, namely the *electron Feature EXtractor* (eFEX), the *jet Feature EXtractor* (jFEX), the *global Feature EXtractor* (gFEX) and the *forward Feature EXtractor* (fFEX). These systems allow to create complex and high-granularity objects exploiting the complete ATLAS calorimeter coverage. LoMuon provides muon objects with sophisticated algorithms and in an extended pseudorapidity η coverage exploiting the entirely new muon trigger electronics. Moreover, the LoMuon upgrade also includes the first use of precision Muon Detectors (MDTs) in the hardware-level trigger.

New functionality of the upgraded Lo trigger is provided by high-rate processing at the *Global Trigger*. After LoCalo, this system improves calorimeter objects using full-granularity energy data coming directly from upgraded calorimeter pre-processors and implementing offline-like algorithms such as topological clustering and anti-k_t-based jet-finding [3]. Additionally, the Global Trigger takes the inputs from the LoCalo and LoMuon systems in order to apply topological selections based on p_T and angular requirements[18].

9.2.2 *Event Filter and Hardware Track Trigger (HTT)*

The *Event Filter* (EF) system is composed of a CPU-based processing farm and a *Hardware Track Trigger* (HTT) co-processor. The main function of the EF is to refine the selection of the 1 MHz Lo output events through sophisticated offline-like reconstruction techniques reducing the final output rate. The HTT includes *regional*

[18] This feature is offered today by the ATLAS L1Topo system.

(rHTT) and *global* (gHTT) track reconstruction, where regional tracking is made in specific *Regions of Interest* (RoIs) limited to approximately 10% of the total Inner Tracker data while global tracking exploits the full tracker coverage, but only for 10% of L0 selected events. Both regional and global tracking are based on associative memory techniques, where tracking is accelerated using pre-loaded pattern banks to be matched to the tracker output (see Figure 9.4). The final output of the EF is fixed at 10 kHz and the trigger decision is communicated to the Dataflow system, which transfers accepted events to permanent storage.

9.3 JET AND E_T^{miss} TRIGGER RECONSTRUCTION AT THE HL-LHC

Jet and E_T^{miss} triggers are used in a large variety of different key ATLAS analysis at the HL-LHC, such as searches for Dark Matter, electroweak supersymmetry, di-Higgs measurement, and many others. This section illustrates the expected functioning of these trigger chains in the upgraded ATLAS TDAQ system.

9.3.1 *Reconstruction at the Global Trigger*

The Global Trigger will exploit full calorimeter granularity, allowing to employ offline-like reconstruction algorithms for jet and E_T^{miss} triggers. The nominal plan for jet reconstruction at the Global Trigger is the utilisation of topoclusters (see Section 5.2.1 for further details) based on the "42" scheme, where topoclusters are grown using calorimeter cells having an energy exceeding by at least twice the cell energy uncertainty ($|E_T| > 2\sigma$) starting from a seed cell having an energy four times larger than its energy uncertainty ($|E_T| > 4\sigma$). This choice is motivated by the fact that only calorimeter cells satisfying $|E_T| > 2\sigma$ will be passed to the Global Trigger due to restrictions to the data flow at 40 MHz input rate. This topoclustering scheme offers optimal performance compared to other jet trigger algorithms, as shown in Figure 9.5. Maximal parallelism for the reconstruction of topoclusters is made possible using Field Programmable Gate Arrays (FPGAs) [3]. Topoclusters are then passed through an anti-k_t-like algorithm (see Section 5.2.2 for more details) in order to build jets at L0. This is an important goal of the Global Trigger, where jets are wanted to be reconstructed as similarly as possible to EF and offline jets.

Similarly to jet reconstruction, E_T^{miss} will also be very close to the offline reconstruction at the L0 global trigger. Due to the availability of anti-k_t jets and other objects such as electron and muons, a realistic offline E_T^{miss} reconstruction can be achieved by subtracting the p_T of all these objects, as explained in Chapter 6. We can therefore define the *missing* H_T (MHT) as

$$\text{MHT} = -\sum_{\text{object } i} \mathbf{p_T}^i \tag{9.1}$$

However, without tracking information for the suppression of pileup jet contributions, this hardware-based E_T^{miss} reconstruction will be extremely sensitive to pileup making the selection of low E_T^{miss} signals challenging. In the baseline Hardware-Track-Trigger (HTT) scenario, no tracking information is expected to be available at the Global

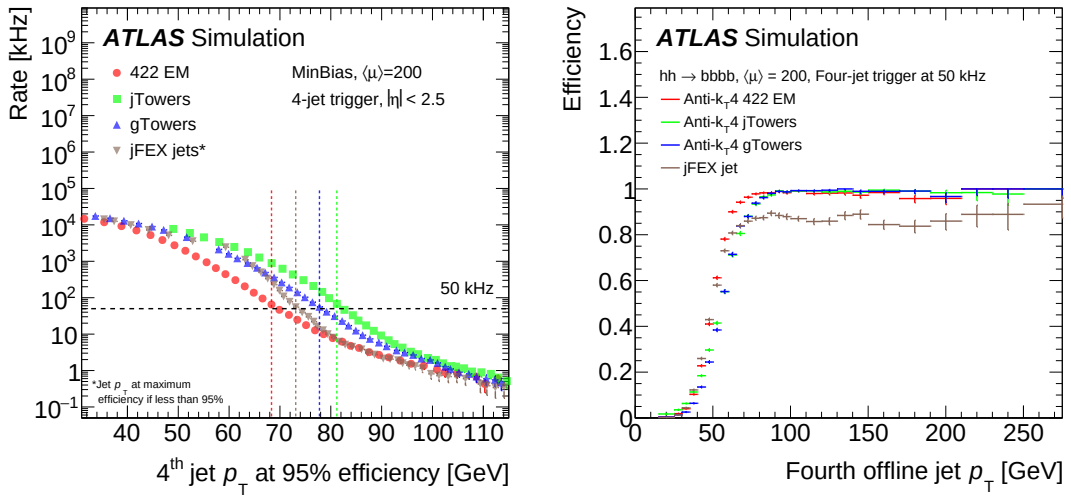

(a) Lo rates

(b) Lo efficiency curves

Figure 9.5 – (a) Lo output rates and (b) Lo efficiency curves obtained for a 4-jet trigger using different jet reconstruction algorithms [3].

Trigger. However, in an evolved scenario, tracks could be available in an intermediate step making track-based pileup suppression on E_T^{miss} quantities possible.

9.3.1.1 *Track-based pileup jet suppression at the Global Trigger*

The evolved ATLAS TDAQ scenario for HL-LHC expects HTT tracks at L1. These tracks are reconstructed within Regions of Interest (RoIs) provided by the Global trigger and, due to the limitation in the readable data accessible from the Inner Tracker (ITk), only 10% of the detector occupancy can be readout from the strip and the two outermost pixel layers corresponding to a tracking processing rate of 400 kHz. It has been estimated from Figure 9.6 that, for a 50 GeV jet threshold, this corresponds to 2.8 jets on average corresponding to $13-14\%$ of the ITk data [3]. This means that at the Global Trigger only jets satisfying $p_T \geqslant 50$ GeV will be provided with tracks due to the ITk readout limitations.

Now that it has been clarified from which RoIs tracks can be reconstructed, it is time to define an algorithm for suppressing pileup jets. Considering that standard vertexing techniques might take a significant amount of time compared to the target Lo trigger latency, a simplified pileup jet tagger was developed in the context of MHT reconstruction. This algorithm works as follows:

1. Split the beamline into a fixed set of segments of length Δz. After optimization, $\Delta z = 7$ mm was found to be an optimal value for signal-to-background discrimination in MHT-based selections.

2. For each jet satisfying $p_T \geqslant 50$ GeV, find the provenance bin i of the jet using the maximal total track p_T as

$$i \equiv \max \left(\sum_{i \in \text{jet}} p_T \left(|z_{\text{track}} - z^i_{\text{bin}}| < \frac{\Delta z}{2} \right) \right), \tag{9.2}$$

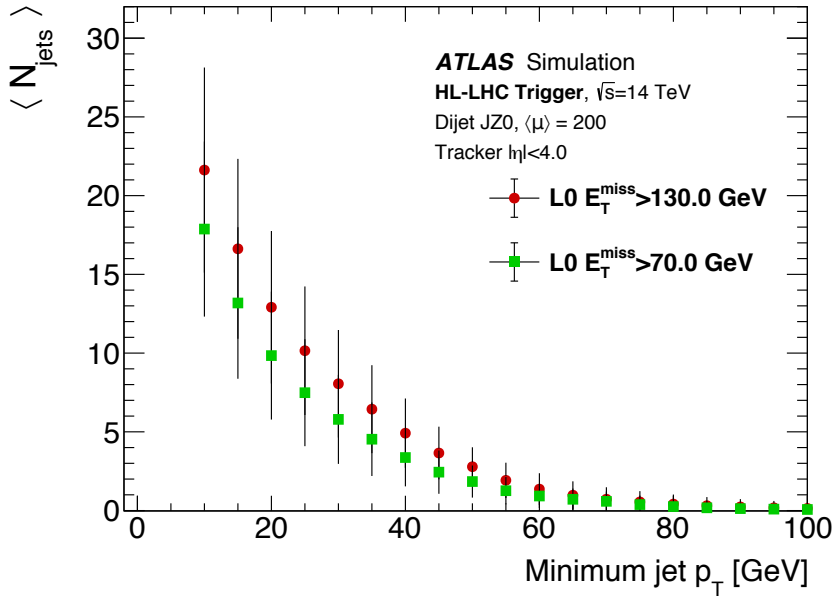

Figure 9.6 – Average number of jets $\langle N_{jets} \rangle$ as a function of the minimum calibrated offline jet p_T for different Lo MHT selections [3].

where z^i_{bin} is the z coordinate associated to segment i. Fore each bin i, the result of this procedure will be a list of associated jets where one jet can be associated only to one segment.

3. Using all the tracks within jets satisfying $p_T \geqslant 50\,GeV$, compute the bin j having the maximal sum of track p_T. This segment will be called *hard-scatter segment* and the jets associated to this segment will be considered as hard-scatter jets. All the other jets will be considered as pileup jets, and not considered in the MHT calculation.

4. Shift the z segmentation by $\frac{\Delta z}{2}$ and repeat the previous procedure. If more hard-scatter jets are found than in the first iteration of the algorithm, consider these new hard-scatter jets instead. This step is fundamental for the treatment of cases where the hard-scatter interaction is very close to the boundary of a Δz segment.

A schematic of this algorithm is provided in Figure 9.7. This algorithm is simple and it provides a fast identification of hard-scatter and pileup jets. These jets are further used to build the MHT value. Further discussion about the impact of this algorithm on jet and E_T^{miss} triggers will be provided later in Section 9.4.

9.3.2 *Reconstruction at the Event Filter*

When events pass the Global Trigger they are sent to the Event Filter for further processing. At this stage, jets can be formed by the anti-k_t algorithm using the "420" topoclusters as inputs, in analogy to the offline reconstruction. At the EF, track information can become available at both regional and at full detector level and the

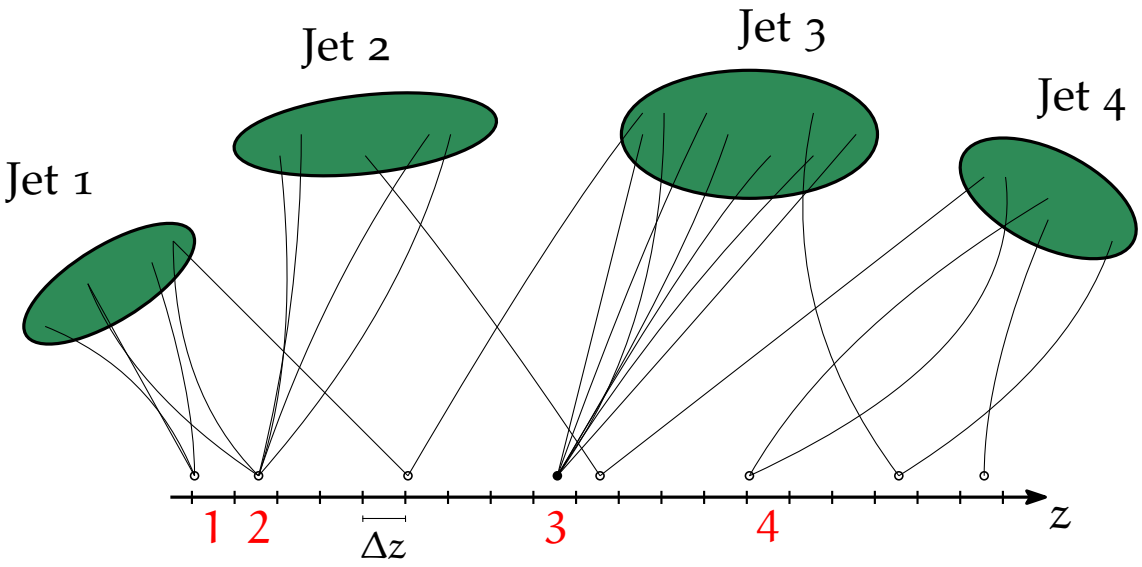

Figure 9.7 – Schematic of simplified pileup jet tagger based on RoI based tracking. Jets (numbered from 1 to 4) are associated to a specific z segment of length Δz by looking for the segment having the maximal jet track p_T sum. Numbers in red indicate the jet associated to a specific z segment. The choice of the final HS segment is made using all the tracks within all jets, looking at the segment having the maximal sum of the track p_T.

larger available processing time allows to create vertices and select hard-scatter jets using standard offline techniques (see Section 5.1 for further details). After vertex formation, tracks can be associated to the hard scatter vertex if these satisfy

$$|z_{track} - z_{vertex}^{HS}| < 2\sigma\left(z_{track}\right). \tag{9.3}$$

From these tracks, pileup jet identification techniques can be based on the R_{p_T} quantity defined in Section 5.2.4. The reconstruction of E_T^{miss} benefits from the pileup suppression made possible by offline techniques and also from the reconstruction of the track-based soft term.

9.4 IMPACT OF HTT ON JET AND E_T^{miss} TRIGGERS

The performance of E_T^{miss} triggers can be studied by looking at the amount of accepted signal events at a given trigger rate. Using a *minimum-bias* sample[19], and assuming a total bunch-crossing rate of the LHC of 40 MHz, it is possible to define from a specific trigger output rate X a threshold T to be applied on a certain online observable t in order to select a specific physics type. The larger the value of T, the lower the output rate X according to the distribution of the considered online event observable. One of the goals of the trigger system is to select, for a given the rate X, the highest possible amount of signal events. For multi-jet and E_T^{miss} triggers, without the presence of online HTT tracks, pileup jets would increase the trigger rate due to

[19] A minimum-bias sample is an inclusive physics sample obtained without applying a specific physics selection on the data.

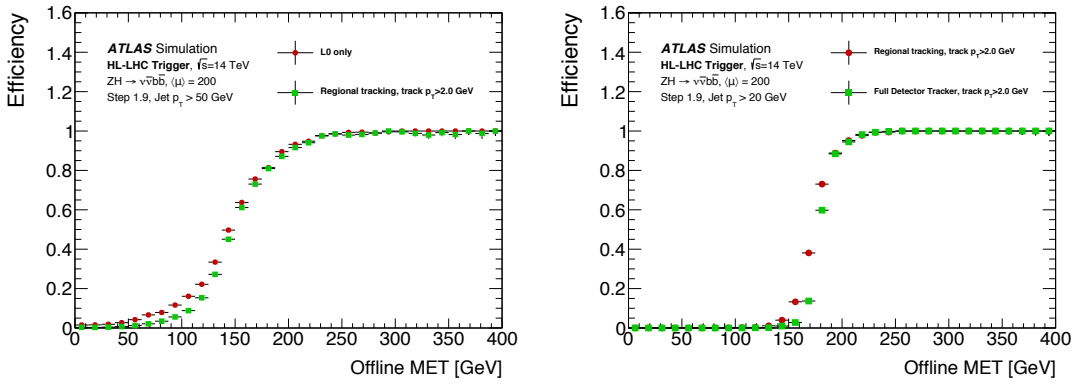

(a) Lo regional tracking

(b) EF tracking

Figure 9.8 – Efficiency curves as a function of the offline E_T^{miss} for the Level-o (a) and an EF (b) MET triggers. For the Lo MHT reconstruction, only jets satisfying $p_T > 50\,GeV$ have been considered while the EF reconstructs offline-like E_T^{miss} using tracks with $p_T > 2\,GeV$. The offline E_T^{miss} has been reconstructed using an identical technique employed in the EF, even though track momentum coverage has been extended to $p_T > 2\,GeV$.

the large amount of selected background events. Therefore, the identification and rejection of pileup jets is particularly important for these triggers in order to decrease their background rates and enhance the acceptance of signal events.

Once a certain threshold value T has been fixed, the *efficiency curve*, as a function of an offline observable, can be derived. This curve illustrates the impact of the online selection $t > T$ on the offline events and two examples obtained for E_T^{miss} triggers are shown in Figure 9.8. Here the impact of different tracking selections on the offline E_T^{miss} is displayed. The offline E_T^{miss} has been reconstructed including jets ($p_T > 20\,GeV$) and a soft term, for which pileup suppression was applied through R_{p_T} and the track-to-vertex association illustrated in Equation (9.3). For different trigger rates, the threshold corresponding to the 95% trigger efficiency T_{95} can be derived. Figure 9.9 reports a scan of different background trigger rates X versus T_{95} for different HTT configurations. In particular, Figure 9.9a and 9.9b show the impact of the simplified pileup jet suppression described in Section 9.3.1.1 on Lo MHT-based triggers for different reconstructed track p_T and η. The inclusion of the simplified pileup jet suppression results in reduction of trigger background rates by a factor of 2 to 10 and no major difference is observed for track p_T between 1 and 4 GeV. The eta dependency is also negligible here, even though this is probably related to the low number of high-pseudorapidity signal jets in $ZH \to \nu\nu bb$ events. Figure 9.9c and 9.9d report the p_T and η dependency from regional tracking in E_T^{miss} triggers at the Event Filter. Since tracks are considered to be only reconstructed within Region of Interests associated to jets, this EF E_T^{miss} definition does not include any soft term. The track p_T dependency is more visible with respect to the simplified pileup jet suppression applied at the Global Trigger while the η dependency is negligible. On the other hand, Figure 9.9e and 9.9f show the p_T and η dependency of full-scan tracks at the Event Filter. Here, the dependency from p_T and η is more pronounced with respect to the regional tracking case due to the inclusion of the soft term. The

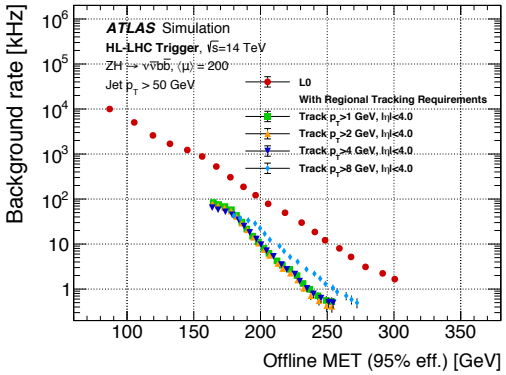

(a) Lo, track p_T dependency

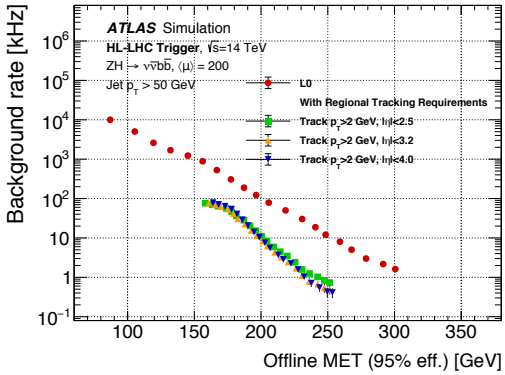

(b) Lo, track η dependency

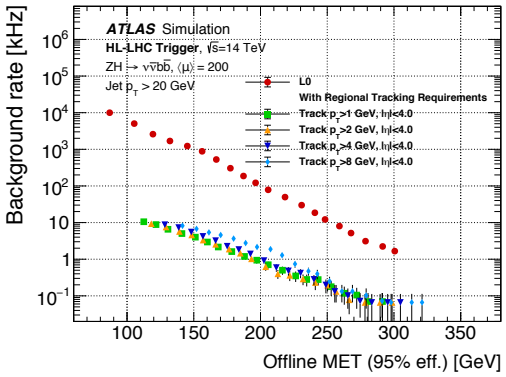

(c) EF, regional track p_T dependency

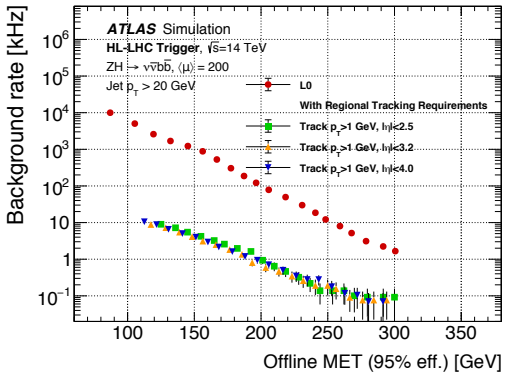

(d) EF, regional track η dependency

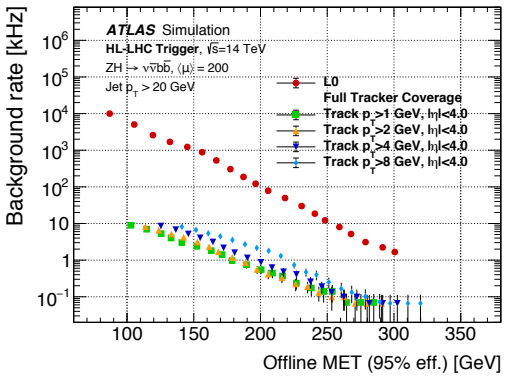

(e) EF, full-scan track p_T dependency

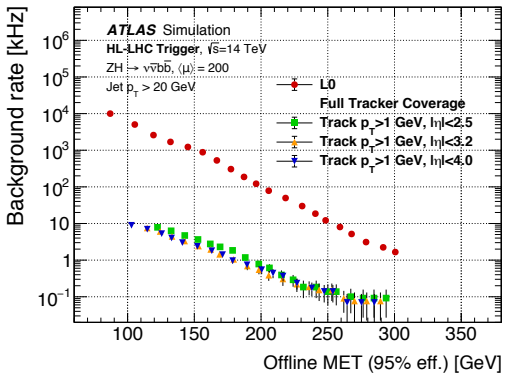

(f) EF, full-scan track η dependency

Figure 9.9 – Background rate versus offline E_T^{miss} threshold defining the 95% signal efficiency on $ZH \to \nu\nu bb$ events for different HTT tracking scenarios and requirements on the track p_T and η [3]. (a) and (b) show the impact of the simplified pileup suppression at Lo described in Section 9.3.1.1. (c) and (d) show the impact of regional tracking at the EF while (e) and (f) the full-scan tracking at the EF.

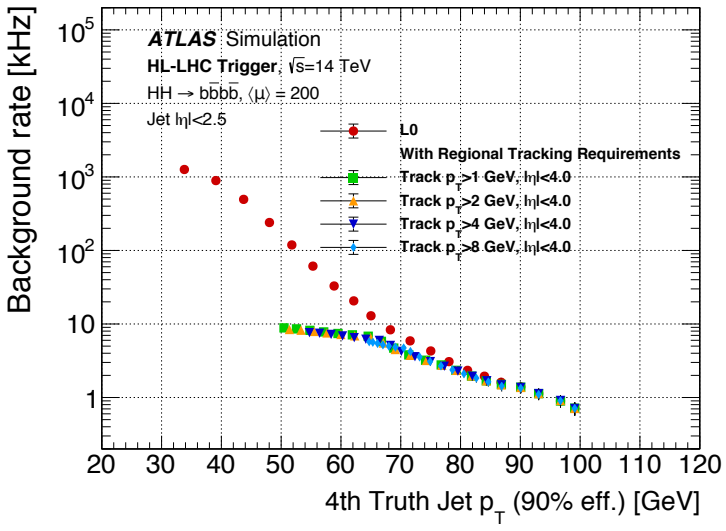

Figure 9.10 – Background rate versus offline E_T^{miss} threshold defining the 95% signal efficiency on $HH \to b\bar{b}b\bar{b}$ events for regional HTT tracking scenarios with different requirements on the online track p_T [3].

full-scan tracking curve with $p_T > 1\,GeV$ and $|\eta| < 4.0$ provides the overall best background rate curve.

Figure 9.10 shows the scan of different background trigger rates X versus T_{95} for the four-jet trigger. This selection is particularly important for the selection of $HH \to b\bar{b}b\bar{b}$ events, one of the main ATLAS physics signatures for Run 4. The track p_T dependency of the regional HTT configuration at the EF is shown. No improvement at for fourth-truth jet p_T larger than 80 GeV is shown due to the only presence of hard-scatter jets at such a high jet p_T. For lower fourth-jet p_T, tracking reduces the trigger rate up to a factor of 10 at 50 GeV. However, the track-p_T dependency stops at certain points due to the lack of tracks passing the p_T requirement for low p_T jets.

9.5 FURTHER IDEAS AND IMPROVEMENTS

For E_T^{miss} triggers, the current design of the upgraded ATLAS TDAQ system and of HTT allows to achieve trigger thresholds very close to the Run 2 values. However, this feature will not be achieved in the current baseline trigger scenario for $HH \to b\bar{b}b\bar{b}$, where the thresholds of the fourth p_T will increase from 45 GeV in Run 2 with one b-tagged jet to 65 GeV in Run 4 with two b-tagged jets [3]. This limitation is currently imposed by the Level-0 system. In future, the acceptance of these events might be further enhanced in several ways:

The following ideas might result in improved Level-0 selections for $HH \to b\bar{b}b\bar{b}$ events. Some of them are currently considered within the ATLAS TDAQ community, but none of them is included in the results presented in this work.

- Inclusion of **jet calibrations** similar to offline at the Global Trigger in order to make the turn-ons of Figure 9.5 sharper.

- Application of **more complex selections** on jet momenta and other topological quantities such as di-jet masses, jet separation and asymmetric selections on the p_T of the four leading jets.
- **Inclusion of b-tagging** in the Global Trigger. In the evolved TDAQ scenario, this could be achieved using L1 tracks for the tagging of displaced b-vertices before the Event Filter. At L0, this might be more complicated considering the lack of tracking information. In this case, pure calorimeter information might possibly be exploited for fast b-tagging estimation, even though further work will be needed for assessing the feasibility of this approach.

9.6 CONCLUSION

This chapter illustrated the impact of different HTT scenarios and requirements on the track p_T and η for the Phase-II TDAQ upgrade. A simplified algorithm for the pileup mitigation at the Global Trigger has been also shown, providing reductions of the trigger rate for E_T^{miss} and multijet triggers up to a value of 10 in the evolved trigger scenario. Impact on both $ZH \to \nu\nu bb$ and $HH \to b\bar{b}b\bar{b}$ signatures has been illustrated, demonstrating capabilities of the new trigger system to reduce significantly the rate and increase the signal purity of multijet and E_T^{miss} triggers output. These studies have been used to define the Phase-II ATLAS trigger menu and have been included in the Phase-II ATLAS TDAQ Technical Design Report (TDR) [3].

Part III

THE HUNT FOR NEW PHENOMENA IN SIGNATURES WITH LARGE JET MULTIPLICITIES

10

HUNTING NEW PHYSICS IN MULTI-JET FINAL STATES

"Newt: I am writing a book about magical creatures.

Porpentina: Like an extermination guide?

Newt: No. A guide to help people understand why we should be protecting these creatures instead of killing them."

– J.K. Rowling, *Fantastic Beasts and Where to Find Them*

Contents

One of the strongest motivations for the construction of the Large Hadron Collider is the search for new phenomena at the high-energy frontier. In this context, the LHC physics program has been extremely successful with discovery of the Higgs boson in 2012 by the ATLAS [20] and CMS [21] collaborations during the first run of the LHC. However, many questions remain open in the Standard Model and no evidence for physics Beyond the Standard Model has been found so far.

This chapter focuses on the description of a search for new physics in events with large jet multiplicities. In general, such signatures may be the result of long cascade decays of heavy particles to stable states, typically provided by SUSY and other BSM theories [87, 88, 89]. After the description of SUSY decays provided in Chapter 3, it is clear that the long decay chains of gluino pairs can produce a high number of jets in the final state and, due to the presence of the LSP and the fact that the collision energy has to be shared across many different particles, the E_T^{miss} in such signatures is generally low. Therefore, the search discussed in this chapter has a moderate E_T^{miss} selection and a different trigger strategy compared to other SUSY searches. The large jet multiplicity in such signatures has the advantage of having an extremely low background due to the low Standard Model cross-sections as, for an emission of N gluons from a certain process, the total cross-section for such process reduces approximately by a factor $(\alpha_S)^N$, where $\alpha_S = 0.145$ is strong coupling constant. This feature makes searches for new physics in high jet multiplicity signatures a good channel for a potential discovery at the LHC. However, the precise estimation of the backgrounds for such final states is extremely challenging since, using standard simulation techniques, large uncertainties on the total background prediction are estimated, resulting in a reduced sensitivity of these searches. This problem can be alleviated using data-driven background estimation techniques, where background predictions are made using large jet multiplicity data, leading to smaller uncertainties on the total background prediction.

With respect to the firs Run of the LHC, a fundamental feature of Run 2 has been the increase of the center-of-mass energy of p-p collisions from $8\,TeV$ to $13\,TeV$, making the long gluino cascade decays more accessible due to the larger available phase space with respect to Run 1. As a consequence, the Run 2 dataset has been analyzed starting from 2015 and four versions of the analysis, using an integrated luminosity of 3.2, 18.2, 36.1 and $139\,fb^{-1}$, have been performed and documented in references [90], [5], [6] and [4]. This chapter illustrates the analyses performed using 36.1 and $139\,fb^{-1}$ collected during the Run 2 of the LHC, and these largely rely on the design and results obtained in the previous Run 1 [91, 92] and Run 2 iterations.

10.1 ANALYSIS OVERVIEW

Every SUSY analysis aims at defining a specific portion of the phase space where a large amount of signal is expected to be present while the backgrounds are rejected as much as possible. Such a region, where signal is the prominent component, is defined from multiple cuts applied to different discriminating variables and it is referred to as a *Signal Region* (SR) of the analysis. In this picture, SRs represent then the main portions of the phase space where we want to compare the total number of background and data events. The compatibility between the prediction and the observation is performed through statistical tests as will be discussed in the next chapter.

In order to precisely estimate the background processes contaminating the SRs in a semi-data-driven way, *Control Regions* (CRs) are defined in order to evaluate the compatibility and adjust the prediction of the dominant backgrounds with respect to the collected data. In this context, CRs need to have a low signal contamination

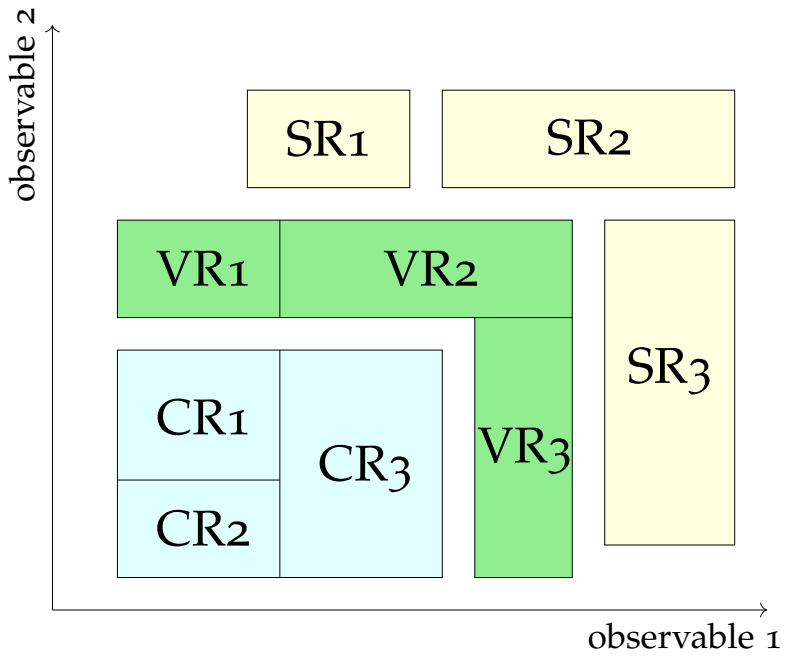

Figure 10.1 – A schematic view of a standard SUSY analysis strategy with associated Signal, Validation and Control Regions (SRs, VRs and CRs). In this schematic, discrimination between signal and background-like events is expected to be provided by different observables build for this purpose, and represented here by the two axes of the cartesian graph.

while ideally having a high purity of a specific background type. Therefore, for one specific SR, multiple CRs can be defined in order to control different background processes.

The last set of analysis regions that every SUSY search want to define is represented by the so-called *Validation Regions* (VRs). After backgrounds correction in the CRs, VRs aim at validating the background prediction with respect to data. Therefore, similarly to CRs, the signal contamination of these regions is again aimed to be as low as possible in order to not reveal the presence of new physics prior to SRs *unblinding*[20]. Due to this reason and to the aimed validation of the background estimation in SRs, VRs are typically placed between the CRs and the SRs as shown in Figure 10.1.

In the analysis discussed later in this chapter, the signal regions are defined by requiring events with at least 8, 9, 10, 11, 12 jets and no leptons (electrons and muons). Sensitivity to different signal models is provided by additional requirements on H_T, $E_T^{miss}/\sqrt{H_T}$, $S(E_T^{miss})$, $N_{b\text{-jets}}$ and M_J^{Σ}. Further details about these kinematic variables are described in Section 10.4.3. Despite the veto applied on leptons in the reconstructed events, backgrounds containing a lepton can still affect analysis signal regions (see Section 10.3.1 for further details). Therefore, leptonic decays of the top-quark, W and Z bosons contaminate the signal regions, especially at high values of E_T^{miss} due to the production of neutrinos associated to the semi-leptonic

[20] SRs are "unblinded" when their background prediction is directly compared to the experimental observation (*i.e.* the data). This step happens only when the background estimation has been fully established and assessed.

decay of the W boson. These backgrounds, referred to as *leptonic backgrounds*, are estimated using Monte Carlo simulation techniques as discussed later in this chapter. On the other hand, the majority of the background in signal regions (in particular at low E_T^{miss}) comes from real zero-lepton states, in particular pure QCD processes and full hadronic decays of top pairs and W, Z bosons. This category of background is referred to as the *multi-jet background*, which is estimated using a data-driven estimation method also known as the *template method* as it will be discussed later in Section 10.6.2.

10.2 SIGNAL MODELS

Though the search described in this chapter does not apply strict cuts on event-based observables, allowing it to be sensitive to any possible type of BSM signature at high jet multiplicity and E_T^{miss}, SUSY signal models are generally used for the interpretation of this search. Different SUSY signals have been considered in Run 2 in order to optimize the analysis selections:

1. A slice of the phenomenological MSSM (pMSSM) phase-space based on the results of the scan of the parameter space done using the Run 1 analysis [93]. This model produces a relatively large number of heavy flavour jets compared to other models.

2. A simplified model of gluino production with a two-step decay of the gluino through a chargino, neutralino-2 and then finally decaying to the LSP. We refer to this model as the *two-step gluino decay model*.

3. Another simplified model of a gluino decay that, through mediation of a top squark, decays to a top quark pair and a neutralino. Therefore, final states can contain a large number of heavy-flavour jets due to the large presence of top quarks in the final state.

4. A R-parity-violating (RPV) model in which a gluino pair decays via a stop to $t\bar{s}\bar{b}$.

All of these models have been used for optimization studies, with particular emphasis on the 2-step and pMSSM models. All models are then considered in the final interpretation and limit setting.

10.2.1 *Phenomenological MSSM slice*

The Minimal Supersymmetric Standard Model (MSSM) has over one hundred parameters describing the spectrum of sparticles and their decay. However, by applying a certain set of requirements imposed by theory choices and experimental results, these numbers of parameters can be reduced to 19 (see Table 10.1). This model is known as the *Phenomenological Minimal Supersymmetric Standard Model* (pMSSM) and it considers the following assumptions [93]:

1. R-parity is exactly conserved.

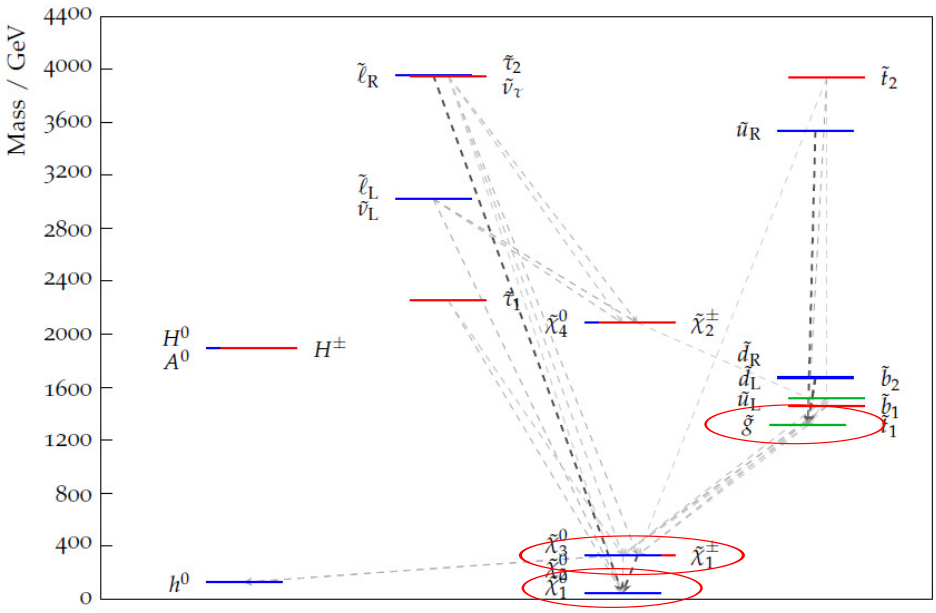

Figure 10.2 – A reference mass spectrum for a pMSSM model which is excluded by the multi-jet search and not by any other ATLAS search. Highlighted are the Bino LSP, the Higgsinos and the gluino.

2. No new sources of CP violation exists, on top of the ones already present in the CKM matrix.

3. Minimal Flavour Violation (MFV) is imposed at the electroweak scale.

4. The two first generations of squarks and sleptons with the same quantum numbers are mass degenerate and their Yukawa couplings are too small to affect sparticle production or precision observables.

5. The LSP is the lightest neutralino, *i.e.* SUSY is broken by gauge mediation.

From the results of the large pMSSM scan that was performed in Run 1 [93] a class of models was identified that were excluded only by the Run 1 version of this analysis and not by any other ATLAS SUSY analysis. This forms an interesting area of the parameter space that would be difficult to discover by other means, and is obviously of great interest for interpretation of this search. An example of the mass spectrum approached by this model is given in Figure 10.2. The gluinos are produced easily at the LHC, and decay via a long cascade to produce many light-flavour- or b-jets and a moderate amount of E_T^{miss}. The low E_T^{miss} selection in this analysis permits greater sensitivity to these sparticle decays than the harsher cuts used in analyses optimized for other parts of the SUSY phase space.

A slice of this parameter space has been formed by varying the higgsino mass parameter and the gluino mass, and fixing the LSP mass to 60 GeV. A two-dimensional projection is then defined by the physical mass of the gluino and the lightest chargino physical mass (M_3 and μ respectively). The rest of the spectrum is generally uninter-

Parameter	Note
$m_{\tilde{L}_1} (\equiv m_{\tilde{L}_2})$	Left-handed slepton (first two gens.) mass
$m_{\tilde{e}_1} (\equiv m_{\tilde{e}_2})$	Right-handed slepton (first two gens.) mass
$m_{\tilde{L}_3}$	Let-handed stau doublet mass
$m_{\tilde{e}_3}$	Right-handed stau mass
$m_{\tilde{Q}_1} (\equiv m_{\tilde{Q}_2})$	Left-handed squark (first two gens.) mass
$m_{\tilde{u}_1} (\equiv m_{\tilde{u}_2})$	Right-handed up-type squark (first two gens.) mass
$m_{\tilde{d}_1} (\equiv m_{\tilde{d}_2})$	Right-handed down-type squark (first two gens.) mass
$m_{\tilde{Q}_3}$	Let-handed squark (third gen.) doublet mass
$m_{\tilde{u}_3}$	Right-handed top squark mass
$m_{\tilde{d}_3}$	Right-handed bottom squark mass
M_1	Bino mass parameter
M_2	Wino mass parameter
M_3	Gluino mass parameter
μ	Bilinear Higgs mass parameter
A_t	Trilinear top coupling
A_b	Trilinear bottom coupling
A_τ	Trilinear τ lepton coupling
M_A	Pseudoscalar Higgs boson mass
$\tan\beta$	Ratio of the Higgs vacuum expectation values

Table 10.1 – Description of the 19 parameters of the Phenomenological Minimal Supersymmetric Standard Model (pMSSM) [93]. In the table, gen(s). refers to generation(s).

esting for collider searches, hence most of the other superpartners are decoupled by choosing the following parameters:

$$\begin{aligned} M_A = M_2 &= 3\,\mathrm{TeV}, \\ \tan\beta &= 10, \\ A_t = A_b = A_\tau &= 0, \\ m_{(\tilde{L}_1,\tilde{L}_2,\tilde{L}_3)} = m_{(\tilde{e}_1,\tilde{e}_2,\tilde{e}_3)} &= 5\,\mathrm{TeV}, \\ m_{(\tilde{Q}_1,\tilde{Q}_2,\tilde{Q}_3)} = m_{(\tilde{u}_1,\tilde{u}_2,\tilde{u}_3)} = m_{(\tilde{d}_1,\tilde{d}_2,\tilde{d}_3)} &= 5\,\mathrm{TeV}. \end{aligned} \tag{10.1}$$

It should also be noted that in this particular plane the Higgs branching ratio to the lightest supersymmetric particle is very low, such that the limits on the invisible width of the Higgs are respected.

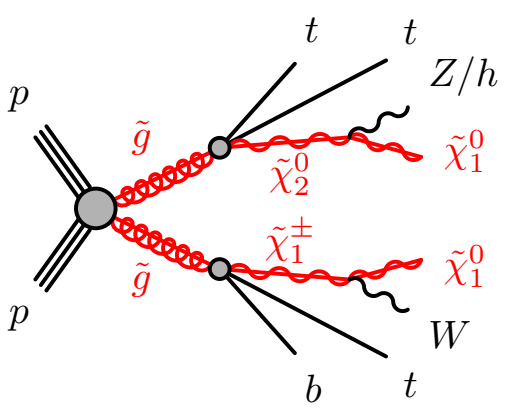

(a) pMSSM feynman diagram

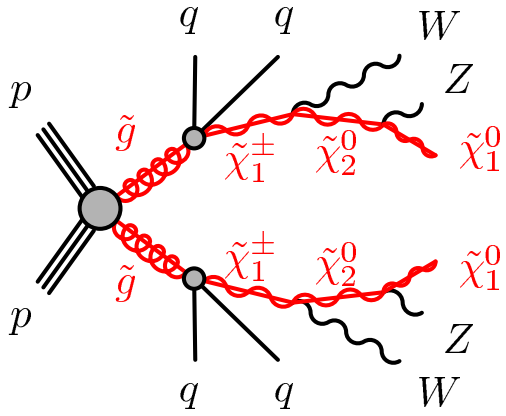

(b) Two-step model feynman diagram

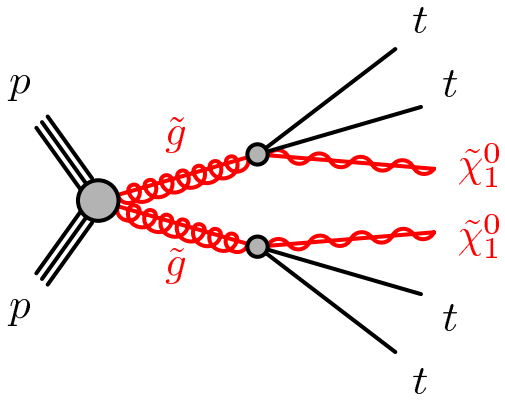

(c) Gtt feynman diagram

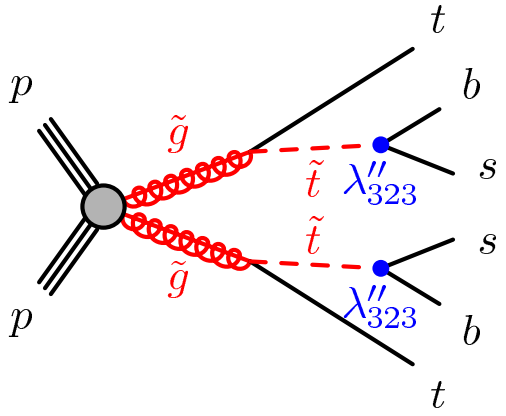

(d) RPV model feynman diagram

Figure 10.3 – Feynman diagrams of the two-step, pMSSM, Gtt and RPV signal models.

For a mass point of $(m(\tilde{g}), m(\tilde{\chi}_1^\pm)) = (1200, 200)\,GeV$, the branching ratios of the decay chain in these models are:

$\tilde{g} \to t + b + \tilde{\chi}_1^\pm$	(44%)	$\tilde{\chi}_1^\pm \to W + \tilde{\chi}_1^0$	(100%)
$\tilde{g} \to t\bar{t} + \tilde{\chi}_{2,3}^0$	(39%)		
$\tilde{g} \to t\bar{t} + \tilde{\chi}_1^0$	(2%)	$\tilde{\chi}_{2,3}^0 \to Z + \tilde{\chi}_1^0$	(70%)
$\tilde{g} \to b\bar{b} + \tilde{\chi}_1^0$	(1%)	$\tilde{\chi}_{2,3}^0 \to h + \tilde{\chi}_1^0$	(30%)
$\tilde{g} \to q\bar{q} + \tilde{\chi}_1^0$	(9%)		

which results in a large amount of jets and soft E_T^{miss}. The Feynman diagram corresponding to the dominant decay is provided in Figure 10.3a.

10.2.2 *Two-step gluino decay model*

To allow direct comparison to different analyses, the "two-step" gluino decay is considered. This model consists of a simplified SUSY model with the production of

a gluino pair decaying to the LSP through a two step decay chain resulting in large jet multiplicity final states. The decay chain can be summarized as

$$\begin{aligned} pp &\to \widetilde{g}\widetilde{g}, \\ \widetilde{g} &\to qq\,\widetilde{\chi}_1^{\pm}, \\ \widetilde{\chi}_1^{\pm} &\to W^{\pm}\,\widetilde{\chi}_2^0, \\ \widetilde{\chi}_2^0 &\to Z\,\widetilde{\chi}_1^0. \end{aligned} \tag{10.2}$$

The parameters of the models are the mass of the gluino $m_{\widetilde{g}}$ and the mass of the neutralino $m_{\widetilde{\chi}_1^0}$. In this simplified model, both steps are considered to happen with 100% probability and other sparticle decays are assumed to not be kinematically accessible. The mass of the chargino is set to $m_{\widetilde{\chi}_1^{\pm}} = \frac{1}{2}(m_{\widetilde{g}} + m_{\widetilde{\chi}_1^0})$, while the mass of the second neutralino is set to $m_{\widetilde{\chi}_2^0} = \frac{1}{2}(m_{\widetilde{\chi}_1^{\pm}} + m_{\widetilde{\chi}_2^0})$. It is possible to note that the number of b-jets of this model is expected to be lower due to the lack of tops in the final state. The Feynman diagram for this simplified model is shown in Figure 10.3b.

10.2.3 *The 'Gtt' model*

This simplified model is characterized by the pair-production of gluinos followed by a 100% branching ratio decay to two top pairs and a neutralino

$$\widetilde{g} \to t\bar{t} + \widetilde{\chi}_1^0. \tag{10.3}$$

In this decay, the gluino decays through a virtual stop particle having a mass of 5 TeV. The parameters of this model are the gluino mass $m_{\widetilde{g}}$ and the neutralino mass $m_{\widetilde{\chi}_1^0}$. In this model, the stop could still be undiscovered at the LHC due to its large mass while the gluino could be accessible by analysis looking at high jet multiplicities and b-flavoured jets. A Feynman diagram for the off-shell model is shown in Figure 10.3c.

10.2.4 *The 'RPV' model*

Supersymmetric models in which R-parity is violated typically give rise to final states with low missing transverse momentum, as described in Chapter 3. Among the inclusive strong-supersymmetry searches considered in ATLAS, the multi-jet analysis accepts final states with sufficiently low missing transverse momentum to be sensitive to these R-parity-violating (RPV) scenarios as shown in Figure 10.4a and 10.4b.

This model assumes production of a gluino pair decaying through $\widetilde{g} \to \widetilde{t} + t$. An R-parity- and baryon-number-violating stop decay is considered for the last step of the decay chain

$$\widetilde{t} \to \bar{s} + \bar{b}, \tag{10.4}$$

implying low values of E_T^{miss} and higher jet multiplicities in the signal final state. Figure 10.3d shows the Feynman diagram of this model, parametrized by the values $m_{\widetilde{g}}$ and $m_{\widetilde{t}}$.

A discussion of how this analysis contributes sensitivity to other RPV models can be found in Section 11.5.

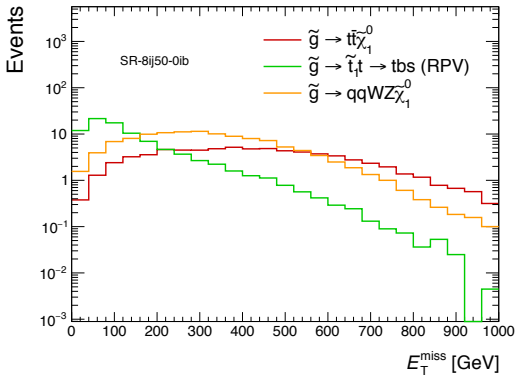

(a) E_T^{miss} distribution

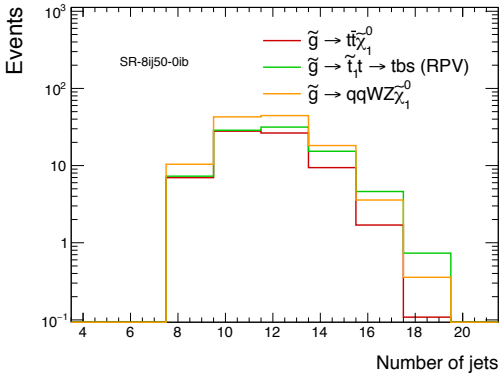

(b) N_{jets} distribution

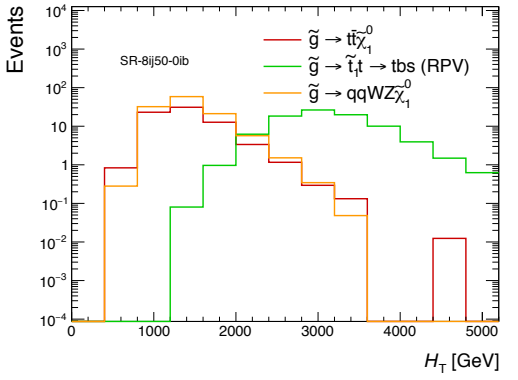

(c) H_T distribution

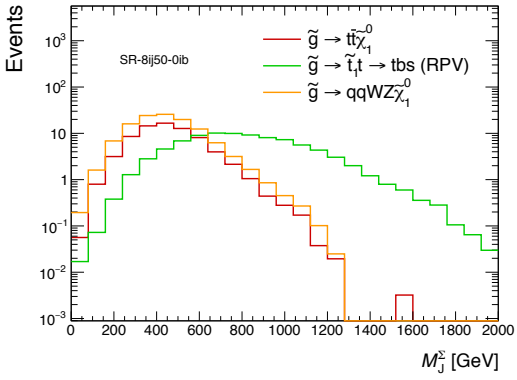

(d) M_J^{Σ} distribution

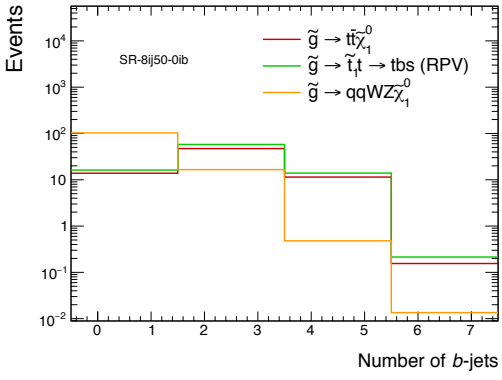

(e) $N_{b\text{-jets}}$ distribution

Figure 10.4 – Distribution of different SUSY signals with $L^{int} = 139\,fb^{-1}$ considered by the multi-jet analysis. All signals models consider $m_{\tilde{g}} = 1.8\,TeV$ and $m_{\tilde{\chi}_1^0} = 1.0\,TeV$ for the R-parity conserving models.

10.3 BACKGROUNDS

In order to increase as much as possible the sensitivity to new physics, it is fundamental to estimate and understand the contamination of the SRs due to Standard Model processes in the best possible way. We refer to this contamination as the *background* of the analysis.

As quickly discussed in the analysis overview (Section 10.1), Standard Model processes can affect events with high jet multiplicity and moderate E_T^{miss} mainly in two ways:

- Through *Leptonic backgrounds* escaping the lepton veto (*i.e.* electrons and muons) applied in the SRs of the analysis. Due to the presence of leptonically-decaying W and Z processes, these backgrounds are generally the dominant ones at high E_T^{miss} values.
- Through the *Multi-jet background*, associated to the full hadronic component of the backgrounds. This background dominates at low and intermediate E_T^{miss} due to the lack of neutrinos in their final state.

The next sections will describe in detail the components of such backgrounds.

10.3.1 *Leptonic backgrounds*

Leptonic backgrounds are caused by leptonically-decaying W and Z bosons events which can not be removed by the lepton veto applied to the signal regions of the analysis. These processes are generally characterized by significant E_T^{miss} due to presence of neutrinos in the final state. There are several causes for leptonic events passing the lepton veto:

1. Since only electrons and muons are treated as *leptons* in this analysis, hadronically-decaying τ leptons can largely affect the backgrounds of the signal regions since these are reconstructed as jets[21]. The contamination from τ leptons is mostly caused by top-pair, W and Z decays.
2. Presence of $Z \to \nu\bar{\nu}$ processes, alone or in association with other hadronically-decaying top-pairs or W, Z bosons, causing large values of E_T^{miss} and the presence of zero leptons in the reconstructed final state.
3. Electrons and muons mis-reconstructed due to a low detector signal or mis-identified as jets.
4. Electron and muons falling out of the detector acceptance.

Two processes dominate leptonic background contributions: leptonic decays of $t\bar{t}$ + jets and W + jets. Despite the large uncertainties on these processes at high jet multiplicity, the contributions from these backgrounds are estimated using Monte-Carlo simulations which are then improved by a global fit to data in dedicated Control Region (see Section 10.4.5).

[21] Tau leptons are the only leptons being able to decay to hadronic final states due to their mass being sufficiently large to allow decays to multiple pions.

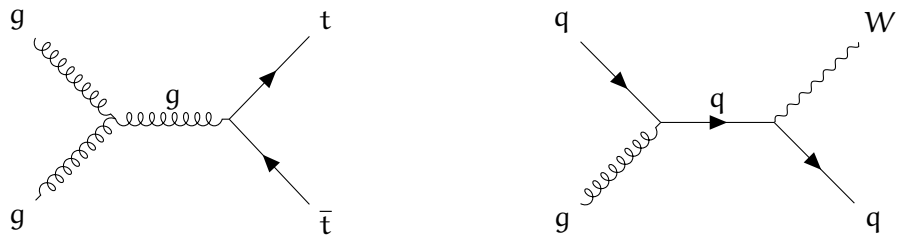

(a) $t\bar{t}$ + jets (b) W + jets

Figure 10.5 – Dominant Feynman diagrams for $t\bar{t}$ + jets and W + jets processes.

In p-p collisions, the processes generating $t\bar{t}$ events are mainly gg interactions due to the large fraction of gluons present in protons. The dominant Feynman diagram of such process is provided in Figure 10.5a. Once top-pairs are produced, due to the diagonal terms of the CKM matrix, we know that the t quark decays 96% of the times to a bottom quark and a W boson [11]. Therefore, the decay of $t\bar{t}$ can be distinguished into three cases:

- *Fully-hadronic*:
$$t\bar{t} \to b\bar{b}W^+W^- \to b\bar{b}q\bar{q}q\bar{q},$$
corresponding ideally to a six jets signature (two b-jets) without real E_T^{miss}.

- *Semi-leptonic*:
$$t\bar{t} \to b\bar{b}W^+W^- \to b\bar{b}q\bar{q}l\nu,$$
corresponding ideally to a signature with four jets (two b-jets), one lepton (positively or negatively charged) and real E_T^{miss}.

- *Di-leptonic*:
$$t\bar{t} \to b\bar{b}W^+W^- \to b\bar{b}l^-\nu l^+\bar{\nu},$$
corresponding to a signature with two b-jets, two opposite-sign leptons and real E_T^{miss}.

Although additional jets can be included in these signatures by Initial and Final State Radiation (ISR and FSR), due to the large jet multiplicity of the analysis, only the first two categories contribute significantly to the total background of this search. However, fully-hadronic modes are generally characterized by lower E_T^{miss} due to the lack of neutrinos in the final states and they are treated together with the Multi-jet background described later in Section 10.3.2. Therefore, the core of the leptonic $t\bar{t}$ + jets background is represented by semi-leptonic $t\bar{t}$ events.

Using a similar argument to the one used for top-pair production, it is easy to understand that the production of W-bosons at the LHC is dominated by the Feynman diagram shown on 10.5b. Clearly, ISR and FSR are needed in order to achieve a jet multiplicity affecting the analysis signal regions, meaning that the W + jets background will be smaller than $t\bar{t}$ + jets due to the larger number of radiations needed for this background. Section 10.6.1 provides further details about the estimation of the $t\bar{t}$ + jets and W + jets backgrounds using Monte-Carlo simulations.

Other leptonic backgrounds include: leptonically-decaying Z bosons (*i.e.* $Z+\text{jets}$), single top production, diboson production (WW, WZ or ZZ) and the production of $t\bar{t}$ events in association with additional heavy particles, including three-top, four-top, $t\bar{t}$ +W, $t\bar{t}$ +Z and $t\bar{t}$ +WW, also referred to as "$t\bar{t}+X$". These backgrounds contaminates less the analysis final states due to the large number of final state particles and low cross-section of electroweak processes.

10.3.2 *Multi-jet background*

The *multi-jet* background identifies all the fully-hadronic Standard Model processes entering in the signal regions of the analysis. In this context, pure QCD processes represent the dominant contribution to this background even though the fully-hadronic $t\bar{t}+\text{jets}$ production, previously described in Section 10.3.1, represents a non-negligible fraction of this background. Other contributions come from fully-hadronic decays of $W+\text{jets}$, $Z+\text{jets}$, diboson and $t\bar{t}+X$ processes.

Due to the low requirement on $\mathcal{S}(E_T^{miss})$, this background represents the dominant background of our SRs. However, its estimation can not be performed using MC simulations due to the difficulty to simulate QCD at such a high jet multiplicity. Therefore, a data-driven "ABCD" method based on the invariance of the $\mathcal{S}(E_T^{miss})$ distribution from the number of jets in the final state N_{jets} has been used for this scope. In the context of this analysis, this method is also known as the *template method*. More details about this technique are provided later in Section 10.6.2.

10.4 ANALYSIS DEFINITION

The results showed in the next chapters where made using the collisions recorder from the LHC Run 2 started in June 2015 and ended in October 2018. Due to the constantly changing conditions of the LHC– mainly due to the better handling of the accelerator operations over time – the triggers used for this analysis changed significantly between 2015 and 2018. Additionally, more sophisticated reconstruction techniques were developed by the ATLAS Collaboration, producing relevant changes in the analysis object definition between the beginning and end of Run 2. This section describes the triggers, event selection and object reconstruction quantities employed for this analysis during the Run 2 of the LHC.

10.4.1 *Triggers*

Triggers are responsible for the selection of the interesting events created by the p-p collisions of the LHC (see Section 4.2.5 for more details). As specified in the introduction of this chapter, the long decay chains provided by the models targeted by this analysis implies lower E_T^{miss} compared to other SUSY searches. In this context, the utilization of a E_T^{miss} trigger could sensibly reduce the reach of the analysis and for this reason multi-jet trigger chains have been employed for the collection of the multi-jet data.

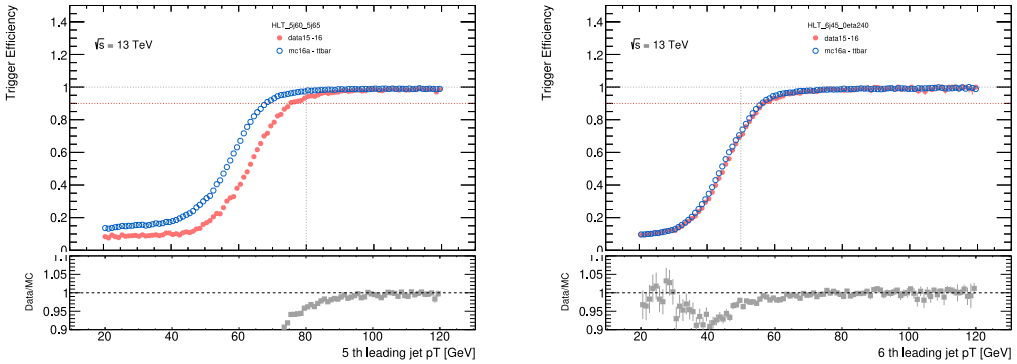

(a) 2015-2016: 5j60||5j65

(b) 2015-2016: 6j45

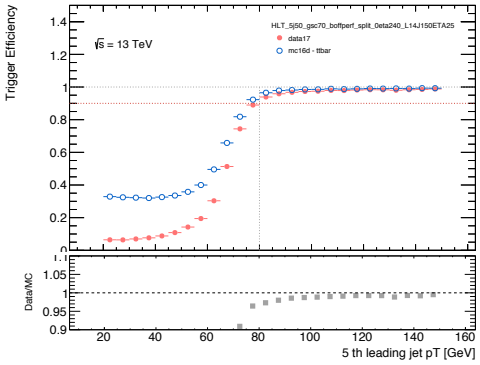

(c) 2017: 5j50_gsc70

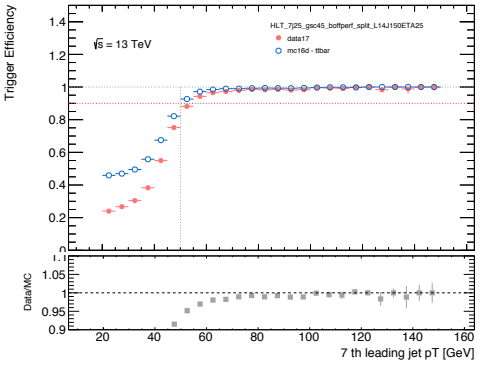

(d) 2017: 7j25_gsc45

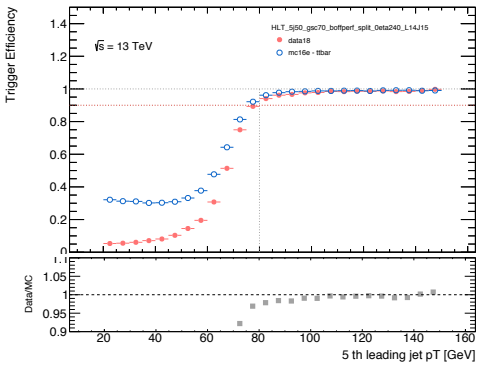

(e) 2018: 5j50_gsc70

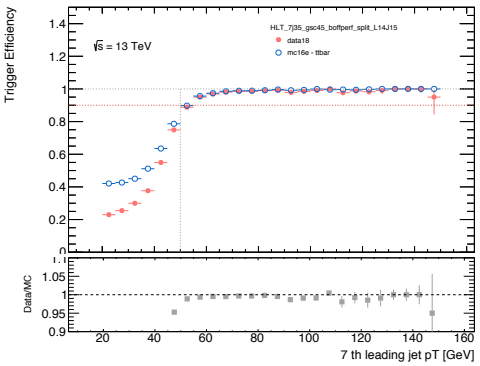

(f) 2018: 7j35_gsc45

Figure 10.6 – Efficiency turn-on curves, on data and MC, of the fifth, sixt and seventh jet and unprescaled triggers used for the data taking of the analysis. The x-axis represents the transverse momentum of the offline jet on which the selection is applied. The offline jets have been reconstructed using the Particle Flow algorithm.

In multi-jet triggers the first level of the trigger selection is provided by hardware triggers, which reconstruct jets with a sliding window algorithm with size 0.8×0.8 in the η-ϕ space. At this stage, events are required to contain four jets with $p_T > 15\,GeV$ at the EM scale (`L1_4J15`) and, in some cases, a further restriction to $|\eta| < 2.5$ is applied (`L1_4J150ETA25`).

Events selected by the first level trigger enter the High-Level Trigger (HLT), which implements a more refined software-based jet reconstruction and selection. In the HLT, the jet selection is made on jets reconstructed from calorimeter topo-clusters of energy measured in the calorimeter cells, and calibrated in a similar fashion to the offline jets described in Section 5.2. Due to the increasing luminosity delivered by the LHC and due to the improved jet reconstruction methods in the HLT, the trigger definitions have evolved significantly during the LHC Run 2. As a result of this feature, different triggers have been combined to select events for this analysis. The selection requirements and the corresponding data periods for each trigger are given in Table 10.2, while integrated luminosities of prescaled triggers[22] are provided in Table 10.3.

Trigger efficiency curves for the main unprescaled triggers are shown in Figure 10.6 for Particle Flow jets reconstructed offline in both data and MC simulations. The bootstrapping sample[23] for these curves was made using the single lepton triggers providing a clear reference dataset for these studies. These efficiency curves are in general not perfect Heaviside step functions due to the differences between the online and offline jet reconstruction. The impact of the updated online jet calibration techniques in 2017 is well visible by comparing the efficiency turn-ons of Figure 10.6b and 10.6d for the `6j45` and `7j45` selections, where the selection efficiency increased from 70% to 90% at the offline jet p_T threshold of 50 GeV. This motivated the usage of multiple multi-jet triggers for the analysis of the complete Run 2 dataset. The discrepancies observed between at low p_T (*i.e.* $20\,GeV - 50\,GeV$) in Figure 10.6, are attributed to mis-modeling of the trigger simulation in MC samples. However, these discrepancies do not affect the background modeling of the analysis since, as described later in Section 10.4.5, offline jet p_T thresholds are applied at 50 and 80 GeV jet p_T for the offline selection of events composing the analysis regions.

The p_T threshold applied on the online jet defining the trigger selection is provided by the output rate of the HLT. Generally, high jet multiplicity triggers can access a p_T threshold lower compared to single or double jet triggers, simply due to the lower cross-section of multi-jet production. This is the main reason why between the fifth, sixt and seventh jet triggers the requirement on the jet p_T decreases.

Once Particle Flow jets became available offline during Run 2, it was clear that the larger differences with respect to the online topocluster-based jet reconstruction would have led to slightly worse turn-on in the trigger efficiency curves with respect to offline topocluster-based jets. This effect is due to the larger differences between

[22] Note that some of the sixt jet triggers became prescaled starting from 2017 due to the large trigger rates.

[23] When calculating trigger efficiencies for a selection A on data, a bootstrapping sample is formed by a selection B being uncorrelated and inclusive for A (*i.e.* $A \subset B$) such that the efficiency of A becomes

$$\epsilon(A) = \epsilon(A|B)\epsilon(B).$$

Trigger item	Jet selection	Jet calibration	Prescale	Data period
5j60	$p_T > 70$ GeV	MC JES	1	2015
5j65_0eta240_L14J15	$p_T > 65$ GeV, $\eta < 2.4$	MC JES	1	2016
5j50_gsc70_0eta240_L14J150ETA25	$p_T > 70$ GeV, $\eta < 2.4$	Track GSC	1	2017
5j50_gsc75_0eta240_L14J150ETA25	$p_T > 75$ GeV, $\eta < 2.4$	Track GSC	1	Run 325789
5j50_gsc70_0eta240_L14J15	$p_T > 70$ GeV, $\eta < 2.4$	Track GSC	1	2018
6j45_0eta240	$p_T > 45$ GeV, $\eta < 2.4$	MC JES	1	2015-2016
7j25_gsc45_L14J150ETA25	$p_T > 45$ GeV	Track GSC	1	2017
7j35_gsc45_L14J15	$p_T > 45$GeV GeV	Track GSC	1	2018
6j45_0eta240	$p_T > 45$ GeV, $\eta < 2.4$	Calo GSC	1 Hz (1.2e33)	2017
6j25_gsc45_0eta240_L14J150ETA25	$p_T > 45$ GeV, $\eta < 2.4$	Track GSC	15 Hz	2017
6j35_gsc45_0eta240_L14J150ETA25	$p_T > 45$ GeV, $\eta < 2.4$	Track GSC	10 Hz	2018

Table 10.2 – Triggers used to collect data for the analysis between 2015 and 2018, stating their prescale and the calibration methods used. If not explicitly stated, the hardware selection was made with L1_4J15. *MC JES* indicates that the trigger was calibrated with only a global scale factor to restore the mean response vs particle-level jets. *Calo GSC* implies that the GSC steps based on fractions of energy in different calorimeters were applied, but not the track-based step. *Track GSC* implies that the full calibration chain including the track-based GSC step was applied, in which case the first trigger threshold specified indicates the preselection cuts applied before calibration with tracks. A single number under the prescale column indicates a flat prescale (*i.e.* no prescale) whereas a value in Hz implies a varying prescale to match the stated target rate (at the stated luminosity).

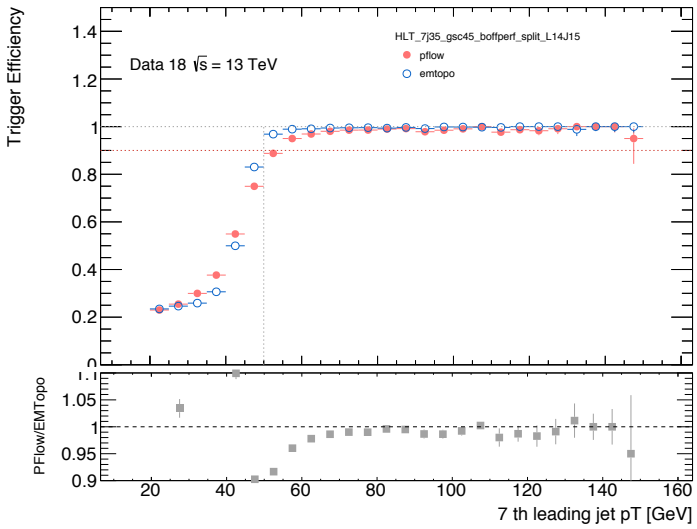

Figure 10.7 – Efficiency curves of the seventh leading jet trigger vs. offline topocluster (blue circles) and Particle Flow (red dots) seventh-leading jet p_T in 2018 data. The `HLT_7j35_gsc45_split_L14J15` string describes the online trigger selection, corresponding to an HLT selection of least 7 jets with p_T greater than 45 GeV after GSC calibration and a L1 selection of at least 4 jets having $p_T \geqslant 45$ GeV. The inefficiency of the Particle Flow approach is the direct consequence of the larger differences between the offline Particle Flow-reconstructed jets and the online jets based on topocluster reconstruction.

Trigger item	Lumi-weighted prescale	Integrated luminosity (fb^{-1})	Data period
`6j45_0eta240`	6.051	7.324	2017
`6j25_gsc45_0eta240_L14J150ETA25`	7.009	6.322	2017
`6j35_gsc45_0eta240_L14J150ETA25`	17.114	3.415	2018

Table 10.3 – Details about luminosity of prescaled multi-jet triggers.

the online and offline jet reconstructions when Particle Flow is considered offline as only topocluster-based jets were built in the HLT during Run 2. This is well illustrated in Figure 10.7 where the efficiency provided with respect to offline Particle Flow jets reaches the plateau later if compared to offline topoclusters jets ($\sim$ 50 GeV for topocluster-based jets and $\sim$ 60 GeV for Particle Flow jets). In order to make certain that the MC simulation completely takes into account these efficiency effects, two requirements have been applied on both data and MC simulations:

1. We select the analysis events based on different offline jet p_T values - namely $p_T > 50$ GeV for 6, 7 jet triggers and $p_T > 80$ GeV for 5 jet triggers - in order to achieve at least 80-90% of trigger selection efficiency.

2. The trigger selection is applied on both data and MC simulation, showing always less than 5% disagreement with respect to the data above the relevant offline jet p_T selection (see Figure 10.6).

10.4.2 *Physics object definition*

The physics objects of ATLAS are designed to be reconstructed as closely as possible to the particles characterizing the signal events. For this analysis, the latest recommendations provided by the different ATLAS combined performance (CP) groups have been used, ensuring the best available calibration and identification of the final state objects.

The information stored in the EM calorimeter is used for the reconstruction of both electron and jet candidates (these include also hadronic calorimeter information). Because of this feature, jets corresponding to a single high-energy electron could be formed, resulting in an energy double counting for the jet multiplicity and E_T^{miss} reconstruction. Due to this feature, a set of *baseline* objects are defined on which the *Overlap Removal* procedure is applied to solve these ambiguities. This procedure will be also described in this section.

The ATLAS object reconstruction has been reviewed in Chapter 5. This section provides a more specific description of the physics objects requirements used in this analysis:

JETS

Jets are reconstructed using the anti-k_t jet algorithm with radius parameter $R = 0.4$ on Particle Flow objects (see Section 7.2.1 for more details). Calibrations include the *MC-based Jet Energy Scale* (JES) correction and the *Global Sequential Calibration* (GSC) described in Section 5.2.3.

Jets are classified as *baseline* jets if they satisfy $p_T > 20\,GeV$, $|\eta| < 2.8$. Baseline jets are then considered as *signal* jets if they pass the overlap removal procedure described below and the Jet Vertex Tagger (JVT) selection:

$$JVT > 0.2 \quad \text{or} \quad |\eta| > 2.4 \quad \text{or} \quad p_T > 120\,GeV. \tag{10.5}$$

Further details about JVT are provided in Section 5.2.4. Scale factors are also applied to jets in order to correct the discrepancies between MC-simulated and data events.

B-JETS

Baseline anti-k_t $R = 0.4$ jets are tagged as b-jets if they pass the 70% efficiency working point of the `MV2c10` algorithm, provided they also satisfy $p_T > 20\,GeV$, $|\eta| < 2.5$ and pass the JVT selection listed in Equation (10.5).

Scale factors are applied to correct the discrepancies between the efficiencies for selecting simulated b-jets from those assessed in data [94].

ELECTRONS

Electrons are classified as baseline if they satisfy $p_T > 10\,GeV$ and $|\eta_{clus}| < 2.47$, and pass *Loose* quality criteria (further details in Chapter 5 and [68]). Baseline electrons are classified as signal if, they pass the *Tight* quality criteria and the *Gradient* isolation working point [68], as well as impact parameter requirements $|z_0 \sin\theta| < 0.5\,mm$ and $d_0/\sigma(d_0) < 5$, and finally also have $p_T > 20\,GeV$.

Correction scale factors derived from data are applied to simulated electrons to improve modeling of reconstruction and identification efficiencies.

MUONS

Muons are classified as baseline if they satisfy $p_T > 10\,GeV$, $|\eta| < 2.7$, pass overlap removal and the *Medium* quality criteria [69]. They are classified as signal if they also pass the "FCLoose" isolation working point, as well as impact parameter requirements $|z_0 \sin\theta| < 0.5mm$ and $d_0/\sigma(d_0) < 3$, and finally also have $p_T > 20\,GeV$.

Correction scale factors derived from data are applied to simulated muons to improve modeling of reconstruction and identification efficiencies.

LARGE-RADIUS JETS

Reclustered jets [95, 96] with radius parameter $R = 1.0$ are produced by a second iteration of the anti-k_t algorithm, where the calibrated $R = 0.4$ Particle Flow jets that have passed overlap removal are the input to the clustering algorithm. Signal jets must also have $p_T > 20\,GeV$ and $|\eta| < 2.0$ to be used for reclustering. Only reclustered jets with $p_T > 100\,GeV$, $|\eta| < 1.5$ are subsequently considered for the purposes of analysis selection.

E_T^{miss}

The Missing Transverse Momentum E_T^{miss} is rebuilt from the various detector objects as illustrated in Chapter 6. This quantity uses fully calibrated primary objects (e, photons, μ, jets) that pass an overlap removal - based on shared energy rather than an analysis overlap removal criteria - as well as residual soft terms comprised purely of tracks associated with the primary vertex.

OVERLAP REMOVAL

Overlap removal is performed using the *baseline* objects defined above. Between baseline leptons and jets, the following requirements are applied sequentially:

- If an electron and muon share and ID track, the electron is removed.
- If a photon is within $\Delta R < 0.4$ of an electron or a muon, the photon is removed.
- If a jet and an electron are within $\Delta R < 0.2$ the jet is removed.
- If an electron and a jet are within $0.2 < \Delta R < 0.4$, the electron is removed.
- If a muon track is associated to a jet, or a jet and a muon are within $\Delta R < 0.2$, then the jet is removed if number of tracks in the jet n_{trk} is lower than 3.
- If a muon and jet are within $0.2 < \Delta R < 0.4$, the muon is removed.

10.4.3 *Kinematic variable definitions*

The kinematic variables described in this section are defined purely from signal objects and they represent key observables for the analysis.

TOTAL EVENT TRANSVERSE MOMENTUM: H_T

This quantity is defined as the scalar sum of the signal jets having $p_T > 40\,GeV$ and $|\eta| < 2.8$

$$H_T = \sum p_T^{jet}. \tag{10.6}$$

If leptons are identified in the event final state, these are also included to this sum if they satisfy the same kinematic requirements of jets. The p_T cut was optimized in Run 1 as part of the studies for improving the data-driven background estimation of the multi-jet background [92].

OBJECT-BASED E_T^{miss} SIGNIFICANCE: $\mathcal{S}(E_T^{miss})$

As illustrated in Section 6.6, the E_T^{miss} significance $\mathcal{S}(E_T^{miss})$ quantifies the hypothesis that a certain E_T^{miss} measurement is consistent with a zero value (null hypothesis) against the hypothesis that the true E_T^{miss} value p_T^{inv} is different from zero. A large value of this quantity indicates that the E_T^{miss} has genuinely been created by non-interacting particles. Assuming that pure Gaussian resolutions affect the resolution of each object, $\mathcal{S}(E_T^{miss})$ can be assumed to be

$$\mathcal{S}(E_T^{miss}) = \frac{E_T^{miss}}{\sigma\left(E_T^{miss}\right)} \tag{10.7}$$

When object resolutions are considered separately for the calculation of $\sigma\left(E_T^{miss}\right)$, an object-based E_T^{miss} significance is built. We will refer to this quantity with the symbol $\mathcal{S}(E_T^{miss})$ in the next part of this chapter.

By definition, the E_T^{miss} significance is expected to be independent of the number of jets in the event N_{jets} when it originates from pure fluctuations due to detector mismeasurement (*i.e.* no invisible particles). This feature represents a key feature of the data-driven background estimation of the multi-jet background and it will be illustrated later in Section 10.6.2.

EVENT-BASED E_T^{miss} SIGNIFICANCE: $E_T^{miss}/\sqrt{H_T}$

We have already illustrated in Equation (10.7) the meaning of the E_T^{miss} significance and its object-based estimation. However, it is possible to approximate this quantity assuming that only stochastic fluctuations of the jet energy affect the jet energy resolution as

$$\sigma(\text{jet}) \propto \sqrt{p_T^{jet}}. \tag{10.8}$$

Therefore, in signatures with only jets, $\sigma\left(E_T^{miss}\right)$ can be estimated as

$$\sigma\left(E_T^{miss}\right) = \sqrt{\sum_{jets} \sigma^2\left(p_T\right)} \propto \sqrt{\sum_{jets} p_T^{jet}} = \sqrt{H_T}, \tag{10.9}$$

and so E_T^{miss} significance becomes

$$\mathcal{S}(E_T^{miss}) \approx \frac{E_T^{miss}}{\sqrt{H_T}}. \tag{10.10}$$

We generally refer to this quantity as the *event-based* E_T^{miss} *significance*, and it represents the main E_T^{miss} significance observable used in this analysis until the $36\,fb^{-1}$ paper [6]. The development of the object-based E_T^{miss} significance approach [71] made this variable outdated and it was replaced by $\mathcal{S}(E_T^{miss})$ due to the complete estimation of the jet resolutions leading to better sensitivity to signal events.

TOTAL LARGE-R JET MASS: M_J^{Σ}

Heavy particles produced in the p-p collisions of the LHC and decaying to light states lead to signatures with large momenta of final state particles. These signatures are generally referred to as the *large mass-splitting* (or simply *boosted*) *scenarios* of a certain signal model due to the large difference in the mass parameters of th model and the large momentum characterizing these final state physics objects. In this context, M_J^{Σ} represents an ideal event-level observable for the identification of these scenarios. This quantity is defined as the total mass of the reclustered large-radius jets ($R = 1.0$)

$$M_J^{\Sigma} = \sum_j m_j^{R=1.0}, \tag{10.11}$$

and it ideally represents the total mass of the heavy particles produced in the collision. Within this definition, large-radius jets are required to satisfy $p_T > 100\,\text{GeV}$ and $|\eta| < 1.5$.

TRANSVERSE MASS: m_T

The *transverse mass* m_T is defined as the mass induced in the transverse plane by a resonance decaying to two objects. For a semi-invisible decay (*e.g.* the W-boson decay), this quantity can be defined from the lepton transverse momentum p_T^{ℓ}, the E_T^{miss} and the angle $\Delta\phi_{\ell,E_T^{\text{miss}}}$ between p_T^{ℓ} and E_T^{miss} as

$$m_T = \sqrt{2 p_T^{\ell} E_T^{\text{miss}} \left(1 - \cos\Delta\phi_{\ell,E_T^{\text{miss}}}\right)}. \tag{10.12}$$

Due to the lepton veto applied in the SRs of the analysis, this quantity is only used for the selection of leptonic CR events as discussed later in Section 10.4.5.

Figure 10.4 shows several of these kinematic variables for different simulated SUSY signals.

10.4.4 *Event cleaning*

In order to avoid noise in the data possibly leading to discrepancies with respect to the background prediction, certain event quality preselections have been applied. These can be summarized as follow:

GOOD RUN LIST

Every time ATLAS starts to collect data from p-p collisions, a new Run of the experiment is started. Each Run is labeled with an integer number and it ideally represents a complete cycle of LHC p-p collisions. However, due to possible issues in the ATLAS sub-detectors or in the data taking mechanism, a list of good quality runs and lumi blocks is centrally defined by the experiment and called *Good Run List*. All data analyses are required to use data events collected only inside good Runs of the ATLAS data taking.

PRIMARY VERTEX

All events are required to have at least one primary vertex with at least 2 associated tracks. The events not passing this requirement are vetoed.

ELECTROMAGNETIC ENDCAP CALORIMETER CLEANING

In 2015 and 2016, electronic noise affected the readout of the Electromagnetic EndCap Calorimeter (EMEC) inner wheel leading to a large rate of fake jets inside certain events [2]. These events can significantly affect the events of the analysis due to the large number of jets possibly created by these noise fluctuations.

These events are identified and vetoed by the presence of a large number of high-E_T clusters in the corresponding $|\eta|$ calorimeter region that have poor quality of the signal pulse shape inside the LAr calorimeter.

BAD JET

Mis-identified jets from non-collision sources - commonly known as *fake jets* - can seriously affect the jet and E_T^{miss} reconstruction of this analysis. In general, we can distinguish three types of fake jet sources [59]:

- Beam-induced muons originating from interactions of protons with collimators and other accelerator components leading to jets in the ATLAS calorimeter system.
- Cosmic ray showers, mostly induced by muons and reconstructed as jets.
- Fake jets originating from large calorimeter noises or isolated pathological cells.

These fake jets can be removed by building variables based on the quality of the calorimeter cells [24] and the fraction of charged particles in a jet. In this scope, events having at least one jet with $p_T > 20\,GeV$ and passing the *LooseBad* quality requirement defined in reference [59] are vetoed.

BAD MUON

Badly reconstructed muons can lead to tails in the E_T^{miss} distribution. Therefore events with baseline muons which have at least 20% estimated track momentum error are vetoed.

PILE-UP JETS

Events are removed if there is a jet with $60 < p_T < 70\,GeV$, $|\eta| < 2.0$, JVT < 0.2 and with $\Delta\phi(\text{jet}, E_T^{miss}) > 2.2$. This veto is necessary to reduce the population of events where a pile-up jet narrowly evades the standard JVT selection.

10.4.5 *Event selection*

We have previously described in Section 10.1 the general strategy for a Supersymmetry analysis through the construction of certain *analysis regions*. We have now defined the physics objects and observables designed to isolate the events resembling to new physics and compare the background prediction with the data. In this section we want to illustrate the set of signal, control and validation regions used to perform this search. For each region of the analysis we require events to pass all the cleaning criteria illustrated in Section 10.4.4.

[24] This can be done by comparing the signal shape with respect to a reference value.

10.4.5.1 *Signal Regions*

Signal Regions are designed to isolate the signal from the background events and to evaluate the presence of new physics. Signal-like events are isolated principally requiring a large jet multiplicity and a moderate E_T^{miss} requirement imposed via the use of a $S(E_T^{miss})$ selection. The presence of long SUSY decay chains allows to exploit the larger jet multiplicity of these final states in order to significantly reduce the backgrounds in the Signal Regions.

Additionally, in order to increase the sensitivity to different SUSY models and extend the sensitivity of the SUSY parameter space, further classification is applied through two observables:

- The number of b-jets $N_{\text{b-jets}}$, enhancing the sensitivity to heavy-flavour-enriched signals.
- The scalar sum of large-radius jet masses M_J^{Σ}, allowing to achieve additional discrimination against Standard Model backgrounds for signal scenarios with large mass-splitting.

Exclusive ranges in $N_{\text{b-jets}}$ and M_J^{Σ} are chosen such that they can be statistically combined to enhance exclusion sensitivity to signals as discussed in Chapter 11. Inclusive signal regions more resembling the previous statistical analyses are also defined for high jet multiplicity and boosted signal regions ($N_{\text{jets}}^{50} \geqslant 11, 12$ and $N_{\text{jets}}^{80} \geqslant 9$).

The selection criteria for signal regions are applied after preselection as follows (see also Table 10.4 for a summary):

1. *Lepton veto*: Events with leptons are rejected to reduce backgrounds in which one or more semi-leptonic W decays produce neutrinos, generating real E_T^{miss}.
2. *Jet multiplicity*: An inclusive N_{jets} requirement is placed on the events. However, due to the different jet p_T thresholds accessible by the fifth and seventh jet triggers (see also 10.4.1), the number of jets with p_T greater than 50 and 80 GeV - labeled as N_{jets}^{50} or N_{jets}^{80}- are used to count jets in signal regions. Due to the different jet multiplicities accessible by these triggers, signal regions are formed for $N_{\text{jets}}^{50} \geqslant 8, 9, 10, 11, 12$ and $N_{\text{jets}}^{80} \geqslant 9$.
3. *Flavour tag multiplicity*: Similarly to the jet multiplicity, the number of b-jets with p_T greater than 50 and 80 GeV - labeled as $N_{\text{b-jets}}^{50}$ and $N_{\text{b-jets}}^{80}$- are used to define the number of b-jets in the signal regions. Three divisions are made: $N_{\text{b-jets}} = 0$, $N_{\text{b-jets}} = 1$ and $N_{\text{b-jets}} \geqslant 2$.
4. *Reclustered jet mass sum*: Within each $N_{\text{b-jets}}$ category, the reclustered jet mass sum M_J^{Σ} permits a further subdivision into regions with M_J^{Σ} thresholds at 0, 340 and 500 GeV.
5. E_T^{miss} *significance*: The final analysis cut is on the $S(E_T^{miss})$ distribution, and is placed at $S(E_T^{miss}) > 5$, a moderate threshold which substantially reduces the multi-jet background component while keeping sensitivity to low and high E_T^{miss} signals high.

Selection criterion	Selection ranges		
Lepton veto	0 baseline leptons, $p_T > 10\,GeV$		
Jet multiplicity, N_{jets}	$N^{50}_{jets} \geqslant 8, 9, 10, 11, 12$		
	$N^{80}_{jets} \geqslant 9$		
Flavour-tag multiplicity, $N_{b\text{-jets}}$	$= 0$	$= 1$	$\geqslant 2$
Jet mass sum, M_J^{Σ}	0-340 GeV	340-500 GeV	$\geqslant 500$ GeV
E_T^{miss} significance, $\mathcal{S}(E_T^{miss})$	$\mathcal{S}(E_T^{miss}) > 5$		

Table 10.4 – Summary of signal region criteria. The criteria in each row are applied to each of the options in the preceding row, *i.e.* three $N_{b\text{-jets}}$ bins are created for each N_{jets} channel, and each is subsequently divided into three M_J^{Σ} bins. The same SR $\mathcal{S}(E_T^{miss})$ cut is applied to all bins.

Up to nine exclusive SR bins are therefore defined for each jet multiplicity channel, and combined in a multi-bin fit, as described in Chapter 11.

10.4.5.2 *Control Regions*

Control Regions are designed to refine the estimation of the $W+$jets, $t\bar{t}+$jets and Multi-jet background in SRs by fitting the predictions of these backgrounds to the data. Due to these reasons, two fundamental features are necessary for CRs:

- Any type of **signal contamination needs to be minimized** in order to avoid the inclusion of signals in the scaling of semi-leptonic backgrounds.
- Design CRs where the **purity of background processes is maximal**.

In this analysis, we distinguish two types of Control Regions:

LEPTONIC CONTROL REGIONS
: These regions are used to control the $W+$jets and $t\bar{t}+$jets backgrounds and they require the presence of a lepton (*i.e.* a muon or an electron) and a cut on the transverse mass $m_T < 120\,GeV$ in order to reduce the presence of possible new physics signals. Additionally, the purity of $W+$jets and $t\bar{t}+$jets is enhanced by requiring $N_{b\text{-jets}}$ equal to 0 and $\geqslant 1$ respectively. Table 10.5 shows a summary of the requirements applied for these regions whereas Figure 10.8 shows different $\mathcal{S}(E_T^{miss})$ distributions obtained using the complete Run 2 dataset ($139\,fb^{-1}$). The cuts are kept as close as possible to the Signal Region ones, but some of them are relaxed in order to increase the statistics in the higher jet multiplicity regions.

MULTIJETS CONTROL REGIONS
: These regions are designed to control the Multi-jet background. The estimation of the multijets background component will be described in Section 10.6.2. These are defined by applying the same SR observable requirements, apart for

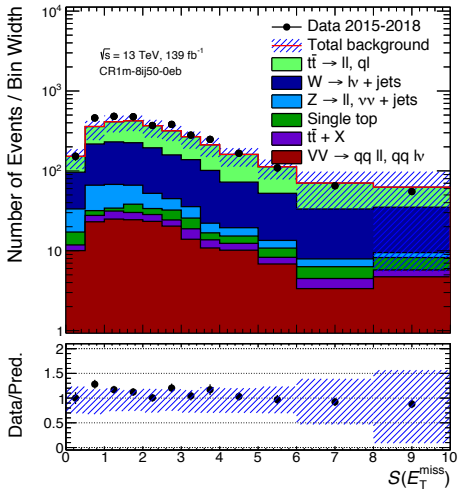

(a) 1 μ, $N_{jets}^{50} \geqslant 8$, $N_{b\text{-jets}} = 0$

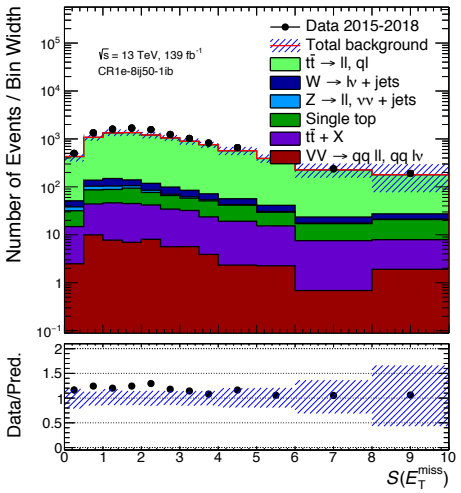

(b) 1 e, $N_{jets}^{50} \geqslant 8$, $N_{b\text{-jets}} \geqslant 1$

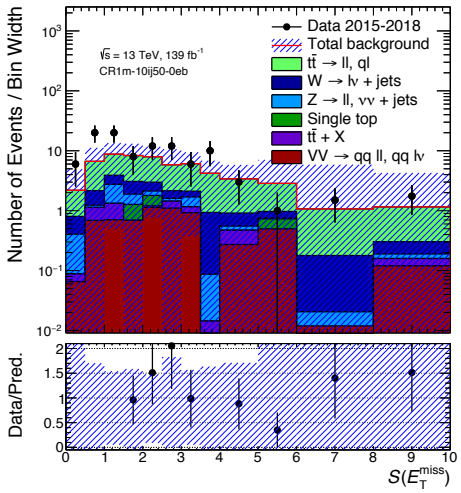

(c) 1 μ, $N_{jets}^{50} \geqslant 10$, $N_{b\text{-jets}} = 0$

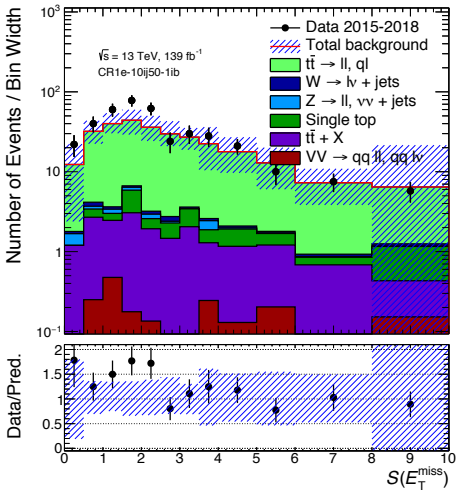

(d) 1 e, $N_{jets}^{50} \geqslant 10$, $N_{b\text{-jets}} \geqslant 1$

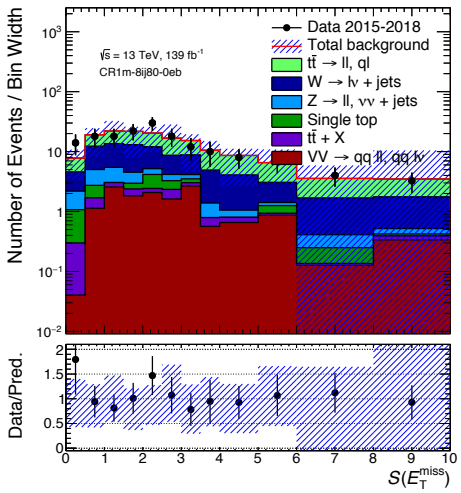

(e) 1 μ, $N_{jets}^{80} \geqslant 10$, $N_{b\text{-jets}} = 0$

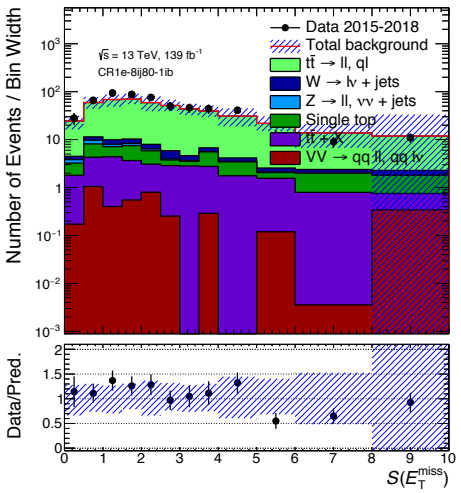

(f) 1 e, $N_{jets}^{80} \geqslant 10$, $N_{b\text{-jets}} \geqslant 1$

Figure 10.8 – $S(E_T^{miss})$ distributions for different electrons (e) and muon (μ) leptonic control regions obtained using the complete Run 2 dataset (139 fb^{-1}).

Selection criterion	Value
Trigger	Same as SR
Number of leptons	Exactly one baseline electron or muon
m_T	lower than 120 GeV
N_{jets}	$N_{SR} - 1$, p_T and η requirements as for SR
$N_{b\text{-jets}}$	Equals to 0 (W + jets) or greater
	and equal than 1 ($t\bar{t}$ + jets)
M_J^{Σ}	Same as SR
$\mathcal{S}(E_T^{miss})$	$\mathcal{S}(E_T^{miss}) > 4.0$

Table 10.5 – Definition of the leptonic Control Regions used to normalize the $t\bar{t}$ + jets and W + jets backgrounds.

the $\mathcal{S}(E_T^{miss})$ one which is fixed as $3.0 < \mathcal{S}(E_T^{miss}) < 4.0$ in order to enhance the presence of Multi-jet background.

10.4.5.3 *Validation Regions*

Validation Regions are used to verify the validity of the background estimation in SRs and to assess the benefits of the CRs adjustments. These regions are generally placed between the signal and control regions (see also Figure 10.1) and are also required to be minimally affected by signal contamination. In this analysis, two sets of validation regions are defined:

E_T^{miss} SIGNIFICANCE VALIDATION REGIONS $VR_{\mathcal{S}(E_T^{miss})}$
: These regions are defined by the same set of cuts applied to SRs, apart for the $\mathcal{S}(E_T^{miss})$ requirement defined as $4.0 < \mathcal{S}(E_T^{miss}) < 5.0$, allowing to test the validity of the Multi-jet background estimation.

JET MULTIPLICITY VALIDATION REGIONS $VR_{N_{jets}}$
: In contrast to $VR_{\mathcal{S}(E_T^{miss})}$ regions, jet multiplicity validation regions are defined through an identical requirement on E_T^{miss} significance to signal regions ($\mathcal{S}(E_T^{miss}) > 5.0$). This allows not only to test the closure of the Multi-jet background and high $\mathcal{S}(E_T^{miss})$, but also to check the prediction of the semi-leptonic contributions provided by W + jets and $t\bar{t}$ + jets after fit of the Leptonic Control Regions. In order to keep signal regions blinded, these VRs are kept away from SRs by looking at lower jet multiplicities where no signals are expected. This is done using the $N_{jets}^{80} = 6$ and $N_{jets}^{50} = 7$ jet multiplicities for 80 GeV and 50 GeV signal regions. Due to the loss of sixt-jet triggers for 50 GeV jets in 2017, the multi-jet estimation at $N_{jets}^{50} = 7$ has been performed using prescaled 6-jet triggers as described in Section 10.4.1 and 10.6.2. Figure 10.9 shows two examples of E_T^{miss} significance distributions in 50 and 80 GeV $VR_{N_{jets}}$ regions.

Table 10.6 reports a summary of the requirements applied for the definitions of $VR_{N_{jets}}$ and $VR_{\mathcal{S}(E_T^{miss})}$.

Region type	$VR_{\mathcal{S}(E_T^{miss})}$	$VR_{N_{jets}}$
Lepton veto	0 baseline leptons (electrons and muons)	
N_{jets}	Same as SR	$N_{jets}^{50} = 7$
	or	
	Same as SR	$N_{jets}^{80} = 6$
$N_{b\text{-jets}}$	Same as SR	
M_J^Σ	Same as SR	
$\mathcal{S}(E_T^{miss})$	$4.0 < \mathcal{S}(E_T^{miss}) < 5.0$	Same as SR

Table 10.6 – Definition of Validation Regions for multijet, $t\bar{t}$ + jets and W + jets background estimation relative to each SR bin.

10.5 OPTIMIZATION STUDIES

A crucial point for an analysis looking for supersymmetric particles is represented by the optimal definition of the signal and control regions. In this section, we illustrate the optimization studies that provided, for the different Run 2 analyses across the years, the definitions of the various variables selections defining the SRs providing the best sensitivity to the targeted signal models.

In the previous version of this analysis using $18.2\,fb^{-1}$ [5], sensitivity plots showed that a cut of $M_J^\Sigma > 500\,GeV$ was optimal to search for models with high gluino mass, whereas $M_J^\Sigma > 340\,GeV$ and $M_J^\Sigma > 0\,GeV$ was more sensitive to models with higher neutralino masses. This feature is essentially due to the different mass splitting between $\Delta m = m_{\tilde{g}} - m_{\tilde{\chi}_1^0}$, defining the p_T of the objects resulting from the intermediate cascade decays such that:

- For $m_{\tilde{g}} \approx m_{\tilde{\chi}_1^0}$, jets have low momenta due to the small amount of energy accessible from $\Delta m = m_{\tilde{g}} - m_{\tilde{\chi}_1^0}$. In this case, the resulting particles are less boosted and therefore a lower M_J^Σ cut gives more sensitivity to these scenarios.
- For $m_{\tilde{g}} \gg m_{\tilde{\chi}_1^0}$, jets have large transverse momenta, resulting in a larger sensitivity from $M_J^\Sigma > 500\,GeV$.

Figure 10.10a and 10.10b shows such trends for 95% CL poisson discovery limits[25] in the signal region having $N_{jets}^{50} \geqslant 9$. These plots represented a fundamental study for the optimization of these cuts.

In analogy with the M_J^Σ cut, the jet-p_T selection has been optimized later for the $36\,fb^{-1}$ analysis [97] in order to define the cuts allowing to exploit the maximal sensitivity coverage in the gluino and LSP mass plane. These studies led to the utilization of 80 GeV jet p_T signal regions, allowing to exploit lower jet multiplicities than 50 GeV signal regions due to the lower jet multiplicity accessible by multijet triggers with 80 GeV. Figure 10.10c and 10.10d shows the 95% CL discovery limits

[25] This has been computed using the `RooStats::NumberCountingUtils::BinomialExpP` function documented inside https://root.cern/doc/master/NumberCountingUtils_8cxx_source.html.

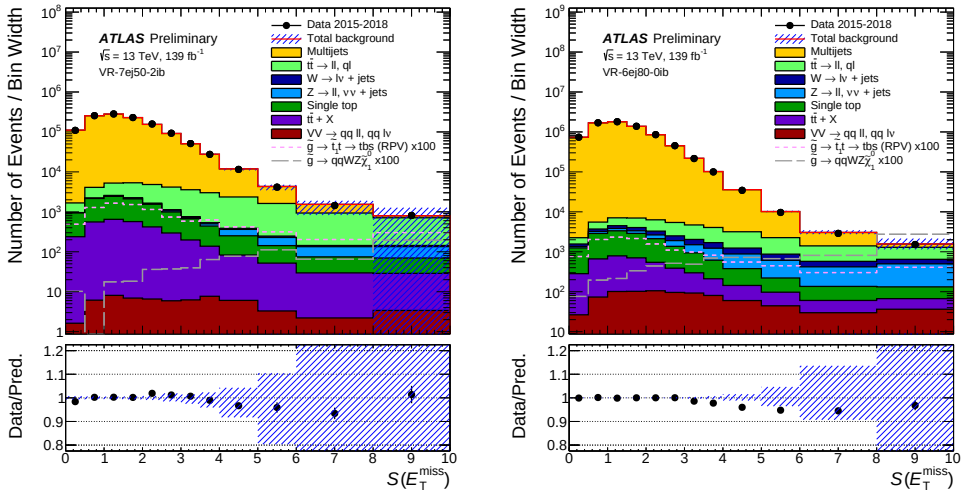

(a) $N_{jets}^{50} = 7$, $N_{b\text{-jets}} \geqslant 2$ (b) $N_{jets}^{80} = 6$, $N_{b\text{-jets}} \geqslant 0$

Figure 10.9 – $\mathcal{S}(E_T^{miss})$ distributions for different $VR_{N_{jets}}$ regions obtained using the complete Run 2 dataset (139 fb^{-1}).

associated to different jet p_T selections, illustrating the larger reach in larger mass splittings of the $p_T > 80\,GeV$ cut.

The low $\mathcal{S}(E_T^{miss})$ cut used to define the signal regions represents a unique feature of this analysis, allowing to target physics scenarios which are unaccessible for many of the other ATLAS searches for SUSY. In the first Run 2 iterations of this analysis [90, 5], $\frac{E_T^{miss}}{\sqrt{H_T}} > 4.0$ was providing an optimal E_T^{miss} significance selection for the analysis signal regions. However, for the 36 fb^{-1} analysis [6], the $E_T^{miss}/\sqrt{H_T}$ cut was optimized using three signal grids: the pMSSM, the two-step and the RPV model. Figure 10.10e and 10.10f compare the sensitivities obtained for the two-step and RPV signal grids for the $N_{jets}^{50} \geqslant 9$ signal region. These plots clearly show that an increased sensitivity can be reached by a cut greater than 4 for the two-step, whereas the RPV sensitivity seems to become worse for the same set of cuts. This feature is not surprising considering that the RPV decay chain does not contain any stable SUSY invisible particle and therefore it is provided with a lower E_T^{miss}. The enhancements of the 95% confidence limits associated to the two-step and the pMSSM model suggested to select a larger $E_T^{miss}/\sqrt{H_T}$ cut for the definition of our SRs and this value was fixed at 5 considering the small sensitivity reduction for the RPV model with this larger $E_T^{miss}/\sqrt{H_T}$ cut.

10.6 BACKGROUND ESTIMATION

As discussed in Section 10.3, the estimation of the background processes at high jet multiplicity is fundamental for the testing of new physics signals in the analysis SRs. This section is dedicated to the description of the estimation of the Standard Model processes entering in the analysis regions.

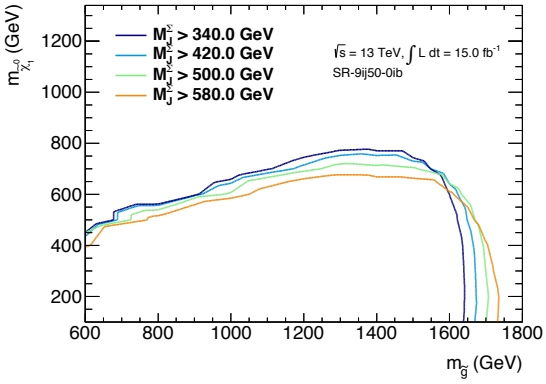

(a) M_J^{Σ} optimization, two-step model

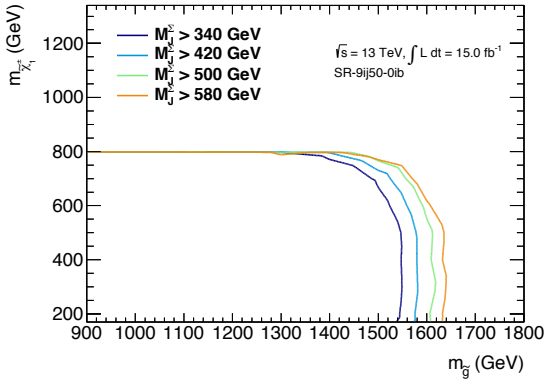

(b) M_J^{Σ} optimization, pMSSM model

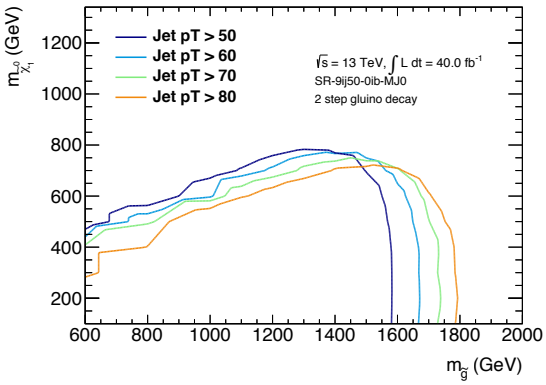

(c) Jet p_T optimization, two-step model

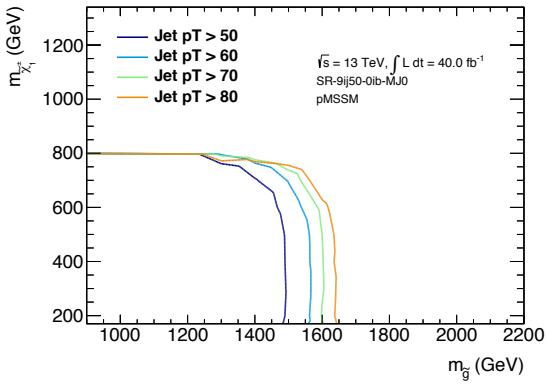

(d) Jet p_T optimization, pMSSM model

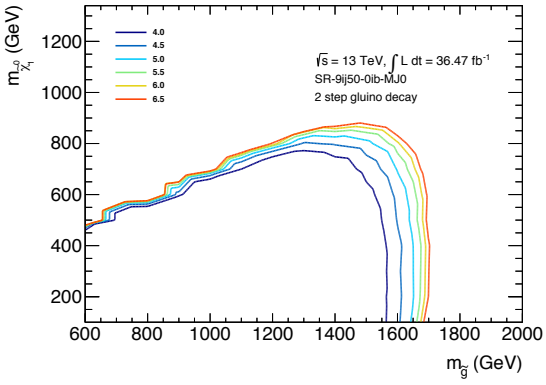

(e) $E_T^{miss}/\sqrt{H_T}$ optimization, two-step model

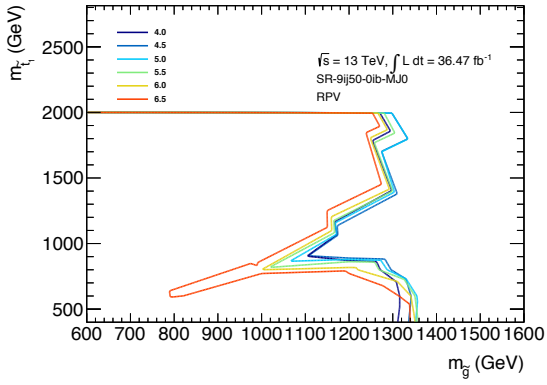

(f) $E_T^{miss}/\sqrt{H_T}$ optimization, RPV model

Figure 10.10 – 95% CL poisson discovery limits for different variable optimizations in the $N_{jets}^{50} \geqslant 9$ signal region.

10.6.1 *Leptonic backgrounds*

Leptonic backgrounds in SRs are estimated using Monte-Carlo simulation techniques. These techniques are able to take the theoretical description provided by the Standard Model Lagrangian (see Chapter 2) and output a dataset containing all the signals that these particles left in the ATLAS detector. The same kind of dataset is recorded during the p-p collision of the LHC and it represents the *data* (or *observation*) of the experiment. Each simulated dataset is also provided with a cross-section allowing to estimate the total contribution with the total data integrated luminosity.

Top-pair events have been simulated using the matrix elements calculated at next-to-leading order (NLO) using the POWHEG-BOX v2 generator with the `NNPDF3.0NLO` PDF set [98]. For this process, the top quarks were decayed using MadSpin [99] to preserve all spin correlations, while parton shower, fragmentation, and the underlying event were simulated using PYTHIA8 [100] with the `NNPDF2.3LO` PDF set [101] and the ATLAS `A14` tune [102]. After hadronisation, interactions of final particles with the ATLAS detector are simulated using the GEANT framework [103]. All $t\bar{t}$ MC samples have been normalized to the NNLO + NNLL cross-section from `Top++` [104].

On the other hand, events containing a W or Z bosons have been simulated using the SHERPA 2.2.1 generator. Matrix elements were calculated for up to two partons at NLO and four partons at LO using the COMIX and OPENLOOPS [105] matrix element generators and merged with the SHERPA parton shower [106] using the ME+PS@NLO prescription [107]. The NNPDF3.0 NNLO PDF set was used in association with a tuning performed by the SHERPA authors.

10.6.2 *Multi-jet background*

Section 10.3.2 discussed the composition of the multi-jet background and the fact that it needs to be estimated in a data-driven way. In this context, an "ABCD" background estimation method is applied, aiming at estimating the amount of multi-jet background in a region D starting from the knowledge of the multi-jet yields in regions A, B and C formed by two uncorrelated variables. In the context of this analysis, this method is commonly known as the *template method* and it relies on several properties of the $\mathcal{S}(E_T^{miss})$ variable:

- New physics signal will appear at high values of $\mathcal{S}(E_T^{miss})$, whereas backgrounds will mostly dominate the low values of the $\mathcal{S}(E_T^{miss})$ shape as previously discussed in Section 6.6.

- The shape of the $\mathcal{S}(E_T^{miss})$ distribution is invariant under changes of the jet multiplicity N_{jets} for events dominated by mis-measurement effects (*i.e.* no real E_T^{miss}).

Therefore, the estimation of the full-hadronic background of the analysis signal regions can be performed using the two uncorrelated variables $\mathcal{S}(E_T^{miss})$ and N_{jets}.

The template method is designed to estimate the amount of multi-jet background at high jet multiplicity and high values of $\mathcal{S}(E_T^{miss})$. This method relies on the invariance of the $\mathcal{S}(E_T^{miss})$ shape generated by fully-hadronic processes from the jet

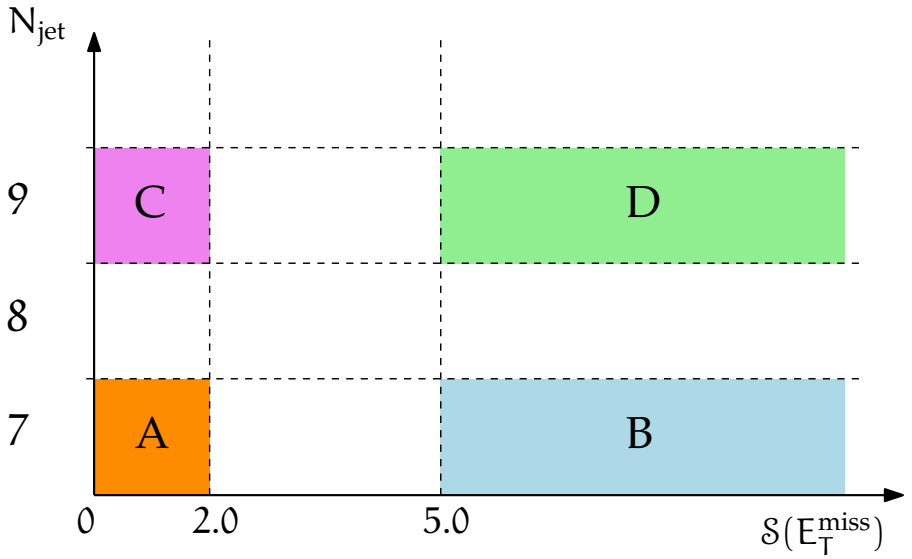

Figure 10.11 – Example of regions used in the template method for the multijet background.

multiplicities N_{jets}, N_{jets}^{50} and N_{jets}^{80}. The procedure is also schematically shown in Figure 10.11.

The idea is the following: the expected multi-jet yield in a signal region called D at high jet multiplicity and $\not{S}(E_T^{miss}) > 5.0$ can be obtained from the multi-jet background estimation at lower jet multiplicities, where no signal is expected (*i.e.* regions A and B). Since the multi-jet cross-section changes significantly between different jet multiplicities, the measured multi-jet yield in region B N_B needs to be normalized somehow to the high jet multiplicity. This can be done using the multi-jet yields in regions A and C where, due to the low $\not{S}(E_T^{miss})$ requirement ($\not{S}(E_T^{miss}) < 2.0$), no signal contamination is expected to affect the scaling of the multi-jet prediction in Signal Region D. Dedicated studies showed that the fraction of signal contamination for the models under test is found to be in the range $< 0.1\%$ to 10% depending on the region. The predicted multi-jet yield in the signal region becomes then:

$$\hat{N}_D = \frac{N_C}{N_A} N_B. \tag{10.13}$$

In this equation, N_A, N_B and N_C are the multi-jet yields estimated from the difference between the data and the simulated leptonic backgrounds. A similar procedure is used to make predictions in the control and validation regions having intermediate ranges of $\not{S}(E_T^{miss})$ (*i.e.* $3.0 < \not{S}(E_T^{miss}) < 5.0$) and documented in Section 10.4.5.

10.6.2.1 *Template regions*

It has been illustrated in the previous section how the extrapolation of the $\not{S}(E_T^{miss})$ template from region "B" needs to be done from a low jet multiplicity $\not{S}(E_T^{miss})$ distribution. We generally refer to these regions as the *Template Region* (TR) of the analysis.

The utilisation of five-jet and seven-jet triggers imposes a different definition of the template regions for N_{jets}^{50} and N_{jets}^{80}. In general, for 50 GeV signal regions

employing seven-jet triggers, the template is extrapolated from $N_{jets}^{50} = 7$ since this is the lowest jet multiplicity accessible in data for this trigger. For the same reason, for 80 GeV signal regions the $N_{jets}^{80} = 5$ $S(E_T^{miss})$ distribution is employed for the extrapolation of the multi-jet estimation.

10.6.2.2 H_T *binning of the template method*

In order to reduce the dependence on H_T caused by the residual dependency of $S(E_T^{miss})$ from the event activity, this procedure is repeated for different bins of this quantity. Considering $i = 1, \ldots, N$ H_T bins, the final multi-jet background estimation is

$$\hat{N}_D = \sum_{i=1}^{N} \hat{N}_D^i = \sum_{i=1}^{N} \frac{N_C^i}{N_A^i} N_B^i \tag{10.14}$$

where the index i denotes multi-jet yields in a specific H_T bin. The choice of the H_T binning is done in an *adaptive* way through the following procedure:

1. We split the H_T distribution into a set of bins with fixed width $W_{adaptive}$.
2. Starting from the lowest H_T bin, the next highest bin is combined with the previous one until a minimum number of events $N_{adaptive}^{min}$ is reached in both low and large jet multiplicity regions.
3. The merged bin ranges are fixed, and the merging procedure is repeated on the next H_T bin.
4. This procedure is iterated until each bin in the H_T distribution has been considered.

The resulting H_T ranges from this procedure represent the final set of bins used for the H_T-binning of the template method. The adaptive bin ranges are defined independently for each signal region in order to maximize the closure of the multi-jet background estimation and to minimize any dependency on a fixed H_T-binning choice. Additionally, it is possible to note how the entire procedure depends on two simple parameters: $W_{adaptive}$ and $N_{adaptive}^{min}$. A systematic uncertainty related to the choice of these two parameters is applied and discussed later in Section 10.7.

10.7 SYSTEMATIC UNCERTAINTIES

Systematic uncertainties are fundamental to quantify the accuracy of the background estimation in the different analysis signal regions. In general, we distinguish three types of systematic uncertainties, which are then considered as nuisance parameters of the profiled likelihood fit described later in Chapter 11:

- The *experimental systematic uncertainties*, quantifying the impact of the mismeasurements effects related to the ATLAS detector.
- The *theoretical systematic uncertainties*, quantifying the precision of the theoretical models used for the MC simulation of the background processes.

- The *template systematic uncertainties*, describing the systematic effects due to the data-driven template estimation.

All these systematics and their estimation are described in the next sections.

10.7.1 *Experimental uncertainties*

These include uncertainties on energy scales/resolutions of various physics objects, including particle reconstruction and identification efficiencies, as well as the integrated luminosity recorded by the ATLAS experiment. As expected, due to the large number of jets characterizing the signal regions of this analysis, the dominant experimental uncertainties are the ones related to jet reconstruction. Additionally, due to the lepton veto in the SRs, systematics on the lepton efficiencies and on lepton energy scale/resolution enter only through the CR measurements of the backgrounds.

The list of important experimental systematics is provided here:

JET ENERGY SCALE
: These take into account the effects of the nuisance parameters associated to the Jet Energy Scale correction (see Section 5.2.3 for further details).

JET ENERGY RESOLUTION
: Uncertainties on the jet resolution are evaluated by smearing the jet energies using a Gaussian, whose mean and width values are determined from the difference between the jet resolutions measured in MC and data.

JET VERTEX TAGGER
: The efficiencies for tagging pileup (hard scatter) jets with the JVT discriminant are corrected in MC simulation by applying scale factors derived by measurement of jet rates in pileup-enriched (depleted) phase space regions.

FLAVOUR-TAGGING
: Scale factors are applied to correct the simulated b-tagging (in)efficiencies to better match the data. Uncertainties on these scale factors are determined from variations in the various jet flavour components and for the extrapolation of systematics into regions where the measurements are statistically limited.

MISSING TRANSVERSE MOMENTUM SOFT TERM
: Uncertainties on the hard object components in the E_T^{miss} are propagated from the systematics on the selected objects. Additional uncertainties on the soft E_T^{miss} component are applied as variations on the scale of the TST, and smearing of the TST by the difference between data and MC resolutions in two orthogonal projections of the soft term with respect to the balancing hard terms. See Section 6.5 for further details.

PILEUP-REWEIGHTING
: Two variations are applied to the data scale factor used for pileup-reweighting, accounting for uncertainties on the degree of mismodelling of the minimum bias overlay used in MC pileup simulation.

10.7.2 *Template uncertainties*

As previously illustrated, the multi-jet background represents the dominant background component of the analysis signal regions, meaning that tne systematic uncertainties associated to this background are particularly important. Considering that this background is purely estimated using data, data must also be used for the evaluation of the systematic uncertainties in signal and validation regions.

In general, uncertainties on the multi-jet template prediction are assessed from three sources:

- An overall non-closure systematic based on testing the accuracy of the predictions in a set of validation regions kinematically close but orthogonal to the signal regions. We generally refer to the uncertainty covering such effect as the *template closure systematic*.
- Potential differences in the template shape due to differences in flavour composition - in particular full-hadronic $t\bar{t}$ processes - between $N_{jets} = 5, 6, 7$ and high jet multiplicities. We generally refer to the uncertainty covering such effect as the *template flavour systematic*.
- Residual kinematic biases due to the binning of the predictions in H_T. We generally refer to the uncertainty covering such effect as the *template* H_T*-binning systematics*.

The sizes of these uncertainties are summarised in Figure 10.12 for the multi-bin signal regions used in the analysis. In general, the non-closure systematic dominates, while the H_T-binning systematic is almost negligible. In a handful of cases, the flavour-dependence systematic is comparable to the non-closure. Single-bin signal regions showed similar results.

10.7.3 *Theoretical uncertainties*

Theoretical systematic uncertainties affect the MC-based predictions of the leptonic backgrounds in the signal, validation and control regions. These are generally estimated from comparisons between the nominal simulated backgrounds and the same backgrounds simulated using different sets of simulated parameters.

The strategy for calculating the $t\bar{t}$ and single top theory uncertainties are summarized in Table 10.7, while W + jets and Z + jets uncertainties are provided in Table 10.8. The diboson systematics are be as for W + jets and Z + jets samples, while an overall 50% uncertainty is fixed on the rare $t\bar{t}$ + X processes.

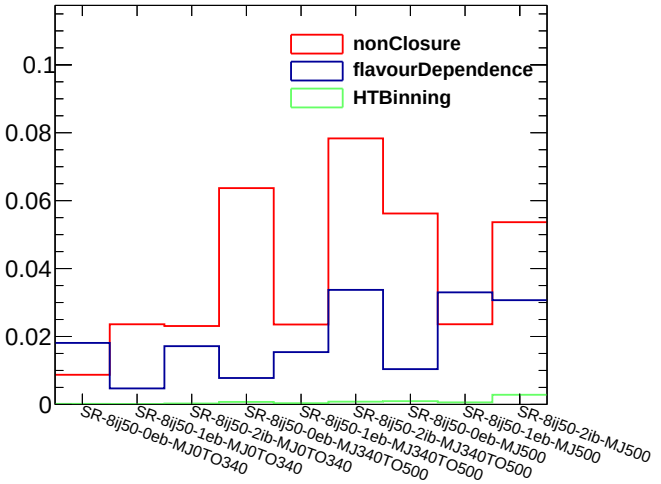

(a) $N_{jets}^{50} \geqslant 8$

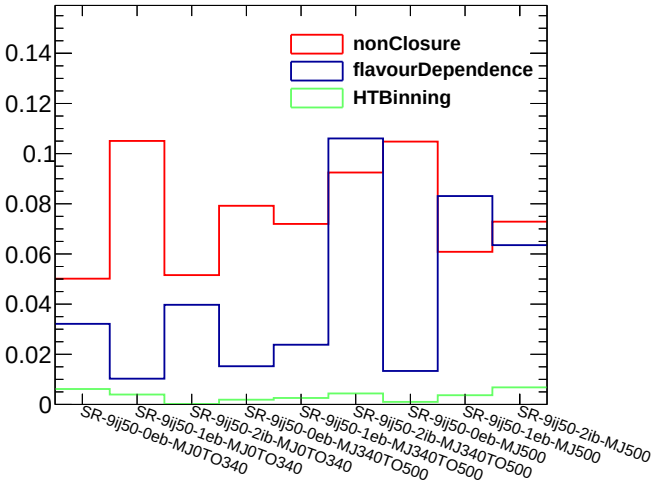

(b) $N_{jets}^{50} \geqslant 9$

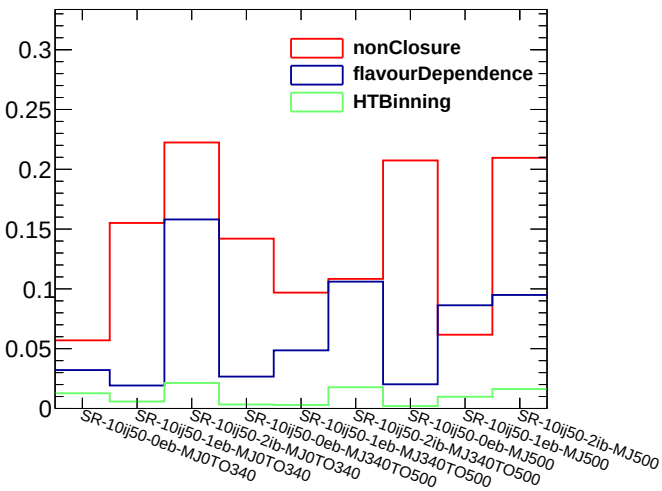

(c) $N_{jets}^{50} \geqslant 10$

Figure 10.12 – Summary of the relative template systematic uncertainties in multi-bin SRs.

Name	Covered uncertainty
Hard Scatter Generation and matching	Variations of matrix element MC calculations and matching scales.
Fragmentation/Hadronization model	Variations of different partonic showering and hadronization models.
Initial State Radiation (ISR), up variation	Variations in the renormalization and factorization scales (0.5 $\times$ the nominal scale) and the variations in the showering.
Initial State Radiation (ISR), down variation	Variations in the renormalization and factorization scales (2 $\times$ the nominal scale) and the variations in the showering.
Parton Density Function	Uncertainties in the PDF calculation parameterized by the error sets.
Final State Radiation (FSR)	Variations of the strong coupling constant α_S for FSR.

Table 10.7 – The theoretical uncertainty components for the $t\bar{t}$ and single top MC backgrounds.

Name	Covered uncertainty
Matrix element matching	Variation of the scale employed for the calculation of the overlap between jets from the ME and the PS. The nominal value for this parameter is 20 GeV. The up variation increases the nominal value to 30 GeV while the down variation decreases it to 15 GeV.
Renormalisation scale	Variation of the scale for the running strong coupling constant for the underlying hard process. The renormalisation scale is modified to 2 and 0.5 with respect to the nominal value.
Factorisation scale	Variation of the scale used for the parton density functions. The factorisation scale is modified to 2 and 0.5 with respect to the nominal value.
Resummation scale	Variation of the scale used for the resummation of soft gluon emission. The resummation scale is modified to 2 and 0.550 with respect to the nominal value.
Parton Density Function	Uncertainties in the PDF calculation.

Table 10.8 – The theoretical uncertainty components for the W + jets and Z + jets MC backgrounds.

11

RESULTS AND INTERPRETATIONS OF THE SUSY MULTI-JET SEARCH

"Harry: I'll be in my bedroom, making no noise and pretending I'm not there."
– J.K. Rowling, *Harry Potter and the Chamber of Secrets*

Contents

The previous chapter described the targeted models and strategy of the multi-jet analysis. In this chapter, we discuss the results of this search. Data have been collected during the complete Run 2 of the LHC, including the 2015-2018 periods. Protons were smashed at the center-of-mass energy of $\sqrt{s} = 13\,\text{TeV}$, leading to events with jet multiplicities never accessed before. Figure 11.1 shows an event recorded on 23 October 2016 and composing one of the SUSY candidates populating the analysis signal regions. This event contains 16 Particle Flow jets and a E_T^{miss} significance above 6.4. Figure 11.2 shows an event with higher jet multiplicity (19 Particle Flow jets) recorded on 18 July 2018 and falling within the control regions of the analysis. The next sections presents the statistical analysis tools used for the interpretation of the experimental data with respect to the background prediction described in the previous chapter.

11.1 STATISTICAL ANALYSIS

We have previously illustrated in Section 10.1 the role of Signal, Control and Validation Regions in a search for Supersymmetry. However, the final test for new

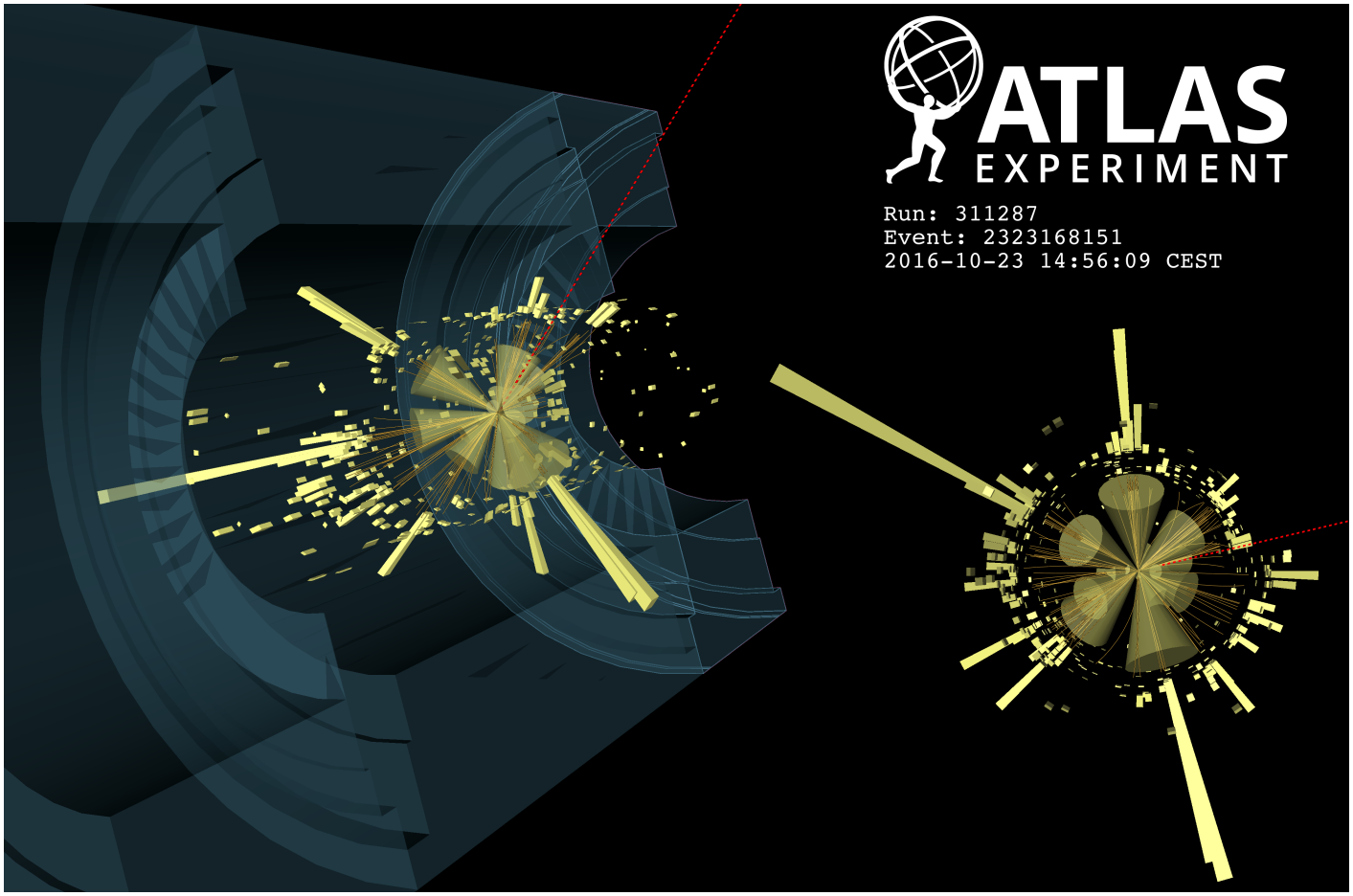

Figure 11.1 – Visualisation of the highest jet multiplicity event selected in signal regions targeting long cascade decays of pair-produced gluinos [4]. This event was recorded by ATLAS on 23 October 2016, and contains 16 jets, illustrated by cones. Yellow blocks represent the calorimeter energy measured in noise-suppressed clusters. Of the reconstructed jets, 13 (11) have transverse momenta above 50 GeV (80 GeV), with 3 (2) being b-tagged. The leading jet has a transverse momentum of 507 GeV, and the sum of jet transverse momenta $H_T = 2.9$ TeV. A value of 343 GeV is observed for the E_T^{miss}, whose direction is shown by the dashed red line, producing a significance $\mathcal{S}(E_T^{miss}) = 6.4$. The sum of the masses of large-radius jets is evaluated as $M_J^{\Sigma} = 1070$ GeV.

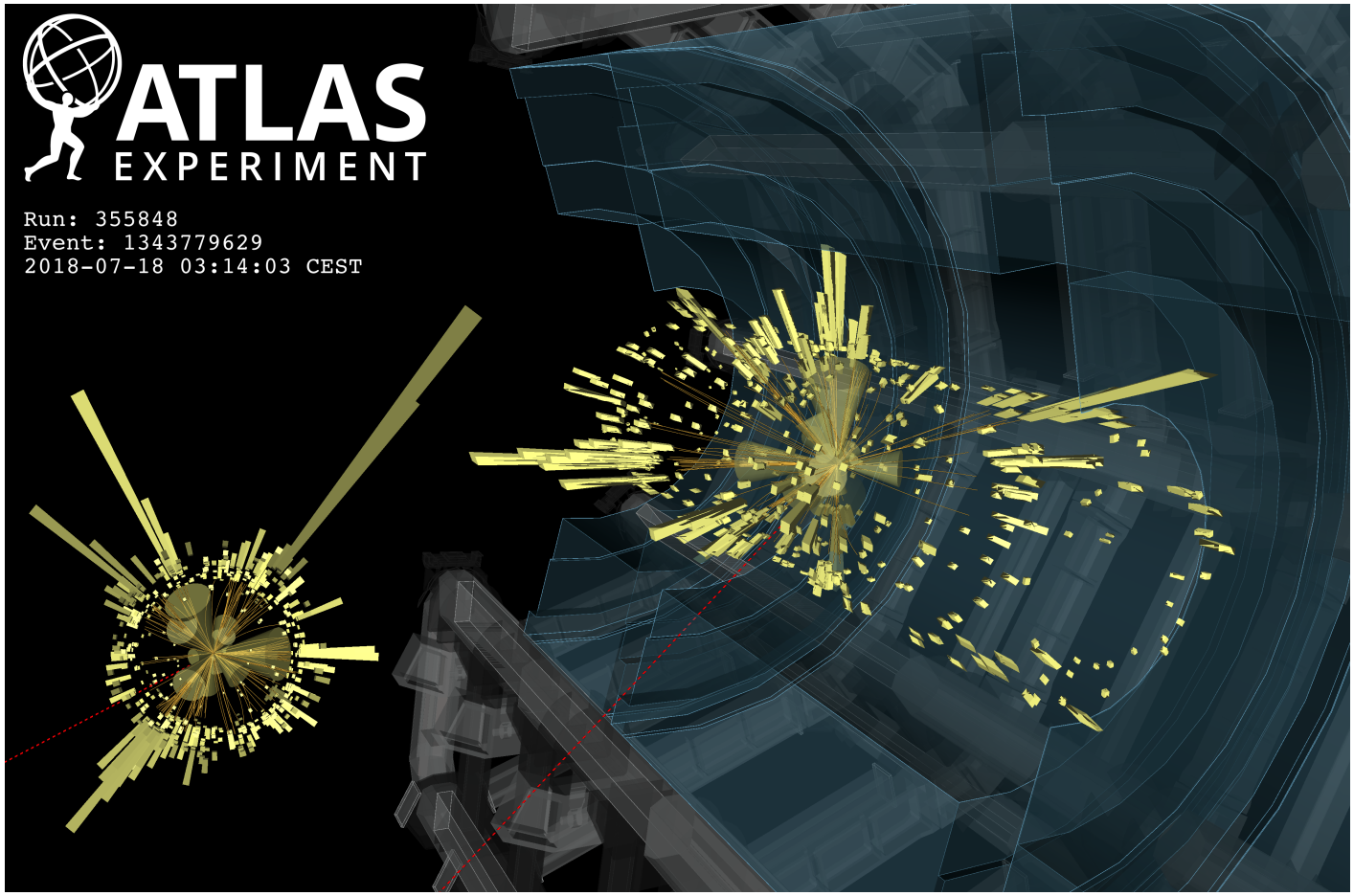

Figure 11.2 – Visualisation of the highest jet multiplicity event selected in a control region used to make predictions of the background from multijet production [4]. This event was recorded by ATLAS on 18 July 2018, and contains 19 jets, illustrated by cones. Yellow blocks represent the calorimeter energy measured in in noise-suppressed clusters. Of the reconstructed jets, 16 (10) have transverse momenta above 50 GeV (80 GeV). No jets are b-tagged. The leading jet has a transverse momentum of 371 GeV, and the sum of jet transverse momenta $H_T = 2.2$ TeV. A value of 8 GeV is observed for the E_T^{miss}, whose direction is shown by the dashed red line, producing a significance $\mathcal{S}(E_T^{miss}) = 0.2$. The sum of the masses of large-radius jets is evaluated as $M_J^{\Sigma} = 767$ GeV.

physics comparing data to Standard Model backgrounds is performed after a *fit* of the backgrounds in order to enhance the precision of the background prediction in Validation and Signal Regions. When no signs of new physics are found, exclusion limits are set for specific SUSY models in order to illustrate the exclusion power of a SUSY analysis. In this section, we introduce the statistical tools necessary for the understanding of the interpretation of this analysis.

11.1.1 *Probability density functions (PDFs)*

Given a continuous observable x, a *Probability Density Function* (PDF) is a continuous function $f(x)$ expressing the probability of obtaining a value of x inside the interval $[x, x + dx]$. This probability is quantified as $f(x)dx$. In Particle Physics, when counting events in specific bins of a certain observable, the most used PDF is the *Poisson distribution* given by

$$\text{Pois}(n; \nu) = e^{-\nu} \frac{\nu^n}{n!}. \tag{11.1}$$

In this equation, n is the number of observed events and ν is the parameter of the distribution, representing its *mean* (or *average*) value. In this context, we suppose that the parameters of the PDF are known while the value n represents the outcome of a single experiment. Another important PDF is the *Gaussian distribution* defined by

$$G(n; \mu, \sigma) = \frac{1}{\sigma\sqrt{2\pi}} e^{-\frac{(n-\mu)^2}{2\sigma}}, \tag{11.2}$$

where μ is the *mean* (or *average*) value and σ the *standard deviation* of the distribution.

A *Likelihood* function is generally used to extrapolate information about the PDF when the outcome of an experiment is known. In the context of a Poisson distribution, for a given measurement N, the likelihood distribution is represented by the function

$$L(\nu) = \text{Pois}(N; \nu) = e^{-\nu} \frac{\nu^N}{N!}. \tag{11.3}$$

It is important to note that the fixed value here is N, and not the parameter ν which can be varied. When performing a *fit* for the estimation of the parameter ν for a certain measurement N, the idea is to find the parameter $\hat{\nu}$ that maximizes the Likelihood $L(\nu)$. Therefore, we can define $\hat{\nu}$ as

$$\hat{\nu} = \arg\max\left(L(\nu)\right). \tag{11.4}$$

In general, it is preferable to estimate $\hat{\nu}$ through minimization of the *Negative Log Likelihood* (NLL) distribution defined as

$$\text{NLL}(\nu) = -2 \ln L(\nu), \tag{11.5}$$

such that

$$\hat{\nu} = \arg\min\left(\text{NLL}(\nu)\right). \tag{11.6}$$

For a binned approach, when multiple bins are combined inside a single PDF, the total likelihood distribution associated to different measurements $\mathbf{N}$ is given by the product of the Poisson distribution of Equation (11.3):

$$L(\mathbf{S}+\mathbf{B}) = \text{Pois}(\mathbf{N};\mathbf{S}+\mathbf{B}) = \prod_{i=1}^{n_b} e^{-(S_i+B_i)} \frac{(S_i+B_i)^{N_i}}{N_i!}. \tag{11.7}$$

Here, n_b is the number of bins to combine and $\mathbf{S},\mathbf{B}$ are the total number of signal and background events associated to each bin. It is possible to note that inside this definition we have considered for each bin $\nu_i = S_i + B_i$.

11.1.2 *Nuisance parameters and systematics*

Typical PDF parameters can be divided in two categories:

- *Parameters of Interest* (POIs), representing the descriptive parameters of the PDF which are generally extracted from the data (*e.g.* number of signal events S_i, average value of a gaussian, etc.).
- *Nuisance Parameters* (NPs), representing the other parameters which are not of immediate interest for the interpretation of a physical result but that must be included in the description of a statistical model.

Typical examples of nuisance parameters are *systematic uncertainties*, noted as $\theta = \{\theta^j\}$ where $j = 1,\dots,n_{syst}$. When interpreting systematic uncertainties in statistical models, these uncertainties are considered as unknown parameters of the model likelihood. In SUSY searches, these generally affect the background estimation B_i for a certain bin i. The impact of systematic uncertainties on bin i is evaluated through variations on the predicted number of events $\left\{\Delta n_i^j\right\}$. In the context of this this analysis, $\left\{\Delta n_i^j\right\}$ refers to the uncertainties described in Section 10.7. Considering that these nuisance parameters are unknown, we consider $\theta = \{\theta^j\}$ to be described by a set of gaussian distributions $G(\theta_j;0,1)$ where $\mu_j = 0$ and $\sigma_j = 1$. The impact of these parameters on the background prediction B_i is then evaluated by scaling Δn_i^j by θ_j. The estimation of θ is then extracted from the observed data and noted $\hat{\theta}$. The total likelihood used for this scope includes all the gaussian constraints $G(\theta_j;0,1)$ for every systematic term $j = 1,\dots,n_{syst}$ and it can be written as

$$L(\mathbf{S}+\mathbf{B};\theta) = \prod_{i=1}^{n_b} e^{-\left(S_i+B_i+\sum_j \Delta n_i^j \theta_j\right)} \frac{\left(S_i+B_i+\sum_j \Delta n_i^j \theta_j\right)^{N_i}}{N_i!} \prod_{j=1}^{n_{syst}} G(\theta_j;0,1). \tag{11.8}$$

We generally refer to this likelihood as the *profile likelihood*. When the $\hat{\theta}$ values are estimated, we say that systematic uncertainties have been *profiled*.

11.2 BACKGROUND-ONLY FIT

The *background-only* fit allows to improve the precision of the background estimation in Signal Regions by adjusting the background yields in Control Regions in

8,9,10ij50 SR, VR definitions	$N_{b\text{-jet}} = 0$	$N_{b\text{-jet}} = 1$	$N_{b\text{-jet}} \geq 2$
$0 < MJ_\Sigma \leq 340$ GeV	R1	R2	R3
$340 < MJ_\Sigma \leq 500$ GeV	R4	R5	R6
$MJ_\Sigma \geq 500$ GeV	R7	R8	R9

(a) Signal Region bins

8,9,10ij50 CR definitions	$N_{b\text{-jet}} = 0$	$N_{b\text{-jet}} \geq 1$
$0 < MJ_\Sigma \leq 340$ GeV	WCR1	TCR1
$340 < MJ_\Sigma \leq 500$ GeV	WCR2	TCR2
$MJ_\Sigma \geq 500$ GeV	WCR3	TCR3

(b) Control region bins

Figure 11.3 – Region definitions for the multibin fit for $N_{\text{jets}}^{50} \geqslant 8, 9, 10$ analysis channels.

order to match the data. It assumes no signal in Equation (11.8) (*i.e.* $\mathbf{S} = 0$) leading to a total Poisson likelihood of the form:

$$L(\mathbf{B};\theta) = \prod_{i=1}^{n_b} e^{-\left(B_i + \sum_j \Delta n_i^j \theta_j\right)} \frac{\left(B_i + \sum_j \Delta n_i^j \theta_j\right)^{N_i}}{N_i!} \prod_{j=1}^{n_{syst}} G(\theta_j; 0, 1). \tag{11.9}$$

Knowing all the background yields in each bin i, the total number of background events B_i can be written as

$$B_i = \sum_p \mu_p B_{i,p}, \tag{11.10}$$

where p corresponds to a specific background process (multi-jet, $W+$jets, $t\bar{t}+$jets, diboson, etc.), $B_{i,p}$ to the background yield measured inside bin i for process p through MC or data-driven estimation methods. The quantities μ_p represent the *transfer factors* (or TFs) corresponding to a scale factor correction, typically within the $[0, 1]$ interval, to be applied to the pre-fit background estimation values $B_{i,p}$.

As described in Section 10.1, we define CRs only for dominant backgrounds (*i.e.* multi-jet, $W+$jets and $t\bar{t}+$jets), meaning that the transfer factors μ_p will be adjusted only for these backgrounds while they will be fixed to unity for all other processes. The fit is performed by combining electron and muon Control Regions. Under these assumptions, the total background yield of Equation (11.10) will be

$$\begin{aligned} B_i = {} & \mu_{t\bar{t}} \cdot B_{t\bar{t},i} + \mu_W \cdot B_{W,i} \\ & + \mu_{\text{multi-jet}} \cdot B_{\text{multi-jet},i} \\ & + \sum_{p \neq t\bar{t},W,\text{multi-jet}} B_{p,i}. \end{aligned} \tag{11.11}$$

The background-only fit procedure allows to estimate the values of $\mu_{t\bar{t}}$, μ_W and $\mu_{\text{multi-jet}}$ from Control Regions and the adjusted values will be noted with $\hat{\mu}_{t\bar{t}}$, $\hat{\mu}_W$ and $\hat{\mu}_{\text{multi-jet}}$.

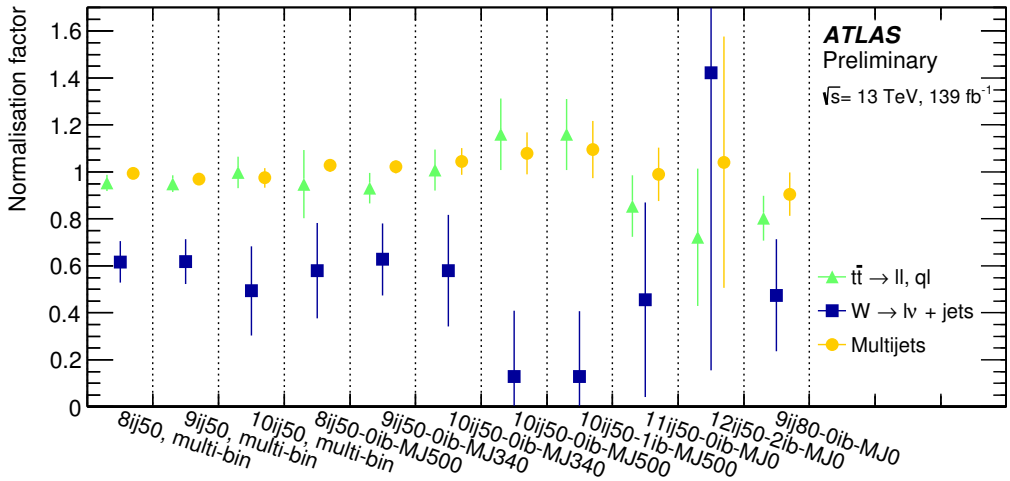

Figure 11.4 – Fitted transfer factors $\hat{\mu}_W, \hat{\mu}_{t\bar{t}}$ and $\hat{\mu}_{\text{multi-jet}}$ in all multi-bin (bins 1-3) and single-bin (bins 4-11) signal regions [4]. The error bars indicate the combination of statistical and systematic uncertainties on the corresponding factors.

11.2.1 *Multi-bin fit*

Multi-bin fits are designed to combine the information from different signal regions in order to improve sensitivity to chosen signal models through uncertainty reduction. In this analysis, the following multi-bin statistical analysis is defined, and performed for 8, 9 and 10 N_{jets}^{50} selections:

- Each N_{jets} selection defines one channel of the fit, which may have up to nine SR bins, divided in exclusive $N_{\text{b-jets}}$ and M_J^Σ selections (see Section 10.4.5). Figure 11.3a shows a schematic of the regions used for this definition.
- Due to the explicit $N_{\text{b-jets}}$ requirements in the $W+\text{jets}$ and $t\bar{t}+\text{jets}$ CRs, these CRs are shared across all $N_{\text{b-jets}}$ bins, but are split in M_J^Σ. Figure 11.3b shows a schematic of the regions used for this definition.
- One set of normalization factors $\hat{\mu}_W, \hat{\mu}_{t\bar{t}}$ and $\hat{\mu}_{\text{multi-jet}}$ is defined, allowing background shapes to be corrected.
- Effect of systematics are estimated through one nuisance parameter per systematic uncertainty correlated across all SR bins. This results in an over-constrained fit, such that some degree of profiling occurs.

The results of the background-only multi-bin fit procedure are reported for $N_{\text{jets}}^{50} \geqslant 8, 9, 10$ in Figure 11.4 (first three bins). Here, we can see that the background prediction is overestimated with respect to the data yields in the analysis control regions and the extracted transfer factors associated to the multi-jet, $W+\text{jets}$ and $t\bar{t}+\text{jets}$ backgrounds can be summarized as

$$\hat{\mu}_{\text{multi-jet}} \approx 0.95, \qquad \hat{\mu}_W \approx 0.6, \qquad \hat{\mu}_{t\bar{t}} \approx 0.9. \tag{11.12}$$

Figure 11.5 shows the pre-fit CR yields and the same yields after the multi-bin fit procedure and the application of $\hat{\mu}_W, \hat{\mu}_{t\bar{t}}$ and $\hat{\mu}_{\text{multi-jet}}$. After the background-only

fit, no large shape mismodelling is observed in the three M_J^Σ bins of the W, $t\bar{t}$ and multi-jet Control Regions (WCR, TCR and QCR).

Figure 11.6 reports the yields of the $\mathtt{VR}_{\mathcal{S}(E_T^{miss})}$ and $\mathtt{VR}_{N_{jets}}$ validation regions after the multi-bin fit procedure. In these figures, we can see that the final backgrounds are in good agreement with data when systematic uncertainties are considered, showing the goodness of the background estimation in the signal regions. Multi-bin signal regions yields are reported in Figure 11.7a, 11.7b and 11.7c, where no significant excess with respect to the background estimation has been observed.

11.2.2 *Single-bin fit*

The *single-bin fit* configuration considers a separate fitting procedure for each selection of N_{jets}, $N_{b\text{-jets}}$ and M_J^Σ. In this context, a channel is defined by an associated set of Signal, Validation and Control Regions as described in Section 10.4.5. This fit approach is only applied to Signal Regions where the M_J^Σ and $N_{b\text{-jets}}$ are inclusive, *i.e.* on 80 GeV and high jet multiplicity 50 GeV signal regions ($N_{jets}^{50} = 11, 12$). Identically to the multi-bin fit regions, the estimation of the multi-jet background is provided in each region using the template estimation described in Section 10.6.2.

Normalization factors $\mu_W, \mu_{t\bar{t}}$ and $\mu_{multi\text{-}jet}$ are defined for each of these three background components and determined after fitting the data in CRs minimizing the Negative Log Likelihood as documented in 11.2. MC modeling and detector systematics are applied as gaussian-constrained *nuisance parameters* (NPs) to each of the MC predictions, while template uncertainties were similarly applied to the template prediction (see Section 11.2).

Figure 11.4 reports the single-bin background-only transfer factors obtained after background-only fit for the single-bin signal region (bins 4-11). From the estimated transfer factors we can see the agreement of the single-bin fit and the multi-bin fit results. Figure 11.8 shows the yields for different associated signal, control and validation regions after the single-bin fit procedure. A summary plot of the post-fit event yields in these signal regions is provided in Figure 11.7d. The agreement between data and background prediction shows no evidence for new physics in the boosted 80 GeV regions and in the high jet multiplicity signal regions with $p_T > 50$ GeV.

Figure 11.9 shows a selection of $\mathcal{S}(E_T^{miss})$ distributions comparing data and total background for several single-bin signal regions. Here, it is possible to note the remarkable agreement between the background estimation and the data across the complete $\mathcal{S}(E_T^{miss})$ distribution, even in event selections with large jet multiplicities ($N_{jets}^{50} \geqslant 12$).

11.3 STATISTICAL TESTS AND MODEL-INDEPENDENT FIT

We often want to evaluate hypotheses about our dataset and to do that according to a certain *confidence level*. In order to achieve this goal, *statistical tests* are performed using a *null hypothesis* H_0 that we would like to ideally reject and an *alternative*

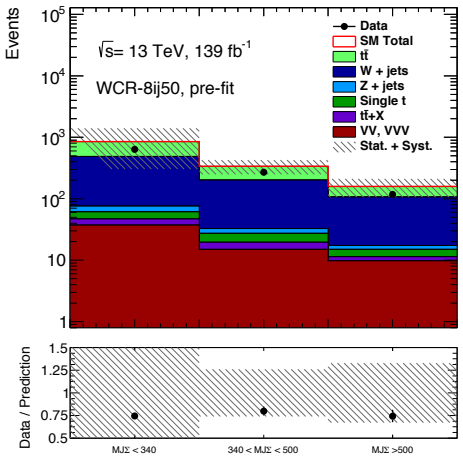

(a) $W+$jets CR, pre-fit

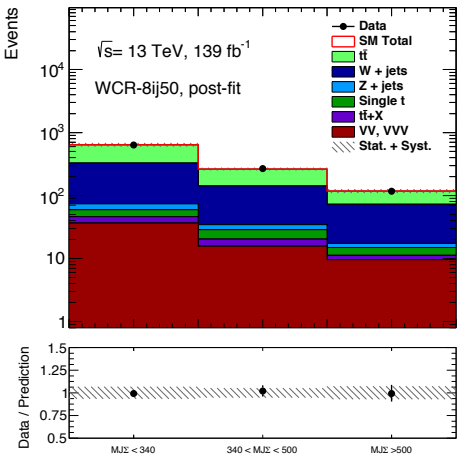

(b) $W+$jets CR, post-fit

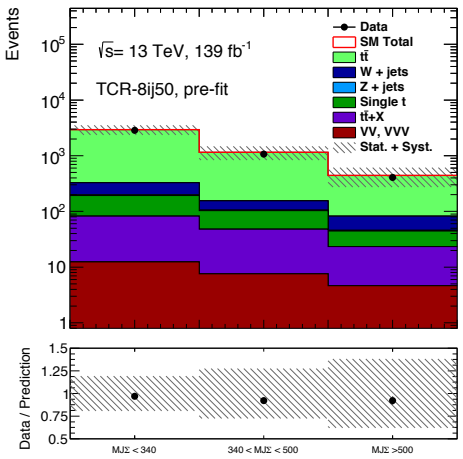

(c) $t\bar{t}$ CR, pre-fit

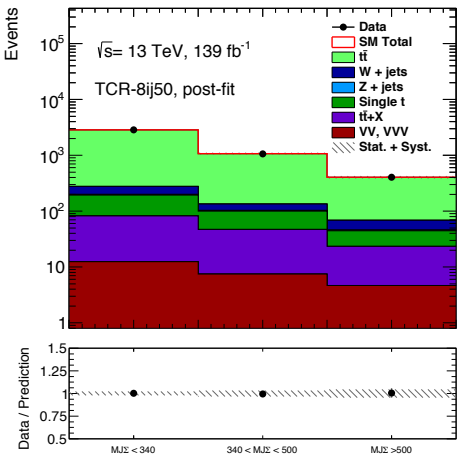

(d) $t\bar{t}$ CR, post-fit

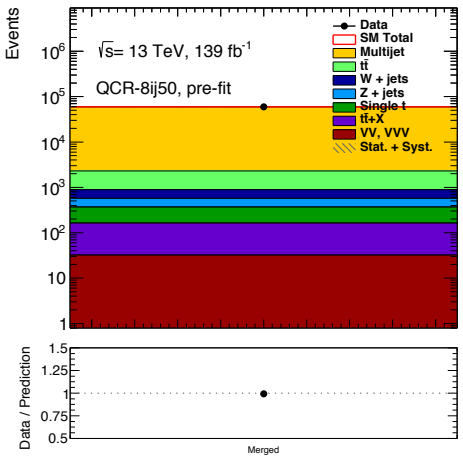

(e) QCR, pre-fit

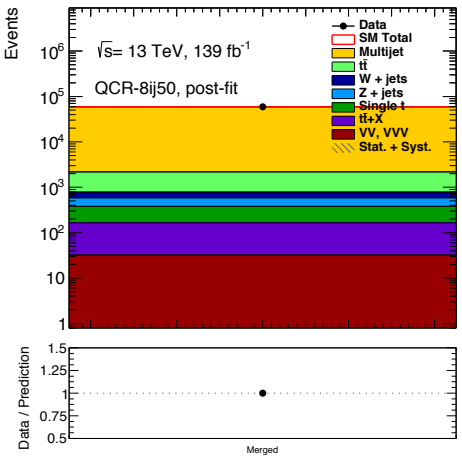

(f) QCR, post-fit

Figure 11.5 – Pre-fit (left) and post-fit (right) yields in the $W+$jets (top), $t\bar{t}$ (middle) and multi-jet (bottom) control regions. Results are reported after the multi-bin fit of the $N_{jets}^{50} \geqslant 8$ signal regions. `WCR`, `TCR` and `QCR` corresponds to the $W+$jets, $t\bar{t}+$jets and Multi-jet Control Regions.

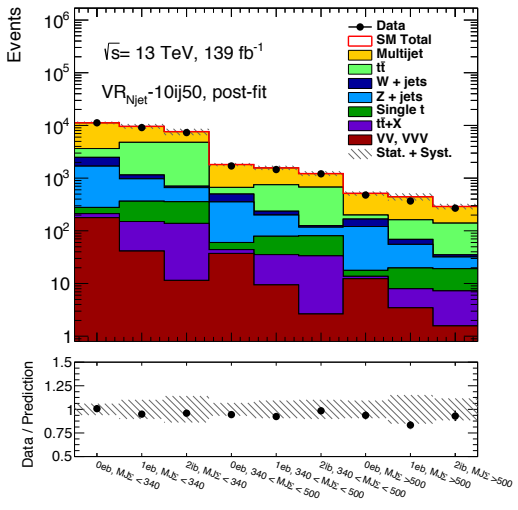

(a) $VR_{N_{jets}}$

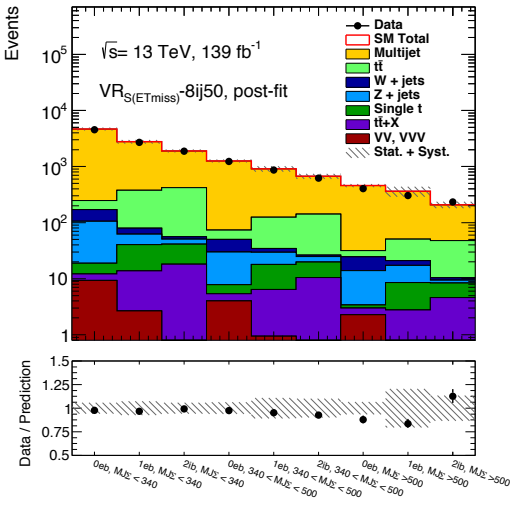

(b) $VR_{\mathcal{S}(E_T^{miss})}$, $N_{jets}^{50} \geqslant 8$

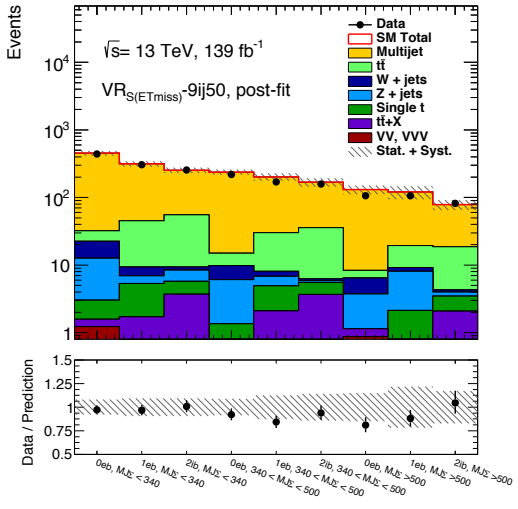

(c) $VR_{\mathcal{S}(E_T^{miss})}$, $N_{jets}^{50} \geqslant 9$

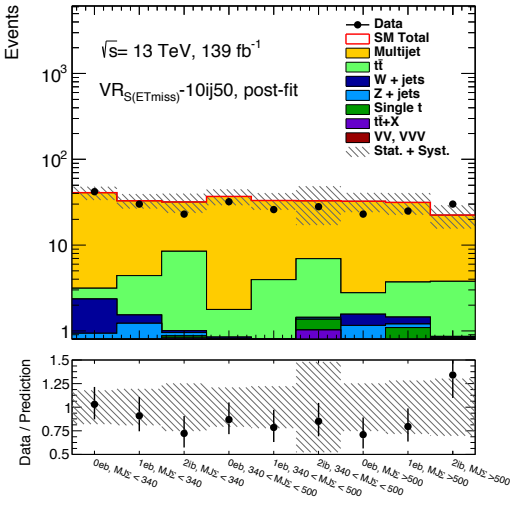

(d) $VR_{\mathcal{S}(E_T^{miss})}$, $N_{jets}^{50} \geqslant 10$

Figure 11.6 – Post-fit yields for the $VR_{N_{jets}}$ and $VR_{\mathcal{S}(E_T^{miss})}$ validation regions. Results are reported after the multi-bin fit of the $N_{jets}^{50} \geqslant 8, 9, 10$ signal regions.

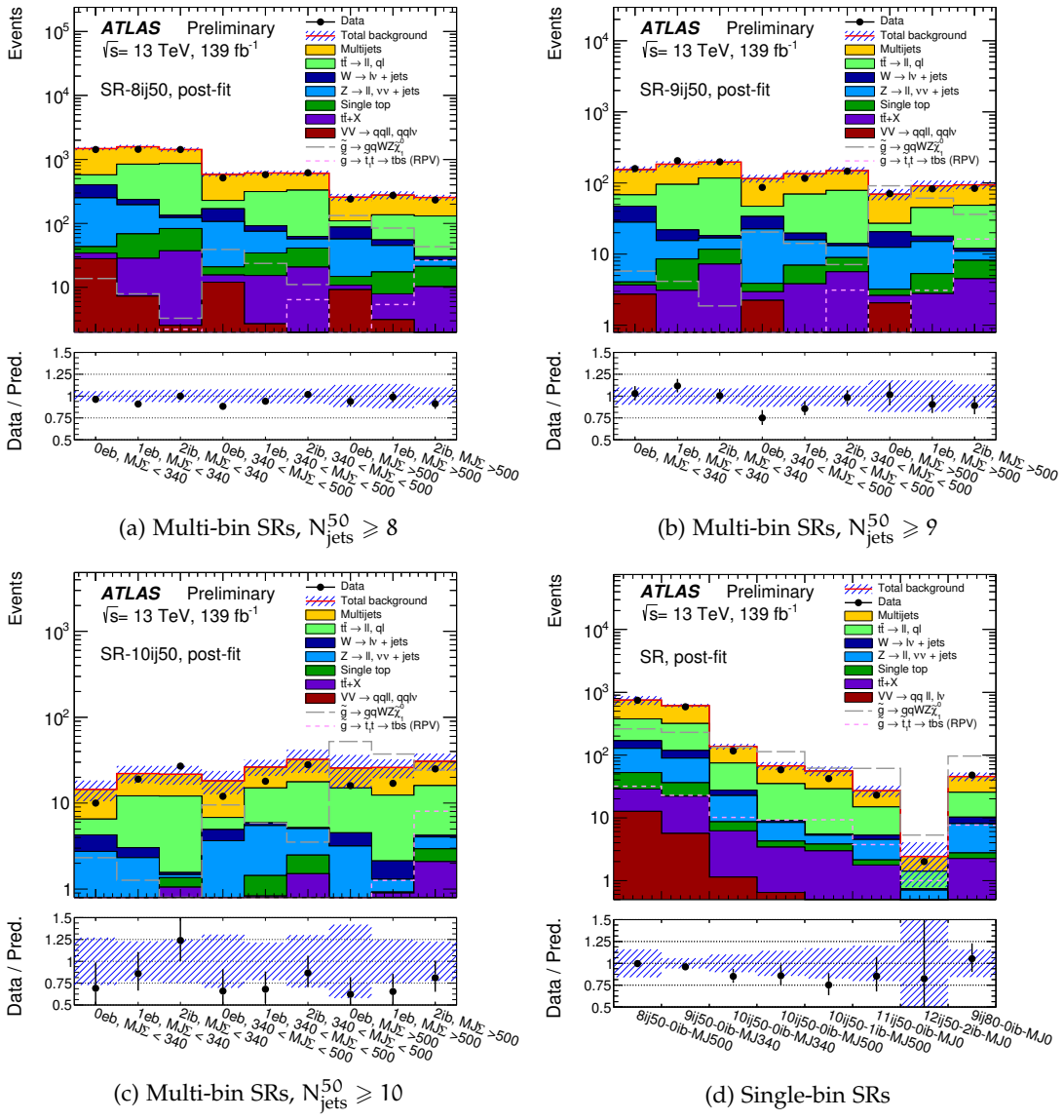

(a) Multi-bin SRs, $N_{jets}^{50} \geqslant 8$

(b) Multi-bin SRs, $N_{jets}^{50} \geqslant 9$

(c) Multi-bin SRs, $N_{jets}^{50} \geqslant 10$

(d) Single-bin SRs

Figure 11.7 – Post-fit yields in the multi-bin and single-bin signal regions of the analysis. No excess with respect to the Standard Model prediction has been observed.

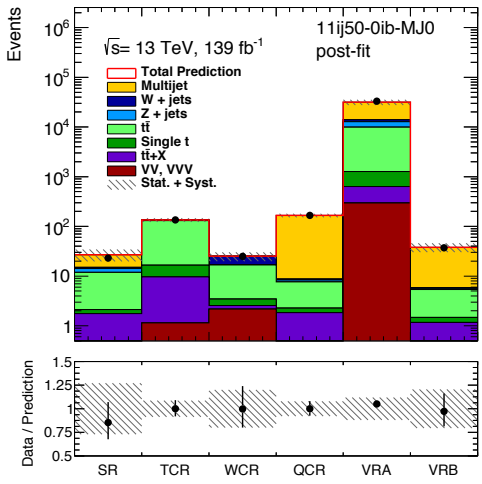

(a) $N_{\text{jets}}^{50} = 11, N_{\text{b-jets}} \geqslant 0$

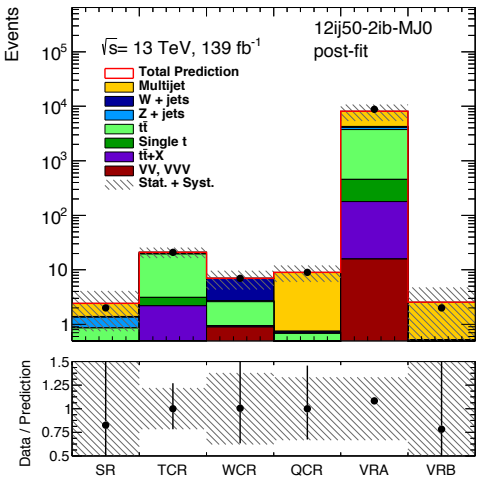

(b) $N_{\text{jets}}^{50} = 12, N_{\text{b-jets}} \geqslant 2$

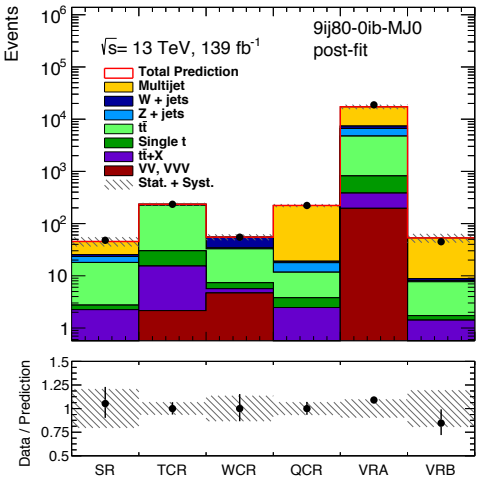

(c) $N_{\text{jets}}^{80} = 9, N_{\text{b-jets}} \geqslant 0$

Figure 11.8 – Post-fit yields summaries in different control, validation and signal regions for the single-bin fit configuration.

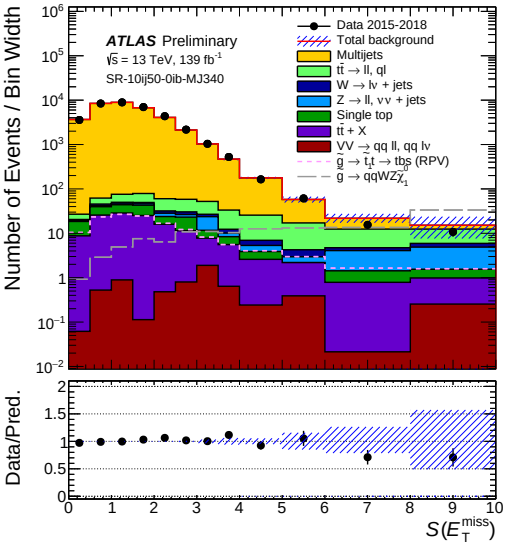

(a) $N_{jets}^{50} \geqslant 10$, $M_J^{\Sigma} > 340\,GeV$

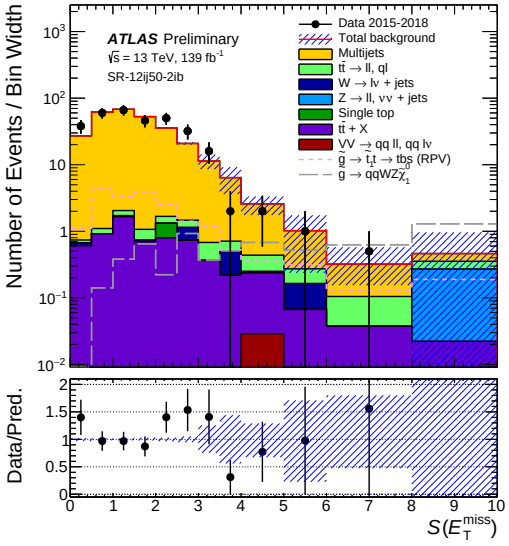

(b) $N_{jets}^{50} \geqslant 12$, $N_{b\text{-jets}} \geqslant 2$

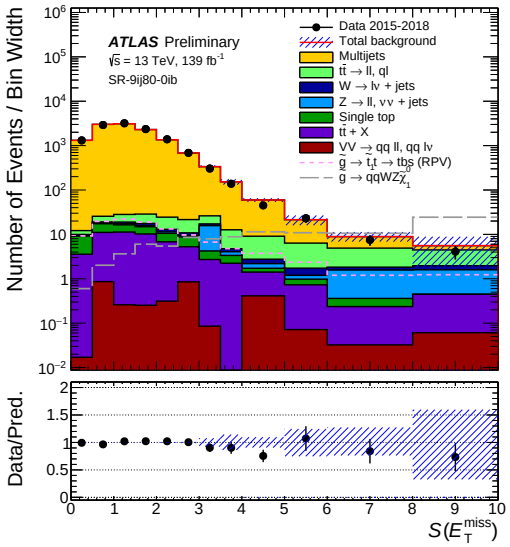

(c) $N_{jets}^{80} \geqslant 9$

Figure 11.9 – Distribution of $\mathcal{S}(E_T^{miss})$ in several signal regions [4]. The $t\bar{t}$ and $W+$jets backgrounds have been normalised according to the background fits, and the multijet background subtraction adjusted accordingly.

hypothesis H_1 that we would to accept in case of rejection of H_0. In searches for SUSY, we generally formulate two types of procedures for statistical tests:

- The *discovery test*, allowing to evaluate if we have effectively observed some sort of signal in the designed signal regions. This statistical test considers as null hypothesis H_0 the fact of having purely background in our data and an alternative hypothesis H_1 corresponding to the observation of signal and background in the analysis signal regions. In case of discovery, the null hypothesis H_0 must be rejected while the alternative hypothesis H_1 must be accepted.
- The *exclusion test*, allowing to find a certain amount of signal which is not rejected by our data according to a certain confidence level.

When we test different hypothesis, the Neyman-Pearson Lemma implies that the optimal discriminator for comparing hypothesis is the likelihood ratio

$$\frac{L(H_0; \text{data})}{L(H_1; \text{data})}. \tag{11.13}$$

11.3.1 *Discovery test and model-independent fit*

In order to test the potential discovery of new physics in the analysis signal regions, a discovery fit is performed by reintroducing a signal to the background-only likelihood defined in Equation (11.9). Using the general profile likelihood definition of Equation (11.8) we can inject one signal event in the analysis bin i and scale it by a transfer factor μ_{sig} by defining

$$S_i = \mu_{sig} \cdot 1. \tag{11.14}$$

μ_{sig} becomes then a parameter of the fit which can be estimated together with the other background transfer factors defined in Equation (11.11) . This approach does not consider any signal contamination in the control and validation regions. Additionally, this fit is considered as *model-independent* due to the usage of a general signal contamination of 1 inside the single signal regions.

By noting with μ the signal strength μ_{sig} and by considering the other transfer factors as nuisance parameters of the model θ, the *discovery test* is performed using the profile likelihood ratio defined by

$$\lambda(\mu) = \frac{L\left(\mu; \hat{\hat{\theta}}\right)}{L\left(\hat{\mu}; \hat{\theta}\right)}, \tag{11.15}$$

where $\hat{\mu}$ and $\hat{\theta}$ are the maximum likelihood estimators and $\hat{\hat{\theta}}$ is the maximum likelihood estimator for a fixed value of μ. The value of $\hat{\mu}$ is forced to be positive such that only physical signals can be tested. By definition, we can see that $0 < \lambda(\mu) \leqslant 1$ where $\lambda(\mu)$ close to 1 means that the signal strength μ is in good agreement with the observed data. Figure 11.10 shows a comparison between the background-only and a discovery fit for an RPV grid point with $m_{\tilde{g}} = 1.4\,\text{TeV}$, $m_{\tilde{t}} = 600\,\text{GeV}$. After the fit, it is possible to see that the signal strength $\hat{\mu}_{sig}$ is set to zero.

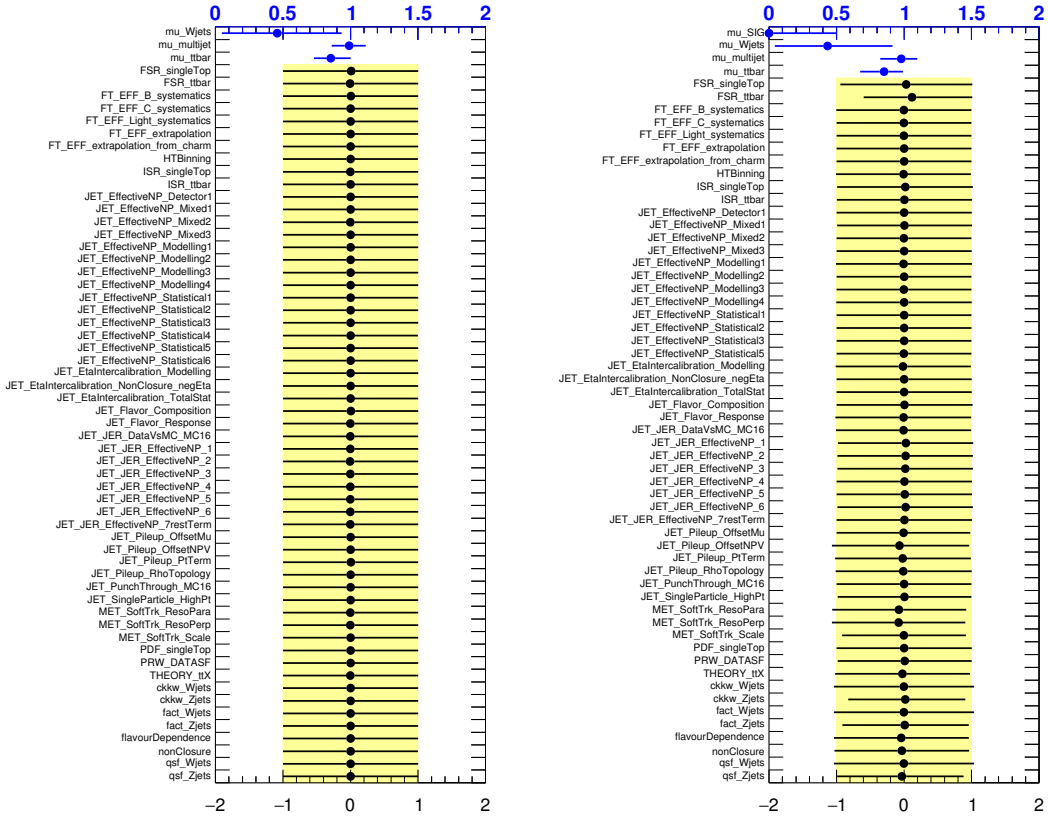

(a) Background-only fit

(b) Exclusion fit

Figure 11.10 – Post-fit parameters and uncertainties for the $N_{jets}^{50} \geqslant 11$ single-bin regions. The results of the background-only fit are shown on the left, and the exclusion fit configuration is shown on the right for an RPV grid point with $m_{\tilde{g}} = 1.4\,TeV$, $m_{\tilde{t}} = 600\,GeV$. Nuisance parameters for systematic uncertainties are shown in black points, while blue points indicate transfer factors, including also the signal strength μ_{sig}.

The *discovery test statistic* is defined as

$$q_0 = \begin{cases} -2\ln\lambda(0) & \text{for } \hat{\mu} \geqslant 0, \\ 0 & \text{for } \hat{\mu} < 0, \end{cases} \tag{11.16}$$

where the background-only hypothesis is the null-hypothesis that we want to reject. The *discovery p-value* represents, given a certain data observation, the fraction of outcomes that allows to accept the alternative hypothesis H_1 (*i.e.* there is signal) while the null-hypothesis H_0 (*i.e.* we have pure backgrounds in our SRs) is true and it can be written as

$$p_0 = \int_{q_0^{obs}}^{\infty} f(q_0|H_0)dq_0 = \int_{q_0^{obs}}^{\infty} f(q_0|\mu = 0)dq_0. \tag{11.17}$$

$f(q_0|H_0)$ represents the PDF of q_0 assuming the background-only hypothesis $\mu = 0$, which can be determined using different background-only pseudo-experiments or, in the asymptotic regime (*i.e.* large number of events) using an analytical approximation [108].

The *discovery significance* Z associated to the p-value p_0 can be defined as

$$Z = \Phi^{-1}(1 - p_0) \tag{11.18}$$

where

$$\Phi(Z) = \int_{-\infty}^{Z} G(x; 0, 1)dx \tag{11.19}$$

and $G(x; 0, 1)$ represents a unit gaussian defined as in Equation (11.2).

11.4 EXCLUSION LIMITS ON RPC MODELS

Exclusion limits can be set by finding a certain number of signal events (*i.e.* a value of μ) for which the exclusion p-value associated to the exclusion test statistic

$$q_\mu = \begin{cases} -2\ln\lambda(\mu) & \text{for } \mu \geqslant \hat{\mu}, \\ 0 & \text{for } \mu < \hat{\mu}, \end{cases} \tag{11.20}$$

corresponds to 5%. Similarly to the discovery p-value, the exclusion p-value can be defined as

$$p_\mu = \int_{q_\mu^{obs}}^{\infty} f(q_\mu|\mu)dq_\mu, \tag{11.21}$$

and the PDF $f(q_\mu|\mu)$ can be estimated by creating several signal-plus-background pseudo-experiments for a fixed value of μ. The value of μ allowing to fix $p_\mu = 0.05$ corresponds to the 95% confidence upper limit on the number of signal events in the signal region, and it is noted as S_{obs}^{95}. As previously explained, this procedure allows to set an upper limit on the number of signal events to which the analysis is sensitive to. However, a low upper limit (*i.e.* a good exclusion) on a certain physics model might be achieved when the analysis has little or no sensitivity to new physics and when the data fluctuates down with respect to the background-only hypothesis. The large exclusion of a certain signal model resulting from an unsensitive analysis is

an unwanted feature of these exclusion limits. In order to protect against this effect, the convention used by the ATLAS SUSY group is to adopt the conservative CL_s prescription [109], where the p-value of the signal-plus-background hypothesis is normalized by the power $1 - p_0$ of the background-only test

$$p_\mu^{CL_s} = \frac{p_\mu}{1 - p_0}. \tag{11.22}$$

This quantity represents the new p-value for a given signal strength μ and it replaces p_μ. The exclusion limits presented in the next part of this thesis are all computed using this CLs approach.

Figure 11.11 and 11.12 report the 95% CL exclusion limits computed using the CL_s prescription previously described. These figures report the expected and observed limits in the multi-bin and single-bin approach described in the previous sections. The multi-bin approach allows to better contrain the signal and background systematics in the various analysis regions due to the larger amount of data points accessible by the fit, allowing to set stronger limits on simplified models than the single-bin fit. Additionally, the limits obtained using the previous version of this analysis using $36\,fb^{-1}$ of Run 2 data [6] are shown, illustrating the improvements obtained from this new fit approach and increased statistic. In the two-step gluino decay grid, the exclusion limits of the gluino mass are improved up to 200 GeV reaching an exclusion on the gluino mass of 2 TeV. The exclusion limits on the neutralino mass are also significantly improved, excluding neutralinos up to a mass of 1 TeV. Similar values are reported also for the gtt model, where the mass limits are improved for the gluino up to 1.8 TeV and 1 TeV for the neutralino.

Table 11.1 reports several exclusion parameters resulting from the single-bin exclusion and discovery fits, including the 95% CL upper limit on the number of expected and observed signal events S_{exp}^{95} and S_{obs}^{95}.

Signal channel	$\langle\epsilon\sigma\rangle_{obs}^{95}$ [fb]	S_{obs}^{95}	S_{exp}^{95}	$p(s=0)$ (Z)
$N_{jets}^{50} \geqslant 8$, $M_J^\Sigma > 500$ GeV	1.16	163	162^{+33}_{-39}	0.50 (0.00)
$N_{jets}^{50} \geqslant 9$, $M_J^\Sigma > 340$ GeV	0.95	133	140^{+30}_{-31}	0.50 (0.00)
$N_{jets}^{50} \geqslant 10$, $M_J^\Sigma > 340$ GeV	0.22	31	40^{+15}_{-11}	0.50 (0.00)
$N_{jets}^{50} \geqslant 10$, $M_J^\Sigma > 500$ GeV	0.16	21.9	$25.9^{+9.6}_{-6.8}$	0.50 (0.00)
$N_{jets}^{50} \geqslant 10$, $M_J^\Sigma > 500$ GeV, $N_{b\text{-jets}} \geqslant 1$	0.12	16.8	$22.8^{+8.5}_{-6.1}$	0.50 (0.00)
$N_{jets}^{50} \geqslant 11$	0.09	13.0	$15.1^{+6.0}_{-4.2}$	0.50 (0.00)
$N_{jets}^{50} \geqslant 12$, $N_{b\text{-jets}} \geqslant 2$	0.04	5.0	$5.2^{+2.5}_{-1.7}$	0.50 (0.00)
$N_{jets}^{80} \geqslant 9$	0.18	25.2	$24.5^{+7.0}_{-6.3}$	0.41 (0.22)

Table 11.1 – Left to right: 95% CL upper limits on the visible cross-section ($\langle\epsilon\sigma\rangle_{obs}^{95}$) and on the number of signal events (S_{obs}^{95}). The third column (S_{exp}^{95}) shows the 95% CL upper limit on the number of signal events, given the expected number (and $\pm1\sigma$ excursions around the expectation) of background events. The last column indicates the discovery p-value ($p(s=0)$), together with the corresponding Gaussian significance (Z).

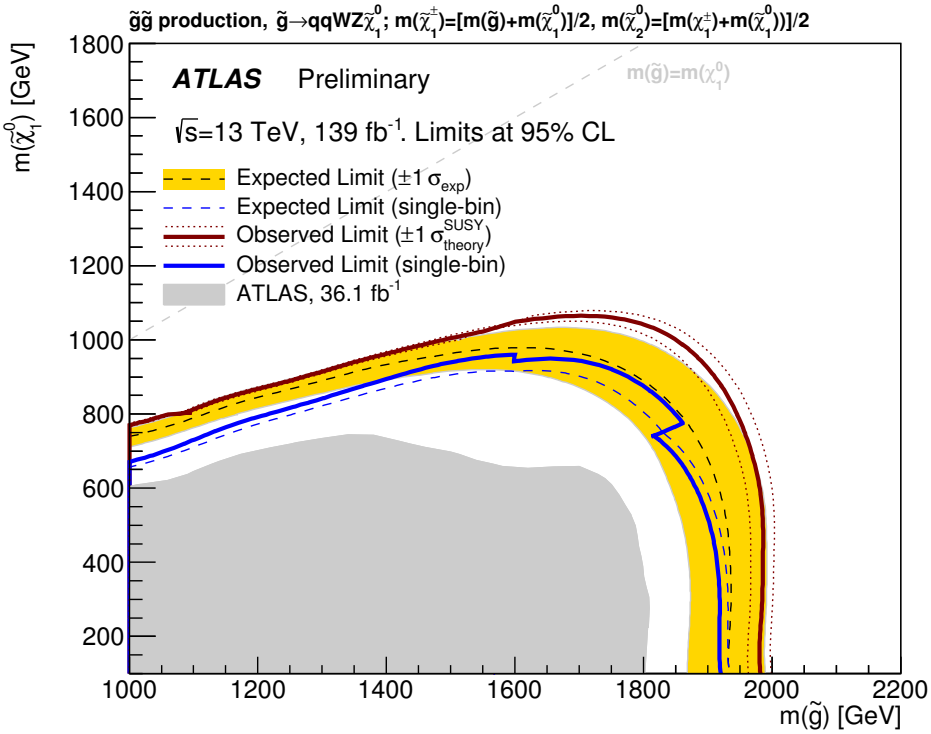

Figure 11.11 – Exclusion limits on the two-step gluino decay. The solid maroon line indicates the observed exclusion limit at 95% CL_S, which is the combination of the individual limits from the multi-bin signal selections on the basis of the best expected exclusion sensitivity. A dashed black line and yellow band respectively indicate the expected limit and its 1σ excursions due to all uncertainties on the signal acceptance and background yields. For illustration, the dashed and solid blue lines show the expected and observed limits considering the single-bin discovery selections only. Grey shading is used to demarcate the observed limit from the previous publication [6].

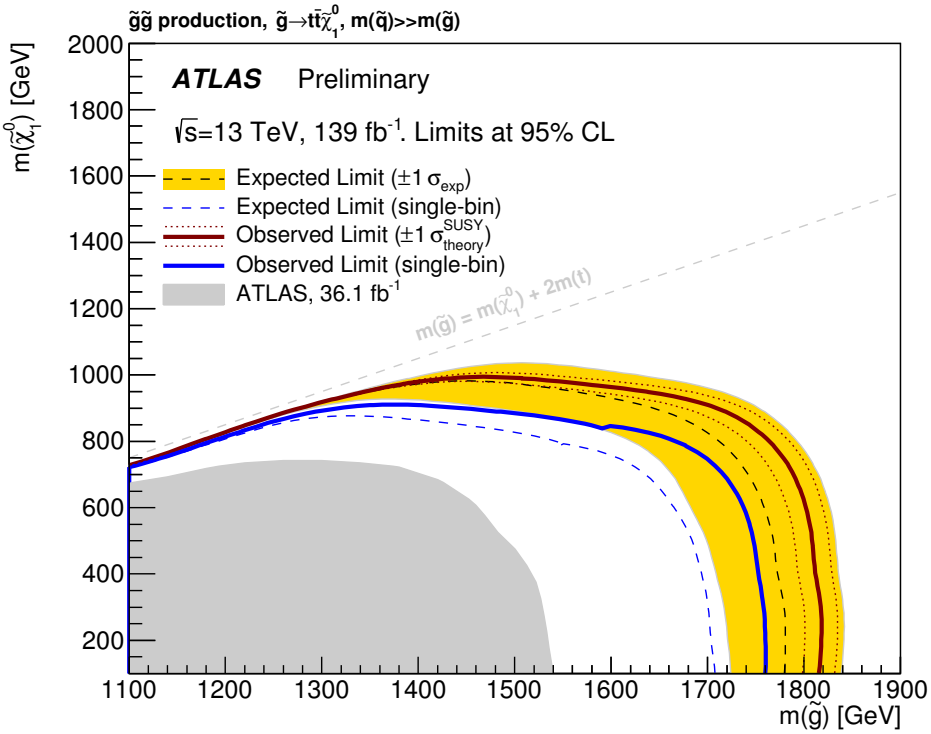

Figure 11.12 – Exclusion limits on the gtt model. The solid maroon line indicates the observed exclusion limit at 95% CL_S, which is the combination of the individual limits from the multi-bin signal selections on the basis of the best expected exclusion sensitivity. A dashed black line and yellow band respectively indicate the expected limit and its 1σ excursions due to all uncertainties on the signal acceptance and background yields. For illustration, the dashed and solid blue lines show the expected and observed limits considering the single-bin discovery selections only. Grey shading is used to demarcate the observed limit from the previous publication [6].

11.5 EXCLUSION LIMITS ON RPV MODELS

Despite the large set of searches for supersymmetry performed by the ATLAS experiment, no evidence for supersymmetric particles has been observed today at the LHC. However, due to the lower E_T^{miss} and large jet multiplicities characterizing R-parity violating (RPV) SUSY scenarios (see Chapter 3 for further details) the analysis described in this work is well suited for studying also these SUSY scenarios. In this section are reported the results obtained from the reinterpretation of the $36\,fb^{-1}$ multi-jet search [6] in the context of different R-parity violating SUSY scenarios [7]. As a matter of fact, the low $S(E_T^{miss})$ cut applied in this analysis also allows to probe SUSY signals with lower E_T^{miss} implied by the RPV SUSY scenarios.

For the RPV grid described in Section 10.2.4, exclusion limits have also been improved by the $139\,fb^{-1}$ Run 2 search as illustrated in Figure 11.13. In particular, the gluino mass reach is improved, reaching an exclusion limit at a maximum of $1.55\,TeV$ and $1.1\,TeV$ for the neutralino mass. The analysis is particularly sensitive to this RPV model due to the presence of semi-leptonic decays of top quarks that, mainly though hadronically-decaying τ leptons, increase the E_T^{miss} of this RPV model making it visible in the analysis signal regions.

Depending on the strength of the RPV couplings $\lambda, \lambda', \lambda''$ described in Section 3.2.3, the introduction of these couplings makes the SUSY LSP unstable, allowing the decay to Standard Model particles after a certain *LSP lifetime* τ_{LSP}. The value of τ_{LSP} depends on these RPV coupling strengths as well as the masses of the sfermions implied in the decay. Most ATLAS searches for RPV SUSY assume coupling values which are large enough to ensure prompt decays of the SUSY LSP. However, intermediate values of τ_{LSP} can be probed by RPC analyses when the LSP decays out of the detector volume due to very small values of the RPV couplings or even inside the detector acceptance, when RPV coupling values are larger. In this context, the RPV-RPC reinterpretation [7] made in 2018 allowed to compare different RPC analyses in order to constrain even further the RPV couplings which are not excluded by current experimental results. A review of the signal models and results provided in this reinterpretation are provided in the rest of this section.

11.5.1 *RPV signals*

For the reinterpretation of the multi-jet analysis, several RPV signals have been generated by setting all the couplings λ and λ' to zero and by variating a single baryon-number-violating coupling λ''_{ijk} at the time. In these models, the LSP is assumed to be lightest neutralino $\tilde{\chi}_1^0$, which is purely bino-like and has a mass of $200\,GeV$. This mass value has been chosen in order to allow the decay of the neutralino to a top quark while the choice of a bino-like neutralino has been done in order to simplify the model by removing charginos from the SUSY decay.

In the context of the multi-jet analysis, two signal models have been considered:

GQQ MODEL

This model contains light gluinos and the LSP, with a non-zero λ''_{112} RPV

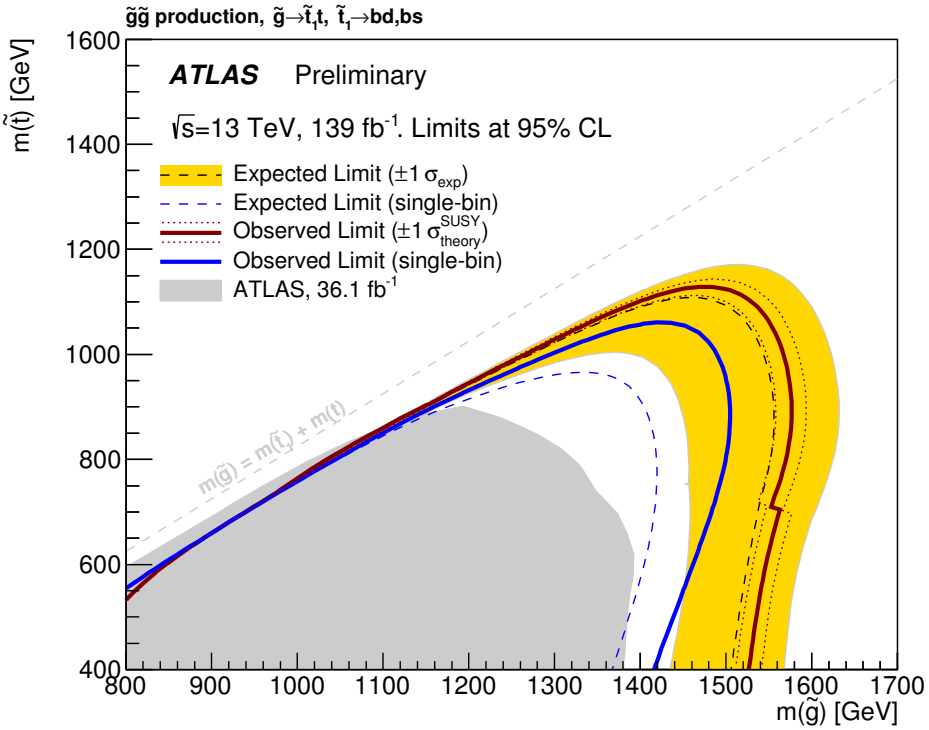

Figure 11.13 – Exclusion limits on the RPV model. The solid maroon line indicates the observed exclusion limit at 95% CL_S, which is the combination of the individual limits from the multi-bin signal selections on the basis of the best expected exclusion sensitivity. A dashed black line and yellow band respectively indicate the expected limit and its 1σ excursions due to all uncertainties on the signal acceptance and background yields. For illustration, the dashed and solid blue lines show the expected and observed limits considering the single-bin discovery selections only. Grey shading is used to demarcate the observed limit from the previous publication [6].

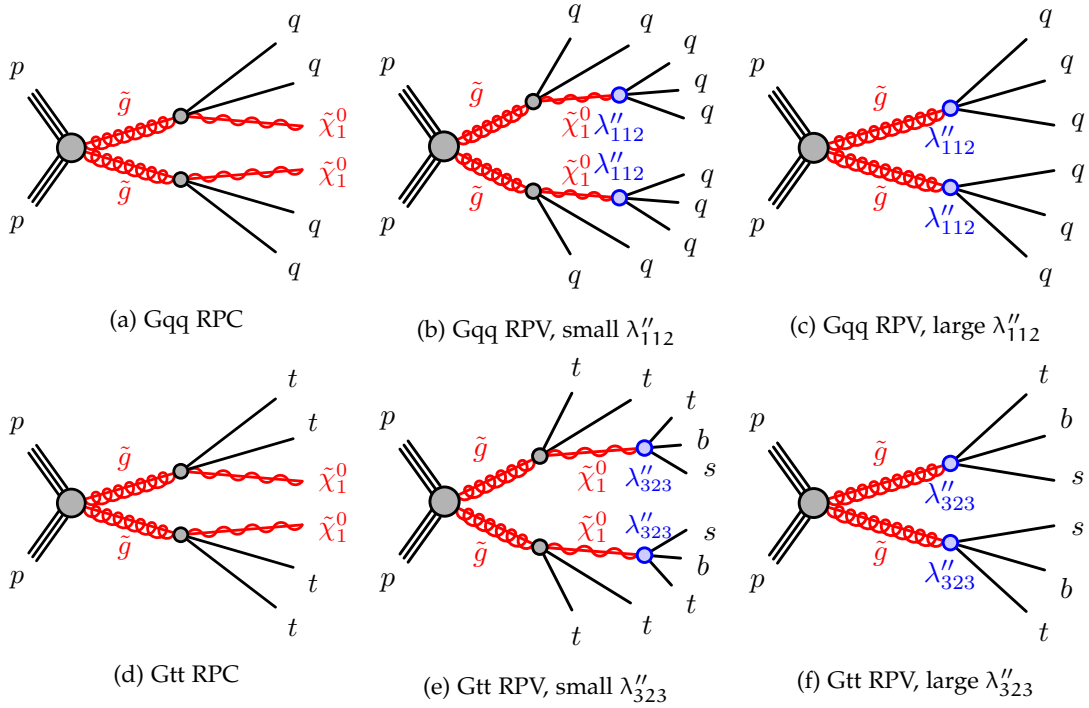

(a) Gqq RPC (b) Gqq RPV, small λ''_{112} (c) Gqq RPV, large λ''_{112}

(d) Gtt RPC (e) Gtt RPV, small λ''_{323} (f) Gtt RPV, large λ''_{323}

Figure 11.14 – Feynman diagrams of Gqq and Gtt models [7].

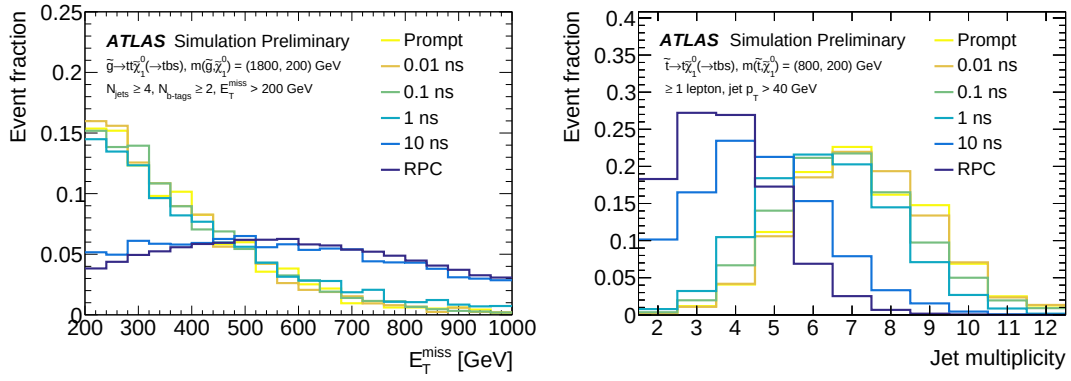

Figure 11.15 – E_T^{miss} and N_{jets} of different SUSY LSP lifetimes τ_{LSP}. The shown models are the Gtt model and the Stop model described in [7].

coupling and all the other couplings equal to zero. In the RPC case, the gluino decays to the lightest neutralino $\widetilde{\chi}_1^0$ through the virtual squark decay

$$\widetilde{g} \to qq\widetilde{\chi}_1^0, \tag{11.23}$$

where $q = (u, d, s, c)$. The mass of the LSP is fixed at 200 GeV. When the RPV coupling λ''_{112} is introduced, the LSP can decay through $\widetilde{\chi}_1^0 \to qqq$. For large values of λ''_{112}, the gluino simply decays as

$$\widetilde{g} \to qqq. \tag{11.24}$$

The masses of the other squarks are assumed to be 3 TeV while the masses of the other sfermions are assumed to be above 5 TeV, including third generation squarks.

GTT MODEL

This model contains light gluinos and the LSP, with a non-zero λ''_{323} RPV coupling and all the other couplings equal to zero. The gluinos are pair-produced and decays through a virtual top squark as

$$\widetilde{g} \to tt\widetilde{\chi}_1^0. \tag{11.25}$$

The produced top quarks can further decay to a bottom quark and two light quarks or a lepton-neutrino pair. The mass of the LSP is fixed at 200 GeV. When λ''_{323} becomes larger, the neutralino can decay to another top quark and a bottom and strange quark $\widetilde{\chi}_1^0 \to tbs$ while when this coupling is very large the total decay chain is

$$\widetilde{g} \to tbs. \tag{11.26}$$

The masses of the third generation squarks are assumed to be 2.4 TeV while the masses of the first- and second-generation squarks are assumed to be larger than 5 TeV. This choice of the third-generation squark mass is made in order to ensure that the branching fraction of $\widetilde{g} \to tbs$ is non-negligible before the prompt decay regime is reached.

The Feynman diagrams associated to these two models are shown in Figure 11.14. Due to the additional decay of the LSP to Standard Model particles, the expected signature for increasing values of λ'' is large number of jets and moderate E_T^{miss}. Figure 11.15 reports the distributions associated to these quantities for different LSP lifetimes and simulated signal models [7], showing the expected behaviors when λ'' starts to become important.

11.5.2 *Results*

Figure 11.16 shows the 95% CL exclusion limits derived using the profile likelihood-ratio test described in Section 11.2. The results are reported for both Gtt and Gqq model.

For the Gqq model, the results are reported as a function of the neutralino lifetime and the gluino branching ratio, as well as the RPV coupling λ''_{112} strength. Due to

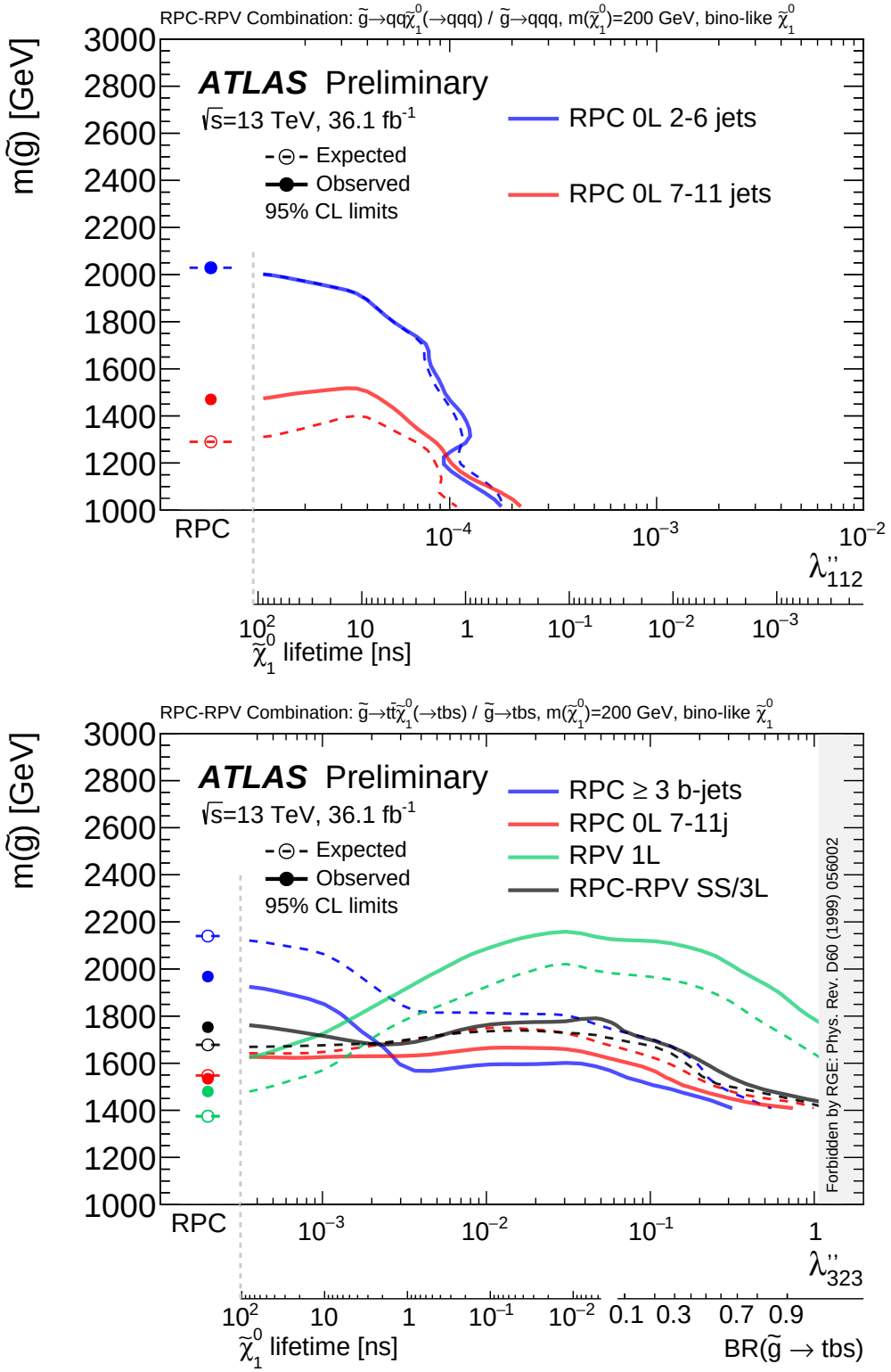

Figure 11.16 – 95% CL exclusion limits for the Gtt and Gqq model. The red line represents the reinterpretation of the multi-jet (7-11 jets) analysis [6]. The other reinterpreted analyses include the RPC zero-lepton 2-6 jets analysis [110], the RPC multi-b analysis (3 or more b-jets) [111], the RPV 1-lepton analysis [112] and the RPC-RPV same-sign (SS) 3-lepton analysis [113]. Exclusion limits are provided versus the RPV couplings λ''_{112},λ''_{323} as well as the LSP lifetime. In the Gtt model, for high values of λ''_{323} the gluino directly decays to tbs quarks (see Figure 11.14) with variable branching ratio, as illustrated on the picture x-axis.

the characteristics of this model, the RPC zero-lepton 2-6 jets analysis [110] sets the largest limits for this model. The 7-11 multi-jet analysis has reduced sensitivity to this model at low values of λ''_{112} due to the lower jet multiplicity of this signal whereas the sensitivity is reduced at lower values of the neutralino lifetime τ_{LSP} due to the E_T^{miss} cut applied by the analysis. For a neutralino lifetime of 100 ns the existence of a gluino is excluded up to a mass of 2 TeV whereas this value is reduced down to 1 TeV for a lifetime of 1 ns. Due to the similar characteristics between jets initiated by first and second generation quarks, this limit can be extended also to λ''_{ijk} with $i, j, k \neq 3$. No exclusion limits are reported in these figures for $\lambda''_{112} > 10^{-4}$. However, previous searches in all-hadronic final states have set a limit of about 1.2 TeV on the gluino mass when considering the prompt decay $\tilde{g} \to qq\tilde{\chi}_1^0$ [97], and 0.9 TeV when considering the prompt and direct gluino decay to light quarks $\tilde{g} \to qqq$ [114].

The Gtt exclusion limits are very different compared to the Gqq ones, considering that the exclusion limits extend much higher in terms of coupling strength λ''_{323} for RPC analyses. This feature is due to the presence of top quarks in the final state, which can lead to the presence of E_T^{miss} in the final state, making the RPC analyses sensitive also to RPV couplings for this model. For low values of λ''_{323}, the multi-b search [111] is the most sensitive one considering the large cuts on the number of b-jets in the final state and the large presence of top quarks in this specific signals. However, for shorter neutralino lifetimes (*i.e.* larger values of λ''_{323}), the E_T^{miss} cut applied in this analysis reduces the sensitivity to RPV models and the RPV 1-lepton search [112] becomes the most sensitive one. As a matter of fact, this analysis was optimized for the high jet multiplicity resulting from the decay $\tilde{g} \to tt\tilde{\chi}_1^0$ with a consequent disintegration of $\tilde{\chi}_1^0$ through $\tilde{\chi}_1^0 \to tbs$, and it is expected to have the largest sensitivity for high values of λ''_{323}. The multi-jet 7-12 jets analysis has a lower sensitivity compared to these two searches for this model, but it provides a very stable sensitivity for different values of τ_{LSP} if compared to the multi-b and RPV 1-lepton search. This feature confirms the generality of this search and the sensitivity to very different models, including also RPV signals due to its low cut on E_T^{miss}-based quantities.

11.6 IMPACT OF PARTICLE FLOW

In order to understand the impact of the Particle Flow jet and E_T^{miss} reconstruction on the analysis sensitivity, a simplified comparison of the results extracted with the topocluster-only reconstruction was performed. Background predictions and expected 95% CL Upper limits on the BSM event yield were extracted using the template method and the statistical tests described in the previous sections. The comparison is summarised in Table 11.2. In this comparison, only the multijet non-closure and jet energy scale/resolution systematic uncertainties were included in the statistical treatment.

It is found that the background yields from SM processes producing neutrinos are mainly unchanged, whereas the multijet background yields are typically reduced by 25-30%, demonstrating the superior suppression of fake E_T^{miss} when using the PFlow reconstruction. This effect was confirmed using MC simulated fully-hadronic $t\bar{t}$ samples as shown in Figure 11.17. Here, the Particle Flow E_T^{miss} distribution

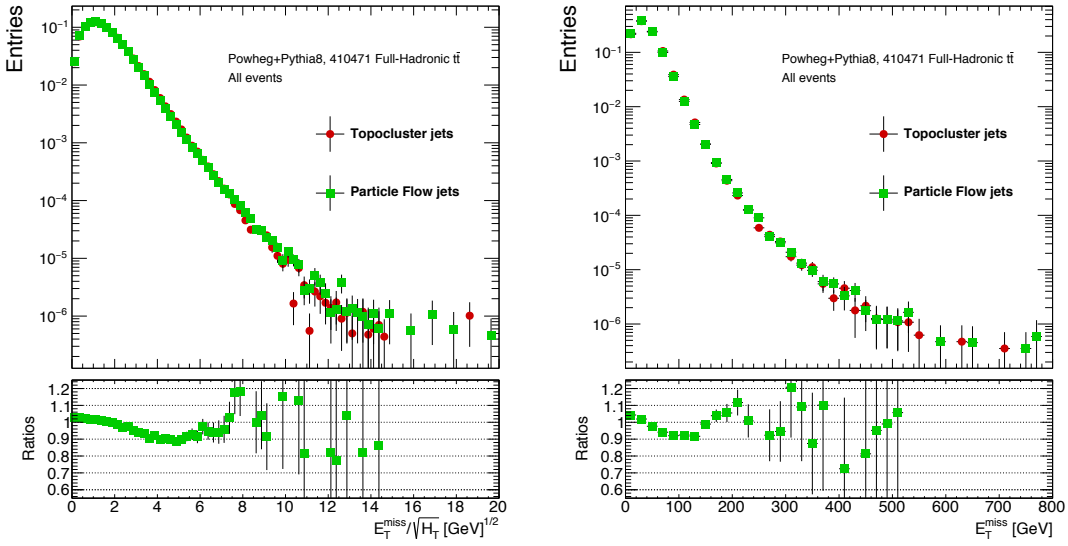

(a) $E_T^{miss}/\sqrt{H_T}$ (b) E_T^{miss}

Figure 11.17 – Comparisons between Particle Flow and Topocluster reconstructions for (a) Event-based E_T^{miss} significance $E_T^{miss}/\sqrt{H_T}$ and (b) E_T^{miss}. The comparison has been made using a MC simulation of full-hadronically decaying top pairs ($t\bar{t}$) with the 2015-2016 pileup conditions.

shows significant enhancements with respect to the topocluster-based approach, indicating better rejection of fake E_T^{miss} backgrounds due to the improved E_T^{miss} reconstruction. Additionally, it has been observed a reduction of the multijet template non-closure uncertainty by approximately 50%. This is an important component of the total background uncertainty, even though it is often not the dominant one. This reduction indicates that when the PFlow reconstruction is used, not only is the multijet background reduced, it is also better determined.

Due to the consistent reduction in overall background yields and a more uneven improvement in background uncertainties, the sensitivity to BSM signals is found to have been improved by up to 30%, when quantified in terms of the upper limit on the number of BSM events.

11.7 COMPARISONS WITH OTHER SEARCHES

The ATLAS Collaboration has published today (March 2020) 154 papers about supersymmetry and, despite the large efforts, no evidence for SUSY particles has been found in Run 1 and 2. Figure 11.18 shows a summary plot for the gluino-neutralino mass plane and the 95% CL exclusion limits of different ATLAS SUSY searches. These limits, even if dependent on the simulated signal models, illustrate the power of this analysis (in light blue) if compared to other SUSY searches. In fact, the long decay chains targeted by this search making it less sensitive than other zero-lepton searches (*e.g.* $\tilde{g} \to q\bar{q}\tilde{\chi}_1^0$) where the short decay chain makes the uncompressed phase space more accessible due to the very clear signature with large the jet p_T and E_T^{miss}. However, the decays associated to these processes become rapidly small when

Signal channel	Jet type	Total SM	Multijet yield	$\sigma_{\text{nonClosure}}$	S^{95}_{exp}	$\Delta S^{95}_{\text{exp}}$
$N^{50}_{\text{jets}} \geqslant 8$, $M^{\Sigma}_{J} > 500\,\text{GeV}$	PFlow	747 ± 47	372 ± 42	10	99^{+36}_{-26}	1.2
	Topocluster	956 ± 63	552 ± 45	17	143^{+175}_{-52}	
$N^{50}_{\text{jets}} \geqslant 9$, $M^{\Sigma}_{J} > 340\,\text{GeV}$	PFlow	612 ± 36	295 ± 35	5.8	91^{+33}_{-25}	0
	Topocluster	738 ± 43	393 ± 32	13	90^{+35}_{-25}	
$N^{50}_{\text{jets}} \geqslant 10$, $M^{\Sigma}_{J} > 340\,\text{GeV}$	PFlow	136 ± 14	62 ± 9	1.2	34^{+14}_{-9}	0.3
	Topocluster	161 ± 16	84 ± 10	3.1	38^{+15}_{-10}	
$N^{50}_{\text{jets}} \geqslant 10$, $M^{\Sigma}_{J} > 500\,\text{GeV}$	PFlow	68 ± 10	33 ± 6	0.9	24^{+11}_{-7}	0.8
	Topocluster	83 ± 21	46 ± 7	2.5	32^{+13}_{-13}	
$N^{50}_{\text{jets}} \geqslant 10$, $M^{\Sigma}_{J} > 500\,\text{GeV}$, $N_{\text{b-jets}} \geqslant 1$	PFlow	56 ± 10	27 ± 6	2.7	19^{+8}_{-5}	0.6
	Topocluster	65 ± 11	35 ± 7	2.7	24^{+10}_{-7}	
$N^{50}_{\text{jets}} \geqslant 11$	PFlow	27 ± 5	12 ± 3	0.6	15^{+6}_{-4}	1.2
	Topocluster	39 ± 9	18 ± 4	1.5	22^{+8}_{-6}	
$N^{50}_{\text{jets}} \geqslant 12$, $N_{\text{b-jets}} \geqslant 2$	PFlow	2.4 ± 1.6	1.0 ± 0.9	0.3	$5.1^{+2.6}_{-1.6}$	0
	Topocluster	2.5 ± 1.8	1.1 ± 0.9	0.2	$5.1^{+2.6}_{-1.6}$	
$N^{80}_{\text{jets}} \geqslant 9$	PFlow	46 ± 7	20 ± 4	2.2	20^{+8}_{+6}	0.25
	Topocluster	57 ± 10	29 ± 5	2.5	22^{+9}_{+6}	

Table 11.2 – Comparison of analysis results for calorimeter (Topocluster) and particle flow (PFlow) jet reconstruction. For each single-bin signal region, results for the two reconstruction methods are compared for the following quantities: the total background yield, the multijet production, the systematic uncertainty due to non-closure in the multijet template estimate ($\sigma_{\text{nonClosure}}$), the expected limit on the number of signal events falling in the SR (S^{95}_{exp}) and the relative increase in S^{95}_{exp} when using Topocluster ($\Delta S^{95}_{\text{exp}}$). Only jet energy scale/resolution and multijet template closure systematic uncertainties have been considered.

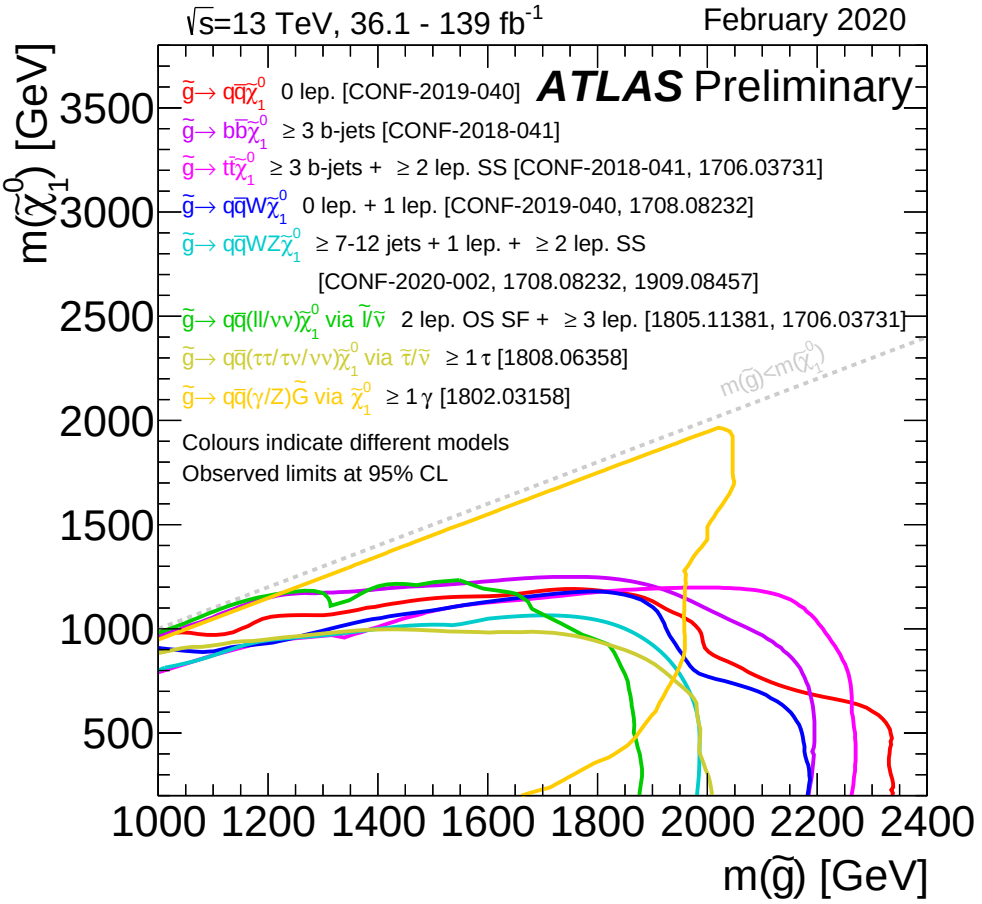

Figure 11.18 – Exclusion limits at 95% CL based on 13 TeV data in the (gluino, lightest neutralino) mass plane for different simplified models featuring the decay of the gluino to the lightest supersymmetric particle (lightest neutralino or gravitino) either directly or through a cascade chain featuring other SUSY particles with intermediate masses. For each line, the gluino decay mode is reported in the legend and it is assumed to proceed with 100% branching ratio. Some limits depend on additional assumptions on the mass of the intermediate states, as described in the references provided in the plot [115].

squark masses increases. Therefore, the $\widetilde{g} \to t\bar{t}\widetilde{\chi}_1^0$ model seems to be more natural as the hierarchy problem imposes stop masses in the order of $O(1\,TeV)$. Even though the zero-lepton multi-jet analysis provided an exclusion up to $1.8\,TeV$ in the iteration using the complete Run 2 dataset, the large number of b-jets in the signals and the $N_{\text{b-jets}} \geqslant 3$ requirement applied by the multi-b analysis makes this latter more sensitive to these kind of models. However, the lower cut applied by the multi-jet analysis due to the usage of multi-jet triggers, makes it sensitive to a portion of the phase space which is inaccessible to the multi-b search.

For the "two-step" model, the zero-lepton multi-jet search described in this work provides the best coverage in the gluino-neutralino mass plane if compared to other sensitive analyses, corresponding to the 1-lepton analysis [116] and the 2 Same-Sign (SS) lepton analysis [117].

11.8 NEW SIGNATURES FOR FLAVOURED DARK MATTER MODELS

Together with other SUSY searches, the results of the ATLAS zero-lepton multi-jet analysis are putting under serious stress our expectations about the naturalness argument and the accessibility of SUSY particles at the LHC. If SUSY does not solve the hierarchy mass problem of the Higgs, the large masses of the gluinos and squarks would also make Dark Matter difficult to be discovered in the LHC p-p collisions due to the low production cross-sections of charginos and neutralinos. However, it must not be forgotten that there is no direct evidence today to have such an intimate connection between the Higgs hierarchy mass problem and the Dark Matter content of the universe, meaning that two different BSM physics models can be considered for these problems, even though one single SUSY model solving everything at once would have been certainly preferable.

In the context of Dark Matter searches at the LHC, several analyses have been performed in the first two runs of the LHC. Commonly explored signatures at the LHC are mono-X signatures, where an object X recoils against E_T^{miss} [118], leading to an observable signal in the ATLAS detector. Additionally, the production of Dark Matter together with heavy flavour quarks has also started to be explored at the LHC [119]. In these simplified models, a Dark Matter particle χ can be produced through the exchange of a colour-neutral scalar or pseudoscalar spin-0 mediator (generally noted ϕ and a, respectively) or a colour-charged scalar mediator ϕ_b.

Different approaches to Dark Matter models has been recently proposed [89] where the presence of a larger number of dark sector states might give rise to final states accessible by the SUSY zero-lepton multi-jet search. Using as guiding principle the fact that the Standard Model seems to be composed only by three quark and lepton families, these models assume that the Dark Matter sector could also be composed of three particles and that, through a colored scalar mediator ϕ, these might be produced in the p-p collisions of the LHC. In this model, these Dark Matter sector particles referred to as χ_u, χ_c and χ_t, couples to up-type quarks through the interaction Lagrangian terms provided by [89]

$$\mathcal{L}_{\text{int}} = \lambda_{ij}\chi_i u_j^c \phi + \text{ h.c.} \tag{11.27}$$

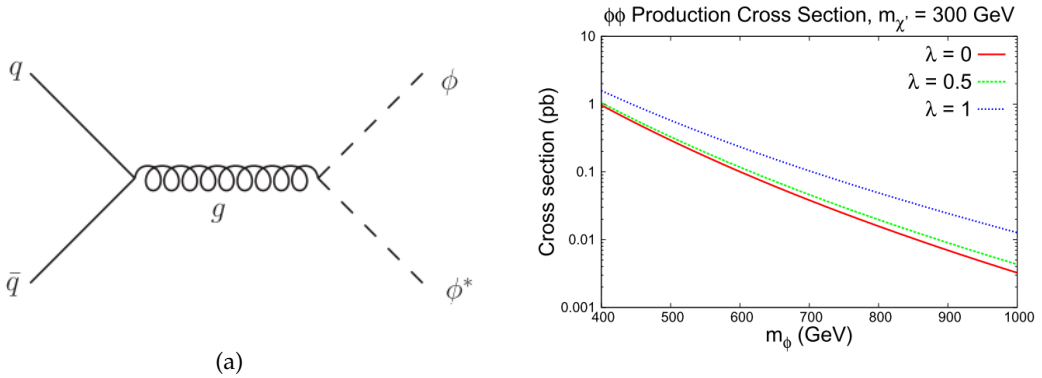

(a) (b)

Figure 11.19 – (a) Dominant ϕ-pair production Feynman diagram and (b)ϕ-pair production cross section [89].

Here, χ_i and u_i^c corresponds to the Dark Matter sector and up-type quark particles with flavour $i = u, c, t$ and colour c. The ϕ scalar mediator is a flavour single but it carries $SU(3)_C$ colour charge, making it interacting also with gluons. The λ_{ij} coupling tensor provides the strength of all the Dark-Matter-Standard-Model interactions for different up-type quarks. Due to the lack of inconsistencies observed in flavour physics, the λ_{ij} tensor is considered to be diagonal in this model (*i.e.* the quark and Dark Matter families are aligned) and, for simplicity reasons, to be characterized by a single value λ for all up-type quarks. Due to this alignment between the new Dark Matter particles and the quark sector, these kind of models are generally known as *Flavoured Dark Matter* (FDM) models.

Given these three new Dark sector particles, this model proposes a relic Dark Matter purely composed of the new top partner χ_t that, due to the low amount of top quarks inside nuclei, can be less accessible by direct Dark Matter detection experiments. However, due to the large presence of strongly-interacting particles in p-p collisions, these scenarios could be more visible at the LHC. Given that the relic Dark Matter is purely composed of χ_t partners and that also χ_u and χ_c (referred to as χ' in the following) must have been abundantly produced in the early stages of the universe, this imposes masses of the χ' partners to be larger than the Dark Matter candidate χ_t (referred to as χ in the following). This makes the χ' unstable and prompt to decay to the χ state, which is stable due to an additional $U(1)$ symmetry. In the assumption that the ϕ can be produced in pairs at the LHC (see Figure 11.20) and considering the mass hierarchy

$$m_\phi > m_{\chi'} > m_\chi, \tag{11.28}$$

this models allows long decays of the ϕ mediator of the type

$$\phi \to q\bar{q}t\chi. \tag{11.29}$$

through the emission of χ' as shown in Figure 11.20. These decays can compete with the short $\phi \to t\chi$ decay when $m_\chi \approx m_{\chi'}$ and, in the full-hadronic decay of the top quark, two long decays resulting from a pair of ϕ mediators can result in a signature with 12 soft jets and moderate E_T^{miss}, being accessible by the SUSY multi-jet search.

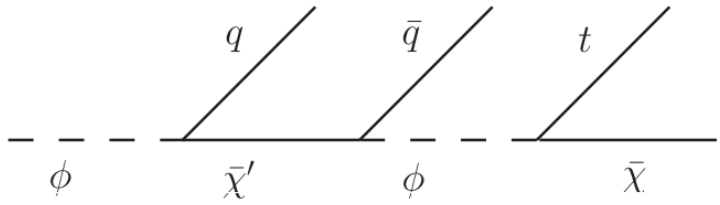

Figure 11.20 – Long decay of the ϕ mediator through $\phi \to q\bar{q}t\chi$ [89].

These models have been simulated at truth level in the ATLAS detector starting from the work of [89]. In these simulations, different values of m_ϕ, m_χ and λ were scanned while the mass of χ' was fixed at

$$m_{\chi'} = \frac{m_\phi + m_\chi}{2}. \tag{11.30}$$

Figure 11.21 shows the kinematic variables of a simulated model, where a large number of jets and moderate E_T^{miss} is visible. After scan of different parameter variables, 95% CL discovery limits have also been computed for 150 fb^{-1} of signal as shown in Figure 11.22. From these figures, it is visible how the multi-jet analysis could be sensitive to these models, in particular to values of λ close to unity.

Therefore, it is clear that these signatures with high jet multiplicity provide a very general and powerful way to test the Standard Model and to look for new physics. Additionally, after decoupling of the Higgs hierarchy mass from the Dark Matter problem and after making certain assumptions about Dark Matter from common Standard Model features, models providing identical signatures have been found [89], justifying the pursuit of this search in the next years at the LHC.

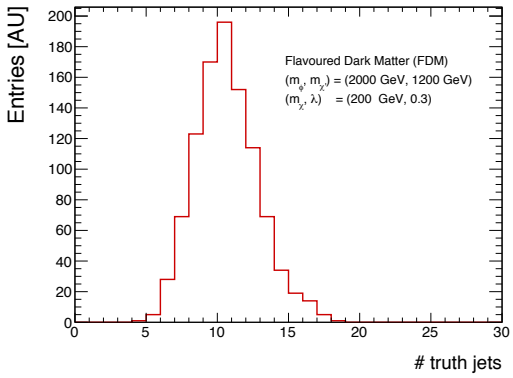

(a)

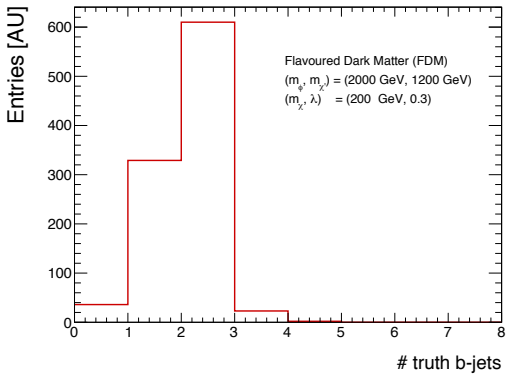

(b)

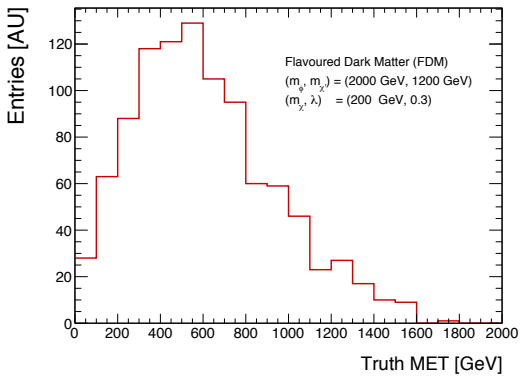

(c)

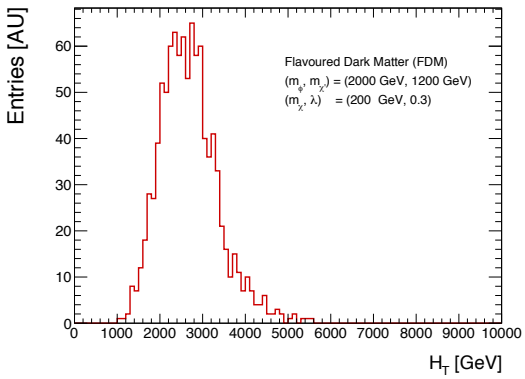

(d)

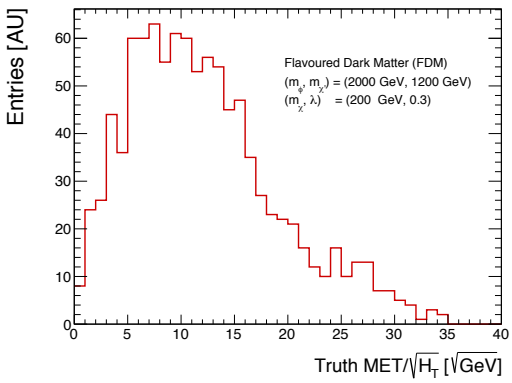

(e)

Figure 11.21 – Truth level (a) number of jets, (b) number of b-jets, (c) truth E_T^{miss}, (d) H_T and (e) E_T^{miss} significance. Simulations have been made using the model described in [89]. The masses of the model particles were fixed at $m_\Phi = 2000\,GeV$, $m_{\chi'} = 1200\,GeV$, $m_{\chi'} = 200\,GeV$ while $\lambda = 0.3$.

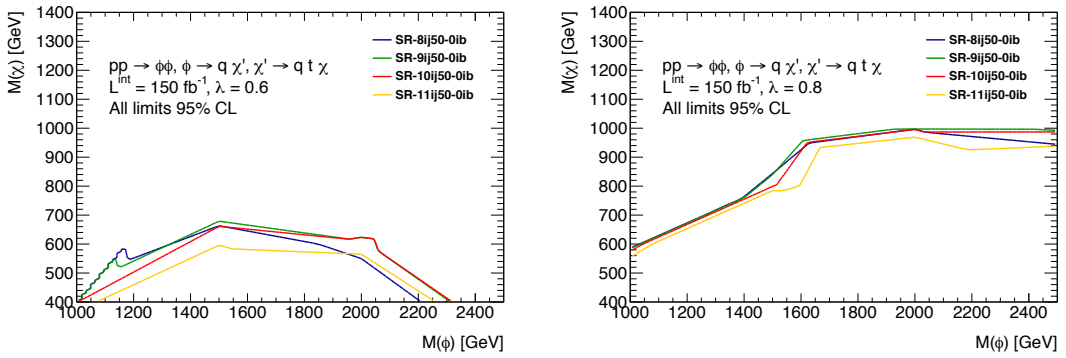

(a) $\lambda = 0.6$ (b) $\lambda = 0.8$

Figure 11.22 – 95% CL poisson discovery limits in the long decays of the FDM ϕ mediator for different analysis signal regions. (a) shows the discovery limits obtained for signals simulated with $\lambda = 0.6$, while (b) considers $\lambda = 0.8$.

12

CONCLUSIONS AND OUTLOOK

"Luna: I think I'll just go down and have some pudding and wait for it all to turn up — it always does in the end."

– J.K. Rowling, *Harry Potter and the Order of the Phoenix*

The Run 2 of the LHC is now finished, setting an extremely important landmark for the exploration of new phenomena and the understanding of the natural world. However, despite the huge efforts made by particle physicists in the last years, the Standard Model is still holding its validity and new physics seems to be either elusive or absent in the TeV range. This work described a specific search for strong supersymmetry performed by the ATLAS experiment in Run 2, targeting gluino-initiated cascade decays leading to final states with large jet multiplicities and Missing Transverse Momentum. Despite the 139 fb^{-1} of data collected for this search between 2015 and 2018, no evidence for new physics has been reported.

The absence of strong supersymmetry is now seriously putting under stress the motivations behind this theory and the hierarchy problem of the Higgs, causing large debates within the scientific community. However, it must not be forgotten that very often in physics, experiments not finding an answer to a specific question are the ones leading to the greatest advancements of that field and to a better understanding of the natural world. A classic example is the Michelson-Morley experiment (1887) that, demonstrating the absence of an aether medium for the propagation of light, led to one of the most significant revolutions in the understanding of the natural world with Einstein's theory of relativity (1905). Therefore, the increased knowledge provided by the second run of the LHC and the increased exclusion limits on strong supersymmetric particles might represent an extremely important achievement that only the next decades will reveal. Meanwhile, explorations for new phenomena and less constrained SUSY scenarios (*e.g.* RPV SUSY, EW SUSY, etc.) must continue in the next years, specially at the High-Luminosity LHC where the 5 times increased luminosity might uncover physics effects that are currently hidden due to their extremely low production rates. In this context, this work also presented a set of studies about online track-based pileup mitigation showing important reductions of the background trigger rates using the Hardware-based Track Trigger (HTT) system designed for the upgrade of the ATLAS Trigger and Data Acquisition system for HL-LHC. This feature will be fundamental to cope with the huge data flow of HL-LHC, allowing to keep efficient selections of important physics signal such as $HH \to b\bar{b}b\bar{b}$ and E_T^{miss}-initiated signatures.

This work described important contributions to the ATLAS detector and reconstruction framework. Particle Flow reconstruction has been commissioned for the ATLAS experiment during the second run of the LHC and the work described in the previous chapters about Particle Flow E_T^{miss} represented an important piece towards the achievement of this goal. Significant enhancements of the Particle Flow reconstruction precision with respect to standard calorimeter-based techniques have been

shown, leading to a new default E_T^{miss} reconstruction for the LHC Run 3 and probably beyond (HL-LHC). This reconstruction might be improved even further in the future, and new ideas for neutral pileup mitigation have been illustrated in the previous chapters, showing potential enhancements for the future of the ATLAS jet and E_T^{miss} reconstruction. Now that both ATLAS and CMS rely on Particle Flow reconstruction, this might strengthen even more the utilization of such techniques in future collider experiments (*e.g.* CLIC, FCC-ee and ILC), where an extremely accurate jet and E_T^{miss} reconstruction will be needed in order to achieve the necessary precision to explore new physics signals through precision Standard Model measurements.

A

ADDITIONAL ELEMENTS OF THEORY

Contents

A.1 GROUP THEORY AND SYMMETRIES

In Particle Physics, two theories provide the description of particles interactions: *quantum mechanics* and *special relativity*. The fusion of those theories is called *theory of quantum fields (QFT)* and it provides the mathematical framework necessary for theoretical predictions in particle physics. These theories rely on the invariance under certain *transformation groups*, leading to conserved quantities due to Noether theorem [1].

In Mathematics, a group is defined as a set G supplied by a binary operation $\otimes$ combining two elements of G and satisfying the following *axioms*:

CLOSURE $\forall a, b \in G$ the result of $a \otimes b$ is also an element of G.

ASSOCIATIVITY $\forall a, b, c \in G$ then $(a \otimes b) \otimes c = a \otimes (b \otimes c)$.

IDENTITY ELEMENT $\forall a \in G$ there exists a unique element $e \in G$ such that $e \otimes a = a \otimes e = a$.

INVERSE ELEMENT $\forall a \in G$ there exists an element $a^{-1} \in G$ such that $a \otimes a^{-1} = a^{-1} \otimes a = e$, where e is the *identity element*.

Moreover, this group is called *Abelian* if it satisfy also the commutativity:

$$a \otimes b = b \otimes a, \quad \forall a, b \in G. \tag{A.1}$$

If this condition is not satisfied, the group is simply called a *non-Abelian group*.

In Quantum Field Theory, we distinguish two types of symmetries:

- **Space-time symmetries:** these symmetries correspond to the transformations acting on space-time coordinates:

$$x^\mu \to x'^\mu(x^\mu) \quad \forall \{\mu, \nu\} \in \{0, 1, 2, 3\}. \tag{A.2}$$

  Classical examples of space-time symmetries are *Lorentz and Poincaré transformations* defining special relativity.

- **Internal symmetries:** these symmetries directly act on the fields leaving space-time unchanged:

$$\Phi^a(x) \to M^a{}_b \Phi^b(x). \tag{A.3}$$

  These symmetries are called **global** if $M^a{}_b$ is space-time independent while **local** if $M^a{}_b$ explicitly depends from space-time coordinates

In the next sections we will introduce a fundamental type of quantum field theory based on the invariance of these symmetries also known as *Yang-Mills theories*.

A.2 YANG-MILLS THEORIES

Yang-Mills theories are gauge theories based on the invariance under Poincaré and $SU(N)$ groups, where $SU(N)$ is the group of *special unitary matrices of order* N[26]. These theories are currently used to describe elementary particle physics using Abelian and non-Abelian groups. The non-Abelian gauge formalism is a milestone for the unification of the weak and electromagnetic forces (*i.e.* $U(1) \times SU(2)$), as well as in the description of quantum chromodynamics (*i.e.* $SU(3)$) for strong interactions (see Section 2.2 and 2.1). A classical example of Abelian Yang-Mills theory is represented by *Quantum Electrodynamics* (QED) which will be discussed in the following section.

A.2.1 *Quantum Electrodynamics (QED)*

We want to illustrate here the concept of gauge invariance and charge conservation using a pratical example: Quantum Electrodynamics (QED). QED corresponds to the simplest Abelian Yang-Mills theory and it is parametrised by the local gauge group $U(1)$. The main ingredients of such theory are a Dirac spinor $\psi(x)$ (representing the electron and the positron), and a gauge field A^μ (representing the photon mediator). In QED, these fields transform as

$$\psi \to e^{ie\alpha(x)}\, \psi(x), \tag{A.4}$$

$$\overline{\psi} \to e^{-ie\alpha(x)}\, \overline{\psi}(x), \tag{A.5}$$

$$A^\mu \to A^\mu + \partial_\mu \alpha(x). \tag{A.6}$$

The gauge invariance of the field A^μ is fundamental as it allows to eliminate those components of the field which are unphysical degrees of freedom[27].

In the case of a local gauge symmetry (*i.e.* α is space-time dependent) a *covariant derivative* D^μ has to be introduced in the spinor kinetic term in order to conserve gauge invariance. This derivative can be defined as

$$D^\mu = \partial^\mu - ieA^\mu, \tag{A.7}$$

[26] A general $n \times n$ matrix $U \in SU(N)$ is characterized by the properties

$$UU^\dagger = 1 \quad \text{and} \quad \det(U) = 1.$$

[27] The vector field A^μ has four degrees of freedom while spin-1 particles have at most 3 degrees of freedom. One of these components can be removed using gauge invariance.

and it's possible to show that the QED Lagrangian

$$\mathcal{L}_{QED} = i\overline{\psi}\gamma^{\mu}D_{\mu}\psi - m\overline{\psi}\psi - \frac{1}{4}F_{\mu\nu}F^{\mu\nu} \tag{A.8}$$

is invariant under $U(1)_{\text{gauge}}$ since

$$D^{\mu}\psi \to e^{ie\alpha(x)}D^{\mu}\psi. \tag{A.9}$$

The kinetic term associated to the vector field $-\frac{1}{4}F^{\mu\nu}F_{\mu\nu}$ is the only possible term that depends on A^{μ} derivatives and which possess at the same time gauge and Lorentz invariance, C and P invariance, and renormalizability. It is possible to note that gauge invariance forbids mass terms of the form $\mu^2 A^{\mu}A_{\mu}$ implying that **massive gauge bosons are forbidden in Yang-Mills theories**. This could represent a problem as the weak gauge bosons $W^{\pm}, Z$ have a well defined mass. The Higgs mechanism provides a solution to this problem as the generation of W and Z masses is provided after the spontaneous breaking of the gauge symmetry (refer to Section 2.3 for more details).

A.2.2 *Non-abelian Yang-Mills theories*

Let us consider now the non-abelian group $SU(N)$ where $UU^{\dagger} = 1$ and $\det(U) = 1$. The U matrices can be written as

$$U = U(\alpha) = \exp(ig\alpha^{A}t^{A}), \tag{A.10}$$

where the $t^{A}, A = 1, \ldots, N^2 - 1$ are a the **generators** of the $SU(N)$ group, g a *coupling constant* and α^{A} are real constants. It is possible to show that the Lie algebra endowed by the set of generators satisfy the commutations relations

$$\left[t^{A}, t^{B}\right] = if^{ABC}t^{C}, \tag{A.11}$$

where f^{ABC} are called the *structure constant* of the $SU(N)$ group. As we have previously seen, the QED $U(1)_{\text{local}}$ group is clearly an abelian Yang-Mills theory simply because of the 1×1 identity matrix spanning the group generators trivially commute with itself.

In general, $SU(N)$ invariant theories can be written using the **N-tuplets** notation Φ such that

$$\Phi = \begin{pmatrix} \phi_1 \\ \phi_2 \\ \vdots \\ \phi_N \end{pmatrix} \quad \text{and} \quad \Phi \to \Phi' = U\Phi. \tag{A.12}$$

For example, the main objects of an $SU(2)$ invariant theory are called *doublets* while *triplets* for an $SU(3)$ invariant theory such as QCD.

We want to determine now the number of degrees of freedom of an $SU(N)$ theory as this will correspond to the number of generators t^{A} spanning the group algebra:

$$\text{ndof}(SU(N)) = \underbrace{2N^2}_{N\times N \text{ complex matrix}} - \underbrace{\left(N + 2\frac{N(N-1)}{2}\right)}_{UU^{\dagger}=1} - \underbrace{1}_{\det(U)=1} = N^2 - 1. \tag{A.13}$$

Therefore, we can distinguish the following number of degrees of freedom:

- $U(1)$ has 1^2 degrees of freedom. This corresponds to the **photon** in QED.
- $SU(2)$ has $2^2 - 1 = 3$ degrees of freedom. These correspond to the W^+, W^- and Z bosons in the weak theory.
- $SU(3)$ has $3^2 - 1 = 8$ degrees of freedom. These correspond to the 8 gluons of QCD.

Let us include now local gauge invariance on top of $SU(N)$. Exactly as we did for the abelian case we need to define a covariant derivative D^μ such that $\left[D^\mu, U\right] = 0$

$$D^\mu = \partial^\mu - igA^\mu, \tag{A.14}$$

where $A^\mu = A^\mu_A t^A$. It is easy to show that the transformation law

$$\boxed{A^\mu \to A'^\mu = UA^\mu U^{-1} + \frac{i}{g} U\partial^\mu U^{-1}} \tag{A.15}$$

implies

$$\boxed{D^\mu \to UD^\mu U^{-1},} \tag{A.16}$$

and that $D^\mu \Phi \to UD^\mu \Phi$. By considering only the first order g terms of Eq. (A.15) we can compute

$$\begin{aligned} A^\mu &\to \left(1 + ig\alpha_A t^A\right) A^\mu \left(1 - ig\alpha_A t^A\right) + \underbrace{\frac{i}{g}\left(1 + ig\alpha_A t^A\right)\partial^\mu\left(1 - ig\alpha_A t^A\right)}_{\partial^\mu \alpha_C t^C} \\ &= A^\mu + ig\left[\alpha_A t^A, A^\mu\right] + \partial^\mu \alpha_C t^C = A^\mu_C t^C + ig\alpha_A A^\mu_C \underbrace{\left[t^A, t^C\right]}_{if^{ACB}t^B} + \partial^\mu \alpha_C t^C \\ &= \left(A^\mu_C - g\alpha_A A^\mu_B f^{ABC} + \partial^\mu \alpha_C\right) t^C \end{aligned}$$

and obtain the gauge transformation for A^μ_C, $C = 1, 2, \ldots, N^2 - 1$

$$\boxed{A^\mu_C \to A^\mu_C - g\alpha_A A^\mu_B f^{ABC} + \partial^\mu \alpha_C.} \tag{A.17}$$

Starting from $\left[D^\mu, D^\nu\right]\phi = -igF^{\mu\nu}\phi$ and (A.14) it is possible to derive a formal definition of $F^{\mu\nu} = F^{\mu\nu}_A t^A$ in non-Abelian gauge theories:

$$F^{\mu\nu} = \partial^\mu A^\nu - \partial^\nu A^\mu - ig\left[A^\mu, A^\nu\right], \tag{A.18}$$

$$F^{\mu\nu}_A = \partial^\mu A^\nu_A - \partial^\nu A^\mu_A + gA^\mu_B A^\nu_C f^{ABC}. \tag{A.19}$$

The Lagrangian density associated to the vector fields $A^\mu_C, C = 1, 2, \ldots, N^2 - 1$ becomes

$$\mathcal{L}_{YM} = -\frac{1}{4} F^{\mu\nu}_A F^A_{\mu\nu} = -\frac{1}{4} \mathrm{Tr}\left[F^{\mu\nu} F_{\mu\nu}\right], \tag{A.20}$$

where the suffix YM stands for Yang-Mills. Due to the presence of quadratic A^μ_C terms in Eq. (A.19), $\mathcal{L}_{YM}$ contains also the self-interactions of vector fields typical of

non-Abelian gauge theories. Indeed, after a simple calculation it is possible to show that

$$\begin{aligned}\mathcal{L}_{YM} = -\frac{1}{4}F^{\mu\nu}_{A}F^{A}_{\mu\nu} = -\frac{1}{4}F^{\mu\nu}_{A}F^{A}_{\mu\nu}\Big|_{\text{abelian}} \\ - g f^{ABC}\left(\partial_\mu A_{A\nu}\right)A^{\mu}_{B}A^{\nu}_{C} \\ - \frac{g^2}{4}f^{ABC}f^{ADE}A^{\mu}_{B}A^{\nu}_{C}A_{D\mu}A_{E\nu},\end{aligned} \tag{A.21}$$

which shows explicitely the rising of the self-interaction terms of degree 3 and 4.

This feature has dramatically important phenomenological consequences since the electroweak and strong gauge boson mediators (*i.e.* gluons and W,Z bosons) carries self interactive terms as documentated in Section 2.1 and 2.2.

A.3 THE WESS-ZUMINO MODEL

The *Wess-Zumino* model represents the simplest possible form of supersymmetric model. This model is essentially composed of two massless fields:

- a complex scalar field ϕ;
- a left-chiral Weyl spinor χ.

The Lagrangian corresponding to this model can be written as

$$\mathcal{L} = \partial_\mu\phi\partial^\mu\phi^\dagger + \chi^\dagger i\bar{\sigma}^\mu\partial_\mu\chi, \tag{A.22}$$

simply representing the combination of the kinetic terms associated to the massless scalar field ϕ and the massless Weyl-spinor field χ.

At first, let us proof that this Lagrangian is invariant under supersymmetry. In order to do this we need to introduce *supersymmetry transformations*. Previously, we have illustrated that supersymmetry represents a boson-fermion symmetry. Therefore, we can expect some type of boson-to-fermion (and also fermion-to-boson) transformation for ϕ and χ. Let us introduce an infinitesimal parameter of this transformation denoted ξ and let us begin the discussion about the ϕ variation $\delta\phi$. We have said that the supersymmetric transformation should transform a boson into a fermion. Therefore, it is natural to choose

$$\delta\phi \approx \xi\chi. \tag{A.23}$$

However, we are already in front of a problem: χ is a Weyl spinor whereas ϕ is a scalar. In order to save the Lorentz invariance of the SUSY transformation it is immediately clear that ξ **must be a Weyl spinor as well** and that $\delta\phi$ must be a Lorentz scalar. This can be achieved by introducing by parametrising the supersymmetry transformation with an infinitesimal left-chiral Weyl spinor ξ such as

$$\xi = \begin{pmatrix}\xi_1 \\ \xi_2\end{pmatrix}. \tag{A.24}$$

This lead us to the transformation of ϕ and $\phi^\dagger$ parametrised by

$$\begin{aligned}\delta\phi &= \xi\cdot\chi = \xi^a\chi_a,\\ \delta\phi^\dagger &= \overline{\xi}\cdot\overline{\chi} = \xi_{\dot{a}}\chi^{\dot{a}}.\end{aligned} \tag{A.25}$$

It is important to remark here that the considered SUSY parameter ξ **is not space-time dependent** (*i.e.* $\partial_\mu\xi = 0$), implying that the considered set of supersymmetric transformations is *global* and not *local*. In this context, it can be shown that the introduction of a space-time dependent SUSY parameter $\xi(x^\mu)$ introduces in the Lagrangian a new gauge field having the same properties of the graviton. Due to this reason local SUSY transformations are called supergravity (or *SUGRA*) theories, which will not be covered here as these go beyond the scope of this document.

We have now found our SUSY parameter ξ and the transformations associated to the two degrees of freedom of the complex scalar field ϕ. We are still missing the transformations of the left-chiral Weyl spinor χ. It is possible to show using a similar argument to what it has been done for $\delta\phi, \delta\phi^\dagger$ that these can be written as

$$\begin{aligned}\delta\chi &= -i\left(\partial_\mu\phi\right)\sigma^\mu i\sigma^2\xi^*,\\ \delta\chi^\dagger &= -i\left(\partial_\mu\phi^\dagger\right)\xi^T i\sigma^2\sigma^\mu,\end{aligned} \tag{A.26}$$

where

$$\xi^* = \begin{pmatrix}\xi_1^*\\ \xi_2^*\end{pmatrix}. \tag{A.27}$$

It is possible to show that the free Wess-Zumino Lagrangian (A.22) is invariant under the SUSY transformations provided by Eq. (A.25) and (A.26). However, this equality holds only when the equation of motion provided by the Euler-Lagrange equation are satisfied. This means that the algebra of this SUSY model closes only when the particles are on-shell which is not a very nice feature considering that we would like to have supersymmetry to be valid also for virtual particles. We will see in the next section that there is a simple workaround for this imposed by the introduction of a non-physical scalar field generally refered as *auxiliary field*. However, before closing this first introduction to the simplesy SUSY model we remark that in order to keep the dimension of the Lagrangian density $\mathcal{L}$ at 4 ($[\mathcal{L}] = 4$) the dimension of ϕ, χ and ξ are respectively

$$\begin{aligned}[\phi] &= \left[\phi^\dagger\right] = 1,\\ [\chi] &= \left[\chi^\dagger\right] = \frac{3}{2},\\ [\xi] &= \left[\xi^\dagger\right] = -\frac{1}{2}.\end{aligned} \tag{A.28}$$

However, as we have previously explained, the SUSY transformation of Eq. (A.25) and (A.26) closes only on-shell for the free Wess-Zumino Lagrangian given in Eq. (A.22). This feature can be avoided using a trick, which consists in the introduction of a new term composed of a unphysical field $F(x^\mu)$ generally called *auxiliary field*. The new Lagrangian density including this field can be written as

$$\mathcal{L} = \partial_\mu\phi\partial^\mu\phi^\dagger + \chi^\dagger i\bar{\sigma}^\mu\partial_\mu\chi + FF^\dagger, \tag{A.29}$$

where we can see that, from the Euler-Lagrange equation, the auxiliary field F is unphysical since $F(x^\mu) = F^\dagger(x^\mu) = 0$.

BIBLIOGRAPHY

[1] E. Noether and M. A. Tavel. Invariante Variationsprobleme. In *Transport Theory and Statistical Physics*, volume 1, pages 183–207. 1971.

[2] The ATLAS Collaboration. E_T^{miss} performance in the ATLAS detector with 2015-2016 LHC p-p collisions. *ATLAS-CONF-2018-023*, 2018.

[3] The ATLAS Collaboration. Technical Design Report (TDR) TDAQ Phase-II Upgrade of the ATLAS detector. *CERN-LHCC-2017-020. ATLAS-TDR-029*, 2018.

[4] The ATLAS Collaboration. Search for new phenomena in final states with large jet multiplicities and missing transverse momentum using $\sqrt{s} = 13$ TeV proton-proton collisions recorded by ATLAS in Run 2 of the LHC. *ATLAS-CONF-2020-002*, 2020.

[5] The ATLAS Collaboration. Pursuit of new phenomena in final states with high jet multiplicity, high jet masses and missing transverse momentum with ATLAS at $\sqrt{s} = 13$ TeV. *ATLAS-CONF-2016-095*, 2016.

[6] The ATLAS Collaboration. Search for new phenomena with large jet multiplicities and missing transverse momentum using large-radius jets and flavour-tagging at ATLAS in 13 TeV pp collisions. *Journal of High Energy Physics*, 2017(12), 2017.

[7] The ATLAS Collaboration. Reinterpretation of searches for supersymmetry in models with variable R-parity-violating coupling strength and long-lived R-hadrons. *ATLAS-CONF-2018-003*, 2018.

[8] B. Odom, D. Hanneke, B. D'urso, and G. Gabrielse. New measurement of the electron magnetic moment using a one-electron quantum cyclotron. *Physical Review Letters*, 97(3), 2006.

[9] A. Purcell. Go on a particle quest at the first CERN webfest. Le premier webfest du CERN se lance à la conquête des particules. *BUL-NA-2012-269. 35/2012*, Aug 2012.

[10] The LHCb Collaboration. Observation of $J/\psi p$ Resonances Consistent with Pentaquark States in $\Lambda_b^0 \to J/\psi K^- p$ Decays. *Physical Review Letters*, 115(7), 2015.

[11] M. Tanabashi et al. (Particle Data Group). Review of Particle Physics. *Physical Review D*, 98(3), 2018.

[12] B. Allanach. Beyond the Standard Model. *Proceedings of the 2016 European School of High-Energy Physics, ESHEP*, 2019.

[13] C.M. Becchi and G. Ridolfi. *An Introduction to relativistic processes and the Standard Model of Electroweak interactions*. Springer, ISBN-10 88-470-0420-9, 2006.

[14] A. Pich. The Standard Model of Electroweak Interactions. *Proceedings of the 2006 European School of High-Energy Physics, ESHEP*, 2007.

[15] The UA1 Collaboration. Experimental observation of isolated large transverse energy electrons with associated missing energy at $\sqrt{s} = 540$ GeV. *Phys. Lett. B 122*, pages 103–116, 1983.

[16] The UA1 Collaboration. Experimental observation of lepton pairs of invariant mass around 95 GeV/c^2 at the CERN SPS collider. *Phys. Lett. B 126*, pages 398–410, 1983.

[17] F. Englert and R. Brout. Broken symmetry and the mass of gauge vector mesons. *Phys. Rev. Lett.*, 13:508, 1964.

[18] P. W. Higgs. Broken Symmetries and the masses of gauge bosons. Technical Report 16, 1964.

[19] G. S. Guralnik, C. R. Hagen, and T. W. B. Kibble. Global Conservation Laws and Massless Particles. *Physical Review Letters*, 13(20):585–587, nov 1964.

[20] The ATLAS Collaboration. Observation of a new particle in the search for the Standard Model Higgs boson with the ATLAS detector at the LHC. *Physics Letters B*, 716(1):1–29, 2012.

[21] The CMS Collaboration. Observation of a new boson at a mass of 125 GeV with the CMS experiment at the LHC. *Physics Letters B*, 716(1):30–61, 2013.

[22] The ATLAS Collaboration. Search for the standard model Higgs boson produced in association with top quarks and decaying into a $b\bar{b}$ pair in pp collisions at $\sqrt{s} = 13$ TeV with the ATLAS detector. *Physical Review D*, 97(7), 2018.

[23] The CMS Collaboration. Observation of Higgs Boson Decay to Bottom Quarks. *Physical Review Letters*, 121(12), 2018.

[24] The ATLAS Collaboration. Combined measurements of Higgs boson production and decay using up to 80 fb^{-1} of proton-proton collision data at $\sqrt{s} = 13$ TeV collected with the ATLAS experiment. *Physical Review D*, 101(1), 2020.

[25] The ATLAS Collaboration. Summary plots from the atlas standard model physics group. https://atlas.web.cern.ch/Atlas/GROUPS/PHYSICS/CombinedSummaryPlots/SM/index.html, 2020-01-15.

[26] S. P. Martin. A Supersymmetry Primer. 2016.

[27] Muon (g-2) Collaboration. Final report of the E821 muon anomalous magnetic moment measurement at BNL. *Physical Review D*, 73(7), 2006.

[28] J. Wess and B. Zumino. Supergauge transformations in four dimensions. *Nuclear Physics B*, 70(1):39–50, feb 1974.

[29] S. Coleman and J. Mandula. All possible symmetries of the S matrix. *Physical Review*, 159(5):1251–1256, 1967.

[30] P. LaBelle. *Supersymmetry DeMYSTiFied*. McGraw-Hill Education, 2010.

[31] C. Borschensky, M. Krämer, A. Kulesza, M. Mangano, S. Padhi, T. Plehn, and X. Portell. Squark and gluino production cross sections in pp collisions at $\sqrt{s} = 13, 14, 33$ and 100 TeV. *European Physical Journal C*, 74(12):1–12, 2014.

[32] B. Fuks, M. Klasen, D. R. Lamprea, and M. Rothering. Precision predictions for electroweak superpartner production at hadron colliders with Resummino. *European Physical Journal C*, 73:2480, 2013.

[33] R. Barbier, C. Bérat, M. Besançon, M. Chemtob, A. Deandrea, E. Dudas, P. Fayet, S. Lavignac, G. Moreau, E. Perez, and Y. Sirois. R-Parity-Violating Supersymmetry. *Physics Reports*, 420:1–202, 2005.

[34] L. Evans and Philip B. LHC machine. *Journal of Instrumentation*, 3(08):S08001–S08001, aug 2008.

[35] E. Mobs. The CERN accelerator complex. Complexe des accélérateurs du CERN. https://cds.cern.ch/record/2684277, 2019.

[36] P. Pugnat and A. Siemko. Review of Quench Performance of LHC Main Superconducting Magnets. *IEEE Transactions on Applied Superconductivity*, 17(2):1091–1096, June 2007.

[37] J. Caron. Cross section of LHC dipole. AC Collection. Legacy of AC. Pictures from 1992 to 2002., May 1998.

[38] J. Caron. LHC quadrupole cross section. AC Collection. Legacy of AC. Pictures from 1992 to 2002., May 1998.

[39] G. Iadarola, L. Mether, and G. Rumolo. Filling schemes and e-cloud contraints for 2017. pages 239–244. 6 p, 2017.

[40] T. Argyropoulos, S. Dubourg, and G. Trad. Proceedings of the 2017 Evian Workshop on LHC Beam Operations. 2019.

[41] The ATLAS Collaboration. Luminosity determination in pp collisions at $\sqrt{s} =$ 13 TeV using the ATLAS detector at the LHC. *ATLAS-CONF-2019-021*, 2019.

[42] The ATLAS Collaboration. ATLAS Run-2 Luminosity public results. https://twiki.cern.ch/twiki/bin/view/AtlasPublic/LuminosityPublicResultsRun2, 2020.

[43] The ATLAS Collaboration. ATLAS Run-1 Luminosity public results. https://twiki.cern.ch/twiki/bin/view/AtlasPublic/LuminosityPublicResults, 2020.

[44] The ATLAS Collaboration. The ATLAS experiment at the CERN large hadron collider. *Journal of Instrumentation*, 3(08):S08003–S08003, aug 2008.

[45] M. Alviggi, V. Canale, S. Patricelli, L. Merola, A. Aloisio, and G. Chiefari. The ATLAS experiment at the CERN Large Hadron Collider. *Journal of Instrumentation*, 3:8003–8008, 2008.

[46] The ATLAS Collaboration. ATLAS pixel detector electronics and sensors. *Journal of Instrumentation*, 3:P07007, 2008.

[47] A. La Rosa. The ATLAS Insertable B-Layer: From construction to operation. *Journal of Instrumentation*, 11(12), oct 2016.

[48] A. Vogel. ATLAS Transition Radiation Tracker (TRT): Straw tube gaseous detectors at high rates. *Nuclear Instruments and Methods in Physics Research*, 732:277–280, 2013.

[49] C. Lippmann. Particle identification. 2018.

[50] N. Ilic. Performance of the ATLAS Liquid Argon Calorimeter after three years of LHC operation and plans for a future upgrade. *Journal of Instrumentation*, 9(3), 2014.

[51] The ATLAS Collaboration. Jet reconstruction and performance using particle flow with the ATLAS Detector. *European Physical Journal C*, 77(7), 2017.

[52] The ATLAS Collaboration. Performance of the ATLAS Trigger System in 2015. *European Physical Journal C*, 77, 2017.

[53] W. Buttinger. The ATLAS Level-1 Trigger System. In *Journal of Physics: Conference Series*, volume 396, 2012.

[54] The ATLAS Collaboration. Performance of the reconstruction of large impact parameter tracks in the inner detector of ATLAS. *ATL-PHYS-PUB-2017-014*, 2017.

[55] The ATLAS Collaboration. Performance of the ATLAS Silicon Pattern Recognition Algorithm in Data and Simulation at $\sqrt{s} = 7$ TeV. *ATLAS-CONF-2010-072*, 2010.

[56] The ATLAS Collaboration. Reconstruction of primary vertices at the ATLAS experiment in Run 1 proton–proton collisions at the LHC. *European Physical Journal C*, 77(5), 2017.

[57] The ATLAS Collaboration. Performance of primary vertex reconstruction in proton-proton collisions at $\sqrt{s} = 7$ TeV in the ATLAS experiment. *ATLAS-CONF-2010-069*, 2010.

[58] The ATLAS Collaboration. Topological cell clustering in the ATLAS calorimeters and its performance in LHC Run 1. *European Physical Journal C*, 77(7), mar 2016.

[59] The ATLAS Collaboration. Selection of jets produced in 13 TeV proton–proton collisions with the ATLAS detector. *ATLAS-CONF-2015-029*, 2015.

[60] S. Sapeta. QCD and Jets at Hadron Colliders. *Prog. Part. Nucl. Phys.*, 89:1–55, 2016.

[61] M. Cacciari, G. Salam, and G. Soyez. The anti-kt jet clustering algorithm. *Journal of High Energy Physics*, 04:063, 2008.

[62] S. Catani, M. H. Seymour, Y. L. Dokshitzer, and B. R. Webber. Longitudinally-invariant kt-clustering algorithms for Hadron-Hadron Collisions. *CERN-TH.6775/93*, 1993.

[63] The ATLAS Collaboration. Jet energy scale measurements and their systematic uncertainties in proton–proton collisions at $\sqrt{s} = 13$ TeV with the ATLAS detector. *Physical Review D*, 96(7):072002, 2017.

[64] The ATLAS Collaboration. Identification and rejection of pile-up jets at high pseudorapidity with the ATLAS detector. *European Physical Journal C*, 77(9):580, 2017.

[65] The ATLAS Collaboration. Tagging and suppression of pileup jets with the ATLAS detector. *ATLAS-CONF-2014-018*, 2014.

[66] The ATLAS Collaboration. ATLAS b-jet identification performance and efficiency measurement with $t\bar{t}$ events in pp collisions at $\sqrt{s} = 13$ TeV. *European Physical Journal C*, 79(11), 2019.

[67] The ATLAS Collaboration. Measurement of the photon identification efficiencies with the ATLAS detector using LHC Run 2 data collected in 2015 and 2016. *European Physical Journal C*, 79(3), 2019.

[68] The ATLAS Collaboration. Electron and photon performance measurements with the ATLAS detector using the 2015-2017 LHC proton-proton collision data. *Journal of Instrumentation*, 14(12):P12006, 2019.

[69] The ATLAS Collaboration. Muon reconstruction performance of the ATLAS detector in proton–proton collision data at $\sqrt{s} = 13$ TeV. *European Physical Journal C*, 76(5), 2016.

[70] The ATLAS Collaboration. Performance of missing transverse momentum reconstruction with the ATLAS detector using proton–proton collisions at $\sqrt{s} = 13$ TeV. *European Physical Journal C*, 78(11):903, 2018.

[71] The ATLAS Collaboration. Object-based missing transverse momentum significance in the ATLAS detector. *ATLAS-CONF-2018-038*, 2018.

[72] The ALEPH Collaboration. Performance of the ALEPH detector at LEP. *Nuclear Instruments and Methods in Physics Research*, 360(3):481–506, jun 1995.

[73] The CMS Collaboration. Particle-flow reconstruction and global event description with the CMS detector. *Journal of Instrumentation*, 12(10), 2017.

[74] The ATLAS Collaboration. Particle flow jet energy resolution in 2017 data and simulation. https://atlas.web.cern.ch/Atlas/GROUPS/PHYSICS/PLOTS/JETM-2019-01/, 2020.

[75] The ATLAS Collaboration. EM+JES and PFlow Pile-Up jet rate. https://atlas.web.cern.ch/Atlas/GROUPS/PHYSICS/PLOTS/JETM-2017-006/, 2020.

[76] The ATLAS Collaboration. Jet energy scale and resolution measured in proton-proton collisions at $\sqrt{s} = 13$ TeV with the ATLAS detector (*In Preparation*). Technical Report ATL-COM-PHYS-2019-281, CERN, Geneva, Apr 2019.

[77] M. Lüthi, M. Valente, and C. Young. Multivariate analysis techniques for Particle Flow-based neutral pileup suppression at the ATLAS experiment. 2019.

[78] D. Bertolini, P. Harris, M. Low, and N. Tran. Pileup per particle identification. *Journal of High Energy Physics*, 1410(10):59, 2014.

[79] M. Cacciari, G. Salam, and G. Soyez. SoftKiller, a particle-level pileup removal method. *European Physical Journal C*, 75(2):1–16, 2015.

[80] G. Soyez. Pileup mitigation at the LHC: A theorist's view. *Physics Reports*, 803:1–158, 2019.

[81] P. Speckmayer, A. Höcker, J. Stelzer, and H. Voss. The toolkit for multivariate data analysis, TMVA 4. In *Journal of Physics: Conference Series*, volume 219, 2010.

[82] The ATLAS Collaboration. Technical Design Report for the ATLAS Inner Tracker Pixel Detector. *CERN-LHCC-2017-021. ATLAS-TDR-030*, Sep 2017.

[83] T. Flick. The phase II ATLAS Pixel upgrade: The Inner Tracker (ITk). *Journal of Instrumentation*, 12(1), 2017.

[84] The ATLAS Collaboration. Technical Design Report for the Phase-I Upgrade of the ATLAS TDAQ System. Sep 2013. CERN-LHCC-2013-018, ATLAS-TDR-023. https://cds.cern.ch/record/1602235.

[85] M. Valente. The ATLAS Trigger and Data Acquisition Upgrades for the High-Luminosity LHC (HL-LHC). *Proceedings of the 2019 European Physical Society meeting in High Energy Physics, EPS-HEP*, 2019.

[86] R. Poggi. Design of the ATLAS Phase-II hardware-based tracking processor. *Nuclear Instruments and Methods in Physics Research*, 936:305 – 307, 2019. Frontier Detectors for Frontier Physics: 14th Pisa Meeting on Advanced Detectors.

[87] K. Dienes, D. Kim, H. Song, S. Su, B. Thomas, and D. Yaylali. Non-Minimal Dark Sectors: Mediator-Induced Decay Chains and Multi-Jet Collider Signatures. 2019.

[88] C. Gao, A. S. Shirazi, and J. Terning. Collider Phenomenology of a Gluino Continuum. *Journal of High Energy Physics*, (1):102, 2020.

[89] C. Kilic, M. D. Klimek, and J. Yu. Signatures of Top Flavored Dark Matter. *Physical Review D*, 91(5):054036, 2015.

[90] The ATLAS Collaboration. Search for new phenomena in final states with large jet multiplicities and missing transverse momentum with ATLAS using $\sqrt{s} = 13$ TeV proton-proton collisions. *Physics Letters B*, 757:334–355, 2016.

[91] The ATLAS Collaboration. Hunt for new phenomena using large jet multiplicities and missing transverse momentum with ATLAS in 4.7 fb^{-1} of $\sqrt{s} = 7$ TeV proton-proton collisions. *Journal of High Energy Physics*, 2012(7):1–39, 2012.

[92] The ATLAS Collaboration. Search for new phenomena in final states with large jet multiplicities and missing transverse momentum at $\sqrt{s} = 8$ TeV proton-proton collisions using the ATLAS experiment. *Journal of High Energy Physics*, 130(10), 2013.

[93] The ATLAS Collaboration. Summary of the ATLAS experiment's sensitivity to supersymmetry after LHC Run 1 - interpreted in the phenomenological MSSM. *Journal of High Energy Physics*, 10(10):134, 2015.

[94] The ATLAS Collaboration. Measurements of b-jet tagging efficiency with the ATLAS detector using $t\bar{t}$ events at $\sqrt{s} = 13$ TeV. *Journal of High Energy Physics*, 89(8), 2018.

[95] The ATLAS Collaboration. Jet reclustering and close-by effects in ATLAS Run 2. *ATLAS-CONF-2017-062*, (July):1–30, 2017.

[96] B. Nachman, P. Nef, A. Schwartzman, M. Swiatlowski, and C. Wanotayaroj. Jets from jets: re-clustering as a tool for large radius jet reconstruction and grooming at the LHC. *Journal of High Energy Physics*, 75(2), 2015.

[97] The ATLAS Collaboration. Search for R-parity-violating supersymmetric particles in multi-jet final states produced in p–p collisions at $\sqrt{s} = 13$ TeV using the ATLAS detector at the LHC. *Physics Letters B*, 785:136–158, 2018.

[98] R. D. Ball, V. Bertone, S. Carrazza, C. S. Deans, L. Del Debbio, S. Forte, A. Guffanti, N. P. Hartland, J. I. Latorre, J. Rojo, and M. Ubiali. Parton distributions for the LHC run II. *Journal of High Energy Physics*, 40(4):1–148, 2015.

[99] P. Artoisenet, R. Frederix, O. Mattelaer, and R. Rietkerk. Automatic spin-entangled decays of heavy resonances in Monte Carlo simulations. *Journal of High Energy Physics*, 2013(3), 2013.

[100] T. Sjöstrand, S. Mrenna, and P. Skands. A brief introduction to PYTHIA 8.1. *Computer Physics Communications*, 178(11):852–867, 2008.

[101] R. D. Ball, V. Bertone, S. Carrazza, C. S. Deans, L. Del Debbio, S. Forte, A. Guffanti, N. P. Hartland, J. I. Latorre, J. Rojo, and M. Ubiali. Parton distributions with LHC data. *Nuclear Physics B*, 867(2):244–289, 2013.

[102] The ATLAS Collaboration. ATLAS Pythia 8 tunes to 7 TeV data. *ATL-PHYS-PUB-2014-021*, 2014.

[103] S. Agostinelli et al. GEANT4 - A simulation toolkit. *Nuclear Instruments and Methods in Physics Research, Section A*, 506(3):250–303, jul 2003.

[104] M. Czakon, P. Fiedler, D. Heymes, and A. Mitov. NNLO QCD predictions for fully-differential top-quark pair production at the Tevatron. *Journal of High Energy Physics*, 34(5):1–41, 2016.

[105] T. Gleisberg and S. Höche. Comix, a new matrix element generator. *JHEP*, 12:039, 2008.

[106] S. Schumann and F. Krauss. A parton shower algorithm based on Catani-Seymour dipole factorisation. *Journal of High Energy Physics*, (3), 2008.

[107] S. Höche, F. Krauss, M. Schönherr, and F. Siegert. QCD matrix elements + parton showers. the NLO case. *Journal of High Energy Physics*, 27(4), 2013.

[108] G. Cowan, K. Cranmer, E. Gross, and O. Vitells. Asymptotic formulae for likelihood-based tests of new physics. *European Physical Journal C*, 71(2), 2011.

[109] A L Read. Presentation of search results: the CLs technique. *J. Phys. G: Nucl. Part. Phys*, 28:2693–2704, 2002.

[110] The ATLAS Collaboration. Search for squarks and gluinos in final states with jets and missing transverse momentum using 36 fb^{-1} of $\sqrt{s} = 13$ TeV pp collision data with the ATLAS detector. *Physical Review D*, 97(11), 2018.

[111] The ATLAS Collaboration. Search for supersymmetry in final states with missing transverse momentum and multiple b-jets in proton-proton collisions at $\sqrt{s} = 13$ TeV with the ATLAS detector. *Journal of High Energy Physics*, 2018(6), 2018.

[112] The ATLAS Collaboration. Search for new phenomena in a lepton plus high jet multiplicity final state with the ATLAS experiment using $\sqrt{s} = 13$ TeV proton-proton collision data. *Journal of High Energy Physics*, 2017(9), 2017.

[113] The ATLAS Collaboration. Search for supersymmetry in final states with two same-sign or three leptons and jets using 36 fb^{-1} of $\sqrt{s} = 13$ TeV pp collision data with the ATLAS detector. *Journal of High Energy Physics*, 2017(9), 2017.

[114] The ATLAS Collaboration. Search for massive supersymmetric particles decaying to many jets using the ATLAS detector in pp collisions at $\sqrt{s} = 8$ TeV. *Physical Review D*, D91(11):112016, 2015.

[115] J. M. Lorenz. Constraining natural supersymmetry with the ATLAS detector. https://indico.cern.ch/event/868249/attachments/1981633/3316008/CERN_seminar_180220_JLorenz.pdf, 2020.

[116] The ATLAS Collaboration. Search for squarks and gluinos in events with an isolated lepton, jets, and missing transverse momentum at $\sqrt{s} = 13$ TeV with the ATLAS detector. *Physical Review D*, 96(11), 2017.

[117] The ATLAS Collaboration. Search for squarks and gluinos in final states with same-sign leptons and jets using 139 fb^{-1} of data collected with the ATLAS detector. *CERN-EP-2019-161*, 2019.

[118] B. Penning. The Pursuit of Dark Matter at Collider - An Overview. *J. Phys. G: Nucl. Part. Phys*, 45(6):063001, 2017.

[119] The ATLAS Collaboration. Search for dark matter produced in association with bottom or top quarks in $\sqrt{s} = 13$ TeV pp collisions with the ATLAS detector. *Eur. Phys. J. C*, 78, 2018.